

**I. Global Simulations of Interactions between Aerosols  
and Future Climate**

**and**

**II. Sensitivity of Multiangle Imaging to the Optical and  
Microphysical Properties of Biomass Burning Aerosols**

Thesis by  
Wei-Ting Chen

In Partial Fulfillment of the Requirements  
for the Degree of  
Doctor of Philosophy



California Institute of Technology  
Pasadena, California

2009  
(Defended December 3, 2008)



## Acknowledgements

The past six and half years in Caltech have become an amazing and life-changing journey. It not only enables me to acquire the fundamental knowledge and proper attitudes of conducting scientific research, but also reveals to me the beauty and wonder of our Great Nature. There are many people who made this journey easier and pleasant by kindly offering their invaluable guidance, inspiration, and companionship.

First and the greatest gratitude to my thesis advisor, Prof. John Seinfeld, who is the most supportive supervisor I can ever imagine. His perpetual enthusiasm for science has motivated me, and he is always accessible and delight to help the students with our studies and research, providing his unmatched experience and superb knowledge.

Special thanks go to Dr. Ralph Kahn, my advisor of the MISR project. Dr. Kahn is always patient, thoughtful, and encouraging. He taught me the sound science of aerosol retrievals, and, as an outstanding and dedicated scientist, he also sets a great role model for me.

I would also like to acknowledge my thesis committee: Prof. Paul Wennberg, Prof. Tapio Schneider, and Prof. Yuk Lin Yung, for their guidance and care during these years.

The projects in this thesis were accomplished with tremendous assistance from many colleagues and peers: Prof. Hong Liao, Prof. Thanos Nenes, Prof. Peter Adams, Dr. Serena Chung, Dr. Loretta Mickley, Dr. David Nelson, Wen-Hao Li, Kevin Yau, and Dr. Barbara Gaitley. They have given their rich knowledge, excellent ideas, and precious time to help me solve numerous problems.

I am fortunate to have joined a wonderful research group. I received many help and inspiring inputs from the “modelers” in the Seinfeld group: Havala Pye, Amir Hakami, Daven Henze, Philip Stier, Yi-Chun Jean Chen, and Zachary Lebo, especially during our “secret coffee meetings”. I am also grateful to the other members in our group for their friendship in these years, especially Sally Ng and Julia Lu. In addition, I appreciate the help from our secretaries Ann Hilgenfeldr, Yvette Grant, Linda Scott, and Dian Buchness, who have made my research work at Caltech hassle-free.

My life in Southern California is enriched by many great friends: Yu Wang, Nina Lin, Hao-Teh Hsu, Hsin-Ling Wang, Jui-Lin Li, Hsi-Yen Ma, Chia-Chun Wu, Chien-Min Wu, Wei-Ju Chen, Chih-Yung Lee, Betsy Wang, my yoga teacher Nancy, and everyone in the Caltech Glee Clubs. My thoughts also go to many old friends in Taiwan: Sue-Ping Liu, Ko-Li Cheng, Meng-Shan Lu, Shu-Han Lin, and my high school teacher Yu-Ya Wu. Their friendships never fade even though we have been physically parted thousands of miles away. I would also like to thank Prof. Jen-Ping Chen at National Taiwan University for advising my undergraduate study and encouraging me to study abroad.

Lastly, but most importantly, I am grateful to the unconditional love and unwavering trust from my dear parents, Liang-Kuang Chen and Chin-Hsiu Szu, grandmother, Yuk-Tong Ou, brother, Wei-Teh Chen, and my life-companion, Eh Tan. To them I sincerely dedicate this thesis. My family members in Taiwan, Hong Kong, Indonesia, Canada, and the United States also show tireless support to my pursuit of the degree. I want to express the deepest gratitude to them from the bottom of my heart.

## **Abstract**

To understand the interaction between aerosols and climate, equilibrium simulations with a general circulation model are carried out in Part I to study the effects of future climate change on aerosol distributions, as well as the climate responses to future aerosol changes. The predicted warmer climate induced by carbon dioxide modifies the climate-sensitive emissions, alters the thermodynamic partitioning, and enhances wet removal of the aerosols. The direct radiative perturbations of aerosols, and the modification of clouds by aerosols can potentially change the temperature distribution, the hydrological cycle, and the atmospheric circulation; the pattern of climatic impacts from aerosols are differentiated from those of anthropogenic greenhouse gases. In Part II, the aerosol retrieval algorithm of the remote sensing instrument, the Multi-angle Imaging SpectroRadiometer (MISR), is assessed for the retrieval of biomass burning aerosols. By comparisons with coincident ground measurements and theoretical sensitivity tests, specific refinements to particle and mixture properties assumed in the algorithm for biomass burning aerosols are proposed. Representative case studies confirm the theoretical results and underline the key role of surface characterization in the remote sensing of aerosols.

## Table of Contents

Acknowledgements .....	iii
Abstract.....	v
Table of Contents .....	vi
List of Figures .....	ix
List of Tables .....	xv
Chapter 1 Introduction .....	1
Part I. Global Simulations of Interactions between Aerosols and Future Climate .....	7
Chapter 2 Roles of Climate Change in Global Predictions of Future Tropospheric Ozone and Aerosols .....	8
Abstract.....	9
2.1 Introduction .....	11
2.2 Model Description and Experimental Design .....	14
2.2.1 The Unified Model .....	14
2.2.2 Climate Simulations.....	16
2.2.3 Chemistry Simulations.....	17
2.2.4 Emission Inventories.....	19
2.3 Predicted Climate Change.....	20
2.3.1 Predicted Changes in Temperature.....	21
2.3.2 Predicted Changes in Hydrological Cycle .....	21
2.3.3 Predicted Changes in Winds .....	22
2.4 Effects of CO <sub>2</sub> -Driven Climate Change on Tropospheric Ozone and Aerosols .....	24
2.4.1 Predicted Changes in Ozone .....	24
2.4.2 Predicted Changes in Carbonaceous Aerosols .....	26
2.4.3 Predicted Changes in Sulfate and Nitrate Aerosols.....	27
2.4.4 Predicted Changes in Sea Salt and Mineral Dust .....	29
2.4.5 Effects of Climate Change in the Presence of Heterogeneous Reactions.....	31
2.5 Predicted O <sub>3</sub> and Aerosol Concentrations with Year 2100 Projected Emissions and Climate.....	33
2.6 Impact of Climate Change on Estimates of Year 2100 Direct Radiative Forcing .....	35

2.7	Summary and Discussion.....	38
	References.....	42
Chapter 3 Future Climate Impacts of Direct Radiative Forcing of Anthropogenic Aerosols, Tropospheric Ozone, and Long-lived Greenhouse Gases .....		
	Abstract.....	68
	Abstract.....	69
3.1	Introduction .....	71
3.2	Model Description and Experimental Design .....	73
3.2.1	The Unified Model .....	73
3.2.2	Climate Simulations.....	74
3.2.3	Present-day and Year 2100 Anthropogenic Aerosols, Tropospheric Ozone, and Greenhouse Gases .....	76
3.3	Estimated Changes in Global Climate .....	80
3.3.1	Surface Air Temperature.....	80
3.3.2	Tropospheric Temperature and Stability.....	82
3.3.3	Global Circulation .....	83
3.3.4	Hydrological Cycle.....	85
3.3.5	Energy Budgets .....	88
3.4	Estimated Regional Climate Changes in Asia in Winter Ozone and Aerosols .....	89
3.5	Summary and Conclusions.....	92
	References.....	95
Chapter 4 Global Climate Response to Anthropogenic Aerosol Indirect Effects: Present Day and Year 2100 .....		
	Abstract.....	119
	Abstract.....	120
4.1	Introduction .....	121
4.2	Descriptions of Global Models.....	124
4.2.1	CACTUS Unified Model and Offline Aerosol Mass Concentration.....	125
4.2.2	GISS-TOMAS Model, FN Activation Parameterization, and Derivation of Aerosol- $N_c$ Relationships .....	128
4.2.3	GISS III GCM and the Modification of Stratiform Cloud Scheme.....	131
4.2.3.1	Droplet Effective Radius and Cloud Optical Depth .....	132
4.2.3.2	Autoconversion Rate.....	133
4.2.3.3	Aerosol Direct Effect .....	134

4.3	Equilibrium Climate Simulations with GISS III GCM .....	135
4.4	Responses of the Equilibrium Climate to Perturbations of $N_c$ .....	139
4.4.1	Predicted Present-Day Equilibrium Climate .....	139
4.4.2	Effects of Change of $N_c$ from Pre-Industrial to Present Day on Equilibrium Climate .....	142
4.4.3	Perturbations of $N_c$ from Present Day to Year 2100 to Equilibrium Climate .....	146
4.5	Predicted Equilibrium Climate Response From Present Day to Year 2100 to the Combined Effects of GHG, ADE and AIE .....	148
4.6	Climate Sensitivities and Hydrological Sensitivities for ADE, AIE, and GHG: Comparing the Present work with Previous Related Studies.....	150
4.7	Summary and Conclusions.....	152
	References.....	156
	Part II. Sensitivity of Multiangle Imaging to the Optical and Microphysical Properties of Biomass Burning Aerosols.....	184
	Chapter 5 Sensitivity of Multiangle Imaging to the Optical and Microphysical Properties of Biomass Burning Aerosols .....	185
	Abstract.....	186
5.1	Introduction .....	187
5.2	Near-Coincident MISR-AERONET Measurements in Major BB Regions.....	190
5.2.1	Data Selection.....	190
5.2.2	Comparison of Near-coincident MISR-AERONET BB Cases.....	192
5.3	BB Particle Property Characterization.....	199
5.4	Theoretical Sensitivity Study for BB Aerosol Components .....	203
5.4.1	BB Aerosol Components and Mixing Groups .....	204
5.4.2	Radiative Transfer Simulations, and the $\chi^2$ Test Variables for Evaluating Agreement Between Simulated Reflectances in the Sensitivity Test.....	205
5.4.3	Results of MISR Theoretical Sensitivity to BB Components .....	207
5.5	MISR Research Retrieval Study of Field Cases with Proposed BB Components and Detailed Surface Characterization .....	211
5.5.1	Patches and Surface Characterization for Selected Field Cases.....	212
5.5.2	MISR Research Retrievals of Selected Field Cases .....	214
5.6	Summary and Conclusions.....	223
	References.....	228

## List of Figures

- Figure 2-1. Temperature responses in the equilibrium climate to the increase in CO<sub>2</sub> concentration from 368 ppmv in year 2000 to 836 ppmv in year 2100, including predicted changes (°C) in (a) annual mean surface air temperature and (b) zonal annual mean atmospheric temperature. The global mean value is indicated at the top right corner of Figure 2-1a. .... 56
- Figure 2-2. (a) Predicted year 2000 zonal annual mean equilibrium specific humidity (g-H<sub>2</sub>O kg-air<sup>-1</sup>) as a function of pressure. (b) Predicted changes in zonal annual mean equilibrium specific humidity (g-H<sub>2</sub>O kg-air<sup>-1</sup>) relative to year 2000. (c) Predicted changes (mm day<sup>-1</sup>) relative to year 2000 in annual mean precipitation. (d) Predicted changes (mm day<sup>-1</sup>) relative to year 2000 in zonal annual mean precipitation. The global mean value is indicated at the top right corner of Figure 2-2c. .... 57
- Figure 2-3. Latitude-pressure distributions of zonal and seasonal mean (a) present-day vertical velocity (10<sup>-5</sup> mb s<sup>-1</sup>), (b) changes in vertical velocity (10<sup>-5</sup> mb s<sup>-1</sup>) from year 2000 to year 2100, and (3) changes in mass stream function (1010 kg s<sup>-1</sup>) from 2000 to 2100. Positive values of the mass stream function indicate anticlockwise circulation. .... 58
- Figure 2-4. Predicted changes (m s<sup>-1</sup>) in (a) annual mean surface wind speed and (b) zonal annual mean surface wind speed from 2000 to 2100. The global mean change is indicated for Figure 2-4a. .... 59
- Figure 2-5. (a) Changes in January and July predicted surface-layer ozone concentrations (ppbv, CL2100EM2000 – CL2000EM2000) resulting from CO<sub>2</sub>-driven equilibrium climate change over 2000–2100. Global mean change is indicated at the top right corner of each panel. (b) Percentage changes ((CL2100EM2000 – CL2000EM2000) × 100/CL2000EM2000) in January and July zonal mean ozone concentrations. .... 60
- Figure 2-6. Changes in annual mean concentrations (ng m<sup>-3</sup>, CL2100EM2000 – CL2000EM2000) of (a) BC, (b) POA, and (c) SOA at selected layers resulted from the CO<sub>2</sub>-driven climate change over 2000–2100. Global mean change is indicated at the top right corner of each panel. .... 61
- Figure 2-7. (a) Zonal mean changes in OH concentrations (10<sup>5</sup> radicals cm<sup>-3</sup>) resulting from CO<sub>2</sub>-driven climate change (CL2100EM2000 – CL2000EM2000). (b) Zonal mean changes in OH concentrations (10<sup>5</sup> radicals cm<sup>-3</sup>) resulting from the changes in both climate and emissions (CL2100EM2100 – CL2000EM2000). Left panels are for January and right panels are for July. .... 62
- Figure 2-8. Predicted changes in annual mean sulfate concentration (pptv, CL2100EM2000 – CL2000EM2000) at the surface layer resulting from CO<sub>2</sub>-driven climate change from 2000 to 2100. Global mean change is indicated at the top right corner of the panel. .... 63

- Figure 2-9. Ratios of the predicted annual and zonal mean nitrate concentrations from CL2100EM2000 to CL2000EM2000. .... 64
- Figure 2-10. Annual mean differences between the effects of CO<sub>2</sub>-driven climate change in the presence and absence of heterogeneous reactions [(CL2100EM2000h – CL2000EM2000h) – (CL2100EM2000 – CL2000EM2000)] for the surface-layer concentrations of (a) O<sub>3</sub>, (b) sulfate, and (c) nitrate. The global mean value is indicated at the top right corner of each panel. .... 65
- Figure 2-11. (a) Predicted year 2100 surface-layer O<sub>3</sub> mixing ratios (ppbv) with changes in both climate and emissions. (b) Predicted changes in surface-layer O<sub>3</sub> mixing ratio (ppbv) from 2000 to 2100. (c) Differences (ppbv) between surface-layer O<sub>3</sub> mixing ratios simulated with changes in both climate and emissions and those with changes in emissions only. Top panels are simulated in the absence of the heterogeneous reactions as discussed in the text, while the bottom panels include heterogeneous reactions. The global mean value is indicated at the top right corner of each panel. .... 66
- Figure 2-12. (a) Predicted year 2100 surface-layer dry aerosol mass concentrations ( $\mu\text{g m}^{-3}$ ) with changes in both climate and emissions. Dry aerosol mass is the sum of sulfate, nitrate, ammonium, BC, POA, and SOA. (b) Predicted changes in surface-layer dry aerosol mass concentrations ( $\mu\text{g m}^{-3}$ ) from 2000 to 2100. (c) Differences ( $\mu\text{g m}^{-3}$ ) between surface-layer dry aerosol mass concentrations simulated with changes in both climate and emissions and those with changes in emissions only. Top panels are simulated in the absence of the heterogeneous reactions as discussed in the text, while the bottom panels include heterogeneous reactions. The global mean value is indicated at the top right corner of each panel. .... 67
- Figure 3-1. Annual and seasonal differences in column concentrations between present-day and year 2100 for anthropogenic aerosols ( $\text{mg m}^{-2}$ ) and tropospheric ozone (Dobson Units). (a) Ammonium sulfate (b) Ammonium nitrate (c) POA (d) SOA, (e) BC, and (f) O<sub>3</sub> (ANN = annual mean, DJF = seasonal mean over December-January-February, and JJA = seasonal mean over June-July-August) ..... 105
- Figure 3-2. Annual mean change in instantaneous forcing ( $\text{W m}^{-2}$ ) (a) at tropopause and (b) at surface imposed by changes of anthropogenic aerosol (left column), tropospheric ozone (middle column), and greenhouse gases (right column) between present-day and year 2100. .... 106
- Figure 3-3. Latitude-pressure distribution of changes in atmospheric forcing ( $\text{W m}^{-2}$ ) in (a) DJF and (b) JJA imposed by changes of anthropogenic aerosol, tropospheric ozone, and GHG between present-day and year 2100. .... 107
- Figure 3-4. Predicted change in global surface air temperature (K) in (a) DJF and (b) JJA. Note the color scale for  $\Delta\text{GHG}$  differs from the other two. .... 108
- Figure 3-5. Predicted zonal mean changes in surface air temperature (K). Note the vertical scale for  $\Delta\text{GHG}$  differs from the other two. .... 109

Figure 3-6. Latitude-pressure distribution of changes in annual mean temperature (K).	110
Figure 3-7. Latitude-pressure distribution of stream function ( $10^{10} \text{ kg s}^{-1}$ , positive values indicate counterclockwise flow) in (a) DJF and (b) JJA, and zonal wind ( $\text{m s}^{-1}$ , positive values indicate westerlies) in (c) DJF and (d) JJA. Left: seasonal mean in simulation PD; middle: $\Delta\text{AER}$ ; right: $\Delta\text{GHG}$ .	111
Figure 3-8. Latitude-pressure distribution of changes in annual mean specific humidity. (a) Absolute change ( $\text{g-H}_2\text{O kg-air}^{-1}$ ) and (b) relative change (%). Note the color scale in (b) differs between $\Delta\text{AER}$ and $\Delta\text{GHG}$ .	112
Figure 3-9. Predicted zonal mean changes in (a) excess precipitation (total precipitation minus evaporation, $\text{mm day}^{-1}$ ) and (b) moist-convective (MC) precipitation ( $\text{mm day}^{-1}$ ). Note the vertical scales differ between $\Delta\text{AER}$ and $\Delta\text{GHG}$ .	113
Figure 3-10. Predicted zonal mean changes in (a) moist-convective (MC) cloud cover (%), and (b) high cloud cover (%). Note the vertical scales differ between $\Delta\text{AER}$ and $\Delta\text{GHG}$ .	114
Figure 3-11. Predicted zonal mean changes in (a) net shortwave (SW) flux and (b) net longwave (LW) flux ( $\text{W m}^{-2}$ ) at TOA. Positive values correspond to downward fluxes. Note the vertical scales differ between $\Delta\text{AER}$ and $\Delta\text{GHG}$ .	115
Figure 3-12. Predicted zonal mean changes in surface fluxes ( $\text{W m}^{-2}$ ) of (a) absorbed (abs.) shortwave radiation (SW, negative values indicate surface solar dimming), (b) sensible heat (SH, positive values indicate flux from atmosphere into surface), and (c) latent heat (LH, positive values indicate decreased evaporation). Note the vertical scales differ between $\Delta\text{AER}$ and $\Delta\text{GHG}$ .	116
Figure 3-13. Regions (shaded) for calculating the statistics of regional climate change presented in Table 3-4. (1) East Asia. (2) South Asia.	117
Figure 3-14. Predicted change over East and South Asia in DJF (a) in precipitation ( $\text{mm day}^{-1}$ ) and (b) in sea level pressure (color shading, hPa) and surface wind field (vector, $\text{m s}^{-1}$ ). Note the color scale differs between $\Delta\text{AER}$ and $\Delta\text{GHG}$ .	118
Figure 4-1. Schematic diagram for experimental design.	172
Figure 4-2. Annual mean total column burden ( $\text{mg m}^{-2}$ ) of sulfate, nitrate, ammonium, POA, SOA, and BC for (a) PI, (b) 20C, (c) 21C. Global average values are given in the upper right corner of each panel.	173
Figure 4-3. Annual mean column burden of sea salt ( $\text{mg m}^{-2}$ ) for 20C. Global average values is given in the upper right corner.	174
Figure 4-4. The left column shows the changes in annual mean $N_c$ at the lowest model layer (972 hPa) (a) from PI to 20C and (b) from 20C to 21C. The right column shows the annual mean instantaneous TOA AIE forcing (i.e. changes in TOA cloud forcing) (c) from PI to 20C and (d) from 20C to 21C. Global average values are given in the upper right corner of each panel.	175

- Figure 4-5. Comparisons of zonal mean cloud properties between predicted present-day equilibrium climate accounting for GHG and anthropogenic aerosol direct and indirect effects ( $DG_{20C}I_{20C}$ , solid lines) and satellite observations (dashed lines): (a) column  $N_c$ , (retrievals based on ISCCP [Han *et al.*, 1998]) (b)  $r_e$  at cloud top (retrievals based on ISCCP [Han *et al.*, 1994], for year 1987), (c) total cloud fraction (measurements from ISCCP, from July 1986 to June 2006) and (d) SW and LW cloud forcing (measurements from ERBE [Kiehl and Trenberth, 1997]; black lines for shortwave component, and gray lines for longwave component). ..... 176
- Figure 4-6. Present-day climate response to perturbation of AIE from pre-industrial to present day ( $DG_{20C}I_{20C} - DG_{20C}I_{PI}$ ): vertical zonal profiles of changes in annual mean (a)  $N_c$  in liquid stratiform clouds ( $\text{cm}^{-3}$ ), (b) total cloud water content ( $10^{-6} \text{ kg-H}_2\text{O kg-air}^{-1}$ ), (c)  $r_e$  in liquid stratiform clouds ( $\mu\text{m}$ ) (d) temperature (K), (e) specific humidity ( $10^{-4} \text{ kg-H}_2\text{O kg-air}^{-1}$ ), and (f) mass stream function ( $10^{10} \text{ kg s}^{-1}$ , positive values indicate counterclockwise flows); annual mean changes in (g)  $T_s$  (K) and (h) Precipitation ( $\text{mm day}^{-1}$ ). Changes that insignificant relative to the 95% confidence ..... 177
- Figure 4-7. Present-day climate response to perturbation of AIE from pre-industrial to present day ( $DG_{20C}I_{20C} - DG_{20C}I_{PI}$ ): zonal mean changes in (a)  $N_c$  at 850 hPa ( $\text{cm}^{-3}$ ), (b) TOA SW CF ( $\text{W m}^{-2}$ ), (c)  $T_s$  (K), and (d) Precipitation ( $\text{mm day}^{-1}$ ) (Black solid lines for annual average, gray lines for average over DJF, and dotted lines for average over JJA). ..... 178
- Figure 4-8. Similar to Figure 4.6 but for present-day climate response to perturbation of AIE from present day to year 2100 ( $DG_{20C}I_{21C} - DG_{20C}I_{20C}$ ).... 179
- Figure 4-9. Similar to Figure 4.7 but for present-day climate response to perturbation of AIE from present day to year 2100 ( $DG_{20C}I_{21C} - DG_{20C}I_{20C}$ ). Note the vertical scales in are different..... 180
- Figure 4-10. Climate responses to combined effects of GHG and anthropogenic aerosol direct and indirect effect from present day to year 2100 ( $DG_{21C}I_{21C} - DG_{20C}I_{20C}$ ): vertical zonal profiles of changes in annual mean (a) total cloud water content ( $10^{-6} \text{ kg-H}_2\text{O kg-air}^{-1}$ ), (b) temperature (K), and (c) specific humidity ( $10^{-4} \text{ kg-H}_2\text{O kg-air}^{-1}$ ); annual mean changes in (d)  $T_s$  (K) and (e) Precipitation ( $\text{mm day}^{-1}$ ). Global average values are given in the upper right corner of (d) and (e). Note the color scales are different from previous figures. 181
- Figure 4-11. Climate responses to combined effects of GHG and anthropogenic aerosol direct and indirect effect from present day to year 2100 ( $DG_{21C}I_{21C} - DG_{20C}I_{20C}$ ): zonal mean changes in (a)  $T_s$  (K), (b) excess precipitation (total precipitation minus evaporation,  $\text{mm day}^{-1}$ ), and (c) precipitation from stratiform clouds ( $\text{mm day}^{-1}$ ), and vertical zonal profiles of changes in annual mean (d) mass stream function ( $10^{10} \text{ kg s}^{-1}$ ). (In (a)–(c), black solid lines for annual average, gray lines for average over DJF, and dotted lines for average over JJA) ..... 182

Figure 4-12. Similar to Figure 4-11, but for climate responses from present day to year 2100 predicted by the standard version of GISS III ( $DG_{21C} - DG_{20C}$ )..... 183

Figure 5-1. Comparisons among coincident MISR-AERONET BB cases with mid-visible AOD>0.15: (a) AERONET mid-visible AOD ( $AOD_A$ ) vs. SSA ( $SSA_A$ ), (b)  $AOD_A$  vs. difference in AOD ( $AOD_{M-A}$ ), (c)  $SSA_A$  vs. difference in SSA ( $SSA_{M-A}$ ), (d)  $AOD_{M-A}$  vs.  $SSA_{M-A}$ , (e) AERONET Ångstrom Exponent ( $\text{Å}_A$ ) vs.  $AOD_{M-A}$ , (f) AERONET SSA spectral dependence ( $\alpha_{\omega 0 A}$ ) vs. SSAA, (g)  $\text{Å}_A$  vs. difference in Ångstrom Exponent ( $\text{Å}_{M-A}$ ), (h)  $\alpha_{\omega 0 A}$  vs. difference in SSA spectral dependence ( $\alpha_{\omega 0 M-A}$ ). In each panel, cases are categorized into four groups (see text for details): black diamonds for group 1, red triangles for group 2, green squares for group 3, and yellow circles for group 4..... 251

Figure 5-2. The means (vertical lines) and ranges (grey bars) of reported physical and optical parameter values for haze, aged, and fresh plumes in different regions: (a) number-weighted geometric mean radius ( $r_{pg,N}$ ), (b) geometric standard deviation ( $\sigma_g$ ), (c) single scattering albedo at 550 nm ( $\omega_{0,550}$ ), (d) real part of refractive index ( $n_r$ ) at 550 nm, and (e) imaginary part of refractive index ( $n_i$ ) at 550 nm. The vertical lines are red for fresh plumes (< 1 day old), blue for aged plumes (1–3 days old), and green for regional haze (> 3 days old or mixed). (Abbreviations: Afc = Africa, S Am = South America, N Am = North America, C Am = Central America) ..... 252

Figure 5-3. Sensitivity results of eight target atmospheric BB components assuming AOD = 0.2. Each individual sub-plot shows the results for comparisons against one target atmospheric component (marked at the upper-left corner of each sub-plot), with the comparison space  $r_{pg,N}$  and  $\omega_{0,558}$  values organized along the x and y axes, respectively. Overall, the plot array is arranged by the  $r_{pg,N}$  and  $\omega_{0,558}$  of the target atmospheric components (marked at the bottom and the left of the plate). The lower-left sub-plot shows positions of all components on the  $r_{pg,N}-\omega_{0,558}$  plane (green spots). Retrieved component fractions are proportional to the area of colored circles; the gray circle in the lower-left plot is the scale of 100% fraction. For the target atmospheric component in each panel, the red circle shows the minimum retrieved fraction, and the blue shows the maximum fraction. For the other components, the circle shows only the maximum fraction, and is shaded black if more than 20%, otherwise, gray. Conditions of 1 atm surface pressure and  $2.5 \text{ m s}^{-1}$  wind speed, for mid-latitude geometry, over a dark water surface, are assumed in these radiative transfer calculations..... 253

Figure 5-4. Same as Figure 5-3, but for atmospheric BB components with having AOD = 0.5..... 254

Figure 5-5. Spectral AOD for coincident AERONET measurements (black solid lines), best-fit MISR v17 Standard Retrievals (black dashed lines), and best-fit Research Retrievals for all patches (gray solid lines for patch with lowest  $\chi^2$ , gray dotted lines for patch P0) for the four coincident BB cases..... 255

Figure 5-6. Normalized number size distributions for coincident AERONET measurements (green lines), best-fit MISR v17 Standard Retrievals (blue

lines), and best-fit Research Retrievals (red lines for the best patch, yellow lines for P0, and gray lines for patches with  $\chi^2 < 1.5$ ) for the four coincident BB cases. The best patch is also denoted by \*\* in the legend. .... 256

Figure 5-7. The third surface RPV parameter retrieved by the MISR v17 Standard Algorithm at all four MISR channels for hazy day (gray dashed lines) and the clean day orbit (black solid lines) for (a) Ilorin\_2001/02/24, (b) Ouagadougou\_2000/12/18, and (c) Ilorin\_2001/ 02/17. For each case, plots are shown for the best patch (left) and for P0 (right)..... 257

## List of Tables

Table 2-1. Summary of Chemistry Simulations .....	48
Table 2-2. Global Annual Anthropogenic Emissions for the Years 2000 and 2100 .....	49
Table 2-3. Climate-sensitive Natural Emissions.....	51
Table 2-4. Predicted Annual and Global Burdens .....	52
Table 2-5. Global Budget for Tropospheric O <sub>3</sub> .....	53
Table 2-6. Global Budget for Sulfate Aerosol.....	54
Table 2-7. Effect of Climate Change on Estimates of Year 2100 TOA Radiative Forcing.....	55
Table 3-1. Summary of Climate Experiments .....	99
Table 3-2. Present-Day (year 2000) and Year 2100 Annual Mean Global Burdens of Anthropogenic Aerosols, Tropospheric Ozone, and Greenhouse Gas Mixing Ratios Used in This Study .....	100
Table 3-3. Global and Hemispherical Annual Mean Differences of Selected Climate Parameters.....	101
Table 3-4. Regional Mean Differences of Selected Climate Parameters in DJF over East and South Asia.....	103
Table 3 -5. Summary and Comparison of Patterns of Equilibrium Climate Response to Changes of Aerosol Direct Forcing and GHG Forcing from Present Day to Year 2100 Predicted in This Study .....	104
Table 4-1. Global Models in This Study .....	161
Table 4-2. Global Annual Burdens (Tg dry mass) of Aerosols Derived by the Caltech Unified Model .....	162
Table 4-3. Experimental Design of the Equilibrium Simulations with GISS III GCM..	163
Table 4-4. Global Annual Mean Values of Key Climate Variables in the Present- Day Equilibrium Simulations With and Without Explicit Droplet- Dependence in Stratiform Clouds .....	164
Table 4-5. Comparison of Global Annual Mean Cloud Properties in Present-Day Simulation GD20CI20C With Remote Sensing Observations and Predictions in Selected GCM Studies.....	165
Table 4-6. Changes in Annual Mean Cloud Properties Between the Equilibrium Climates .....	166
Table 4-7. Similar to Table 4.6, but for Changes in Annual Mean Temperature, Precipitation, Hydrological Sensitivity, and Surface Radiative Fluxes .....	168
Table 4-8. Change in Global Annual Mean Values of Key Climate Variables Between the Present-day and Year 2100 Equilibrium Simulations, Predicted by the Modified and Standard Version of GISS III .....	169

Table 4-9. Comparisons of Present Day to Year 2100 Forcing and Climate Response Between the Present Study and Previous Related Studies.....	170
Table 4-10. Summary of Patterns of Equilibrium Climate Responses in the Present Study.....	171
Table 5-1. AERONET Sites in Major BB Regions Selected for Coincident MISR-AERONET Measurement Comparisons.....	235
Table 5-2. Characteristics of Four Groups of BB Cases, Based on Comparisons of AOD and SSA for Coincident MISR-AERONET Measurements .....	236
Table 5-3. BB Aerosol Physical and Optical Property References Covered in This Review of the Field Experiment Literature .....	238
Table 5-4. Profiles of Fresh Plumes, Aged Plumes, and Haze Based on the Literature .....	240
Table 5-5. BB Aerosol Component Models .....	241
Table 5-6. BB Aerosol Mixing Groups .....	242
Table 5-7. Summary of Sensitivity Results for Unimodal BB Particle Cases.....	243
Table 5-8. Additional Components Used in the MISR Research Aerosol Retrieval Algorithm for the Four Representative Coincident BB Cases.....	245
Table 5-9. Additional Components Used in the MISR Research Aerosol Retrieval Algorithm for the Four Representative Coincident BB Cases.....	246
Table 5-10. AOD at 558 nm and Angstrom Exponent from AERONET Measurements, MISR v17 Standard Retrieval and Research Retrieval Results, for the Four Coincident BB Cases .....	247
Table 5-11. Aerosol Fine Mode Fraction, Fine Mode Size, and Coarse Mode Size From AERONET Measurements, MISR v17 Standard Retrievals, and Research Retrieval Results, for the Four Coincident BB Cases .....	248
Table 5-12. Total and Fine Mode SSA and SSA Spectral Dependence From AERONET Measurements, MISR v17 Standard Retrieval, and Research Retrieval Results, for the Four Coincident BB Cases .....	250

# Chapter 1

---

## Introduction

Aerosols, suspended fine solid and liquid particles in the atmosphere, are one of the most critical factors controlling Earth's climate system. Advances in understanding the role of aerosols in the climate system are imperative in the assessment and prediction of climate change. In Part I of this thesis, numerical simulations from a general circulation model are used to systematically explore the important interactions between aerosols and the climate. In Part II, the aerosol retrieval algorithm of a remote sensing instrument is investigated and refined, specifically for the measurements of biomass burning aerosols.

Aerosols can be categorized on the basis of their origins. "Primary aerosols" are those released into the atmosphere directly in the form of particles from natural and anthropogenic sources. Examples of primary aerosols include wind-blown dust particles from soils and deserts, sea salt particles from bursting bubbles in the sea spray, and black carbon and primary organic particles from combustion processes of fossil fuel burning and biomass burning. "Secondary aerosols", on the other hand, are generated in the atmosphere through physical or chemical transformations of the "precursor" gases. Important secondary aerosols include sulfate ( $\text{SO}_4^{2-}$ ) particles from oxidation of  $\text{SO}_2$  and the subsequent condensation of sulfuric acid, nitrate ( $\text{NO}_3^-$ ) particles from the oxidation of  $\text{NO}_2$  and the subsequent condensation of nitric acid, and secondary organic particles from the oxidation and condensation of biogenic volatile organic compounds (VOC). The formation of secondary aerosols can be very complicated, involving mechanisms such as gas-to-particle conversion (e.g., homogeneous and heterogeneous nucleation), gas phase and liquid phase chemical reactions (e.g., ring-opening processes of aromatic hydrocarbons), and cloud processing.

Changes in climate can affect the emission strength, removal processes, thermodynamic equilibrium, chemical reactions, and the temporal and spatial distributions of aerosols. In turn, aerosols can impact the climate by perturbing the energy balance of the Earth system. The climate and the aerosols thus form a complex feedback system. Numerical experiments with a General Circulation Model (GCM) are one of the key approaches in studying the responses of the climate system to an introduced perturbation (forcing). Transient simulations, in which the perturbation (or forcing) changes along the course of the integration, are usually designed to reproduce current climate conditions or forecasting future climate change. Equilibrium simulations, in which the forcing is held fixed at a certain level during the entire integration, generally result in more pronounced responses than the transient simulation, and are usually chosen to delineate and compare relative impacts of various forcing mechanisms.

In Part I, we use equilibrium simulations with the Goddard Institute for Space Studies (GISS) GCM as our tool to answer the following questions: (1) How will aerosol burden and composition be influenced by future climate change? (2) How will future climate respond to the direct radiative perturbations of aerosols? (3) How will future climate respond to the modifications of clouds by aerosols?

CO<sub>2</sub> and the other major greenhouse gases (GHG) are the dominant contributors to current and future climate change. Using a unified climate-chemistry-aerosol model within GISS GCM II', the effect of future (year 2100) CO<sub>2</sub>-driven equilibrium climate change on the global distributions of tropospheric ozone, anthropogenic aerosols (sulfate, nitrate, ammonium, black carbon, primary organic carbon, secondary organic carbon), sea salt and dust aerosols is predicted in Chapter 2. Increased CO<sub>2</sub> is predicted to lead to

warmer temperature and enhanced precipitation, which increases wet removal, changes emissions that are sensitive to climate, and shifts the thermodynamic partitioning of the aerosols. The changes in future direct radiative forcing associated with the impact of climate change on aerosol burdens are also calculated and compared to those associated with future emission changes.

Aerosols can modify the dominant, long-term, and more spatially homogeneous GHG-induced climate change and create more complexity, especially on a regional basis. Aerosols directly alter the Earth's radiative budget by scattering and absorbing sunlight. This so-called "aerosol direct radiative effect" and its climatic impact is explored in Chapter 3 with the 9-layer GISS GCM II'. Increased aerosol burdens in the atmosphere, through their direct effect, decrease the solar radiation received by the surface, while at the top of the atmospheric column, the net (incident plus reflected) solar flux can be either enhanced or reduced, depending on the relative magnitude of particle scattering versus particle absorption. The radiative perturbation of aerosol direct effect can change the temperature distribution, the strength of the hydrological cycle, and the atmospheric circulations. The characteristics of future equilibrium climate responses to the change in anthropogenic aerosol direct effect, tropospheric ozone, and GHG are analyzed and differentiated.

Aerosols can also indirectly influence the radiation by modifying the amount, reflectivity (albedo), and lifetime of the clouds; these "indirect effects" are studied in Chapter 4. Soluble aerosols may act as cloud condensation nuclei (CCN), controlling the number concentration of cloud droplets. Given the same amount of cloud liquid water, increased droplet number concentrations owing to more abundant aerosols may produce

smaller droplets, thereby leading to higher cloud albedo (i.e., “first indirect effect” or “cloud albedo effect”). Changes in droplet number concentrations and droplet size distributions also have impacts on the formation of precipitation in the clouds, termed the “second indirect effect” or “cloud lifetime effect”. In Chapter 4, a new formulation is developed to provide correlations between aerosols and cloud droplet number concentrations, and the 23-layer GISS GCM III is modified to include processes related to aerosol indirect effects in the stratiform clouds. The equilibrium climate responses to indirect effects between pre-industrial and present day, and between present day to year 2100, are diagnosed and compared to the climate responses to GHG and aerosol direct effect.

The climatic impacts of aerosols are determined by the abundance, size, chemical composition, and optical properties of the particles. Satellite remote sensing, such as the Multi-angle Imaging SpectroRadiometer (MISR), can provide frequent, long-term, global observation of these important properties for climate research, especially GCM studies. However, to ensure correct interpretation of the retrieved results, it is necessary to systematically assess the aerosol properties assumed in the instrument’s retrieval algorithm. In Part II (Chapter 5), discrepancies in the Standard Aerosol Retrieval Algorithm of MISR are identified, by comparisons with coincident ground-based sun photometer measurements, for the retrievals of biomass burning particles, one of aerosol types with low scientific understanding. Based on the review of in situ observations in the literature, as well as a set of theoretical sensitivity calculations, specific refinements are proposed to the particle and mixture properties assumed for biomass burning aerosols in the algorithm. Representative case studies confirm the theoretical results and also

highlight the importance for satellite aerosol retrievals of surface reflectance characterization.

**Part I. Global Simulations of  
Interactions between Aerosols and  
Future Climate**

## Chapter 2

---

# **Roles of Climate Change in Global Predictions of Future Tropospheric Ozone and Aerosols**

Published in *Journal of Geophysical Research* (2006) by Hong Liao, Wei-Ting Chen, and John Seinfeld, *111*, D12304, doi:10.1029/2005JD006852.

Copyright © 2006 American Geophysical Union. Reprinted with permission from American Geophysical Union.

## Abstract

A unified climate-chemistry-aerosol model within the Goddard Institute for Space Studies (GISS) general circulation model (GCM) II' is applied to simulate a equilibrium CO<sub>2</sub>-forced climate in year 2100 to examine effects of climate change on global distributions of tropospheric ozone and sulfate, nitrate, ammonium, black carbon, primary organic carbon, secondary organic carbon, sea salt, and mineral dust aerosols. The year 2100 CO<sub>2</sub> concentration as well as the anthropogenic emissions of ozone precursors and aerosols/aerosol precursors are based on the IPCC SRES A2. Year 2100 global O<sub>3</sub> and aerosol burdens predicted with changes in both climate and emissions are generally 5–20% lower than those simulated with changes in emissions alone; as exceptions, the nitrate burden is 38% lower and secondary organic aerosol (SOA) burden is 17% higher. Although the CO<sub>2</sub>-driven climate change alone reduces O<sub>3</sub> burden as a result of lower net chemical production of O<sub>3</sub> in the warmer climate, it increases surface-layer O<sub>3</sub> concentrations over or near populated and biomass burning areas because of slower transport and enhanced biogenic hydrocarbon emissions, which has import implications for future air quality. The warmer climate influence aerosol burdens by increasing aerosol wet deposition, changing climate-sensitive emissions, and shifting aerosol thermodynamic equilibrium. The climate change affects the estimates of year 2100 direct radiative forcing as a result of the climate-induced changes in burdens and different climatological conditions; accounting for full gas-aerosol coupling as well as ozone and aerosols from both natural and anthropogenic sources, year 2100 global mean TOA direct radiative forcings by O<sub>3</sub>, sulfate, nitrate, black carbon, and organic carbon are predicted to be +0.93, –0.72, –1.0, +1.26, –0.56 W m<sup>–2</sup>, respectively, using present-day climate and

2100 emissions, while they are predicted to be +0.76, -0.72, -0.74, +0.97, -0.58 W m<sup>-2</sup>, respectively, with year 2100 climate and emissions.

## 2.1 Introduction

Tropospheric O<sub>3</sub> and aerosols have made important contributions to radiative forcing since preindustrial times [*Intergovernmental Panel on Climate Change (IPCC)*, 2001] and are predicted to do so in the future. Their abundances are controlled by a combination of direct and precursor emissions, chemical reactions in the atmosphere, and meteorological processes, all of which can be significantly affected by climate change with resulting feedbacks. Tropospheric O<sub>3</sub> and aerosols have relatively short atmospheric lifetimes (days to weeks) and hence inhomogeneous atmospheric distributions, complicating the link between radiative forcing and climate response [*Hansen et al.*, 1997].

Climate change influences tropospheric ozone and aerosols through effects on emissions, transport, and atmospheric chemistry. Biogenic emissions of NO<sub>x</sub> and hydrocarbons [*Atherton et al.*, 1995; *Yienger and Levy*, 1995; *Guenther et al.*, 1995, *Constable et al.*, 1999] are sensitive to temperature. Increasing deep convection enhances the lightning NO<sub>x</sub> source [*Toumi et al.*, 1996; *Sinha and Toumi*, 1997]. Changes in surface winds have impact on emissions of dimethylsulfide (DMS) [*Bopp et al.*, 2004], sea salt, and mineral dust. The potential impacts of climate change on transport of ozone and aerosols have been demonstrated by general circulation model (GCM) studies. *Rind et al.* [2001] predicted that increased convection in a doubled-CO<sub>2</sub> atmosphere leads to improved ventilation of the lowest layers of the atmosphere, reducing boundary layer concentrations of tracers. *Holzer and Boer* [2001] reported that if a warmer climate leads to weaker winds, higher tracer concentrations will exist in the vicinity of sources.

Changes in boundary layer conditions and the hydrological cycle influence dry and wet deposition. Furthermore, chemical reaction rates are influenced by changes in atmospheric water vapor and temperature.

The effects of climate change on tropospheric ozone have been reported in several global studies. On the basis of the doubled CO<sub>2</sub> climate predicted by the NCAR CCM and projected year 2050 ozone precursor emissions from the IS92a scenario, *Brasseur et al.* [1998] predicted a 7% increase in the global mean OH abundance and a 5% decrease in O<sub>3</sub> in the tropical upper troposphere relative to current climate. In offline chemistry simulations, *Johnson et al.* [1999] predicted that a doubled CO<sub>2</sub> climate with precursor emissions kept at present-day levels would reduce the tropospheric ozone burden by about 10%. Coupled chemistry-GCM simulations by *Johnson et al.* [2001] predicted that with projected precursor emissions over 1990–2100, the global burden of O<sub>3</sub> calculated with simulated 2100 climate would be lower than that predicted with present-day climate. These studies concluded that higher temperature and water vapor content in a warmer climate would lead to the reduction in global O<sub>3</sub>.

No study has systematically addressed the effect of climate change on future global aerosol concentrations. Previous global projections of future aerosol levels have generally simulated concentrations on the basis of present-day climate and accounted only for projected changes in emissions [*Adams et al.*, 2001; *Koch*, 2001; *Iversen and Seland*, 2002; *Liao and Seinfeld*, 2005]; also, present-day gas-phase oxidant concentrations were used for future aerosol simulations [*Adams et al.*, 2001; *Koch*, 2001; *Iversen and Seland*, 2002].

We examine here the changes in global concentrations of ozone, sulfate, nitrate, ammonium, black carbon, primary organic carbon, secondary organic carbon, sea salt, and mineral dust aerosols over the period 2000–2100 using a unified tropospheric chemistry-aerosol model within the Goddard Institute for Space Studies (GISS) GCM II'. We first predict equilibrium climate change resulting from projected changes in CO<sub>2</sub> over 2000–2100, then examine the effect of CO<sub>2</sub>-induced climate change on abundances of ozone and aerosols at present-day anthropogenic emissions levels, and finally estimate the O<sub>3</sub> and aerosol levels in 2100 corresponding to the combined effects of both climate change and changes in emissions. The ozone and aerosol simulations account for the coupling between aerosols and gas-phase chemistry. Heterogeneous reactions on aerosols affect the concentrations of HO<sub>x</sub>, NO<sub>x</sub>, and O<sub>3</sub>. In addition, aerosols affect gas-phase photolysis rates, and climate change influences natural emissions of NO<sub>x</sub>, hydrocarbons, DMS, sea salt, and mineral dust. Full simulation of gas-phase chemistry and aerosols provides consistent chemical species for both present-day and future scenarios.

*Liao and Seinfeld* [2005] estimated year 2100 radiative forcing by tropospheric ozone and aerosols based on present-day climate. With coupled climate, chemistry, and aerosols, we also examine here the effect of climate change on estimates of future radiative forcing. The model description and experimental design is given in section 2.2. Section 2.3 presents the simulated climate change over 2000–2100. The impact of climate change alone on the predictions of O<sub>3</sub> and aerosols is then examined in section 2.4. Section 2.5 presents the changes in ozone and aerosol concentrations over 2000–2100 simulated with both predicted climate change and projected emissions. In section 2.6, we

examine the effect of climate change on estimates of year 2100 direct radiative forcing by O<sub>3</sub> and aerosols.

## 2.2 Model Description and Experimental Design

### 2.2.1 The Unified Model

The simulations in this work are performed using the unified model reported in *Liao et al.* [2003; 2004] and *Liao and Seinfeld* [2005], which is a fully coupled chemistry-aerosol-climate GCM with detailed O<sub>3</sub>-NO<sub>x</sub>-hydrocarbon chemistry and sulfate/nitrate/ammonium/sea salt/water, black carbon, primary organic carbon, secondary organic carbon, and mineral dust aerosols within the Goddard Institute for Space Studies (GISS) GCM II' [*Rind and Lerner*, 1996; *Rind et al.*, 1999]. The GCM has a resolution of 4° latitude by 5° longitude, with 9 vertical layers in a  $\sigma$ -coordinate system extending from the surface to 10 mbar. The chemical mechanism includes 225 chemical species and 346 reactions for simulating gas-phase species and aerosols. Tracers that describe O<sub>3</sub>-NO<sub>x</sub>-hydrocarbon chemistry include odd oxygen ( $O_x = O_3 + O + NO_2 + 2NO_3$ ), NO<sub>x</sub> (NO + NO<sub>2</sub> + NO<sub>3</sub> + HNO<sub>2</sub>), N<sub>2</sub>O<sub>5</sub>, HNO<sub>3</sub>, HNO<sub>4</sub>, peroxyacetyl nitrate, H<sub>2</sub>O<sub>2</sub>, CO, C<sub>3</sub>H<sub>8</sub>, C<sub>2</sub>H<sub>6</sub>, ( $\geq C_4$ ) alkanes, ( $\geq C_3$ ) alkenes, isoprene, acetone, CH<sub>2</sub>O, CH<sub>3</sub>CHO, CH<sub>3</sub>OOH, ( $\geq C_3$ ) aldehydes, ( $\geq C_4$ ) ketones, methyl vinyl ketone, methacrolein, peroxyethacryloyl nitrate, lumped peroxyacyl nitrates, and lumped alkyl nitrates. Aerosol related tracers include SO<sub>2</sub>, SO<sub>4</sub><sup>2-</sup>, dimethyl sulfide (DMS), NH<sub>3</sub>, NH<sub>4</sub><sup>+</sup>, NO<sub>3</sub><sup>-</sup>, sea salt in 11 size bins (0.031–0.063, 0.063–0.13, 0.13–0.25, 0.25–0.5, 0.5–1, 1–2, 2–4, 4–8, 8–16, 16–32, 32–64  $\mu\text{m}$  dry radius), mineral dust in 6 size bins (0.0316–0.1, 0.1–0.316, 0.316–1.0, 1.0–

3.16, 3.16–10, and 10–31.6  $\mu\text{m}$  dry radius), black carbon (BC), primary organic aerosols (POA), as well as 5 classes of reactive hydrocarbons and 28 organic oxidation products involved in secondary organic aerosol (SOA) formation. The partitioning of ammonia and nitrate between gas and aerosol phases is determined by the on-line thermodynamic equilibrium model ISORROPIA [Nenes *et al.*, 1998], and the formation of secondary organic aerosol is based on equilibrium partitioning and experimentally determined yield parameters [Griffin *et al.*, 1999a, 1999b; Chung and Seinfeld, 2002]. Two-way coupling between aerosols and gas-phase chemistry provides consistent chemical fields for aerosol dynamics and aerosol mass for heterogeneous processes and calculations of gas-phase photolysis rates. Heterogeneous reactions considered in the model include those of  $\text{N}_2\text{O}_5$ ,  $\text{NO}_3$ ,  $\text{NO}_2$ , and  $\text{HO}_2$  on wet aerosols, uptake of  $\text{SO}_2$  by sea salt, and uptake of  $\text{SO}_2$ ,  $\text{HNO}_3$  and  $\text{O}_3$  by mineral dust; the uptake coefficients are taken to depend on atmospheric temperature and relative humidity, as described in Liao and Seinfeld [2005].

Dry and wet deposition schemes for tracers are described by Liao *et al.* [2003, 2004]. For the purpose of this study, we have updated the dry deposition velocities used for carbonaceous aerosols. In the studies of Liao *et al.* [2003, 2004] and Liao and Seinfeld [2005], a fixed deposition velocity of  $0.1 \text{ cm s}^{-1}$  was used for black carbon, primary organic carbon, and secondary organic carbon aerosols following the studies of Lioussé *et al.* [1996], Kanakidou *et al.* [2000], and Chung and Seinfeld [2002]. To account for possible effects of climate change on dry deposition, dry deposition velocities of carbonaceous aerosols are determined using the resistance-in-series scheme of Wesely [1989], that which has been used for dry deposition of other aerosol species [Liao *et al.*, 2003].

### 2.2.2 Climate Simulations

We perform two simulations of equilibrium climate using the unified model, one for year 2000 with a CO<sub>2</sub> concentration of 368 ppmv and the other for year 2100 with a CO<sub>2</sub> concentration of 836 ppmv, based on IPCC Special Report on Emissions Scenarios (SRES) A2 [IPCC, 2001]. The settings of these two simulations, except for the CO<sub>2</sub> concentration, are identical, each with a Q-flux ocean [Hansen *et al.*, 1984; Russell *et al.* 1984]. In the Q-flux ocean, ocean heat transport is held constant but sea surface temperatures and ocean ice respond to changes in climate. The monthly mean ocean heat transport fluxes are from the work of Mickley *et al.* [2004], which used the same version of the GCM as here to generate observed, present-day sea surface temperatures. In these two climate simulations, present-day climatological aerosol and ozone concentrations are used in the GCM radiative calculations to isolate the climate change driven by the change in CO<sub>2</sub> concentration. Each climate simulation is integrated for 50 years to allow the climate to reach an equilibrium state, and the simulated climate over year 50–55 is used to drive the chemistry simulations described in section 2.2.3.

Because future emissions scenarios are, of course, uncertain, we have chosen here to consider a future greenhouse climate as driven by CO<sub>2</sub> only and, as noted, have applied IPCC SRES A2. Future climate will be influenced in addition by changes in CH<sub>4</sub>, N<sub>2</sub>O, and CFCs, but these species need not be included here, as CO<sub>2</sub> under SRES A2 provides ample climate change to examine the effects of climate-chemistry-aerosol coupling.

Traditionally, climate simulations take one of two forms: (1) equilibrium climate, in which the long-term climate that would result from a fixed greenhouse gas concentration

is computed; and (2) transient climate, in which climate is simulated from a standpoint, say preindustrial, with specified annual emissions changes. Predicted changes from an equilibrium climate simulation generally exceed those from a transient climate simulation. For example, the ratio of transient climate response (the change in surface air temperature at the time of doubled CO<sub>2</sub>) to the equilibrium response (the equilibrium change in surface air temperature from doubled CO<sub>2</sub>) lies with 0.47–0.68 [*IPCC, 1995; Kiehl et al., 2005*]. Although non-CO<sub>2</sub> greenhouse gases are not included in the present year 2100 equilibrium climate simulation, the predicted climate responses are comparable to or slightly larger than those predicted from a transient climate simulation driven by the changes in all greenhouse gases over 2000–2100. Hereafter for convenience we refer to the simulated CO<sub>2</sub>-driven equilibrium climate as year 2000 or 2100 climate, but we note that the CO<sub>2</sub>-driven equilibrium climate differs from a transient climate including all greenhouse gases and aerosols, as discussed above.

### **2.2.3 Chemistry Simulations**

Chemistry simulations are performed when the climate simulations reach equilibrium states. The simulated climates over years 50–55 drive the chemistry simulations, with the first year of each chemistry simulation considered spin up. Four chemistry simulations are designed to identify the effects of climate change on levels of tropospheric ozone and aerosols (Table 2-1):

1. CL2000EM2000 is the control simulation with the year 2000 climate and the present-day (approximately year 2000) anthropogenic emissions of precursors and aerosols/aerosol precursors (non-CO<sub>2</sub> anthropogenic emissions).

2. CL2100EM2000 is the simulation with year 2100 CO<sub>2</sub>-driven climate and present-day non-CO<sub>2</sub> anthropogenic emissions;

3. CL2000EM2100 is the simulation with year 2000 climate and year 2100 non-CO<sub>2</sub> anthropogenic emissions;

4. CL2100EM2100 uses year 2100 CO<sub>2</sub>-driven climate and year 2100 non-CO<sub>2</sub> anthropogenic emissions.

Climate-sensitive natural emissions are calculated based on predicted climate in all the simulations (section 2.2.4). By holding non-CO<sub>2</sub> anthropogenic emissions at present-day levels, the difference between CL2100EM2000 and CL2000EM2000 reflects the effects of CO<sub>2</sub>-driven climate change alone on concentrations of O<sub>3</sub> and aerosols. The difference between CL2100EM2100 and CL2000EM2000 represents the impacts of both climate and emission changes on O<sub>3</sub> and aerosol levels. CL2000EM2100 uses present-day climate and year 2100 anthropogenic emissions, in a manner used in a number of previous studies, to predict future O<sub>3</sub> and aerosols. We will compare the radiative forcings calculated in CL2000EM2100 and CL2100EM2100 to examine the effect of climate change on radiative forcing.

Heterogeneous reactions have been shown to be potentially influential in coupling processes involving O<sub>3</sub> and aerosols [*Liao and Seinfeld, 2005*]. In this work we perform each of the four chemistry simulations, CL2100EM2000, CL2000EM2000, CL2000EM2100, and CL2100EM2100, in the absence and presence of heterogeneous reactions of N<sub>2</sub>O<sub>5</sub>, NO<sub>3</sub>, NO<sub>2</sub>, and HO<sub>2</sub> on wet aerosols, uptake of SO<sub>2</sub> by sea salt, as well as the uptake of SO<sub>2</sub>, HNO<sub>3</sub> and O<sub>3</sub> by mineral dust. The simulations that include

heterogeneous reactions will be designated as CL2100EM2000h, CL2000EM2000h, CL2000EM2100h, and CL2100EM2100h. Uptake coefficients for heterogeneous reactions are given by *Liao and Seinfeld* [2005]. The chemistry simulations performed in this work are summarized in Table 2-1.

Unless otherwise noted, the annual, seasonal, or monthly chemical fields presented in this work are averaged over the last 5 years of each chemistry simulation, and the meteorological fields are averaged over years 51–55 of each climate simulation. The climate-chemistry coupling is a one-way coupling; simulated O<sub>3</sub> and aerosols do not feed back into the GCM.

#### **2.2.4 Emission Inventories**

Present-day and year 2100 non-CO<sub>2</sub> anthropogenic emissions used in the chemistry simulations are given in Table 2-2. Year 2100 emissions are based on the IPCC SRES A2 emissions scenario. Biomass burning emissions listed in Table 2-2 are partly anthropogenic and partly natural. We assume in this study that the biomass burning emissions remain unchanged in 2000 and 2100 simulations; the effect of climate change on the occurrence and intensity of wildfires is not considered. The seasonal and geographical distributions of BC and POA emissions in year 2100 are obtained by scaling year 2000 monthly values, grid by grid, using projected changes in IPCC SRES A2 CO emissions.

Climate-sensitive natural emissions include lightning NO<sub>x</sub>, NO<sub>x</sub> from soil, biogenic hydrocarbons, DMS, sea salt, and mineral dust. The meteorological variables that influence these emissions and the schemes used to predict them are listed in Table 2-3.

Emissions of biogenic hydrocarbons and mineral dust are calculated based on fixed distributions of land-surface type and vegetation. We calculate the global monoterpene emissions as a function of vegetation type, monthly adjusted leaf area index, and model predicted temperature, using the base monoterpene emission flux and the formulation of *Guenther et al.* [1995]. The vegetation type and the calculation of leaf area index follow the treatment in *Wang et al.* [1998]. Predicted present-day total monoterpene emissions of 117 TgC yr<sup>-1</sup> agree reasonably well with the 127 TgC yr<sup>-1</sup> reported in *Guenther et al.* [1995]. For present-day emission inventories of other reactive volatile organic compounds (ORVOCs), we use the offline monthly fields from the Global Emissions Inventory Activity (GEIA), but year 2100 emissions of ORVOCs in a grid cell are scaled by the monthly mean ratio of year 2100 emissions to the year 2000 values predicted for monoterpenes. Representation of future isoprene emissions is similar to the approach used for future monoterpenes and follows the algorithm of *Guenther et al.* [1995], which considers immediate light and temperature dependence but does not account for the suppression of isoprene emissions under elevated ambient CO<sub>2</sub> concentrations [*Rosenstiel et al.*, 2003] and the acclimation of plants to higher temperatures [*P'etron et al.*, 2001]. In all chemistry simulations, transport of ozone from the stratosphere is held fixed at 401 Tg O<sub>3</sub> yr<sup>-1</sup>.

## 2.3 Predicted Climate Change

In this section, we briefly summarize the changes in meteorological fields over the period 2000–2100 based on the two equilibrium CO<sub>2</sub>-driven climate simulations described above.

### 2.3.1 Predicted Changes in Temperature

Predicted changes in surface and zonal mean atmospheric temperature over 2000–2100 as a result of the increase in CO<sub>2</sub> mixing ratio from 368 ppmv to 836 ppmv are shown in Figures 2-1a and 2-1b. Annual average surface air temperature is predicted to increase by 4.8°C. Doubling CO<sub>2</sub> relative to the present-day yields a climate sensitivity of 0.8 °C m<sup>2</sup> W<sup>-1</sup>, a value that lies within the range of sensitivity reported for current GCMs [Ramaswamy, 2001; Hansen *et al.*, 1997]. Predicted zonal mean changes in atmospheric temperature exhibit the same pattern as those summarized in IPCC [2001]. Enhanced warming in the tropical mid to upper troposphere results from enhanced latent heating owing to more vigorous moist convection in a warmer climate [Hansen *et al.*, 1984; Mitchell, 1989] and from increased longwave radiative heating when upper tropospheric cloudiness and water vapor increase with temperature [Dai *et al.*, 2001]. The strong warming predicted in the high latitudes of the Northern Hemisphere is a result of the sea-ice climate feedback.

### 2.3.2 Predicted Changes in Hydrological Cycle

Figure 2-2a shows predicted year 2000 zonal annual mean specific humidity (g-H<sub>2</sub>O kg-air<sup>-1</sup>) as a function of pressure. The predicted distribution of specific humidity is similar to that from the NCEP-NCAR reanalysis [Kalnay *et al.*, 1996]. As air temperature rises over 2000 – 2100, specific humidity is predicted to generally increase, with the largest increases of 3–4.5 g-H<sub>2</sub>O kg-air<sup>-1</sup> located in the lower troposphere (below 800 mb) over the low latitudes (Figure 2-2b), because of the nonlinear temperature dependence of the Clausius-Clapeyron equation. The predicted pattern of changes in

specific humidity is similar to that predicted in other GCM simulations [IPCC, 1995; Dai *et al.*, 2001].

The predicted change in global mean precipitation is  $0.32 \text{ mm day}^{-1}$  over 2000–2100 (Figure 2-2c), a 10% increase from the global mean value predicted for year 2000. Precipitation increases over middle to high latitudes in both hemispheres, associated with the large warming at the surface and in the lower troposphere [Dai *et al.*, 2001]. Reductions in precipitation are predicted over tropics and subtropics, which are associated with the predicted weakening of the Hadley circulation, as discussed below. Zonal mean precipitation increases (Figure 2-2d) at all latitudes except around  $20^{\circ}\text{S}$ , which agrees qualitatively with the changes from the 1990s to the 2090s simulated by Dai *et al.* [2001] using the NCAR GCM. Increases in precipitation are predicted over North Africa, changes that are consistent with the predictions of other GCMs [IPCC 2001, Chapter 9.3.2]; these will influence mineral dust emissions, as discussed subsequently.

### **2.3.3 Predicted Changes in Winds**

Enhanced warming at the high latitudes in both hemispheres and changes in the vertical temperature profiles (Figures 2-1a and 2-1b) lead to changes in atmospheric circulation. Figures 2-3a and 2-3b show the predicted zonal and seasonal mean distributions of the present-day vertical velocity and the changes in vertical velocity from year 2000 to year 2100, respectively. The most obvious effect shown in Figure 2-3 is the weakening of the Hadley cells in both hemispheres. The ascending branches of the Hadley cells are predicted to be at  $25^{\circ}\text{S}$ – $12^{\circ}\text{N}$  in DJF, and at  $13^{\circ}\text{S}$ – $28^{\circ}\text{N}$  in JJA (Figure

2-3a). The upward velocities are predicted to be reduced where ascending branches are located (Figure 2-3b), except that the main equatorial convection zone (about 0–5°S in DJF and 2–8°N in JJA) is predicted to be stronger and penetrate higher in year 2100 than in year 2000, a result that again agrees qualitatively with that of *Dai et al.* [2001]. As a result, the precipitation associated with the main equatorial convection zone is enhanced, while that associated with the rest of the ascending branches of the Hadley cells is reduced (Figures 2-2c and 2-2d). The changes in the stream function relative to year 2000 (Figure 2-3c) also indicate the weakening of both the Hadley and Ferrel cells. The predicted weakening in Hadley cells depends on the predicted changes in latitudinal temperature gradient between the tropics and subtropics [*Rind and Rossow*, 1984]. In previous studies that examined climate change with doubled CO<sub>2</sub>, the Hadley Cells are predicted in some studies to be weakened [*Rind et al.*, 1990; *Dai et al.*, 2001; *Rind et al.*, 2001; *Holzer and Boer*, 2001] and in others to be enhanced [*Rind et al.*, 1998]. *Hansen et al.* [2005] also predicted that the changes in greenhouse gases from the preindustrial time to present-day have led to a strengthening of the Hadley Cells.

Predicted changes in annual mean surface wind speed over 2000–2100 are shown in Figure 2-4a. Local changes in surface wind speed lie mostly within  $\pm 1.0 \text{ m s}^{-1}$ , with changes exceeding  $1.0 \text{ m s}^{-1}$  predicted only over the northwestern and tropical Pacific Ocean. Zonal mean changes in surface wind speed (Figure 2-4b) are predicted to be within  $\pm 0.37 \text{ m s}^{-1}$ . Zonal mean reductions in wind speed are predicted at 30–60°S, 5°S–40°N, and around 60°N.

## 2.4 Effects of CO<sub>2</sub>-Driven Climate Change on Tropospheric Ozone and Aerosols

To separate the effects of CO<sub>2</sub>-driven (pure) climate change from those of changing non-CO<sub>2</sub> anthropogenic emissions, we hold non-CO<sub>2</sub> anthropogenic emissions at present-day levels with the allowance that climate-sensitive emissions respond to the climate change. We examine the changes in levels of O<sub>3</sub> and aerosols (CL2100EM2000 – CL2000EM2000) resulting from pure climate change in the absence of heterogeneous reactions. The effects of pure climate change in the presence of heterogeneous reactions do not differ qualitatively from those in their absence, except those discussed at the end of this section. Predicted changes in global burdens of ozone and aerosols as a result of pure climate change are summarized in Table 2-4.

### 2.4.1 Predicted Changes in Ozone

Figure 2-5a shows the effect of CO<sub>2</sub>-driven climate change on surface-layer ozone mixing ratios (CL2100EM2000 – CL2000EM2000) for January and July. Ozone concentrations are generally lower in the warmer climate, except for those near heavily populated and biomass burning areas. July O<sub>3</sub> mixing ratios over the eastern United States, Europe, and South Africa, as well as those near the east coast of China are predicted to increase by up to 8–12 ppbv. In January, ozone concentrations over biomass burning areas in Africa are predicted to increase by as much as 11 ppbv. The predicted regional increases of O<sub>3</sub> can be explained as follows. Global temperature increase leads to less vigorous atmospheric flow, resulting in near-source enhancement of tracer mixing

ratios [Boer, 1995; Carnell and Senior, 1998; Holzer and Boer, 2001]. Increases in ozone also result from increases in emissions of biogenic hydrocarbons as surface temperature increases. As shown in Table 2-3, emissions of biogenic hydrocarbon are predicted to increase by 55% by year 2100. Sensitivity studies in the absence or presence of temperature dependence of biogenic emissions indicate that the increases in biogenic hydrocarbon emissions explain about 30–50% of the predicted increases in O<sub>3</sub> in the areas mentioned above. The climate-induced increases in biogenic hydrocarbons were also found to increase future daily maximum O<sub>3</sub> concentrations in summertime over the eastern United States [Hogrefe *et al.*, 2004]. Some other processes might also contribute to those regional increases of O<sub>3</sub>. Peroxyacetyl nitrate (PAN) will be less stable at higher temperatures, so oxidized nitrogen is more likely to be present as NO<sub>x</sub> near source regions [Stevenson *et al.*, 2005]. Murazaki and Hess [2006] found that the higher levels of water vapor have different effects on O<sub>3</sub>, depending on the background NO<sub>x</sub> level; with increased water vapor in a warmer climate, O<sub>3</sub> destruction is enhanced at low NO<sub>x</sub> levels, while O<sub>3</sub> production is enhanced if NO<sub>x</sub> concentrations are high.

The zonal mean percentage changes in O<sub>3</sub> concentrations are shown in Figure 2-5b for January and July. Zonal mean O<sub>3</sub> concentrations are reduced throughout the troposphere as a result of CO<sub>2</sub>-induced warming, with the largest percentage reductions of 20–30% predicted near the surface over the North Pole, over the tropics and subtropics in the lower troposphere, and within  $\pm 30^\circ$  near the tropopause, correlating with the predicted largest increases in temperature or water vapor. Increased water vapor has an overall effect of leading to more ozone loss through ozone photolysis followed by O<sub>1</sub>(D) reaction with H<sub>2</sub>O, which, together with the increases in temperature, lead to a reduction

in net chemical production of O<sub>3</sub> [Johnson *et al.*, 2001]. Global O<sub>3</sub> budgets from CL2100EM2000 and CL2000EM2000 (Table 2-5) give a net chemical O<sub>3</sub> production of 412 Tg yr<sup>-1</sup> under present-day climate conditions, and 331 Tg yr<sup>-1</sup> in the year 2100 atmosphere. Pure CO<sub>2</sub>-induced climate change is predicted to reduce the global ozone burden by 12%, from 349 Tg in present-day to 307 Tg with year 2100 climate.

## 2.4.2 Predicted Changes in Carbonaceous Aerosols

Figure 2-6 shows the changes (CL2100EM2000 – CL2000EM2000) in BC, POA, and SOA concentrations resulting from the climate change alone at selected vertical levels. BC and POA aerosols are chemically inert tracers that respond to changes in meteorological fields. The pattern of the predicted changes in BC is similar to that of the changes in POA. POA aerosols near the equator arise mainly from biomass burning and fossil fuel emissions located in South Asia. In a warmer climate, the weaker Hadley cell leads to weaker trade winds and consequently less POA being transported away from the source regions; this finding agrees with that reported in *Holzer and Boer* [2001]. The weaker Hadley cell leads to reduced precipitation (Figure 2-2) and weaker upward transport (Figure 2-3), which also helps to increase the POA concentrations.

Surface POA concentrations are predicted to generally decrease from mid to high latitudes in both hemispheres, as a result of increased precipitation (Figure 2-2c). The effects of climate change on POA concentrations over North America, Europe, and eastern China depend on the changes in precipitation and transport. While slower transport in the warmer climate increases POA concentrations near the source regions, larger annual mean precipitation in these populated areas leads to larger wet deposition of hydrophilic POA (50% of emitted POA is assumed to be hydrophilic [Liao *et al.*, 2003]). The net effect of

these two competing factors leads to a complex response: increased POA concentrations over and near western Europe, and reduced concentrations over the United States and eastern China (Figure 2-6b). The predicted 10% increase in global mean precipitation in year 2100 has a large impact on aerosol loadings. The predicted annual global budget of POA shows that climate change alone leads to a reduction in the POA global burden by 9.3%, from 1.29 Tg in the present-day to 1.17 Tg in year 2100, as a result of a 3.8% increase (from 50.2 Tg yr<sup>-1</sup> in present-day to 52.1 Tg yr<sup>-1</sup> in year 2100) in POA wet deposition. The global BC burden is predicted to be reduced by 13% (Table 2-4) for the same reason.

Climate change influences SOA distributions in several ways. First, increased precipitation leads to increased wet deposition of SOA and its gas-phase precursors, as well as less POA available for the absorption of SOA. Also, higher temperatures shift the gas-particle partitioning of volatile oxidation products toward the gas-phase. Each of these effects leads to decreased SOA. On the other hand, there is a 58% predicted increase in emissions of monoterpenes and ORVOCs in year 2100 (Table 2-3). The net effect of these opposing influences is a modest increase in global SOA from 2000 to 2100. With anthropogenic POA emissions held at present-day levels, the predicted SOA burden is 0.38 Tg in year 2100 atmosphere, an 8.6% increase relative to the 0.35 Tg predicted with the present-day climate (Table 2-4).

### **2.4.3 Predicted Changes in Sulfate and Nitrate Aerosols**

Dimethyl sulfide (DMS) emissions depend on ocean surface wind speed and temperature. In year 2100 climate, while higher temperature increases DMS emissions,

the slower wind speed over the oceans (Figure 2-3b) reduces air-sea exchange. The temperature effect dominates, leading to an overall increase in DMS emissions by about 11% from 2000 to 2100 (Table 2-3). Note that this estimate is based on an assumption of constant marine DMS concentrations. *Bopp et al.* [2004] predicted a 3% increase in DMS emissions on the basis of the GCM predicted sea-surface DMS concentrations and a doubled CO<sub>2</sub> climate.

Both the oxidation of DMS and sulfate formation from the gas-phase reaction of SO<sub>2</sub>+OH are determined by the predicted OH concentrations. We show in Figure 2-7a the predicted zonal mean changes in OH concentration in the warmer climate (CL2100EM2000 – CL2000EM2000). In both January and July, OH concentrations increase mainly above 650 mb altitude in the tropics of the summer hemisphere, corresponding to the region with the largest increases in water vapor. Over the tropics and in the summer hemisphere, OH concentrations in the lower troposphere are predicted to decrease, as a result of lower O<sub>3</sub> and increased OH loss from the CH<sub>4</sub>+OH reaction at higher temperature [*Johnson et al.*, 1999].

The annual mean changes in surface layer sulfate mixing ratios (CL2100EM2000 – CL2000EM2000) by CO<sub>2</sub>-induced warming are presented in Figure 2-8. The predicted changes in surface-layer sulfate mixing ratios are similar to those of POA, with sulfate mixing ratios reduced at the middle to high latitudes in both hemispheres but increased over the tropics. The surface-layer sulfate mixing ratios over Europe, the eastern US, and eastern China are predicted to increase by up to 400 pptv. Besides the near-source effects mentioned in connection with POA, the locally higher O<sub>3</sub>, OH, and H<sub>2</sub>O<sub>2</sub> concentrations in the warmer climate contribute to larger sulfate formation in these areas. Although the zonal mean surface-layer OH concentrations decrease, the predicted OH concentrations

near sources increase corresponding to the locally increased  $O_3$  (Figure 2-5).  $H_2O_2$  formation increases in a warmer climate, because the rate coefficient of the reaction  $HO_2+HO_2\rightarrow H_2O_2$  increases with temperature. The global burden of  $H_2O_2$  is predicted to increase by 25% as a results of climate change alone (Table 2-4).

The global mean annual sulfate budget is given in Table 2-6. Climate change alone slightly reduces sulfate formation via the gas-phase OH reaction while increasing in-cloud formation by about 5%. Sulfate lifetime from 4.7 days to 4.0 days as a results of the increased wet deposition. The global burdens of  $SO_2$  and sulfate are predicted to be reduced by 16% and 14%, respectively, in the warmer climate (Table 2-4).

Changes in temperature influence aerosol equilibrium significantly. Figure 2-9 shows the ratios of the predicted zonal mean nitrate concentrations from the simulation CL2100EM2000 to those from CL2000EM2000. In the warmer climate, more  $HNO_3$  remains in the gas-phase, leading to significant percentage reductions in nitrate concentrations throughout the troposphere except in the tropical lower troposphere. The reasons for the increases over the tropics are the same as those for the increases of POA in that region. The global burden of nitrate is predicted to be reduced by 47.2% as a result of  $CO_2$  warming over 2000–2100, if emissions of nitrate precursors remain at 2000 levels.

#### **2.4.4 Predicted Changes in Sea Salt and Mineral Dust**

As shown in Table 2-3, sea salt emissions are predicted to be reduced by 6% as a result of the reductions in zonal mean surface wind speed at 30–60°S, 5°S–40°N, and around 60°N (Figure 2-4b). These reductions in emissions, together with the increases in

precipitation, lead to an overall 19% reduction in global sea salt burden from the present-day to year 2100 (Table 2-4).

Mineral dust emissions depend on both wind speed and soil moisture. With the predicted reductions of surface wind speed over the Sahara Desert and central Asia (Figure 2-4a), two major sources of mineral dust, and the increases in precipitation over North Africa, a 14% reduction in dust emissions from year 2000 to year 2100 is predicted (Table 2-3). Since the increased precipitation also leads to larger wet deposition of dust, predicted global burden of dust is reduced from 18.2 Tg in present-day to 15.2 Tg in year 2100 (Table 2-4). Because land type and vegetation are likely to change as climate changes, more accurate simulation of future mineral dust requires prognostic simulation of land surface use.

The changes in emissions of sea salt and mineral dust predicted in this work diverge from those in Chapter 5.5.2 of the IPCC 2001 report. The IPCC estimates were based on the ratios of monthly average wind speeds for the years 2090–2100 to those for the years 1990–2000 associated with the IS92a scenario simulated by *Dai et al.* [2001]. Although the changes in temperature, precipitation, and meridional circulations predicted here agree qualitatively with those of *Dai et al.* [2001], our equilibrium climate simulation with IPCC SRES A2 CO<sub>2</sub> only is different from the transient climate simulation with IS92a sulfate, CO<sub>2</sub>, and non-CO<sub>2</sub> greenhouse gases by *Dai et al.* [2001]. As discussed by *Dai et al.* [2001], the predicted regional climate changes may also be model dependent.

## 2.4.5 Effects of Climate Change in the Presence of Heterogeneous Reactions

The heterogeneous reactions considered are those of  $\text{N}_2\text{O}_5$ ,  $\text{NO}_3$ ,  $\text{NO}_2$ , and  $\text{HO}_2$  on wet aerosols, the uptake of  $\text{SO}_2$  by sea salt, as well as the uptake of  $\text{SO}_2$ ,  $\text{HNO}_3$  and  $\text{O}_3$  by mineral dust; the heterogeneous reactions influence mainly the concentrations of  $\text{O}_3$ , sulfate, and nitrate [Liao and Seinfeld, 2005]. The effects of pure climate change on the predictions of  $\text{O}_3$ , sulfate, and nitrate in the presence of the heterogeneous reactions are represented by the differences in concentrations between the simulations CL2100EM2000h and CL2000EM2000h. The annual mean differences between the effects of climate change with heterogeneous reactions and those without  $[(\text{CL2100EM2000h} - \text{CL2000EM2000h}) - (\text{CL2100EM2000} - \text{CL2000EM2000})]$  are shown in Figure 2-10 for the surface layer.

The effects of climate change on surface  $\text{O}_3$  concentrations in the presence of heterogeneous reactions are qualitatively the same as those shown Figure 2-5 in their absence. However, since the uptake coefficient for the hydrolysis of  $\text{N}_2\text{O}_5$  depends on temperature and relative humidity [Evans and Jacob, 2005; Liao and Seinfeld, 2005], at higher atmospheric temperature, hydrolysis of  $\text{N}_2\text{O}_5$  is reduced [Hallquist *et al.*, 2003], leading to more  $\text{NO}_x$  and hence larger increases in  $\text{O}_3$  concentrations near sources and less  $\text{O}_3$  reduction in other areas, as indicated by the positive values shown in Figure 2-10a. On an annual mean basis, the climate-induced changes in surface  $\text{O}_3$  concentrations predicted in the presence of heterogeneous reactions differ from those predicted in their absence by 1–4 ppbv in the Northern Hemisphere where aerosol concentrations are high.

In the absence of sea salt and mineral dust uptake of  $\text{SO}_2$ , the surface-layer sulfate concentrations are predicted to be reduced at middle to high latitudes in both Hemispheres (Figure 2-8). Because of the predicted reductions in sea salt and mineral dust burdens in year 2100, less  $\text{SO}_2$  is taken up by sea salt and dust. As a result, the largest differences in the effects of pure climate change on sulfate are predicted over oceans and near dust sources (Figure 2-10b).

Predicted climate-induced reductions in surface-layer nitrate concentrations in the presence of heterogeneous reactions are less over the oceans and near the dust sources, again because of the reduced uptake of  $\text{HNO}_3$  by sea salt and mineral dust in year 2100 (Figure 2-10c). Over Europe, eastern Asia, and eastern United States, climate-induced reductions of nitrate concentrations in the presence of heterogeneous reactions exceed those in their absence, as a result of the less hydrolysis of  $\text{N}_2\text{O}_5$  at higher temperature and less  $\text{HNO}_3$  available for nitrate formation in year 2100.

It should be noted that the results shown in Figure 2-10 are based on the changes in climate alone. Heterogeneous reactions assume greater importance when year 2100 anthropogenic emissions are used in the chemistry simulations. With the large increases in aerosol concentrations and  $\text{NO}_x$  emissions in year 2100, hydrolysis of  $\text{NO}_x$  becomes more influential in predicting  $\text{O}_3$  and nitrate formation [*Liao and Seinfeld, 2005*].

## 2.5 Predicted O<sub>3</sub> and Aerosol Concentrations with Year 2100

### Projected Emissions and Climate

Predicted year 2100 surface-layer O<sub>3</sub> mixing ratios, the changes relative to the year 2000 concentrations, and the differences between the surface-layer O<sub>3</sub> mixing ratios simulated with the changes in both climate and emissions and those obtained with changes in emissions only are shown in Figure 2-11. Compared to the present-day O<sub>3</sub> levels, year 2100 surface-layer O<sub>3</sub> concentrations are predicted to generally increase by 30–70 ppbv over populated and biomass burning areas (Figure 2-11b). Such large increases in O<sub>3</sub> concentrations over the emission source regions result mainly from the increases in anthropogenic emissions of O<sub>3</sub> precursors over 2000–2100, but climate change also contributes to the increases. As shown in Figure 2-11c, accounting for the changes in emissions and climate increases the surface-layer O<sub>3</sub> concentrations over or near emission source areas increase by up to 17 ppbv, relative to the case in which only emission changes are considered. Climate change alone has the overall effect of reducing global O<sub>3</sub> burden; the year 2100 global O<sub>3</sub> burden of 521 Tg (or 450 Tg) predicted in CL2100EM2100 (or CL2100EM2100h) is about 13.4% (or 11.6%) lower than that predicted in CL2000EM2100 (or CL2000EM2100h) (Table 2-4). The difference in predicted O<sub>3</sub> burden between CL2100EM2100h and CL2100EM2100 reflects the importance of heterogeneous reactions.

With changes in emissions and climate considered, burdens of all anthropogenic aerosol species increase from 2000 to 2100 except for sulfate (Table 2-4). Relative to year 2000, the predicted sulfate burden is lower in year 2100, as a result of the projected

lower emissions and larger wet deposition (Table 2-6). While sulfate is the most significant anthropogenic aerosol component in 2000, POA is predicted to have the largest global burden in year 2100, followed by sulfate, nitrate, and BC. Although the warmer climate does not favor the formation of nitrate aerosol, the nitrate burden is predicted to increase from 0.53 Tg (or 0.51 Tg) in 2000 to 1.49 Tg (or 1.27 Tg) in 2100 in the absence (or presence) of heterogeneous reactions, as a result of the significant increases in  $\text{NO}_x$  and  $\text{NH}_3$  emissions.

Figure 2-12a shows the year 2100 dry aerosol mass, the sum of sulfate, nitrate, ammonium, BC, POA, and SOA, at the surface layer from the simulations CL2100EM2100 and CL2100EM2100h. Dry aerosol mass concentrations exceeding  $15 \mu\text{g m}^{-3}$  are predicted over Europe, eastern United States, eastern China, and the biomass burning regions. As a result of the large increases in POA and nitrate concentrations, the dry mass concentrations over eastern United States, Europe, and eastern Asia are predicted to increase by 0–10, 20–40, and 40–90  $\mu\text{g m}^{-3}$ , respectively, relative to the present-day values (Figure 2-12b). The dry aerosol mass concentrations predicted in CL2100EM2100 (or CL2100EM2100h) differ from those predicted in CL2000EM2100 (or CL2000EM2100h) by  $-10 \mu\text{g m}^{-3}$  to  $+4 \mu\text{g m}^{-3}$  regionally (Figure 2-12c).

The global budgets for year 2100  $\text{O}_3$  and sulfate in the absence of heterogeneous reactions are given in Tables 2-5 and 2-6, respectively. When changes in emissions and climate are accounted for, the lifetime of  $\text{O}_3$  changes from 27 days in present-day to 17 days in year 2100, while that of sulfate changes from 4.7 to 3.8 days. In year 2100, the shorter lifetimes of  $\text{O}_3$  is caused mainly by the increased removal of  $\text{O}_3$  by the reaction of

$O_1(D)$  with HO [Johnson *et al.*, 1999, 2001], while the shorter lifetime of sulfate results from increased wet removal.

## 2.6 Impact of Climate Change on Estimates of Year 2100

### Direct Radiative Forcing

To examine the effect of climate change on future forcing estimates, we compare the instantaneous radiative forcings calculated using CL2000EM2100 concentrations and climate with those calculated with CL2100EM2100 conditions. Radiative forcings by  $O_3$ , sulfate, nitrate, BC, OC (POA+SOA), as well as by the internal and external mixture of these aerosols are calculated. In the external mixture, particles from different sources remain separated, while in the internal mixture, the various chemical components are mixed uniformly in each particle. The top of the atmosphere (TOA) forcing by a species is calculated as the difference in the net fluxes at TOA in its presence and absence, so the forcing values reported here represent the effect of both natural and anthropogenic ozone/aerosols on global radiative balance. The assumptions for water uptake by aerosols, aerosol size distributions, and refractive indices follow those described by Liao *et al.* [2004].

The global and annual mean TOA  $O_3$  and aerosol forcings from simulations CL2000EM2100, CL2100EM2100, CL2000EM2100h, and CL2100EM2100h are summarized in Table 2-7. Compared with the TOA  $O_3$  forcing calculated in simulation CL2000EM2100, the 13% lower global  $O_3$  burden and the different climate in simulation CL2100EM2100 lead to 20% reduction in global mean  $O_3$  radiative forcing (Tables 2-5

and 2-7). In the warmer climate, the reduced burden and the melting of snow and ice lead to 0.2–0.4 W m<sup>-2</sup> reductions in shortwave O<sub>3</sub> forcing at the North Pole, and the reduced O<sub>3</sub> burden also leads to about the same magnitude reductions in O<sub>3</sub> longwave forcing over tropics and subtropics.

Although the global BC burden predicted in CL2100EM2100 is just 11% lower than that predicted in CL2000EM2100, the global mean BC forcing is reduced by 23% in year 2100 climate (CL2100EM2100), because BC forcing at high northern latitudes is reduced significantly as a result of the reduction in both BC column burden and surface albedo in the warmer climate. The global burden of OC predicted in CL2100EM2100 is 6% lower than that predicted in CL2000EM2100, but the global mean TOA forcing by OC changes slightly from –0.56 W m<sup>-2</sup> in present-day climate to –0.58 W m<sup>-2</sup> in the warmer climate. The TOA OC forcings over the polar regions change from warming in simulation CL2000EM2100 to cooling in simulation CL2100EM2100, because of the weak absorbing feature of OC and the reduced surface albedo in the warmer climate.

Relative to the simulation CL2000EM2100, the global mean sulfate cooling is 4% less with a 9% reduction in global burden in CL2100EM2100, and the global mean nitrate cooling is 28% lower with a 39% reduction in global burden when climate change is considered (Tables 2-4 and 2-7). The percentage change in the global mean TOA forcing by a scattering aerosol is less than the percentage change in its global burden, because of the changes in surface albedo and clouds over Polar Regions and the predicted increases in concentrations in the Tropics. Relative to the simulation CL2000EM2100, sulfate TOA cooling in CL2100EM2100 increases at high northern latitudes, although sulfate column burdens there are predicted to be reduced. This forcing behavior at high

latitudes is a result of the reduced ice and snow cover, as well as fewer low clouds and more high clouds in the warmer climate. As shown by *Liao and Seinfeld* [1998], TOA sulfate cooling under clear sky conditions increases when surface albedo decreases, and thin stratus or cirrus clouds above sulfate aerosol enhance sulfate cooling.

The global mean TOA forcing by the internally mixed sulfate, nitrate, BC, and OC changes from  $-0.26 \text{ W m}^{-2}$  in CL2000EM2100 to  $-0.48 \text{ W m}^{-2}$  in CL2100EM2100, while the global mean forcing by the external mixture in the year 2100 climate differs from that in year 2000 climate by a modest amount of  $0.02 \text{ W m}^{-2}$  (Table 2-7). Because an internal mixture has lower single-scattering albedo and hence stronger absorption of both incoming and outgoing solar radiation than an external mixture, the radiative forcing by an internal mixture is more sensitive to the changes in surface albedo. At the high northern latitudes, TOA forcing by either the internal or the external mixture is always positive, but the heating estimated in CL2100EM2100 is  $2\text{--}4 \text{ W m}^{-2}$  (or  $1\text{--}2 \text{ W m}^{-2}$ ) less than that calculated in CL2000EM2100 for the internal (or external) mixture as a result of the reduction in surface albedo. Over populated areas, estimated TOA cooling by either the internal and external mixtures is  $1\text{--}3 \text{ W m}^{-2}$  less in year 2100 climate than in year 2000 atmosphere because of the reduction in aerosol column burdens.

The effects of climate change on forcing estimates in the presence of heterogeneous reactions are similar to those predicted in their absence (Table 2-7); the  $\text{CO}_2$ -driven climate change is influential in estimating year 2100 TOA forcing of absorbing species and nitrate.

## 2.7 Summary and Discussion

We have examined the impact of an equilibrium climate in year 2100 driven by the projected change in CO<sub>2</sub> concentration from IPCC SRES A2 on predictions of global ozone and aerosols by online GCM simulation of coupled tropospheric ozone-NO<sub>x</sub>-hydrocarbon chemistry and sulfate, nitrate, ammonium, black carbon, primary organic carbon, secondary organic carbon, sea salt, and mineral dust aerosols.

Using the GISS GCM II' with a Q-flux ocean, we predict an increase of 4.8°C in global mean surface temperature in year 2100, as a result of the projected increase in CO<sub>2</sub> from 368 ppmv in year 2000 to 836 ppmv in year 2100. Year 2100 global mean precipitation is predicted to be 10% higher than that for year 2000; predicted changes in temperature and precipitation agree qualitatively with those of previous studies. The model predicts a weakening of the Hadley cells in the warmer 2100.

We have performed four chemistry simulations, CL2000EM2000, CL2100EM2000, CL2000EM2100, and CL2100EM2100, to assess the roles of CO<sub>2</sub>-driven climate change and IPCC projected changes in emissions in influencing levels of tropospheric O<sub>3</sub> and aerosols. The differences between CL2000EM2000 and CL2100EM2000 indicate that, with no changes in anthropogenic emissions, the CO<sub>2</sub>-driven climate would change global burdens of O<sub>3</sub>, sulfate, nitrate, BC, POA and SOA burdens by -12%, -14%, -47%, -13%, -9% and +9%, respectively. Although the global O<sub>3</sub> burden is predicted to be reduced as a result of faster removal of O<sub>3</sub> in the warmer climate, surface-layer O<sub>3</sub> concentrations over populated and biomass burning areas are predicted to increase as a result of climate change, owing to slower transport [*Holzer and Boer, 2001*], enhanced

biogenic hydrocarbon emissions, decomposition of PAN at higher temperature, and the increase of O<sub>3</sub> production by increased water vapor at high NO<sub>x</sub> levels. Climate change influences aerosol burdens mainly by altering wet deposition, climate-sensitive emissions, and aerosol thermodynamic equilibrium.

Accounting for both the CO<sub>2</sub>-driven climate change and changes in emissions in CL2100EM2100, the year 2100 global burdens of O<sub>3</sub>, sulfate, nitrate, BC, POA and SOA are predicted to change by +49%, -16%, +181%, +109%, +111% and +54%, respectively, as compared with simulation CL2000EM2000. On the basis of the IPCC SRES A2, the changes in anthropogenic emissions play a more dominant role in determining future levels of tropospheric ozone and aerosols than does climate change. Sea salt and mineral dust burdens are predicted to be reduced by 19% and 16%, respectively, in the year 2100.

We also examine the effects of CO<sub>2</sub>-driven climate change on estimates of year 2100 direct radiative forcing by O<sub>3</sub> and aerosols. By comparing simulations CL2000EM2100 and CL2100EM2100, the effect of climate change alone on radiative forcings can be discerned; accounting for ozone and aerosols from both natural and anthropogenic sources, the predicted global mean TOA direct radiative forcings of O<sub>3</sub>, sulfate, nitrate, BC, OC, internal mixture (internally mixed sulfate, nitrate, BC, and OC), and external mixture (externally mixed sulfate, nitrate, BC, and OC) change from +1.06, -0.97, -1.09, +1.26, -0.56, -0.26, -1.22 W m<sup>-2</sup> in CL2000EM2100 to +0.85, -0.93, -0.78, +0.97, -0.58, -0.48, -1.20 W m<sup>-2</sup> in CL2100EM2100, respectively. The CO<sub>2</sub>-induced changes in global burden, surface albedo, and clouds have the largest influence on forcing estimates of absorbing species and nitrate aerosol.

The climate induced percentage changes in global O<sub>3</sub> and aerosol burdens as well as the absolute changes in year 2100 direct radiative forcings summarized above for the simulations in the absence of heterogeneous reactions agree closely with those obtained in their presence. When the reactions of N<sub>2</sub>O<sub>5</sub>, NO<sub>3</sub>, NO<sub>2</sub>, and HO<sub>2</sub> on wet aerosols, the uptake of SO<sub>2</sub> by sea salt, as well as the uptake of SO<sub>2</sub>, HNO<sub>3</sub> and O<sub>3</sub> by mineral dust are considered, although hydrolysis of N<sub>2</sub>O<sub>5</sub> is less in the warmer climate and the uptake by sea salt and mineral dust is reduced as a result of lower burdens of sea salt and mineral dust in year 2100, heterogeneous reactions are still influential in predicting the year 2100 concentrations of O<sub>3</sub>, sulfate, and nitrate; accounting for the changes in both climate and emissions, the year 2100 burdens of O<sub>3</sub>, sulfate, and nitrate predicted in the presence of heterogeneous reactions are 14%, 26%, 15%, respectively, lower than those predicted in their absence.

The results of this study suggest several avenues for improvement and future research. First, the biogenic emissions of O<sub>3</sub> and SOA precursors as well as the mineral dust emissions are based on fixed vegetation and land types, which can be improved with a prognostic treatment of vegetation and land type. As shown by *Sanderson et al.* [2003] and *Lathi re et al.* [2005], climate-vegetation coupling is important for predicting future biogenic hydrocarbon emissions. Second, O<sub>3</sub> transport from the stratosphere is fixed in all the simulations reported here; this process is climate-sensitive [*Sudo et al.*, 2003; *Collins et al.*, 2003; *Zeng and Pyle*, 2003] and can be improved with a GCM having a better representation of the stratosphere. Finally, and most importantly, the radiative effects of predicted ozone and aerosols in future years should be fed back into the GCM to assess complete chemistry-aerosol-climate coupling.

**Acknowledgment.** This work was supported by the National Aeronautics and Space Administration Earth Observing System Interdisciplinary Science program (NASA EOS-IDS) and the U.S. Environmental Protection Agency under Science to Achieve Results (STAR) grant R830959. We also acknowledge the Center for Advanced Computing Research at Caltech for computing resources.

## References

- Adams, P. J., J. H. Seinfeld, D. M. Koch, L. Mickley, and D. Jacob (2001), General circulation model assessment of direct radiative forcing by the sulfate-nitrate-ammonium-water inorganic aerosol system, *J. Geophys. Res.*, *106*, 1097–1111.
- Atherton, C. S., J. E. Penner, C. Price, and J. Walton (1995), Climate change and its effect on tropospheric ozone, in *Atmospheric Ozone as a Climate Gas*, Ed. By W.-C. Wang and I. S. A. Isaksen, 65–85, *NATO ASI Ser. I32*, Springer-Verlag, Berlin.
- Boer, G. J. (1995), Some dynamical consequences of greenhouse gas warming. *Atmos.–Ocean*, *33*, 731–751.
- Bopp, L., O. Boucher, O. Aumont, S. Belviso, J.-L. Dufresne, M. Pham, and P. Monfray (2004), Will marine dimethylsulfide emissions amplify or alleviate global warming? A model study, *Can. J. Fish. Aquat. Sci.* *61*, 826–835.
- Bouwman, A. F., D. S. Lee, W. A. H. Asman, F. J. Dentener, K. W. Van Der Hoek, and J. G. J. Olivier (1997), A global high-resolution emission inventory for ammonia, *Global Biogeochem. Cycles*, *11*(4), 561–588.
- Brasseur, G. P., J. T. Kiehl, J.-F. Müller, T. Schneider, C. Granier, X. X. Tie, and D. Hauglustaine (1998), Past and future changes in global tropospheric ozone: Impact on radiative forcing, *Geophys. Res. Lett.*, *25*(20), 3807–3810.
- Carnell, R. E., and C. A. Senior (1998), Changes in mid-latitude variability due to increasing greenhouse gases and sulphate aerosols, *Climate Dyn.*, *14*, 369–383.
- Chung, S. H., and J. H. Seinfeld (2002), Global distribution and climate forcing of carbonaceous aerosols, *J. Geophys. Res.*, *107*(D19), 4407, doi:10.1029/2001JD001397.
- Collins, W. J., R. G. Derwent, B. Garnier, C. E. Johnson, M. G. Sanderson, and D. S. Stevenson (2003), Effect of stratosphere-troposphere exchange on the future tropospheric ozone trend, *J. Geophys. Res.*, *108*(D12), 8528, doi:10.1029/2002JD002617.
- Constable, J. H., A. B. Guenther, D. S. Schimel, and R. K. Monson (1999), Modeling changes in VOC emission in response to climate change in the continental United States, *Glob. Change Biol.*, *5*, 791–806.
- Dai, A., T. M. L. Wigley, B. A. Boville, J. T. Kiehl, and L. E. Buja (2001), Climates of the twentieth and twenty-first centuries simulated by the NCAR climate system model, *J. Clim.*, *14*(4), 485–519.

- Evans, M. J., and D. J. Jacob (2005), Impact of new laboratory studies of  $\text{N}_2\text{O}_5$  hydrolysis on global model budgets of tropospheric nitrogen oxides, ozone, and OH, *Geophys. Res. Lett.*, *32*, L09813, doi:10.1029/2005GL022469.
- Gauss, M., et al. (2003), Radiative forcing in the 21st century due to ozone changes in the troposphere and the lower stratosphere, *J. Geophys. Res.*, *108*(D9), 4292, doi:10.1029/2002JD002624.
- Gillette, D. (1978), A wind tunnel simulation of the erosion of soil: Effect of soil texture, sandblasting, wind speed, and soil consolidation on dust production, *Atmos. Environ.*, *12*, 1735–1743.
- Griffin, R. J., D. R. Cocker, J. H. Seinfeld, and D. Dabdub (1999a), Estimate of global atmospheric organic aerosol from oxidation of biogenic hydrocarbons, *Geophys. Res. Lett.*, *26*, 2721–2724.
- Griffin, R. J., D. R. Cocker, R. C. Flagan, and J. H. Seinfeld (1999b), Organic aerosol formation from the oxidation of biogenic hydrocarbons, *J. Geophys. Res.*, *104*, 3555–3567.
- Guenther, A., C. N. Hewitt, D. Erickson, R. Fall, C. Geron, T. Graedel, P. Harley, L. Klinger, M. Lerdau, W. A. Mckay, T. Pierce, B. Scholes, R. Steinbrecher, R. Tallamraju, J. Taylor, and P. Zimmerman (1995), A global model of natural volatile organic compound emissions, *J. Geophys. Res.*, *100*, 8873–8892.
- Hallquist, M., D. J. Stewart, S. K. Stephenson, and R. A. Cox (2003), Hydrolysis of  $\text{N}_2\text{O}_5$  on sub-micron sulfate aerosols, *Phys. Chem. Chem. Phys.*, *5*(16), 3453–3463.
- Hansen, J., A. Lacis, G. Russell, P. Stone, I. Fung, R. Ruedy, and J. Lerner (1984), Climate sensitivity: Analysis of feedback mechanisms, in *Climate Processes and Climate Sensitivity*, *Geophys. Monogr. Ser.*, Vol. 29, edited by J. E. Hansen and T. Takahashi, pp. 130–163, American Geophysical Union, Washington, D.C..
- Hansen, J., M. Sato, and R. Ruedy (1997), Radiative forcing and climate response, *J. Geophys. Res.*, *102*, 6831–6864.
- Hansen, J., et al. (2005), Efficacy of climate forcings, *J. Geophys. Res.*, *110*, D18104, doi:10.1029/2005JD005776.
- Hogrefe, C., J. Biswas, B. Lynn, K. Civerolo, J.-Y. Ku, J. Rosenthal, C. Rosenzweig, R. Goldberg, and P. L. Kinney (2004), Simulating regional-scale ozone climatology over the eastern United States: Model evaluation results, *Atmos. Environ.*, *38*, 2627–2638.
- Holzer, M., and G. J. Boer (2001), Simulated changes in atmospheric transport climate, *J. Clim.*, *14*, 4398–4420.

- Intergovernmental Panel on Climate Change (IPCC) (1995), *Climate Change 1995*, edited by J. T. Houghton et al., Cambridge Univ. Press, New York.
- Intergovernmental Panel on Climate Change (IPCC) (2001), *Climate Change 2001*, edited by J. T. Houghton et al., Cambridge Univ. Press, New York.
- Iversen, T., and Ø. Seland (2002), A scheme for process-tagged SO<sub>4</sub> and BC aerosols in NCAR CCM3: Validation and sensitivity to cloud processes, *J. Geophys. Res.*, *107*(D24), 4751, doi:10.1029/2001JD000885.
- Johnson, C. E., W. J. Collins, D. S. Stevenson, and R. G. Derwent (1999), Relative roles of climate and emissions changes on future tropospheric oxidant concentrations, *J. Geophys. Res.*, *104*, 18,631–18,645.
- Johnson, C. E., D. S. Stevenson, W. J. Collins, and R. G. Derwent (2001), Role of climate feedback on methane and ozone studied with a coupled Ocean-Atmosphere-Chemistry model, *Geophys. Res. Lett.*, *28*(9), 1723–1726, 2001.
- Kalnay, E., et al. (1996), The NCEP/NCAR 40-year reanalysis project, *Bull. Am. Meteorol. Soc.*, *77*, 437–471.
- Kanakidou, M., K. Tsigaridis, F. J. Dentener, and P. J. Crutzen (2000), Human activity-enhanced formation of organic aerosols by biogenic hydrocarbon oxidation, *J. Geophys. Res.*, *105*, 9243–9254.
- Kettle, A. J., et al. (1999), A global database of sea surface dimethylsulfide (DMS) measurements and a procedure to predict sea surface DMS as a function of latitude, longitude and month, *Global Biogeochem. Cycles*, *13*, 399–444.
- Kiehl, J. T., C. A. Shields, J. J. Hack, and W. D. Collins (2006), The climate sensitivity of the Community Climate System Model: CCM3, *J. Clim.*, *19*(11), 2584–2596.
- Koch, D. M. (2001), Transport and direct radiative forcing of carbonaceous and sulfate aerosols in the GISS GCM, *J. Geophys. Res.*, *106*, 20311–20332.
- Lathi re, J., D. A. Hauglustaine, N. De Noblet-Ducoudr , G. Krinner, and G. A. Folberth (2005), Past and future changes in biogenic volatile organic compound emissions simulated with a global dynamic vegetation model, *Geophys. Res. Lett.*, *32*, L20818, doi:10.1029/2005GL024164.
- Liao, H., and J. H. Seinfeld (1998), Effect of clouds on direct aerosol radiative forcing of climate, *J. Geophys. Res.*, *103*, 3781–3788.
- Liao, H., and J. H. Seinfeld (2005), Global impacts of gas-phase chemistry-aerosol interactions on direct radiative forcing by anthropogenic aerosols and ozone, *J. Geophys. Res.*, in press,.

- Liao, H., P. J. Adams, S. H. Chung, J. H. Seinfeld, L. J. Mickley, and D. J. Jacob (2003), Interactions between tropospheric chemistry and aerosols in a unified general circulation model, *J. Geophys. Res.*, *108*(D1), 4001, doi:10.1029/2001JD001260.
- Liao, H., J. H. Seinfeld, P. J. Adams, and L. J. Mickley (2004), Global radiative forcing of coupled tropospheric ozone and aerosols in a unified general circulation model, *J. Geophys. Res.*, *109*, D16207, doi:10.1029/2003JD004456.
- Liousse, C., J. E. Penner, C. Chuang, J. J. Walton, H. Eddleman, and H. Cachier (1996), A global three-dimensional model study of carbonaceous aerosols, *J. Geophys. Res.*, *101*, 19,411–19,432.
- Liss, P., and Merlivat (1986), Air–sea gas exchange: introduction and synthesis, In *The role of air–sea exchange in geochemical cycling*, Edited by P. Buat-Ménard. D. Reidel, Dordrecht,.
- Mickley, L. J., P. Murti, D. Jacob, J. Logan, and D. Rind (1999), Radiative forcing from tropospheric ozone calculated with a unified chemistry-climate model, *J. Geophys. Res.*, *104*, 30,153–30,172.
- Mickley, L. J., D. J. Jacob, B. D. Field, and D. Rind (2004), Climate response to the increase in tropospheric ozone since preindustrial times: A comparison between ozone and equivalent CO<sub>2</sub> forcings, *J. Geophys. Res.*, *106*, D05106, doi:10.1029/2003JD003653,.
- Mitchell, J. F. B. (1989), The “greenhouse” effect and climate change, *Rev. Geophys.*, *27*, 115–139.
- Monahan, E. C., D. E. Spiel, and K. L. Davidson (1986), A model of marine aerosol generation via whitecaps and wave disruption, in *Oceanic Whitecaps and Their Role in Air-Sea Exchange*, edited by E. C. Monahan and G. MacNiocaill, pp. 167–174, D. Reidel, Norwell, Mass.
- Murazaki, K., and P. Hess (2006), How does climate change contribute to surface ozone change over the United States?, *J. Geophys. Res.*, *111*, D05301, doi:10.1029/2005JD005873.
- Nenes, A., C. Pilinis, and S. N. Pandis (1998), Isorropia: A new thermodynamic equilibrium model for multiphase multicomponent inorganic aerosols, *Aquat. Geochem.*, *4*, 123–152.
- Penner, J. E., H. Eddleman, and T. Novakov (1993), Towards the development of a global inventory for black carbon emissions, *Atmos. Environ. Part A*, *27*, 1277–1295.
- P’etron, G., P. Harley, J. Greenberg, and A. Guenther (2001), Seasonal temperature variations influence isoprene emission, *Geophys. Res. Lett.*, *28*, 1707–1710.

- Ramaswamy, V. (2001), Radiative forcing of climate change, in *Climate Change 2001: The Scientific Basis. Contribution of Working Group I to the Third Assessment Report of the Intergovernmental Panel on Climate Change*, 881 pp., Cambridge Univ. Press, New York.
- Rind, D., and J. Lerner (1996), The use of on-line tracers as a diagnostic tool in general circulation model development, 1, Horizontal and vertical transport in the troposphere, *J. Geophys. Res.*, *101*, 12,667–12,683.
- Rind, D., and W. Rossow (1984), The effects of physical processes on the Hadley circulation, *J. Atmos. Sci.*, *41*, 479–507.
- Rind, D., R. Suozzo, N. K. Balachandran, and M. Prather (1990), Climate change and the middle atmosphere, part 1, The doubled CO<sub>2</sub> climate, *J. Atmos. Sci.*, *47*, 475–494.
- Rind, D., D. Shindell, P. Lonergan, and N. K. Balachandran (1998), Climate change and the middle atmosphere, part III, The doubled CO<sub>2</sub> climate revisited, *J. Clim.*, *11*, 876–894.
- Rind, D., J. Lerner, K. Shah, and R. Suozzo (1999), Use of on-line tracers as a diagnostic tool in general circulation model development, 2. Transport between the troposphere and stratosphere, *J. Geophys. Res.*, *104*, 9151–9167.
- Rind, D., J. Lerner, and C. McLinden (2001), Changes of tracer distribution in the doubled CO<sub>2</sub> climate, *J. Geophys. Res.*, *106*, 28,061–28,080.
- Rosenstiel, T. N., M. J. Potosnak, K. L. Griffin, R. Fall, and R. K. Monson (2003), Increased CO<sub>2</sub> uncouples growth from isoprene emission in an agriforest ecosystem, *Nature*, *421*(6920), 256 – 259.
- Russell, G. L., J. R. Miller, and L.-C. Tsang (1984), Seasonal ocean heat transports computed from an atmospheric model, *Dynam. Atmos. Oceans*, *9*, 253–271.
- Sanderson, M. G., C. D. Jones, W. J. Collins, C. E. Johnson, and R. G. Derwent (2003), Effect of climate change on isoprene emissions and surface ozone levels, *Geophys. Res. Lett.*, *30*(18), 1936, doi:10.1029/2003GL017642
- Sinha A., and R. Toumi (1997), Tropospheric ozone, lightning, and climate change, *J. Geophys. Res.*, *102*, 10,667–10,672.
- Smith, K. H., and N. M. Harrison (1998), The sea spray generation function, *J. Aerosol Sci.*, *29*, suppl. 1, S189–S190.
- Stevenson, D. S., R. M. Doherty, M. G. Sanderson, C. E. Johnson, W. J. Collins, and R. G. Derwent (2005), Impacts of climate change and variability on tropospheric ozone and its precursors, *Faraday Discuss.*, *130*, doi:10.1039/b417412g.

- Sudo, K., M. Takahashi, and H. Akimoto (2003), Future changes in stratosphere-troposphere exchange and their impacts on future tropospheric ozone simulations, *Geophys. Res. Lett.*, *30*(24), 2256, doi:10.1029/2003GL018526.
- Toumi R., J. D. Haigh, and K. S. Law (1996), A tropospheric ozone-lightning climate feedback, *Geophys. Res. Lett.*, *23*, 1037–1040,.
- Wang, Y. H., and D. J. Jacob (1998), Anthropogenic forcing on tropospheric ozone and OH since preindustrial times, *J. Geophys. Res.*, *103*, 31,123–31,135.
- Wesely, M. L. (1989), Parameterization of surface resistances to gaseous dry deposition in regional-scale numerical models, *Atmos. Environ.*, *23*, 1293–1304.
- Yienger, J. J., and H. Levy (1995), Empirical model of global soil biogenic NO<sub>x</sub> emissions, *J. Geophys. Res.*, *100*, 11,447–11,464.
- Zeng, G., and J. A. Pyle (2003), Changes in tropospheric ozone between 2000 and 2100 modeled in a chemistry-climate model, *Geophys. Res. Lett.*, *30*(7), 1392, doi:10.1029/2002GL016708.

Table 2-1. Summary of Chemistry Simulations<sup>a</sup>

Experiments	CO <sub>2</sub> Mixing Ratio, ppmv	Nominal Year of GCM Climate	Non-CO <sub>2</sub> Anthropogenic Emissions	Heterogeneous Reactions
CL2000EM2000	368	2000	Present-day	No
CL2000EM2000h	368	2000	Present-day	Yes
CL2100EM2000	836	2100	Present-day	No
CL2100EM2000h	836	2100	Present-day	Yes
CL2000EM2100	368	2000	2100	No
CL2000EM2100h	368	2000	2100	Yes
CL2100EM2100	836	2100	2100	No
CL2100EM2100h	836	2100	2100	Yes

<sup>a</sup> Climate-sensitive natural emissions depend on the simulated climate in all the simulations. See Table 2-3 for details.

Table 2-2. Global Annual Anthropogenic Emissions for the Years 2000 and 2100

Species	Present-Day 2000 Scenario	IPCC SRES A2 2100 Scenario
<b>NO<sub>x</sub>,<sup>a</sup> Tg N yr<sup>-1</sup></b>		
Fossil Fuel Combustion	20	96
Biomass Burning	11	11
Soil (fertilizer)	0.5	0.5
Aircraft	0.5	2.2
Total	32	109.7
<b>CO,<sup>a</sup> Tg CO yr<sup>-1</sup></b>		
Fossil Fuel Combustion	390	1858
Wood Fuel Combustion	130	130
Biomass Burning	510	510
Total	1030	2498
<b>Ethane,<sup>a</sup> Tg C yr<sup>-1</sup></b>		
Industrial	6.2	97.7
Biomass Burning	2.4	2.4
Total	8.6	100.1
<b>Propane,<sup>a</sup> Tg C yr<sup>-1</sup></b>		
Industrial	6.7	28.1
<b>≥ C<sub>4</sub> Alkenes,<sup>a</sup> Tg C yr<sup>-1</sup></b>		
Industrial	30.1	60.5
<b>≥ C<sub>3</sub> Alkenes,<sup>a</sup> Tg C yr<sup>-1</sup></b>		
Industrial	10	29
Biomass Burning	12	12
Total	22	41
<b>Acetone,<sup>a</sup> Tg C yr<sup>-1</sup></b>		
Biomass Burning	9	9
<b>SO<sub>2</sub>, Tg S yr<sup>-1</sup></b>		
Industrial	69	60.3
Biomass Burning	2.3	2.3
Total	71.3	62.6

Table 2-2. (Continued)

Species	Present-Day 2000 Scenario	IPCC SRES A2 2100 Scenario
$\text{NH}_3$ , <sup>b</sup> Tg N yr <sup>-1</sup>		
Agricultural	37.4	88.8
Biomass Burning	6.4	6.4
Other	3.1	7.4
Total	46.9	102.6
POA, Tg OM yr <sup>-1</sup>		
Biomass Burning	54	
Fossil Fuel	28.2	
Total	82.2 <sup>c</sup>	189.5 <sup>e</sup>
BC, Tg C yr <sup>-1</sup>		
Biomass Burning	5.6	
Fossil Fuel	6.6	
Total	12.2 <sup>c,d</sup>	28.8 <sup>e</sup>

<sup>a</sup> *Mickley et al.* [1999]; *Gauss et al.* [2003].

<sup>b</sup> *Bouwman et al.* [1997]; *Adams et al.* [2001]. Natural  $\text{NH}_3$  emissions from oceans, undisturbed soils, and wild animals are assumed to be 10.7 Tg N yr<sup>-1</sup> in both 2000 and 2100 simulations.

<sup>c</sup> *Liousse et al.* [1996].

<sup>d</sup> *Penner et al.* [1993].

<sup>e</sup> Scaled to projected changes in CO.

Table 2-3. Climate-sensitive Natural Emissions

Species	GCM Variables that Influence Emissions	Emission Schemes	Year 2000 Predicted Emissions	Year 2100 Predicted Emissions
NO <sub>x</sub> from Soil	temperature; precipitation	<i>Wang et al.</i> [1998]	4.5 Tg N yr <sup>-1</sup>	5.6 Tg N yr <sup>-1</sup>
NO <sub>x</sub> from Lightning	frequency of convective events	<i>Wang et al.</i> [1998]	3.3 Tg N yr <sup>-1</sup>	4.0 Tg N yr <sup>-1</sup>
Isoprene	temperature, solar radiation	<i>Guenther et al.</i> [1995]; <i>Wang et al.</i> [1998]	437.9 Tg C yr <sup>-1</sup>	680.4 Tg C yr <sup>-1</sup>
Biogenic Acetone	temperature, solar radiation	<i>Wang et al.</i> [1998]	10.9 Tg C yr <sup>-1</sup>	17.0 Tg C yr <sup>-1</sup>
Biogenic ≥ C <sub>3</sub> Alkenes	temperature, solar radiation	<i>Wang et al.</i> [1998]	12.5 Tg C yr <sup>-1</sup>	19.5 Tg C yr <sup>-1</sup>
Monoterpenes	temperature, solar radiation	<i>Guenther et al.</i> [1995]; <i>Wang et al.</i> [1998]	117 Tg C yr <sup>-1</sup>	185 Tg C yr <sup>-1</sup>
ORVOCs	temperature, solar radiation	see section 2.2.4	260 Tg C yr <sup>-1</sup>	411 Tg C yr <sup>-1</sup>
DMS	surface wind; temperature	<i>Kettle et al.</i> [1999]; <i>Liss and Merlivat</i> [1986]	22.5 Tg S yr <sup>-1</sup>	24.9 Tg S yr <sup>-1</sup>
Sea Salt	wind	<i>Monahan et al.</i> [1986]; <i>Smith and Harrison</i> [1998]; <i>Liao et al.</i> [2004]	6314.2 Tg	5947.8 Tg
Mineral Dust	wind; soil moisture	<i>Gillette</i> [1978]; <i>Liao et al.</i> [2004]	1816.9 Tg	1567.6 Tg

Table 2-4. Predicted Annual and Global Burdens<sup>a</sup>

No Heterogeneous Reactions				
Species	CL2000 EM2000	CL2100 EM2000	CL2000 EM2100	CL2100 EM2100
O <sub>3</sub>	349	307 (-12.0%)	602 (+72.5%)	521 (+49.3%)
H <sub>2</sub> O <sub>2</sub>	3.37	4.21 (+24.9%)	7.16 (+112.5%)	8.86 (+162.9%)
SO <sub>2</sub>	1.14	0.96 (-15.8%)	0.59 (-48.2%)	0.57 (-50.0%)
SO <sub>4</sub> <sup>2-</sup>	2.14	1.84 (-14.0%)	1.96 (-8.4%)	1.79 (-16.4%)
NO <sub>3</sub> <sup>-</sup>	0.53	0.28 (-47.2%)	2.43 (+358.5%)	1.49 (+181.1%)
BC	0.23	0.20 (-13.0%)	0.54 (+134.8%)	0.48 (+108.7%)
POA	1.29	1.17 (-9.3%)	2.96 (+129.5%)	2.72 (+110.9%)
SOA	0.35	0.38 (+8.6%)	0.46 (+31.4%)	0.54 (+54.3%)
Sea Salt	5.44	4.39 (-19.3%)	5.44 (0%)	4.39 (-19.3%)
Mineral Dust	18.17	15.20 (-16.3%)	18.17 (0%)	15.20 (-16.3%)
With Heterogeneous Reactions				
	CL2000 EM2000h	CL2100 EM2000h	CL2000 EM2100h	CL2100 EM2100h
O <sub>3</sub>	313	277 (-11.5%)	509 (+62.6%)	450 (+43.8%)
SO <sub>4</sub> <sup>2-</sup>	1.42	1.30 (-8.5%)	1.39 (-2.1%)	1.33 (-6.3%)
NO <sub>3</sub> <sup>-</sup>	0.51	0.27 (-47.1%)	2.02 (+296.1%)	1.27 (149.0%)

<sup>a</sup> Numbers in parentheses are percentage changes compared with present-day climate and emissions (CL2000EM2000 or CL2000EM2000h). Units are in Tg.

Table 2-5. Global Budget for Tropospheric O<sub>3</sub><sup>a</sup>

	CL2000 EM2000	CL2100 EM2000	CL2000 EM2100	CL2100 EM2100
Sources, Tg O <sub>3</sub> yr <sup>-1</sup>				
In Situ Chemical Production	4384	4799	10076	10811
Transport from Stratosphere	401	401	401	401
Total Sources	4785	5200	10477	11212
Sinks, Tg O <sub>3</sub> yr <sup>-1</sup>				
In Situ Chemical Loss	3972	4468	8965	9832
Dry Deposition	808	724	1541	1386
Total Sinks	4780	5192	10479	11218
Burden, Tg O <sub>3</sub>	349	307	602	521
Lifetime, days	27	22	21	17
Net Chemical Production	412	331	1111	979

<sup>a</sup> Budgets are for the odd oxygen family defined as the sum of O<sub>3</sub>, O, NO<sub>2</sub>, 2×NO<sub>3</sub>, HNO<sub>4</sub>, 3×N<sub>2</sub>O<sub>5</sub>, and the peroxyacylnitrates. Values are averaged over the 5-year chemistry simulation.

Table 2-6. Global Budget for Sulfate Aerosol

	CL2000EM2000	CL2100EM2000	CL2100EM2100
Sources, TgS yr <sup>-1</sup>			
Industrial Emissions	2.07	2.07	1.81
SO <sub>2</sub> +OH	11.35	11.13	11.42
In-cloud SO <sub>2</sub> +H <sub>2</sub> O <sub>2</sub>	32.91	35.75	41.47
In-cloud SO <sub>2</sub> +O <sub>3</sub>	9.49	8.63	5.22
Total Sources	55.82	57.58	59.92
Sinks, TgS yr <sup>-1</sup>			
Dry Deposition	8.70	8.06	8.27
Wet Deposition	45.93	48.29	49.62
Total Sinks	54.63	56.35	57.89
Burden, TgS	0.71	0.61	0.60
Lifetime, days	4.7	4.0	3.8

Table 2-7. Effect of Climate Change on Estimates of Year 2100 TOA Radiative Forcing<sup>a</sup>

Species	No Heterogeneous Reactions	
	CL2000EM2100	CL2100EM2100
O <sub>3</sub>	0.42(S) + 0.64(L) = 1.06	0.33(S) + 0.52(L) = 0.85
Sulfate	-0.97	-0.93
Nitrate	-1.09	-0.78
BC	+1.26	+0.97
OC	-0.56	-0.58
INT	-0.26	-0.48
EXT	-1.22	-1.20
O <sub>3</sub> +INT	+0.80	+0.37
O <sub>3</sub> +EXT	-0.16	-0.35
With Heterogeneous Reactions		
	CL2000EM2100h	CL2100EM2100h
O <sub>3</sub>	0.36(S) + 0.57(L) = 0.93	0.29(S) + 0.47(L) = 0.76
Sulfate	-0.72	-0.72
Nitrate	-1.00	-0.74
BC	+1.26	+0.97
OC	-0.56	-0.58
INT	+0.06	-0.26
EXT	-0.87	-0.96
O <sub>3</sub> +INT	+0.99	+0.50
O <sub>3</sub> +EXT	+0.06	-0.20

<sup>a</sup> Units are W m<sup>-2</sup>. Both natural and anthropogenic aerosols are considered in the forcing calculations; S, shortwave forcing by O<sub>3</sub>; L, longwave forcing by O<sub>3</sub>; INT, internally mixed sulfate, nitrate, BC, and OC (POA+SOA); EXT, externally mixed sulfate, nitrate, BC, and OC (POA+SOA).

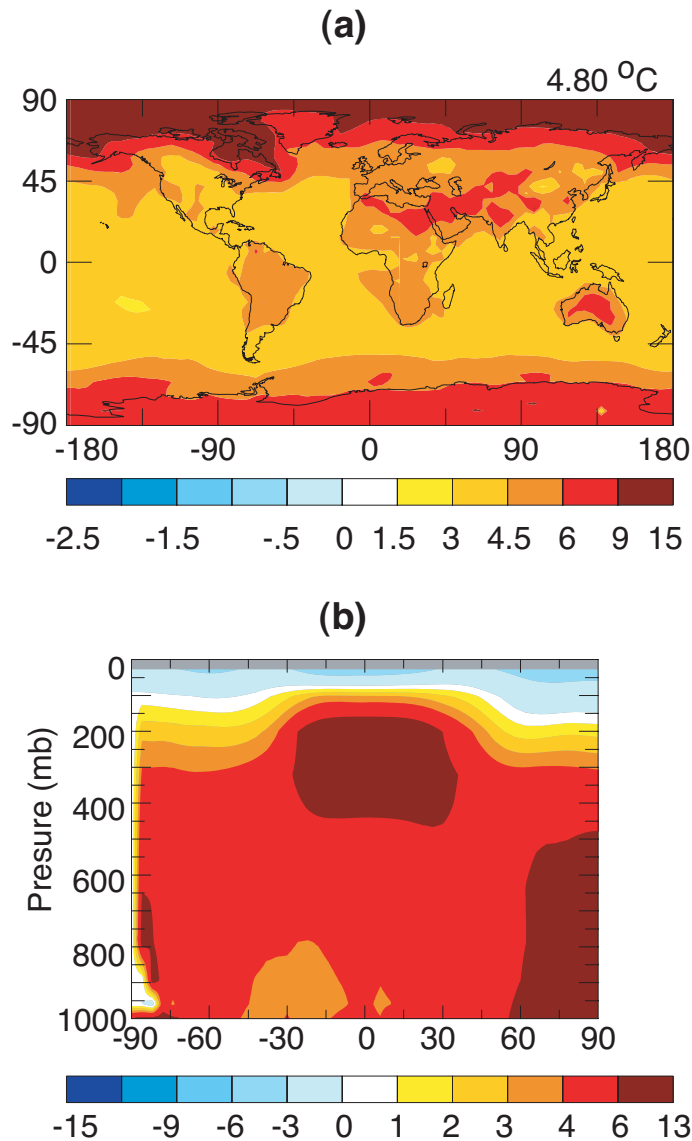


Figure 2-1. Temperature responses in the equilibrium climate to the increase in CO<sub>2</sub> concentration from 368 ppmv in year 2000 to 836 ppmv in year 2100, including predicted changes (°C) in (a) annual mean surface air temperature and (b) zonal annual mean atmospheric temperature. The global mean value is indicated at the top right corner of Figure 2-1a.

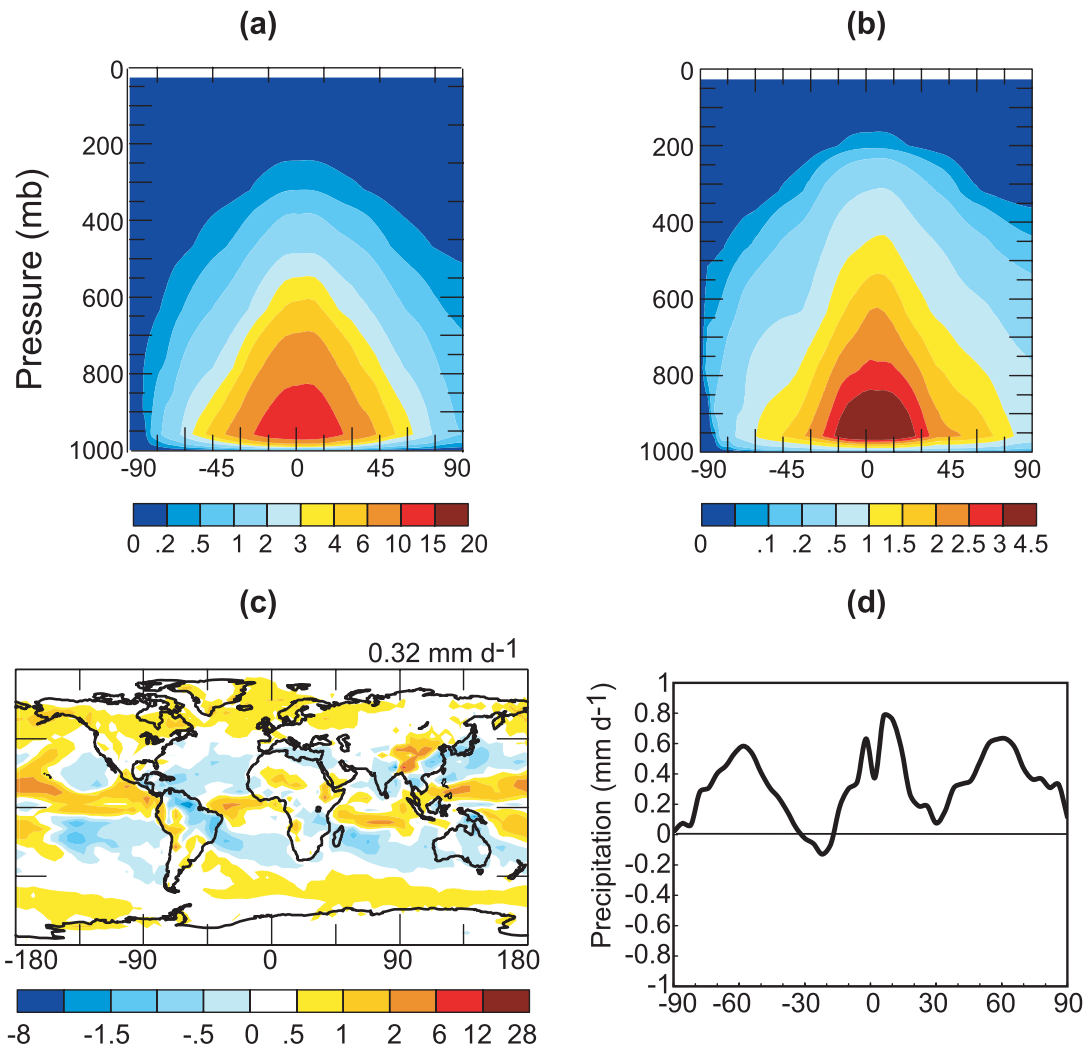


Figure 2-2. (a) Predicted year 2000 zonal annual mean equilibrium specific humidity ( $\text{g-H}_2\text{O kg-air}^{-1}$ ) as a function of pressure. (b) Predicted changes in zonal annual mean equilibrium specific humidity ( $\text{g-H}_2\text{O kg-air}^{-1}$ ) relative to year 2000. (c) Predicted changes ( $\text{mm day}^{-1}$ ) relative to year 2000 in annual mean precipitation. (d) Predicted changes ( $\text{mm day}^{-1}$ ) relative to year 2000 in zonal annual mean precipitation. The global mean value is indicated at the top right corner of Figure 2-2c.

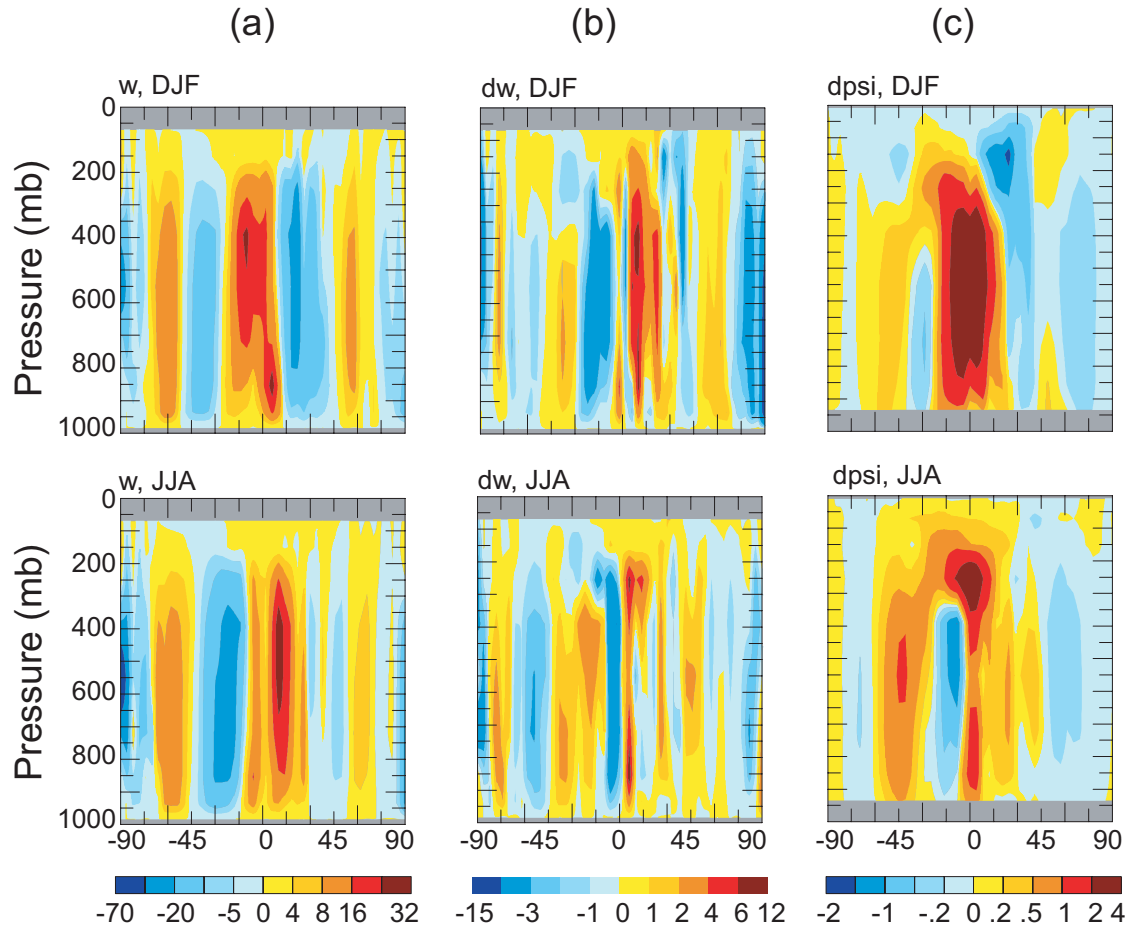


Figure 2-3. Latitude-pressure distributions of zonal and seasonal mean (a) present-day vertical velocity ( $10^{-5} \text{ mb s}^{-1}$ ), (b) changes in vertical velocity ( $10^{-5} \text{ mb s}^{-1}$ ) from year 2000 to year 2100, and (c) changes in mass stream function ( $10^{10} \text{ kg s}^{-1}$ ) from 2000 to 2100. Positive values of the mass stream function indicate anticlockwise circulation.

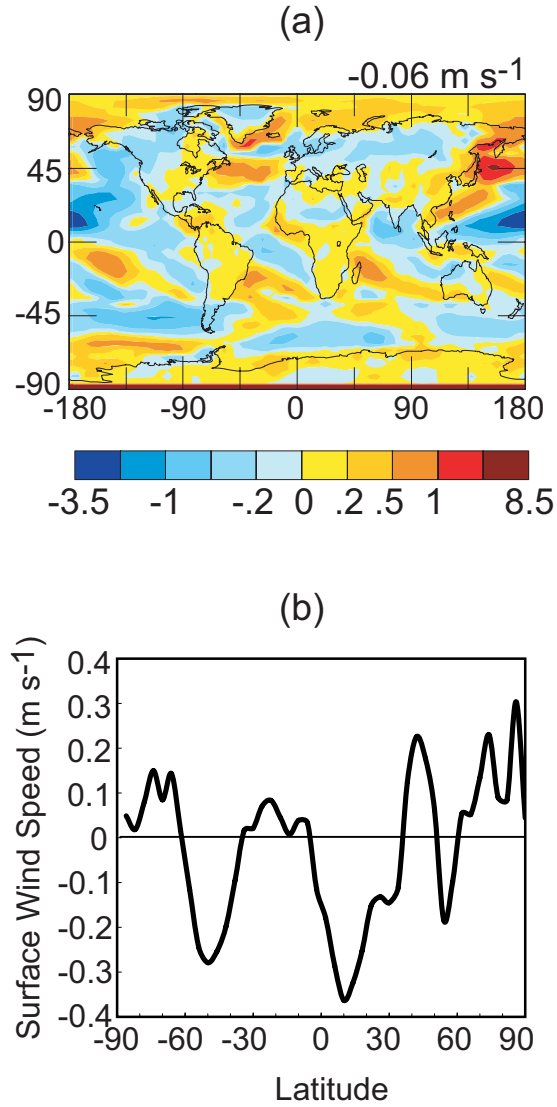


Figure 2-4. Predicted changes ( $\text{m s}^{-1}$ ) in (a) annual mean surface wind speed and (b) zonal annual mean surface wind speed from 2000 to 2100. The global mean change is indicated for Figure 2-4a.

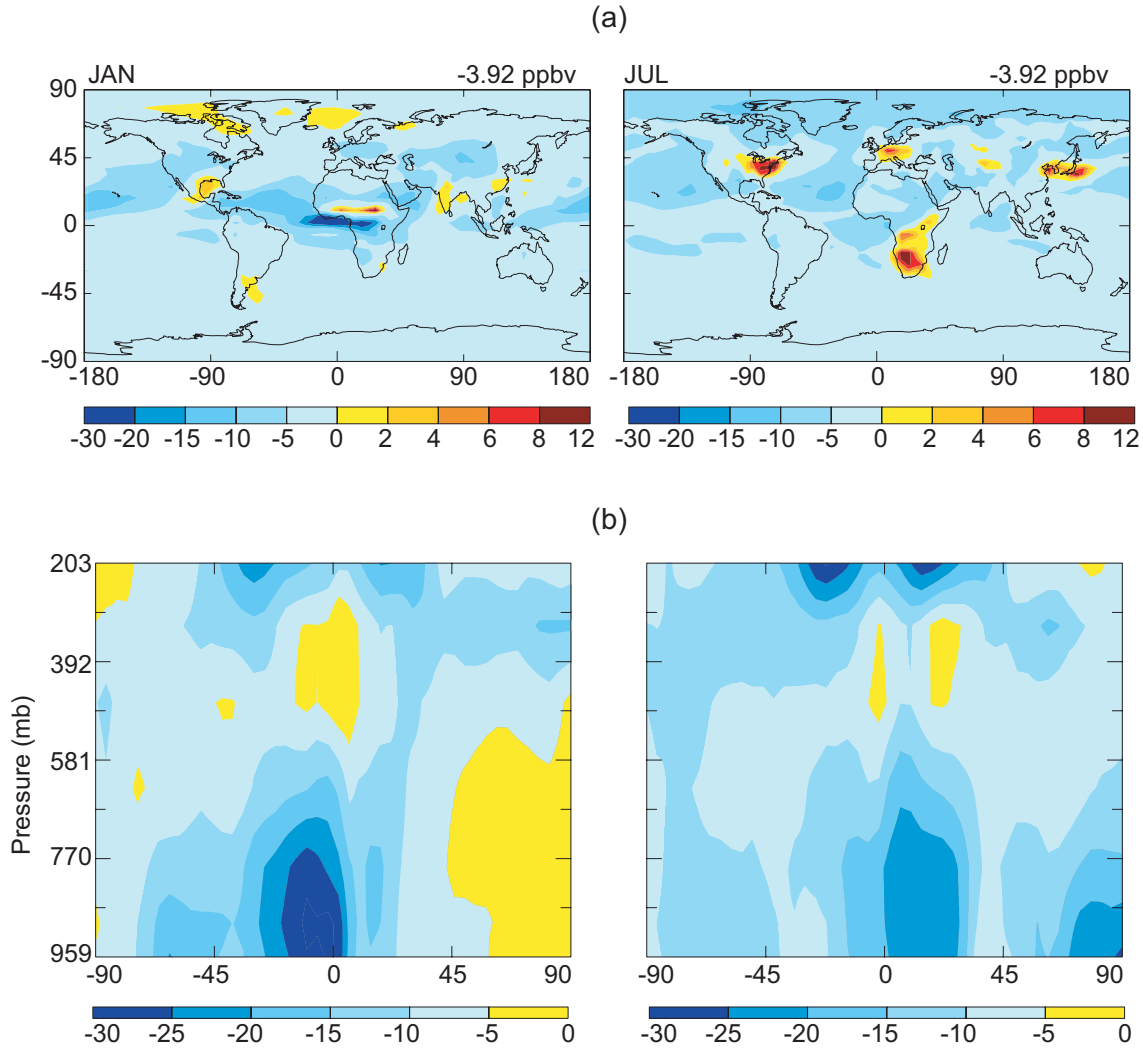


Figure 2-5. (a) Changes in January and July predicted surface-layer ozone concentrations (ppbv, CL2100EM2000 – CL2000EM2000) resulting from CO<sub>2</sub>-driven equilibrium climate change over 2000–2100. Global mean change is indicated at the top right corner of each panel. (b) Percentage changes  $((\text{CL2100EM2000} - \text{CL2000EM2000}) \times 100 / \text{CL2000EM2000})$  in January and July zonal mean ozone concentrations.

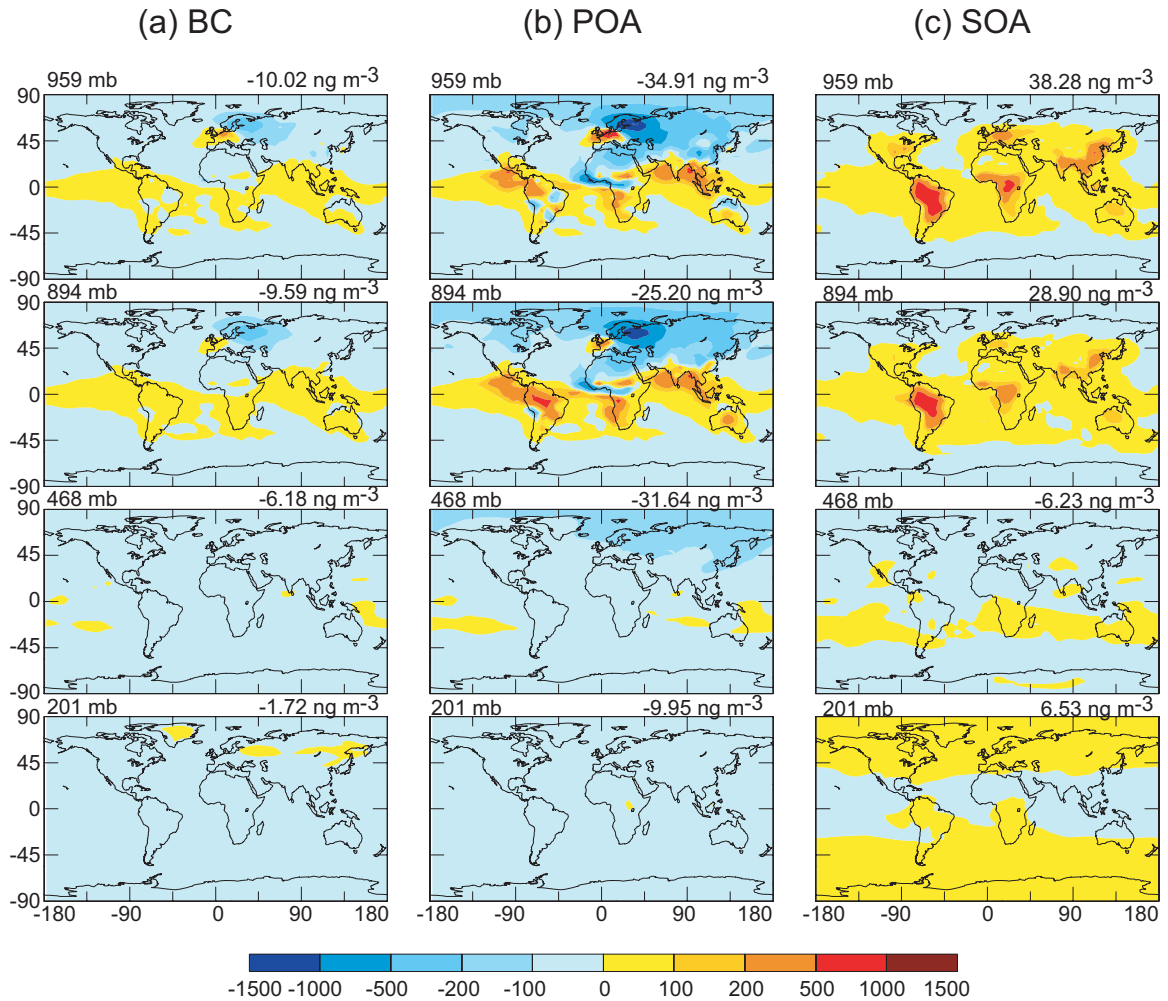


Figure 2-6. Changes in annual mean concentrations (ng m<sup>-3</sup>, CL2100EM2000 – CL2000EM2000) of (a) BC, (b) POA, and (c) SOA at selected layers resulted from the CO<sub>2</sub>-driven climate change over 2000–2100. Global mean change is indicated at the top right corner of each panel.

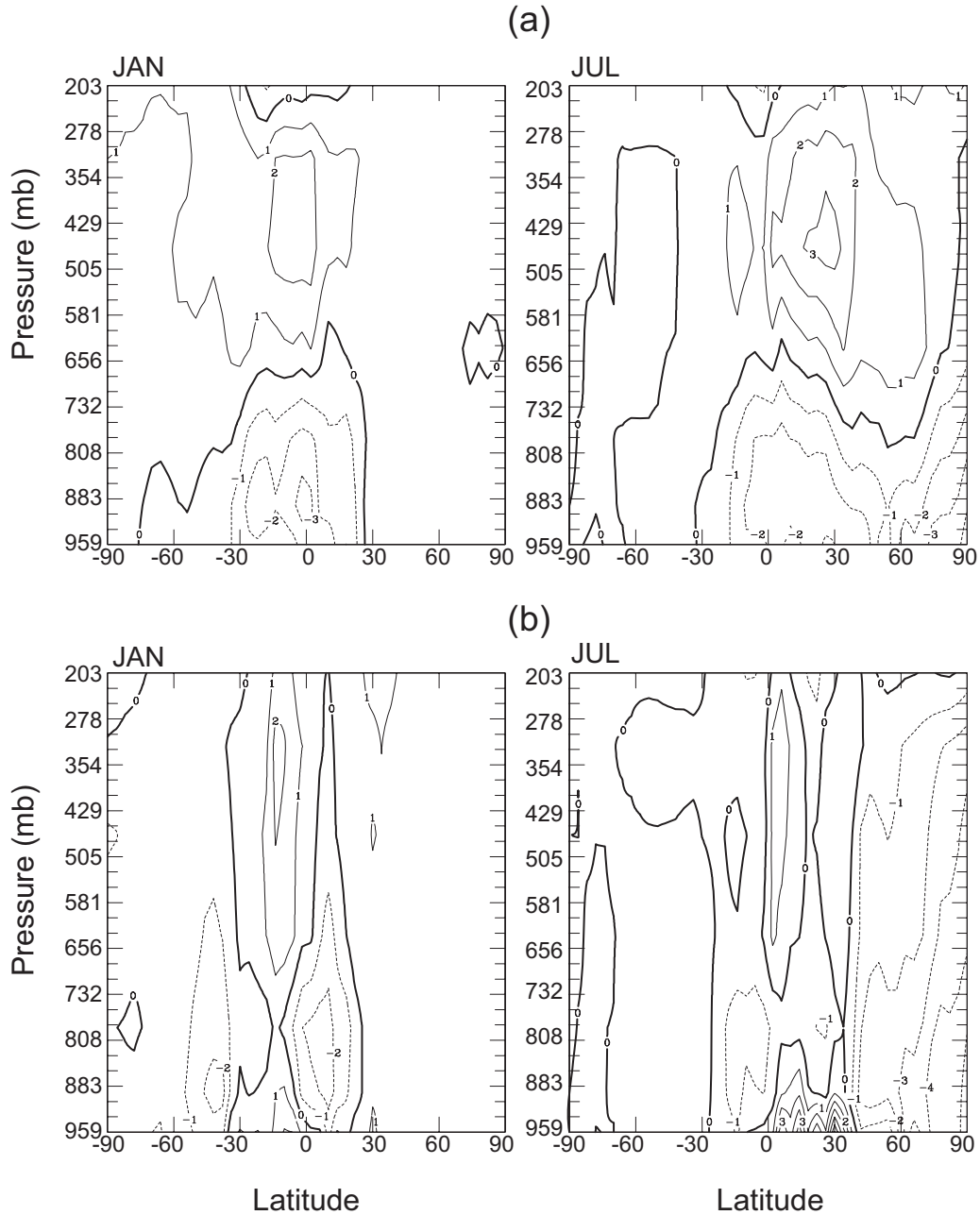


Figure 2-7. (a) Zonal mean changes in OH concentrations ( $10^5$  radicals  $\text{cm}^{-3}$ ) resulting from  $\text{CO}_2$ -driven climate change (CL2100EM2000 – CL2000EM2000). (b) Zonal mean changes in OH concentrations ( $10^5$  radicals  $\text{cm}^{-3}$ ) resulting from the changes in both climate and emissions (CL2100EM2100 – CL2000EM2000). Left panels are for January and right panels are for July.

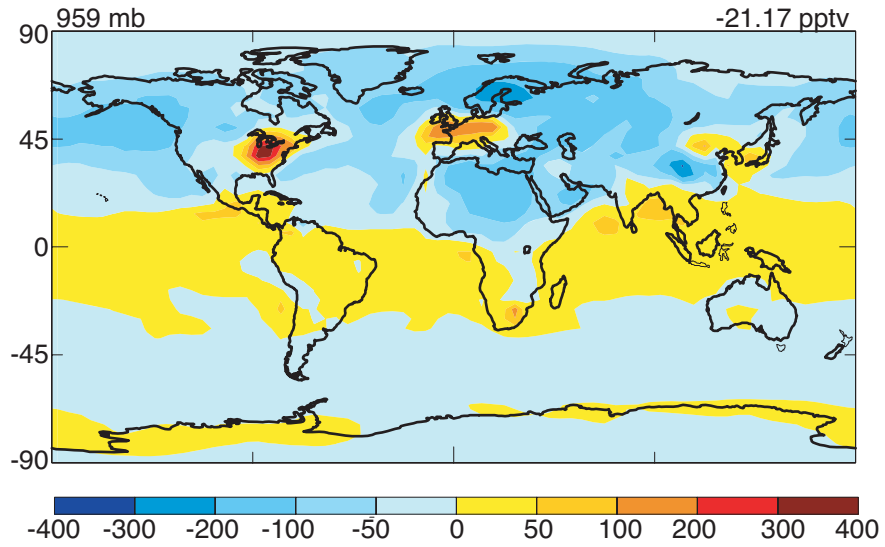


Figure 2-8. Predicted changes in annual mean sulfate concentration (pptr, CL2100EM2000 – CL2000EM2000) at the surface layer resulting from CO<sub>2</sub>-driven climate change from 2000 to 2100. Global mean change is indicated at the top right corner of the panel.

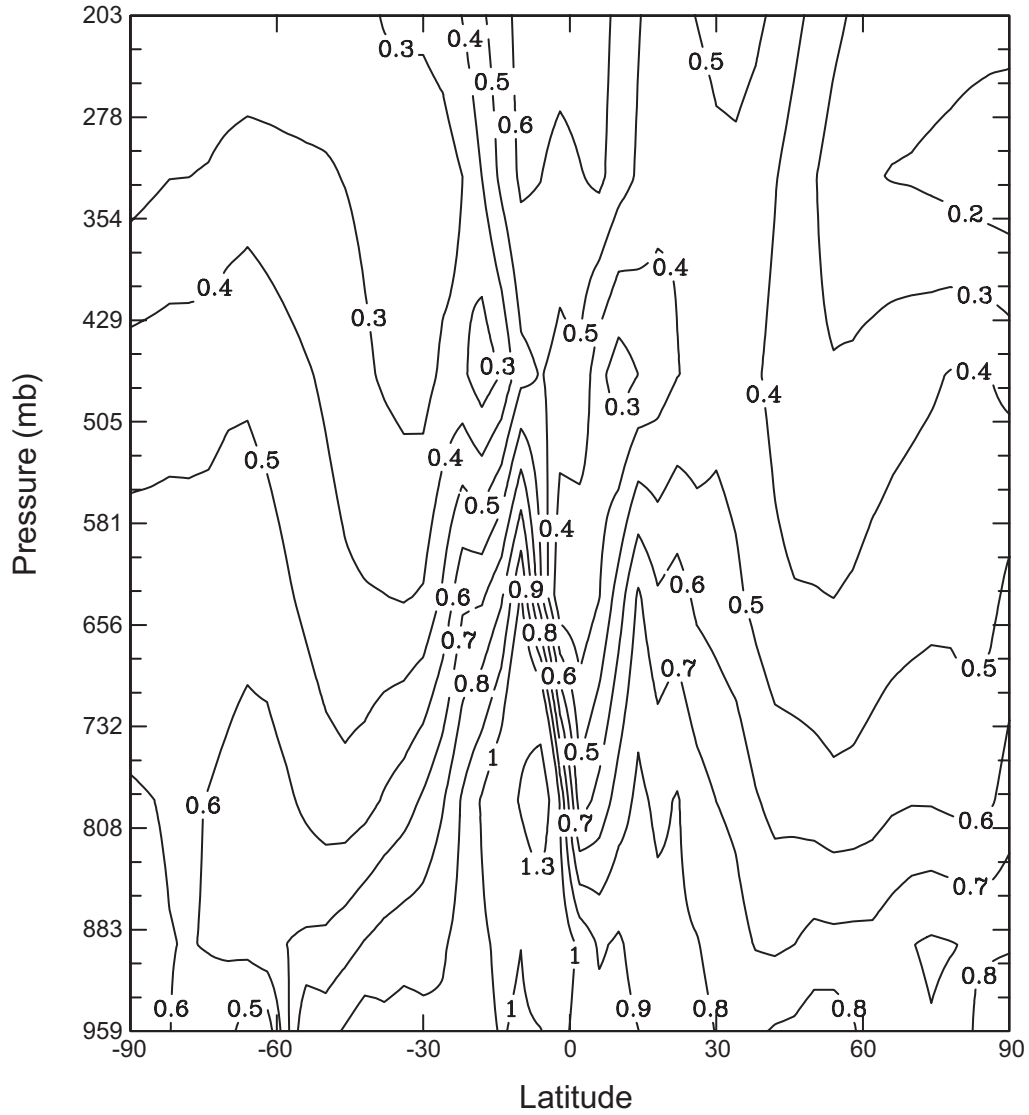


Figure 2-9. Ratios of the predicted annual and zonal mean nitrate concentrations from CL2100EM2000 to CL2000EM2000.

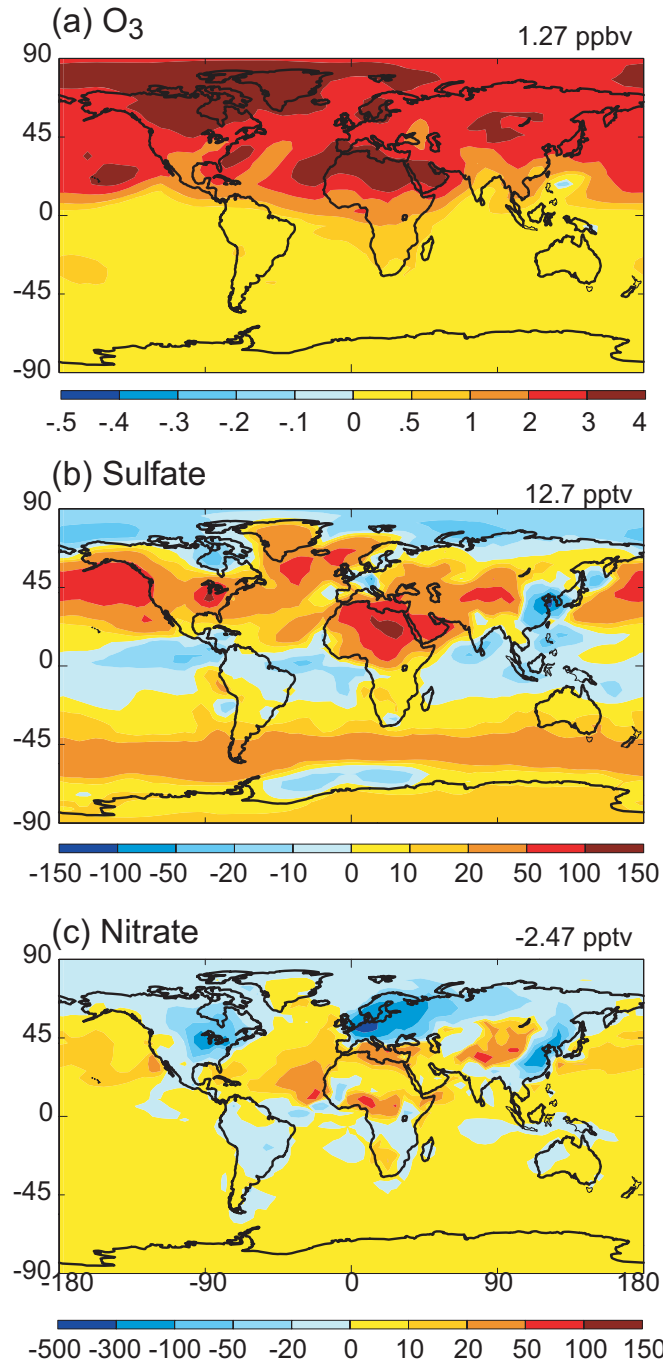


Figure 2-10. Annual mean differences between the effects of CO<sub>2</sub>-driven climate change in the presence and absence of heterogeneous reactions  $[(\text{CL2100EM2000h} - \text{CL2000EM2000h}) - (\text{CL2100EM2000} - \text{CL2000EM2000})]$  for the surface-layer concentrations of (a) O<sub>3</sub>, (b) sulfate, and (c) nitrate. The global mean value is indicated at the top right corner of each panel.

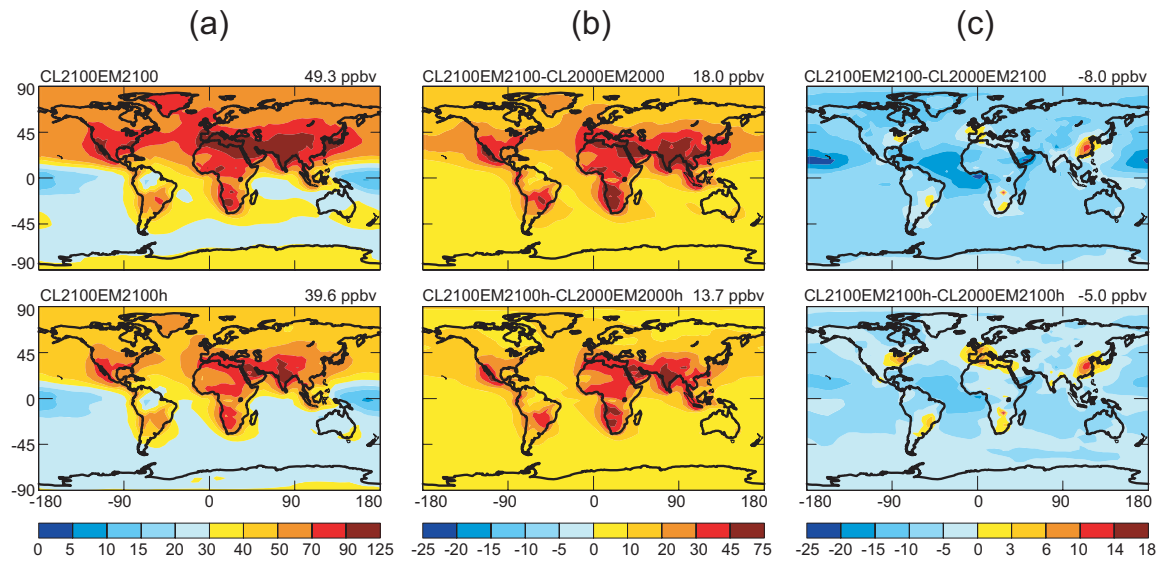


Figure 2-11. (a) Predicted year 2100 surface-layer O<sub>3</sub> mixing ratios (ppbv) with changes in both climate and emissions. (b) Predicted changes in surface-layer O<sub>3</sub> mixing ratio (ppbv) from 2000 to 2100. (c) Differences (ppbv) between surface-layer O<sub>3</sub> mixing ratios simulated with changes in both climate and emissions and those with changes in emissions only. Top panels are simulated in the absence of the heterogeneous reactions as discussed in the text, while the bottom panels include heterogeneous reactions. The global mean value is indicated at the top right corner of each panel.

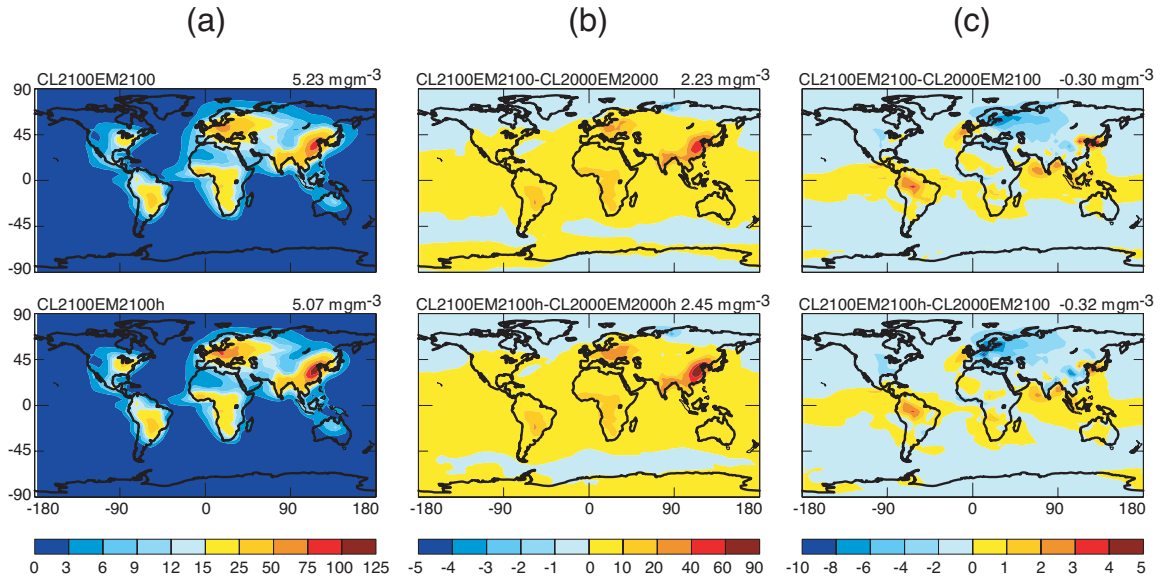


Figure 2-12. (a) Predicted year 2100 surface-layer dry aerosol mass concentrations ( $\mu\text{g m}^{-3}$ ) with changes in both climate and emissions. Dry aerosol mass is the sum of sulfate, nitrate, ammonium, BC, POA, and SOA. (b) Predicted changes in surface-layer dry aerosol mass concentrations ( $\mu\text{g m}^{-3}$ ) from 2000 to 2100. (c) Differences ( $\mu\text{g m}^{-3}$ ) between surface-layer dry aerosol mass concentrations simulated with changes in both climate and emissions and those with changes in emissions only. Top panels are simulated in the absence of the heterogeneous reactions as discussed in the text, while the bottom panels include heterogeneous reactions. The global mean value is indicated at the top right corner of each panel.

# Chapter 3

---

## **Future Climate Impacts of Direct Radiative Forcing of Anthropogenic Aerosols, Tropospheric Ozone, and Long- lived Greenhouse Gases**

Published in *Journal of Geophysical Research* (2007) by Wei-Ting Chen, Hong Liao, and John Seinfeld, 112, D14209, doi:10.1029/2006JD008051.

Copyright © 2007 American Geophysical Union. Reprinted with permission from American Geophysical Union.

## Abstract

Long-lived greenhouse gases (GHG) are the most important driver of climate change over the next century. Aerosols and tropospheric ozone are expected to induce significant perturbations to the GHG-forced climate. To distinguish the equilibrium climate responses to changes in direct radiative forcing of anthropogenic aerosols, tropospheric ozone, and GHG between present day and year 2100, four 80-year equilibrium climates are simulated using a unified tropospheric chemistry-aerosol model within the Goddard Institute for Space Studies General Circulation Model II'. Concentrations of sulfate, nitrate, primary organic carbon, secondary organic carbon, black carbon aerosols, and tropospheric ozone for present day and year 2100 are obtained *a priori* by coupled chemistry-aerosol GCM simulations, with emissions of aerosols, ozone and precursors based on the Intergovernmental Panel on Climate Change Special Report on Emissions Scenario A2. Changing anthropogenic aerosols, tropospheric ozone, and GHG from present day to year 2100 is predicted to perturb the global annual mean radiative forcing by +0.18 (considering aerosol direct effects only), +0.65, and +6.54 W m<sup>-2</sup> at the tropopause, and to induce an equilibrium global annual mean surface temperature change of +0.14, +0.32, and +5.31 K, respectively, with the largest temperature response occurring at northern high latitudes. Anthropogenic aerosols, through their direct effect, are predicted to alter the Hadley circulation owing to an increasing inter-hemispheric temperature gradient, leading to changes in tropical precipitation. When changes in both aerosols and tropospheric ozone are considered, the predicted patterns of change in global circulation and the hydrological cycle are similar to those induced by aerosols alone. GHG-induced climate changes, such as amplified warming over high latitudes, weakened

Hadley circulation, and increasing precipitation over the Tropics and high latitudes, are consistent with predictions of a number of previous GCM studies. Finally, direct radiative forcing of anthropogenic aerosols is predicted to induce strong regional cooling over East and South Asia. Wintertime rainfall over southeastern China and the Indian subcontinent is predicted to decrease because of the increased atmospheric stability and decreased surface evaporation, while the geographic distribution of precipitation is also predicted to be altered as a result of aerosol-induced changes in wind flow.

### 3.1 Introduction

Growth in well-mixed, long-lived greenhouse gas (GHG, including CO<sub>2</sub>, CH<sub>4</sub>, N<sub>2</sub>O, and halocarbons) levels in the atmosphere is the dominant contributor to future climate change [*Intergovernmental Panel on Climate Change (IPCC)*, 2001]. Against GHG-dominated climate change, radiative forcing from changing aerosols and tropospheric ozone has the potential to modify GHG-induced climate effects, especially regionally. Moreover, ozone and aerosols interact tightly through tropospheric chemical processes, which themselves will be affected by future climate change [*Liao and Seinfeld*, 2005; *Liao et al.*, 2006]. An important issue, and that to which the present work is directed, concerns the extent to which aerosols and tropospheric ozone will modify future climate change from that predicted to occur solely on the basis of greenhouse gases.

Scattering and absorption of solar radiation by aerosols cool the surface by reducing incident solar radiation on it. Absorbing aerosols, such as black carbon and mineral dust, can heat the atmosphere. Ozone traps outgoing longwave radiation, thereby warming the atmosphere and surface. These effects alter the energy balance of the earth-atmosphere system beyond that arising from GHG alone and induce responses in atmospheric circulations, clouds, and precipitation; for aerosols, see, for example, *Hansen et al.* [1997], *Boer et al.* [2000], *Chung et al.* [2002], *Menon et al.* [2002], *Jacobson* [2004], *Wang* [2004], *Chung and Seinfeld* [2005], *Ramanathan et al.* [2005], *Stier et al.* [2006], *Takemura et al.* [2005], *Roeckner et al.* [2006], and *Wang* [2007], and for ozone: *Ramaswamy and Bowen* [1994], *Hansen et al.* [1997], *Stuber et al.* [2001], *Mickley et al.* [2004], and *Shindell et al.* [2006].

The goal of the present study is to investigate future climatic impacts from direct aerosol radiative forcing and tropospheric ozone as compared to those predicted to occur from greenhouse gases alone. In this study we consider only direct radiative effects; indirect radiative effects of aerosols, namely effects of changes in anthropogenic aerosols on cloud processes, are not considered. In that regard the current study does not present an entire picture of aerosol effects on climate relative to those of greenhouse gases. Nonetheless, it is important to understand the direct aerosol radiative effects on climate, so that these may be contrasted in future work with those arising from effects resulting from perturbations in cloud processes. We use the unified Goddard Institute for Space Studies (GISS) general circulation model (GCM) II' with fully coupled simulations of tropospheric chemistry and aerosols [*Liao et al.*, 2003; 2004; *Liao and Seinfeld*, 2005] to calculate concentrations of aerosols and tropospheric ozone for present-day and year 2100, based on the IPCC Special Report on Emissions Scenario (SRES) [*Nakićenović et al.*, 2000] A2 anthropogenic emissions of aerosols/aerosol precursors and ozone precursors. Prediction of both present-day and year 2100 levels of aerosols and ozone is carried out under present-day climate conditions. We then apply the GCM to study climate responses to the changes in ozone and aerosols from present-day to 2100, using saved monthly mean fields of ozone and aerosols. We should note that *Liao et al* [2006] have used the same version of the model and shown that CO<sub>2</sub>-driven climate change can influence the predictions of year 2100 concentrations of ozone and aerosols. The full coupled impacts of chemistry-aerosol-climate interactions on future climate will be reported subsequently.

A description of model and experimental design is given in section 3.2. We examine global climate impacts resulting from aerosols, ozone, and greenhouse gases in section 3.3. Predicted regional climate changes in southeastern Asia and India are addressed in section 3.4.

## **3.2 Model Description and Experimental Design**

### **3.2.1 The Unified Model**

The unified tropospheric chemistry-aerosol model within the GISS GCM II' [*Liao et al.*, 2003; 2004; *Liao and Seinfeld*, 2005] is used in this work. The GISS GCM II' is described by *Rind and Lerner* [1996] and *Rind et al.* [1999] and is coupled with a "Q-flux" ocean [*Hansen et al.*, 1984]. The GISS model has been used extensively to probe the climate response to perturbations in greenhouse gas concentrations, solar luminosity, and tropospheric ozone and aerosol burdens [e.g. *Grenfell et al.*, 2001; *Rind et al.*, 2001; *Shindell et al.*, 2001; *Menon*, 2004; *Mickley et al.*, 2004; *Chung and Seinfeld*, 2005]. The version used has a horizontal resolution of 4° latitude by 5° longitude, with 9 vertical  $\sigma$  layers from surface to 10 hPa, centered at 959, 894, 786, 634, 468, 321, 201, 103, and 27 hPa. The dynamical time step is 1 hr. In the Q-flux ocean, monthly horizontal heat transport fluxes are held constant as in *Mickley et al.* [2004], while changes in the sea surface temperature and sea ice are calculated based on energy exchange with the atmosphere, ocean heat transport, and the ocean mixed layer heat capacity [*Hansen et al.*, 1984; *Russell et al.*, 1985].

Present-day and year 2100 concentrations of sulfate, nitrate, ammonium, primary organic carbon, secondary organic carbon, black carbon aerosols, and tropospheric ozone are obtained *a priori* by two separate simulations, each integrating the unified model for five years in present-day climate with present-day or year-2100 emissions of aerosols/aerosol precursors and ozone precursors, based on the IPCC SRES A2 emission scenarios (in which heterogeneous world, no emphasis on sustainability, and slow technology development is assumed, and the highest year-2100 CO<sub>2</sub> and SO<sub>2</sub> emissions of all SRES are predicted); these two simulations are similar to those denoted CL2000EM2000 and CL2000EM2100 in *Liao et al.* [2006] with the difference that heterogeneous reactions on mineral dust and sea salt are neglected here because we focus here on the effects of anthropogenic aerosol components. Hydrolysis of N<sub>2</sub>O<sub>5</sub> and irreversible absorption of NO<sub>3</sub>, NO<sub>2</sub>, and HO<sub>2</sub> on wetted surfaces of SO<sub>4</sub><sup>2-</sup>, NO<sub>3</sub><sup>-</sup>, NH<sub>4</sub><sup>+</sup>, and OC aerosols are accounted for. The differences between the calculated present-day and year 2100 aerosol/O<sub>3</sub> concentrations, as discussed later in section 3.2.3, result entirely from future emission changes, since present-day climate is used in both simulations.

### 3.2.2 Climate Simulations

To study the climate change resulting from direct radiative forcing of anthropogenic aerosols, tropospheric ozone, and GHG, four equilibrium climate experiments, as summarized in Table 3-1, were carried out to study the climatic effects of aerosol/O<sub>3</sub>/GHG changes from present-day to year 2100. The GCM is integrated in each case for 80 years, with the first 50 years used as spin-up to reach equilibrium, and the results over the last 30 years of each simulation analyzed and compared. The first

simulation, denoted PD, is the baseline, present-day climate with aerosol, O<sub>3</sub>, and GHG at year 2000 levels. The second simulation, 21A, uses year 2100 anthropogenic aerosols but present-day tropospheric O<sub>3</sub> and GHG concentrations. The difference between the equilibrium states (the last 30 years in the simulation) of PD and 21A, referred to as  $\Delta$ AER in subsequent discussion, represents the climatic influence of the change in anthropogenic aerosols from present-day to year 2100. In the third experiment, 21AO, both anthropogenic aerosols and tropospheric O<sub>3</sub> are set at year 2100 levels with GHG levels at present-day; the difference between simulations PD and 21AO, referred to as  $\Delta$ AERO<sub>3</sub>, assesses the combined climate effect of changes in both aerosols and tropospheric O<sub>3</sub>. Lastly, the simulation 21G, which uses present-day aerosol/O<sub>3</sub> but year 2100 GHG, is compared to PD to evaluate the climate effect of GHG changes only ( $\Delta$ GHG). In these equilibrium climate simulations, GHG mixing ratios are taken from the IPCC SRES A2 and grid-by-grid aerosol/O<sub>3</sub> concentrations in present-day (year 2000) or year 2100 levels (see section 3.2.3) are imported into the model on monthly basis (a 12-month cycle is repeated every simulated year).

We have chosen to simulate equilibrium climate because the focus of this study is on the relative impacts of anthropogenic aerosol direct effect, tropospheric O<sub>3</sub>, and GHG on climate, and an equilibrium climate is able to clearly delineate this. Note that the equilibrium climate generally results in more pronounced responses than the transient climate [e.g. *IPCC*, 1995; *Kiehl et al.*, 2006], in which emissions (and forcing) change year by year.

### 3.2.3 Present-day and Year 2100 Anthropogenic Aerosols, Tropospheric Ozone, and Greenhouse Gases

Table 3-2 lists present-day and year 2100 global mixing ratios of long-lived greenhouse gases and global burdens of tropospheric ozone and aerosols. Present-day and year 2100 GHG levels are derived based on the SRES A2 scenarios. Atmospheric CO<sub>2</sub> increases from 367 ppmv in present-day to 836 ppmv in year 2100 and remains the single most important contributor to GHG radiative forcing in year 2100.

Figure 3-1 shows annual and seasonal mean (DJF = December-January-February, JJA = June-July-August) latitude-longitude differences in column burdens between present-day and year 2100 for anthropogenic aerosols and O<sub>3</sub>. All anthropogenic aerosol species are predicted to increase between 2000-2100 except for sulfate. Global burdens of POA, nitrate, and BC are predicted to exhibit substantial growth. East Asia, India, Europe, and the eastern United States are the regions in which the largest increases in aerosol concentrations are predicted. In response to the rising anthropogenic emissions of O<sub>3</sub> precursors over 2000–2100, the global O<sub>3</sub> burden is predicted to increase by around 200 Tg with the increase higher in the NH, especially in the vicinity of India, the Near East, southern Africa, and the western United States.

Calculation of aerosol optical properties follows the work of *Liao et al.* [2004]. We assume that sulfate, nitrate, black carbon, organic carbon (primary organic carbon plus secondary organic carbon) and aerosol water associated with SO<sub>4</sub><sup>2-</sup>, NO<sub>3</sub><sup>-</sup>, and OC are internally mixed. Densities for dry sulfate, nitrate, OC, and BC are assumed to be 1.8, 1.7, 1.8, and 1.0 g cm<sup>-3</sup>, respectively, and the particle density of the internal mixture is

computed as the mass-averaged density of water and all dry aerosols. A volume-weighted mixing rule is applied to derive the composite, wavelength-dependent refractive indices. The spectral refractive index of dry nitrate is assumed the same as that of dry sulfate [Toon *et al.*, 1976], while the refractive indices for water, OC and BC are from *d'Almeida et al.* [1991] (OC as “water soluble”, and BC as “soot”). A standard gamma size distribution is assumed for the aerosol with a surface area-weighted dry radius = 0.3  $\mu\text{m}$  and variance = 0.2. Mie theory is then applied to determine the optical properties (extinction efficiency, single-scattering albedo, and asymmetry parameter) based on the refractive indices and size distribution.

Figures 3-2a and 3-2b show the global distributions of the annual mean instantaneous direct radiative forcing at the tropopause (here defined at the bottom of GCM layer 8) and the surface, respectively, owing to changes in anthropogenic aerosols, tropospheric  $\text{O}_3$ , and GHG between present-day and 2100. The instantaneous direct radiative forcing is calculated as the difference in net (solar plus thermal) irradiance at each model layer corresponding to a change in aerosol,  $\text{O}_3$ , or GHG concentration. Aerosols, depending on their optical properties and the albedo of the underlying surface, produce either a positive or a negative forcing at the tropopause, but always result in a negative surface forcing by virtue of reduction of the incident solar radiation at the surface. The overall change of anthropogenic aerosols between present-day and year 2100 is predicted to lead to a global annual mean direct forcing of  $+0.18 \text{ W m}^{-2}$  at the tropopause and  $-3.02 \text{ W m}^{-2}$  at the surface. Since internal mixing of all anthropogenic aerosol components is assumed, the strong heating at mid- to high latitudes in the Northern Hemisphere as a result of increasing BC over highly reflective surfaces of snow, sea ice, and desert leads to an

overall positive forcing at the tropopause. However, negative aerosol forcing is predicted over eastern China, India, and western Europe because of the predicted large increase in scattering ( $\text{NO}_3^-$ , POA, and  $\text{SO}_4^{2-}$  in India and southern China) aerosols, although BC also increases in these regions. The predicted global annual mean forcing attributed to changes in tropospheric ozone from present day to year 2100 is  $+0.65 \text{ W m}^{-2}$  at the tropopause and  $+0.02 \text{ W m}^{-2}$  at the surface, with the maximum forcing changes concentrated in the areas of largest increases of tropospheric ozone. Increasing GHG levels from present-day to year 2100 according to scenario A2 results in a forcing at the tropopause of  $+6.54 \text{ W m}^{-2}$  and at surface of  $+1.37 \text{ W m}^{-2}$ .

Figure 3-3 shows the vertical distribution of the zonal mean atmospheric forcing, calculated by differencing the instantaneous forcing between top and bottom of each layer, imposed by changes in anthropogenic aerosols, tropospheric ozone, and GHG between present day and year 2100. The enhanced SW absorption by internally-mixed, BC-containing aerosols is predicted to lead to positive atmospheric forcing immediately above the surface. The positive atmospheric forcing is most pronounced in NH where the aerosol concentration increase is largest. In DJF, the positive forcing peaks between  $0-45^\circ\text{N}$ , associated with the large increase in wintertime fossil fuel emissions in NH midlatitudes and higher biomass burning emissions over the Sahel region. In JJA, the large aerosol-induced forcing ( $1-2 \text{ W m}^{-2}$ ) at  $30-60^\circ\text{N}$  in the low to mid-troposphere can be explained by stronger solar insolation, while the increasing biomass burning over the Amazon and southern Africa is responsible for the increase in the lower atmosphere between  $0-30^\circ\text{S}$ . A maximum atmospheric forcing of  $2-3 \text{ W m}^{-2}$  is predicted in mid- to high troposphere (around 350 hPa, approximately at altitude of 8-9 km) in the northern

high latitudes, which can be explained by the stronger convection in NH in JJA than in DJF; strongly absorbing BC and slightly absorbing OC are transported to high latitudes while being transported to mid- to high troposphere, leading to the maximum forcing over the high-albedo surface of snow and low level cloud deck. When compared to the AeroCom model simulations [Schulz *et al.*, 2006], stronger polar transport of black carbon is predicted in this study than other AeroCom models besides GISS model E, indicating less efficient washout processes, or more efficient vertical transport in GISS GCM [Schulz *et al.*, 2006]. Therefore, the predicted positive atmospheric aerosol forcing (and hence the predicted tropospheric warming in section 3.3) in northern polar region in this study should be considered as a higher-end estimate, owing to the higher loads of internally-mixed black carbon predicted in northern high latitudes.

The change of tropospheric O<sub>3</sub> is predicted to increase atmospheric forcing through the entire troposphere by +0.1 to +0.3 W m<sup>-2</sup> (Figure 3-3), especially in the altitude range of 150 to 300 hPa in the summer hemisphere because of the predicted increase in O<sub>3</sub> concentrations and the high incoming SW radiation. In addition, the increase of tropospheric O<sub>3</sub> blocks more outgoing LW flux and decreases atmospheric forcing in the stratosphere, especially over the Tropics. The GHG-induced positive atmospheric forcing change maximizes between the 900–600 hPa (2–3 W m<sup>-2</sup>) because GHG has to compete for LW absorption with water vapor, of which the concentration is highest in the lowest layer and decreases with altitude in the troposphere. Above 600 hPa, the GHG LW absorption saturates and the atmospheric forcing shows relatively small change. A negative GHG atmospheric forcing between 200 and 400 hPa is predicted because the upward LW flux entering the upper troposphere (UT)/lower stratosphere (LS) from

below is reduced due to the stronger GHG LW absorption in the lower troposphere, and also because more LW radiation in the UT/LS is lost to space owing to increased GHG LW emission. The distribution of GHG-induced atmospheric forcing shows less latitudinal and seasonal variations when compared to those induced by changes of aerosol and O<sub>3</sub>.

### 3.3 Estimated Changes in Global Climate

Table 3-3 summarizes globally- and hemispherically-averaged annual mean differences of selected variables in  $\Delta\text{AER}$ ,  $\Delta\text{AERO}_3$ , and  $\Delta\text{GHG}$ , with changes insignificant at a 95% confidence level parenthesized. The 95% intervals are calculated based on the two-sample “usual” t-test [Zwiers and von Storch, 1995; Chung and Seinfeld, 2005] (see footnote in Table 3-3).

#### 3.3.1 Surface Air Temperature

As shown in Table 3-3, the change in anthropogenic aerosols ( $\Delta\text{AER}$ ), aerosols plus tropospheric ozone ( $\Delta\text{AERO}_3$ ), and GHG ( $\Delta\text{GHG}$ ) from present day to year 2100 is predicted to increase the global annual mean surface air temperature by 0.14 K, 0.46 K, and 5.31 K, respectively. The difference between  $\Delta\text{AER}$  and  $\Delta\text{AERO}_3$  shows that change in tropospheric ozone alone is predicted to lead to a warming by 0.32 K. With the TOA instantaneous forcing perturbations given in section 3.2.3 and the above equilibrium global annual mean surface temperature responses, the predicted climate sensitivity, defined as the ratio of equilibrium global annual mean surface air temperature change to the global annual mean radiative forcing, is 0.78, 0.49, and 0.81 K m<sup>2</sup> W<sup>-1</sup> for aerosols,

ozone, and GHG, respectively. Note that for radiative forcing of tropospheric aerosols, the instantaneous forcing at TOA is more often adopted in the literature, while for GHG, the adjusted forcing, i.e. the radiative forcing at tropopause after the stratospheric temperature adjusts to radiative equilibrium, is normally used [e.g. *IPCC*, 2001]. Here we use the instantaneous forcing at the tropopause to calculate the climate sensitivity. For GHG the adjusted forcing is typically 10–20% lower than the instantaneous forcing, while for aerosols the two are approximately equal [*Hansen et al.*, 1997].

Maps of surface air temperature change in DJF and JJA are shown in Figure 3-4. The slight global warming of 0.14 K predicted for the aerosol-induced climate change ( $\Delta AER$ ) is actually a result of regional cooling (in areas predicted to have a substantial increase in scattering aerosols) offset by regional warming (due to internally-mixed, BC containing particles over highly reflective surfaces). In DJF, strong aerosol-induced regional cooling is predicted to occur in eastern China, Indochina, India, the Sahel, western Europe, and eastern United States; regional warming is predicted over mid-latitude deserts and northern high latitudes. In JJA, because of the larger decrease in  $SO_4^{2-}$  and smaller increase in  $NO_3^-$  and POA, prevailing warming appears globally except in India, southwestern Africa, and South America where  $SO_4^{2-}$  is still increasing from present-day to year 2100. The predicted regional cooling in DJF due to anthropogenic aerosol direct effect over East and South Asia is addressed in more detail in section 3.4. Figure 3-5 displays the predicted zonal mean surface air temperature change. Aerosol-induced warming is concentrated in the NH and is maximized in the high latitudes. The predicted annual mean surface air temperature change in the NH is 0.29 K, while in the SH the surface air temperature shows virtually no change. The

resulting interhemispheric temperature gradient can potentially affect the pattern of global circulation, as will be discussed in section 3.3.3.

When both changes in aerosols and ozone are considered ( $\Delta\text{AERO}_3$ ), the ozone adds to the aerosol-induced climate change a prevailing surface warming. Altogether, the global annual mean surface air temperature is predicted to increase by 0.46 K, with local maxima located in the urban areas of Europe, Central Asia, the Middle East, and North America, and downwind of the biomass burning regions in South Africa and South America. Over eastern China and India, the  $\text{O}_3$ -induced warming does not override the strong aerosol surface cooling, and a regional temperature decrease is still predicted under the scenario of  $\Delta\text{AERO}_3$ . The geographic distribution of the predicted  $\text{O}_3$ -induced surface temperature change is consistent with the results in *Mickley et al.* [2004], which studied the climate response to changes in tropospheric ozone from preindustrial times to present day using the same GCM as in the present study.

As a result of GHG increase from present day to 2100 ( $\Delta\text{GHG}$ ), substantial warming is predicted in the northern high latitudes owing to ice-albedo feedback, as well as in the desert areas of China, central Asia, Middle East, and Northern Africa (Figure 3-4). The temperature responses are always greater in the NH than the SH (Figure 3-5), due to heat uptake by the Southern Ocean. The predicted hemispheric mean surface temperature difference is about 1.81 K.

### 3.3.2 Tropospheric Temperature and Stability

Figure 3-6 displays the zonally averaged vertical distribution of annual mean temperature change. Change in aerosols from present day to 2100 is predicted to lead to

maximum warming in the mid-troposphere north of 30°N ( $\Delta AER$ ), corresponding to the location of maximum atmospheric forcing increase (Figure 3-3). The pattern of maximum warming in the tropical mid-troposphere owing to GHG change ( $\Delta GHG$ ) is similar to that of other GHG-driven GCM equilibrium [e.g. *Manabe and Wetherald, 1975; Hansen et al., 1997*] and transient [e.g. *IPCC, 2001*] simulations. This pattern can be explained by enhanced thermal radiative heating due to increased water vapor, as well as by the vertical temperature convective adjustment toward the moist adiabatic lapse rate [*Manabe and Wetherald, 1975*]. The enhanced mid-tropospheric heating induced by GHG leads to a more stable atmosphere in low to midlatitudes, while in high latitudes the stability decreases owing to large surface warming. The change in stability can affect the Tropical Hadley circulation, as will be discussed in section 3.3.3. The result of  $\Delta AERO_3$  shows that tropospheric ozone is predicted to lead to additional tropospheric warming and stratospheric cooling beyond that of  $\Delta AER$  with the pattern similar to that induced by GHG change but of a considerably smaller magnitude.

### 3.3.3 Global Circulation

Figures 3-7a and 3-7b displays the zonal mean of the mass stream function in the baseline simulation PD and its change resulting from change in aerosols ( $\Delta AER$ ) and GHG ( $\Delta GHG$ ). The aerosol-induced change in the stream function has comparable magnitude to that induced by GHG, likely owing to the larger ratio of change in interhemispheric surface temperature gradient to change in global annual mean temperature in the aerosol perturbation (0.29 K/0.14 K, and for  $\Delta GHG$ , 1.81 K/5.31 K). The change in aerosols is predicted to impose an anomalous counter-clockwise flow

located between 5°N–5°S ( $\Delta AER$ ), which is out-of-phase to the DJF Hadley circulation and indicates the weakening of the Hadley cell, while during JJA, this predicted aerosol-induced anomalous flow becomes in-phase and thus strengthens the Hadley circulation. This pattern of stream function change is related to the enhanced interhemispheric temperature difference in the aerosol perturbation. In the GHG perturbation ( $\Delta GHG$ ), the Hadley cell is weakened as a result of the pronounced increase of static stability over the Tropics [Knutson and Manabe, 1995; Mitas and Clement, 2006], especially in DJF; only the ascending branch in the convection zone north of the equator is strengthened and penetrates higher in response to temperature and moisture increase. A similar change in Hadley circulation induced by transient GHG warming is predicted by most of the IPCC Fourth Assessment Report (AR4) GCMs, although not in the reanalyses data. We refer the reader to Mitas and Clement [2006] for detailed analyses and discussion.

The changes in zonal wind component are shown in Figures 3-7c and 3-7d. The change of zonal wind due to change in aerosols ( $\Delta AER$ ) is relatively small (within  $2 \text{ m s}^{-1}$ ). The core of the jet stream is predicted to be slightly strengthened in the NH in DJF and in the SH in JJA. This can be induced by a stronger latitudinal temperature gradient in the lower troposphere between the Tropics and the midlatitudes, a result of surface cooling around 25–45°N in DJF, and cooling in the Southern Ocean in JJA. In the GHG-induced change ( $\Delta GHG$ ), the increasing easterlies in the mid-troposphere in low- and midlatitudes are a result of decreasing latitudinal gradient of surface temperature.

Note that the change in global circulation is influenced heavily by the predicted change in the thermodynamic structure of the atmosphere and the convective cumulus

parameterization; we note that these predictions can be quite model-dependent. Since there is only one vertical stratospheric layer in the 9-layer GISS GCM II', we do not analyze the changes in stratospheric winds. The changes of stream function and zonal wind induced by aerosol plus ozone ( $\Delta\text{AERO}_3$ ) are similar to those induced by aerosols only, and therefore are not shown here.

### 3.3.4 Hydrological Cycle

Changes in temperature and global circulation have important effects on the global hydrological cycle, including the distribution of water vapor, evaporation, precipitation, strength and frequency of moist convection, and cloud coverage. On the other hand, the increase of water vapor creates a positive feedback on warming.

Figure 3-8 shows the latitude-pressure distribution of the annual mean difference in specific humidity. The absolute increase of water vapor (Figure 3-8a) always maximizes in the tropical lower troposphere; perturbations from changing aerosols from present day to 2100 ( $\Delta\text{AER}$ ) is predicted to be around 0.2–0.8 g-H<sub>2</sub>O kg-air<sup>-1</sup>, and from changing GHG ( $\Delta\text{GHG}$ ), around 3–4 g-H<sub>2</sub>O kg-air<sup>-1</sup>. On the other hand, the pattern of the relative change in specific humidity (Figure 3-8b) is controlled largely by the pattern of temperature change through the Clausius-Clapeyron relationship. A relative increase in water vapor in the case of  $\Delta\text{AER}$  concentrates in high latitudes in the NH (around 10–30%) because of the predicted warming, whereas in SH, the relative change is insignificant (<5%). The pattern predicted with GHG perturbation ( $\Delta\text{GHG}$ ) shows a doubling to tripling of water vapor in the Tropical upper-troposphere (because of the strong water vapor feedback) and low to mid-troposphere in the northern high latitudes

(owing to amplified warming in the Arctic region); the minimum of the relative increase in humidity (around 15%) appears in the Tropics near surface (location of maximum absolute increase) because humidity here is already much higher and the predicted warming is as significant as near the Tropical tropopause.

As given in Table 3-3, globally the aerosol perturbation  $\Delta AER$  produces a slight decrease in total precipitation ( $0.03 \text{ mm day}^{-1}$ ), most of which is related to lower convective precipitation. The change in global mean precipitation is controlled by the change in global evaporation rate, which also decreases by around  $0.03 \text{ mm day}^{-1}$  due to surface cooling. The decrease in the global annual mean of moist convective (MC) cloud cover (0.19%) is balanced by the increase in large-scale supersaturation (SS) cloud cover (0.15%), and therefore the total cloud cover remains essentially unchanged. Note that the above changes are due only to aerosol direct forcing; aerosol indirect effects are not considered. The results in  $\Delta AERO_3$  show that the inclusion of ozone change is predicted to lead to, in addition to the aerosol-induced change, a slight increase in total precipitation and SS cloud, but a small decrease in MC cloud. The climate effect of increasing GHG on the hydrological cycle is similar, but with much more pronounced magnitude, to that of tropospheric ozone, as revealed by  $\Delta GHG$ . The GHG perturbation leads to a predicted increase in annual mean total precipitation as a result of increasing evaporation ( $0.34 \text{ mm day}^{-1}$ ). The SS cloud cover increases (0.66%) owing to increasing humidity, whereas MC cloud cover decreases (0.15%) because of the enhanced tropospheric static stability over the Tropics, especially over the southern equatorial convection zone, which we will return to later.

The zonal mean change in excess precipitation (total precipitation minus evaporation) and MC precipitation is shown in Figure 3-9, while the zonal mean change in MC and high cloud cover are shown in Figure 3-10. The predicted  $\Delta$ AER excess precipitation change is confined mainly to the tropics. The ascending/descending branch of the anomalous flow in  $\Delta$ AER (Figures 3-7a and 3-7b) results in an increase/decrease in MC precipitation ( $\sim 0.2 \text{ mm day}^{-1}$ ), MC cloud fraction ( $\sim 0.01$ ), and high cloud fraction ( $\sim 0.01\text{--}0.02$ ) in the northern/southern equatorial region. The small dip of MC cloud around  $30^\circ\text{N}$  (0.4%) may be related to the increase in atmospheric stability associated with surface cooling. In  $\Delta$ GHG, precipitation significantly exceeds evaporation between  $0\text{--}10^\circ\text{N}$  by as much as  $1 \text{ mm day}^{-1}$ , mostly related to the large predicted increase in MC precipitation as a result of stronger penetrating convection and additional moisture convergence, as indicated by the large increase in high cloud (6%) over the same region. In the remainder of the Hadley cell, the circulation is weakened (Figures 3-7 a and 3-7b) and therefore the MC cloud cover is predicted to decrease in response to weaker updraft velocity, especially in the southern equatorial zone; however, the MC precipitation shows very little change between  $0\text{--}15^\circ\text{S}$ . Outside the Tropics, the increased moisture is transported by the mid-latitude eddies away from the Subtropics to mid- and high latitudes. The predicted moisture divergence associated with eddy activities explains the precipitation deficit (excess evaporation) of  $0.3\text{--}0.5 \text{ mm day}^{-1}$  over  $30^\circ\text{N/S}$  and the precipitation residue of  $0.5 \text{ mm day}^{-1}$  around  $60^\circ\text{N/S}$ . The predicted response of the hydrological cycle to increased GHG is generally in agreement in previous modeling studies for the equilibrium response [e.g. *Dai et al.*, 2001; *Liepert et al.*, 2004] (a coupled dynamic ocean is used in *Dai et al.*, [2001]) and for the transient response [e.g. *IPCC*,

2001; *Watterson and Dix, 2003; Held and Soden, 2006*]. Note that change in aerosols ( $\Delta AER$ ) does not produce the secondary peak of excess precipitation increase in high latitudes because of the relative small change in specific humidity. The pattern of precipitation and cloud cover change predicted for  $\Delta AERO_3$  is primarily the same as that for  $\Delta AER$ , only of slightly larger magnitude, and is therefore not shown.

### 3.3.5 Energy Budgets

Figure 3-11a displays the latitudinal distribution of the net shortwave (SW) radiative fluxes at TOA. The change of TOA SW flux is affected mainly by changes in cloud cover (Figure 3-10) as well as by changes in surface albedo. The decrease of surface albedo in NH owing to the melting of sea ice and snow leads to a large increase in downward SW flux at TOA in all three perturbations. Change in SW flux at TOA is small elsewhere in the aerosol- and aerosol-plus- $O_3$ -induced climate change, while in the GHG perturbation, the increased cloud cover in the Tropics results in increased outgoing TOA SW flux. The change of the net longwave (LW) radiative flux at TOA is shown in Figure 3-11b. Changes due only to aerosols ( $\Delta AER$ ) and aerosol plus  $O_3$  ( $\Delta AERO_3$ ) are small at all latitudes. In the GHG-induced change  $\Delta GHG$ , the strongly increased water vapor and high cloud over the Tropics blocks more outgoing LW radiation below TOA, while the amplified surface warming is responsible for the increased outgoing LW flux at high latitudes.

Figure 3-12 shows the zonal annual mean change of absorbed SW flux, net (downward minus upward) LW flux, sensible heat (SH) flux, and latent heat (LH) flux at the surface. Scattering and absorption of solar radiation by aerosols is predicted to

decrease the absorbed SW flux at the surface in most latitudes ( $\Delta AER$ ), especially between  $0^{\circ}$ – $60^{\circ}N$  ( $\sim 7 \text{ W m}^{-2}$ ) where the highest aerosol burden is located. This reduction of surface SW radiation is compensated primarily by the increase of atmosphere-to-surface SH flux and also the small decrease in surface-leaving LH flux due to evaporation suppression. The GHG-induced latitudinal distribution of the absorbed SW flux change at the surface is similar to that of the SW flux change at TOA; the increased cloud cover (Figure 3-10) reduces the incident solar radiation at the surface in the Tropics and the Southern Ocean by about  $10 \text{ W m}^{-2}$ , while in the NH subpolar and polar regions, the surface receives more SW radiation because of the decreased surface albedo. On the other hand, the GHG perturbation is predicted to increase downward LW flux at all latitudes (not shown) because of higher atmospheric temperature and enhanced water vapor greenhouse effect and higher downward SH flux due to higher atmospheric temperature. The changes in surface SW, LW and SH is balanced by the increased upward LH flux, especially over the mid- and high latitudes, where evaporation is enhanced due to surface warming and additional exposure of water surface owing to melting of sea ice.

### **3.4 Estimated Regional Climate Changes in Asia in Winter**

#### **Ozone and Aerosols**

The inhomogeneous geographical distribution of direct radiative forcing of anthropogenic aerosols (Figure 3-2) leads to potential impacts on regional climate, one example of which is the significant regional cooling in East and South Asia, especially in DJF (Figure 3-4a,  $\Delta AER$ ). In this section, the predicted regional climate change in East and South Asia in DJF is analyzed (see Figure 3-13 for locations of grid cells selected for

statistical calculation). Detailed analyses of regional-scale climate changes is limited by the coarse horizontal resolution of the GISS GCM II' and the Q-flux ocean in this study, particularly in regions influenced by complicated monsoon systems, such as Asia. Presented here are only the most significant and spatially extensive changes of regional temperature, precipitation, and synoptic winds directly attributable to aerosol surface cooling predicted in the equilibrium simulations with a mixed layer ocean model. Responses associated with changes in monsoon dynamics and SST are beyond the scope of the current study.

If only perturbed by the significant regional increases in aerosol burden from 2000 to 2100 ( $\Delta AER$ ), the East and South Asia continent is predicted to undergo substantial cooling by aerosol direct effect. Table 3-4 summarizes the DJF mean changes of key parameters ( $\Delta AER$ ,  $\Delta AERO_3$ , and  $\Delta GHG$ ) over these regions. In DJF when the aerosol burden increase is largest due to enhanced emissions from biofuel burning and decreased wet removal in the dry season, anthropogenic aerosols (see  $\Delta AER$ ), through only their direct effect, are predicted to reduce the regional mean SW flux absorbed at the surface in DJF by  $22.2 \text{ W m}^{-2}$  in East Asia and  $18.9 \text{ W m}^{-2}$  in South Asia. The reduction in surface SW flux, though balanced by increased atmosphere-to-surface SH and/or LW fluxes, still leads to a strong decrease in mean surface temperature (2.5 K in East Asia and 1.9 K in South Asia). In East Asia, the cooler surface results in less evaporation ( $0.3 \text{ mm day}^{-1}$ ) and higher tropospheric stability ( $0.3 \text{ K km}^{-1}$ ), which effectively slows down the local hydrological cycle and leads to a significant decrease in total precipitation by  $0.7 \text{ mm day}^{-1}$ . In South Asia, however, the predicted regional mean precipitation only decreases slightly by  $0.1 \text{ mm day}^{-1}$  because of the smaller change in evaporation rate ( $0.1 \text{ mm day}^{-1}$ ).

<sup>1</sup>). If the combined aerosol-ozone climate effect ( $\Delta\text{AERO}_3$ ) is considered, the mean surface temperature is predicted to decrease by 2.1 K and 1.1 K over East and South Asia, respectively. The regional mean changes in precipitation and surface energy fluxes are similar to those predicted for the aerosol-only perturbation ( $\Delta\text{AER}$ ).

The direct cooling resulting from changes in aerosol from 2000 to 2100 over East and South Asia affects precipitation as well as the synoptic-scale wind flow. The geographic distribution of predicted changes in DJF precipitation, sea level pressure, and surface wind field over East and South Asia are displayed in Figure 3-13. The aerosol-induced surface cooling is predicted to induce an anomalous high pressure (2-4 hPa) over the continental area of East and South Asia (Figure 3-14b), including southern China, Indochina, the Tibetan plateau, and the Indian Subcontinent. Precipitation over land in East Asia and the north and central Indian Subcontinent decreases in response to more cold, dry air outflow resulting from the anomalous high (Figure 3-14a). On the other hand, in the western Subtropical Pacific (115°–135°E, 20°–30°N) and in the North Indian Ocean (0°–8°N), precipitation increases in response to the enhanced convergence associated with the change in wind pattern. A substantial rainfall decrease over the South Indian Ocean and western Tropical Pacific is also predicted.

It is of interest to compare the regional climate changes in DJF owing to the direct effect of anthropogenic aerosols to those owing to GHG warming. The predicted change in East and South Asia predicted from GHG forcing alone ( $\Delta\text{GHG}$ ) in this study is generally in agreement with other simulations [*Bhaskaran and Mitchell, 1998; IPCC, 2001*]. GHG induce large regional mean surface temperature increases in DJF over East Asia (5.8 K) and South Asia (5.1 K), which leads to an increase in regional mean

evaporation of 0.4 and 0.2 mm day<sup>-1</sup>, respectively. The additional moisture from increasing evaporation causes precipitation increase of 0.4 mm day<sup>-1</sup> in East Asia, whereas the DJF mean precipitation change in India in GHG perturbation is small and statistically insignificant. Figure 3-14a also shows a strong precipitation increase is predicted from subtropical to the midlatitude western Pacific, likely associated with the equatorward shift of the storm track due to the decrease of the latitudinal temperature gradient between mid- and high latitudes.

### 3.5 Summary and Conclusions

The direct climatic effect of projected changes in anthropogenic aerosols (sulfates, nitrates, OC and BC), tropospheric ozone, and long-lived greenhouse gases between present day and year 2100 is investigated by means of four equilibrium climate simulations. Concentrations of anthropogenic aerosols and tropospheric ozone for years 2000 and 2100 are derived by the online GCM simulation of coupled tropospheric chemistry and aerosols. Emissions of aerosol/aerosol precursors, ozone precursors, as well as the mixing ratios of GHG are based on the IPCC SRES A2 scenario. Aerosol indirect effects are not considered; therefore, the current study does not present an entire picture of aerosol effects on climate. The resulting global annual mean direct radiative forcing for aerosol, ozone, and GHG from year 2000 to 2100 are predicted to be +0.18, +0.65, and +6.54 W m<sup>-2</sup> at the tropopause, and -3.02, +0.02, and +1.37 W m<sup>-2</sup> at the surface, respectively.

The predicted climate effect of changing anthropogenic aerosol direct forcing from present day to year 2100,  $\Delta$ AER, shows a small increase in global annual mean surface

temperature of 0.14 K with substantial regional cooling of around 1–2 K in East Asia, South Asia, West Europe, and the Sahel, especially in the months DJF. The perturbation in anthropogenic aerosols is also predicted to change the inter-hemispheric temperature gradient, which leads to a year-round anomalous vertical circulation over the Tropics and slight changes in the global zonal wind field. The predicted change in the global hydrological cycle in  $\Delta AER$ , following the change in circulation and water vapor concentration, is only pronounced in the Tropical region: the enhancement/reduction in water vapor concentration and convective precipitation/cloud in the northern/southern equatorial regional. Change in both aerosol and tropospheric ozone from present day to 2100 is predicted to lead to a global mean temperature increase of 0.48 K. Corresponding changes in latitudinal temperature gradient, global circulation, water vapor, and precipitation are similar to that predicted in the aerosol-only perturbation but of a greater magnitude. The predicted GHG climate effect in the present study generally agrees with previous GCM simulations compiled in *IPCC* [2001], with an increase in global annual mean surface temperature by 5.31 K, an amplified warming in the NH polar region, maximized heating in the tropical upper troposphere, weakening of the Hadley circulation, and precipitation increase in the Tropics and mid- to high latitudes. The latitudinal distribution of changes in tropospheric temperature, circulation, water vapor, and precipitation induced by changing GHG, however, is very different from that induced by anthropogenic aerosol direct forcing; a summary is provided in Table 3-5.

Analysis of regional climate change predicted over the East and South Asia in DJF reveals that aerosol direct effect alone ( $\Delta AER$ ) can lower the surface SW flux by as much as  $22 \text{ W m}^{-2}$ . The induced surface cooling predicted with the aerosol-only perturbation

( $\Delta AER$ ) can potentially alter the synoptic-scale wind flow and precipitation patterns: East and South Asia is predicted to experience aerosol-induced rainfall suppression in DJF owing to the predicted high pressure anomaly residing over southern China, the Tibetan Plateau, and India, together with an increase in atmospheric stability and decrease in evaporation. On the other hand, regional warming due to the change of GHG ( $\Delta GHG$ ) is predicted to significantly enhance evaporation over South and East China, and to increase precipitation over East China and subtropical western Pacific.

**Acknowledgment.** This work was supported by the National Aeronautics and Space Administration Earth Observing System Interdisciplinary Science Program (NASA EOS-IDS). Hong Liao was partially supported by the 100-Talent Project of Chinese Academy of Sciences. The authors thank Tapio Schneider for helpful comments.

## References

- Bhaskaran, B., and J. F. B. Mitchell (1998), Simulated changes in southeast Asian monsoon precipitation resulting from anthropogenic emissions, *Int. J. of Climatol.*, *18*(13), 1455–1462.
- Boer, G. J., G. Flato, M. C. Reader, and D. Ramsden (2000), A transient climate change simulation with greenhouse gas and aerosol forcing: Experimental design and comparison with the instrumental record for the twentieth century, *Clim. Dyn.*, *16*(6), 405–425.
- Chung, S. H., and J. H. Seinfeld (2005), Climate response of direct radiative forcing of anthropogenic black carbon, *J. Geophys. Res.*, *110*(D11), doi:10.1029/2004JD005441
- Chung, C. E., V. Ramanathan, and J. T. Kiehl (2002), Effects of the south Asian absorbing haze on the northeast monsoon and surface-air heat exchange, *J. Clim.*, *15*(17), 2462–2476.
- Dai, A. G., T. M. L. Wigley, B. A. Boville, J. T. Kiehl, and L. E. Buja (2001), Climates of the twentieth and twenty-first centuries simulated by the NCAR climate system model, *J. Clim.*, *14*(4), 485–519.
- d’Almeida, G. A., P. Koepke, and E. P. Shettle (1991), *Atmospheric Aerosol: Global Climatology and Radiative Characteristics*, edited by A. Deepak Pub., Hampton, Va.
- Grenfell, J. L., D. T. Shindell, D. Koch, and D. Rind (2001), Chemistry-climate interactions in the Goddard Institute for Space Studies general circulation model 2. New insights into modeling the preindustrial atmosphere, *J. Geophys. Res.*, *106*(D24), 33435–33451.
- Hansen, J., A. Lacis, G. Russel, P. Stone, I. Fung, R. Ruedy, and J. Lerner (1984), Climate sensitivity: Analysis of feedback mechanisms, in *Climate Processes and Climate Sensitivity*, Geophys. Monogr. Ser., edited by J. Hansen and T. Takahashi, pp. 130–163, AGU, Washington D. C.
- Hansen, J., M. Sato, and R. Ruedy (1997), Radiative forcing and climate response, *J. Geophys. Res.*, *102*(D6), 6831–6864.
- Held, I. M., and B. J. Soden (2006), Robust responses of the hydrological cycle to global warming, *J. Clim.*, *19*(21), 5686 – 5699.
- Intergovernmental Panel on Climate Change (IPCC) (1995), *Climate Change 1995*, edited by J. T. Houghton et al., Cambridge Univ. Press., New York.
- Intergovernmental Panel on Climate Change (IPCC) (2001), *Climate Change 2001*, edited by J. T. Houghton et al., Cambridge Univ. Press., New York.

- Jacobson, M. Z. (2004), Climate response of fossil fuel and biofuel soot, accounting for soot's feedback to snow and sea ice albedo and emissivity, *J. Geophys. Res.*, *109*(D21201), doi:10.1029/2004JD004945.
- Kiehl, J. T., C. A. Shields, J. J. Hack, and W. D. Collins (2006), The climate sensitivity of the Community Climate System Model: CCM3, *J. Clim.*, *19*(11), 2584–2596.
- Knutson, T. R., and S. Manabe (1995), Time-mean response over the tropical Pacific to increased CO<sub>2</sub> in a coupled ocean-atmosphere model, *J. Clim.*, *8*(9), 2189–2199.
- Liao, H., and J. H. Seinfeld (2005), Global impacts of gas-phase chemistry-aerosol interactions on direct radiative forcing by anthropogenic aerosols and ozone, *J. Geophys. Res.*, *110*(D18208), doi:10.1029/2005JD005907.
- Liao, H., P. J. Adams, S. H. Chung, J. H. Seinfeld, L. J. Mickley, and D. J. Jacob (2003), Interactions between tropospheric chemistry and aerosols in a unified general circulation model, *J. Geophys. Res.*, *108*(D1), 4001, doi:10.1029/2001JD001260.
- Liao, H., J. H. Seinfeld, P. J. Adams, and L. J. Mickley (2004), Global radiative forcing of coupled tropospheric ozone and aerosols in a unified general circulation model, *J. Geophys. Res.*, *109*(D16207), doi:10.1029/2003JD004456.
- Liao, H., W.-T. Chen, and J. H. Seinfeld (2006), Role of climate change in global predictions of future tropospheric ozone and aerosols, *J. Geophys. Res.*, *111*(D12304), doi:10.1029/2005JD006852.
- Liepert, B. G., J. Feichter, U. Lohmann, and E. Roeckner (2004), Can aerosols spin down the water cycle in a warmer and moister world?, *Geophys. Res. Lett.*, *31*(L06207), doi:10.1029/2003GL019060.
- Manabe, S., and R. T. Wetherald (1975), Effects of doubling CO<sub>2</sub> concentration on climate of a general circulation model, *J. Atmos. Sci.*, *32*(1), 3–15.
- Menon, S. (2004), Current uncertainties in assessing aerosol effects on climate, *Annu. Rev. Environ. Res.*, *29*(1), 1–30.
- Menon, S., J. Hansen, L. Nazarenko, and Y. F. Luo (2002), Climate effects of black carbon aerosols in China and India, *Science*, *297*(5590), 2250–2253.
- Mickley, L. J., D. J. Jacob, B. D. Field, and D. Rind (2004), Climate response to the increase in tropospheric ozone since preindustrial times: A comparison between ozone and equivalent CO<sub>2</sub> forcings, *J. Geophys. Res.*, *109*(D5106), doi:10.1029/2003JD003653.
- Mitas, C. M., and A. Clement (2006), Recent behavior of the hadley cell and tropical thermodynamics in climate models and reanalyses, *Geophys. Res. Lett.*, *33*(L01810), doi:10.1029/2005GL024406.

- Nakićenović, N., et al. (2000), *Emissions Scenarios. A Special Report of Working Group III of the Intergovernmental Panel on Climate Change*, 599 pp., Cambridge University Press, Cambridge, United Kingdom and New York, NY, USA.
- Ramanathan, V., C. Chung, D. Kim, T. Bettge, L. Buja, J. T. Kiehl, W. M. Washington, Q. Fu, D. R. Sikka, and M. Wild (2005), Atmospheric brown clouds: Impacts on South Asian climate and hydrological cycle, *Proc. Natl. Acad. Sci.*, *102*(15), 5326–5333.
- Ramaswamy, V., and M. M. Bowen (1994), Effect of changes in radiatively active species upon the lower stratospheric temperatures, *J. Geophys. Res.*, *99*(D9), 18909–18921.
- Rind, D., and J. Lerner (1996), Use of on-line tracers as a diagnostic tool in general circulation model development .1. Horizontal and vertical transport in the troposphere, *J. Geophys. Res.*, *101*(D7), 12667–12683.
- Rind, D., J. Lerner, K. Shah, and R. Suozzo (1999), Use of on-line tracers as a diagnostic tool in general circulation model development, 2, Transport between the troposphere and stratosphere, *J. Geophys. Res.*, *104*(D8), 9151–9167.
- Rind, D., J. Lerner, and C. McLinden (2001), Changes of tracer distributions in the doubled CO<sub>2</sub> climate, *J. Geophys. Res.*, *106*(D22), 28061–28079.
- Roeckner, E., P. Stier, J. Feichter, S. Kloster, M. Esch, and I. Fischer-Bruns (2006), Impact of carbonaceous aerosol emissions on regional climate change, *Clim. Dyn.*, *27*(6), 553–571, doi:10.1007/s00382-006-0147-3.
- Russell, G. L., J. R. Miller, and L. C. Tsang (1985), Seasonal oceanic heat transports computed from an atmospheric model, *Dyn. Atmos. Oceans*, *9*(3), 253–271.
- Schulz, M., C. Textor, S. Kinne, Y. Balkanski, S. Bauer, T. Berntsen, T. Berglen, O. Boucher, F. Dentener, S. Guibert, I. S. A. Isaksen, T. Iversen, D. Koch, A. Kirkevåg, X. Liu, V. Montanaro, G. Myhre, J. E. Penner, G. Pitari, S. Reddy, O. Seland, P. Stier, and T. Takemura (2006), Radiative forcing by aerosols as derived from the AeroCom present-day and pre-industrial simulations, *Atmos. Chem. and Phys.*, *6*, 5225–5246.
- Shindell, D. T., J. L. Grenfell, D. Rind, V. Grewe, and C. Price (2001), Chemistry-climate interactions in the Goddard Institute for Space Studies general circulation model: 1. Tropospheric chemistry model description and evaluation, *J. Geophys. Res.*, *106*(D8), 8047–8075.
- Shindell, D., G. Faluvegi, A. Lacis, J. Hansen, and R. Ruedy (2006), Role of tropospheric ozone increases in 20th-century climate change, *J. Geophys. Res.*, *111*(D08302), doi: 10.1029/2005JD006348.

- Stier, P., J. Feichter, E. Roeckner, S. Kloster, and M. Esch (2006), The evolution of the global aerosol system in a transient climate simulation from 1860 to 2100, *Atmos. Chem. Phys.*, *6*, 3059–3076.
- Stuber, N., M. Ponater, and R. Sausen (2001), Is the climate sensitivity to ozone perturbations enhanced by stratospheric water vapor feedback?, *Geophys. Res. Lett.*, *28*(15), 2887–2890.
- Takemura, T., T. Nozawa, S. Emori, T. Y. Nakajima, and T. Nakajima (2005), Simulation of climate response to aerosol direct and indirect effects with aerosol transport-radiation model, *J. Geophys. Res.*, *110*(D02202), doi:10.1029/2004JD005029.
- Toon, O. B., J. B. Pollack, and B. N. Khare (1976), Optical-constants of several atmospheric aerosol species – ammonium-sulfate, aluminum-oxide, and sodium-chloride, *J. Geophys. Res.*, *81*(33), 5733–5748.
- Wang, C. (2004), A modeling study on the climate impacts of black carbon aerosols, *J. Geophys. Res.*, *109*(D03106), doi:10.1029/2003JD004084.
- Wang, C. (2007), Impact of direct radiative forcing of black carbon aerosols on tropical convective precipitation, *Geophys. Res. Lett.*, *34*(L05709), doi:10.1029/2006GL028416.
- Watterson, I. G., and M. R. Dix (2003), Simulated changes due to global warming in daily precipitation means and extremes and their interpretation using the gamma distribution, *J. Geophys. Res.*, *108*(D13), 4379, doi:10.1029/2002JD002928.
- Zwiers, F. W., and H. von Storch (1995), Taking serial-correlation into account in tests of the mean, *J. Clim.*, *8*(2), 336-351.

Table 3-1. Summary of Climate Experiments

Experiments	Anth. Aerosol Concentration	Trop. O <sub>3</sub> Concentration	GHG Levels	Perturbation
PD	year 2000	year 2000	year 2000	present-day climate
21A	year 2100	year 2000	year 2000	21A-PD = $\Delta$ AER
21AO	year 2100	year 2100	year 2000	21AO-PD = $\Delta$ AERO <sub>3</sub>
21G	year 2000	year 2000	year 2100	21G-PD = $\Delta$ GHG

Table 3-2. Present-Day (year 2000) and Year 2100 Annual Mean Global Burdens of Anthropogenic Aerosols, Tropospheric Ozone, and Greenhouse Gas Mixing Ratios Used in This Study<sup>a</sup>

	Year 2000	Year 2100
Ammonium Sulfate	2.83 Tg	2.70 Tg
Ammonium Nitrate	0.66 Tg	2.82 Tg
POA	1.25 Tg	2.90 Tg
SOA	0.28 Tg	0.39 Tg
BC	0.23 Tg	0.53 Tg
Trop. O <sub>3</sub>	327 Tg	520 Tg
CO <sub>2</sub>	367 ppmv	836 ppmv
CH <sub>4</sub>	1760 ppbv	3731 ppbv
N <sub>2</sub> O	316 ppbv	447 ppbv
CFC-11	267 pptv	45 pptv
CFC-12	535 pptv	222 pptv

<sup>a</sup>Emissions are based on SRES A2 scenario; see *Liao et al.* [2006] for details of anthropogenic aerosol and tropospheric O<sub>3</sub> concentrations.

Table 3-3. Global and Hemispherical Annual Mean Differences of Selected Climate Parameters<sup>a</sup>.

	$\Delta$ AER			$\Delta$ AERO <sub>3</sub>			$\Delta$ GHG		
	Global	NH	SH	Global	NH	SH	Global	NH	SH
Surface Temperature, K	0.14	0.29	(0.00)	0.46	0.71	0.22	5.31	6.21	4.40
TSS., <sup>b</sup> K km <sup>-1</sup>	0.06	0.07	0.05	0.07	0.07	0.08	0.10	0.02	0.19
Evaporation, mm day <sup>-1</sup>	-0.03	-0.05	-0.02	-0.01	-0.03	(0.00)	0.34	0.35	0.33
SS precipitation, mm day <sup>-1</sup>	(0.00)	-0.01	(0.00)	0.01	(0.00)	0.01	0.13	0.13	0.12
MC precip., mm day <sup>-1</sup>	-0.03	(0.01)	-0.06	-0.02	0.03	-0.07	0.21	0.34	0.09
SS cloud fraction, %	0.15	0.38	(-0.09)	0.21	0.48	(-0.07)	0.66	1.19	0.11
MC cloud fraction, %	-0.19	-0.11	-0.27	-0.24	-0.12	-0.36	-0.15	0.24	-0.54
Atmospheric water, mm	0.41	0.74	0.08	0.89	1.31	0.47	8.06	8.90	7.21
TOA net SW flux, W m <sup>-2</sup>	0.45	0.88	(-0.02)	0.70	1.09	-0.31	0.84	1.59	(0.10)
TOA net LW flux, W m <sup>-2</sup>	-0.52	-0.43	-0.61	-0.75	-0.66	-0.84	-1.19	-1.27	-1.10
Ground albedo, %	-0.03	-0.08	0.03	-0.16	-0.33	(0.01)	-1.80	-3.33	-0.28
Surface net SW flux, W m <sup>-2</sup>	-3.04	-4.76	-1.32	-3.27	-5.04	-1.49	-1.69	-1.01	-2.37
Surface net LW flux, W m <sup>-2</sup>	0.90	1.49	0.33	1.48	2.08	0.88	7.55	7.75	7.36
Surface SH flux, W m <sup>-2</sup>	1.14	1.93	0.35	1.36	2.11	0.61	3.67	3.36	4.02
Surface LH flux, W m <sup>-2</sup>	0.95	1.34	0.55	0.41	0.85	(-0.05)	-9.79	29.21	38.71

Table 3-3. (Continued)

<sup>a</sup> Differences insignificant relative to the 95% confidence intervals are parenthesized. The usual t-test takes into account the temporal correlation in each set of sample data (i.e., in our cases here, the global/hemispherical annual average of the climate variable of interest in the last 30 year in each simulation), and therefore the sample size  $n$  and  $m$  is reduced to the equivalent sample size  $n_e$  and  $m_e$  (see Eq. 6 in *Zwiers and von Storch* [1995]). The difference in mean is significant if it exceeds the 95% confidence interval, which equals to  $1.98 \times s \times (1/n_e + 1/m_e)^{0.5}$  if  $n_e + m_e \geq 30$ , where  $s$  is the pooled standard deviation, or is determined by a lookup table if  $n_e + m_e < 30$ . For more detailed explanation of the “usual” t-test and the lookup tables, please refer to *Zwiers and von Storch* [1995].

<sup>b</sup> Tropospheric static stability, defined as the slope of the vertical change of potential temperature throughout the troposphere.

Table 3-4. Regional Mean Differences of Selected Climate Parameters in DJF over East and South Asia<sup>a</sup>

	(1) East Asia			(2) South Asia		
	$\Delta$ AER	$\Delta$ AERO <sub>3</sub>	$\Delta$ GHG	$\Delta$ AER	$\Delta$ AERO <sub>3</sub>	$\Delta$ GHG
Surface Temperature, K	-2.51	-2.14	5.82	-1.85	-1.11	5.09
TSS., K km <sup>-1</sup>	0.26	0.28	0.26	0.16	0.18	0.47
Evaporation, mm day <sup>-1</sup>	-0.29	-0.26	0.37	0.12	0.14	0.23
SS Precipitation, mm day <sup>-1</sup>	-0.37	-0.26	0.08	-0.08	(-0.07)	(-0.05)
MC precipitation, mm day <sup>-1</sup>	-0.12	-0.07	(0.27)	-0.06	-0.04	(0.03)
Ground albedo, %	1.90	1.87	-2.59	0.27	0.26	-0.12
Surface net SW flux, W m <sup>-2</sup>	-22.16	-23.26	(-1.29)	-18.87	-19.58	-2.83
Surface net LW flux, W m <sup>-2</sup>	(0.18)	(0.86)	4.73	(2.33)	4.03	(1.19)
Surface SH flux, W m <sup>-2</sup>	0.87	10.26	4.02	12.65	12.22	3.95
Surface LH flux, W m <sup>-2</sup>	4.73	4.46	-6.97	(-0.23)	(-0.70)	-1.94

<sup>a</sup> Figure 3-13 shows the regions over which the statistics of the usual t-test are computed. Differences insignificant relative to the 95% confidence intervals are parenthesized.

Table 3-5. Summary and Comparison of Patterns of Equilibrium Climate Response to Changes of Aerosol Direct Forcing and GHG Forcing from Present Day to Year 2100 Predicted in This Study

	$\Delta$ AER	$\Delta$ GHG
Surface Temperature	Cooling in high aerosol burden regions; warming in northern high latitudes; small change in SH	Warming globally with polar amplification (NH > SH)
Inter-hemispheric temperature gradient	Significant compared to the slight global mean temperature increase	Not as significant compared to the large global mean warming
Tropospheric temperature and relative water vapor change	Maximum increase in NH high latitude mid-troposphere	Maximum increase in Tropical upper troposphere and northern high latitude lower troposphere
Hadley circulation	Strengthened in DJF and weakened in JJA	Weakened (especially in DJF) except in the ascending branch in the convection zone
Excess Precipitation and MC cloud	Changes confined to the Tropics (increase in north, decrease south of the Equator)	Increase peaks in both the Tropics and mid- to high latitudes.
Surface energy balance	Reduction of SW flux in NH balanced by increase of downward SH flux and small decrease of upward LH flux	Increase of downward LW flux, downward SH flux, and SW flux in high latitudes balanced by increase of upward LH flux

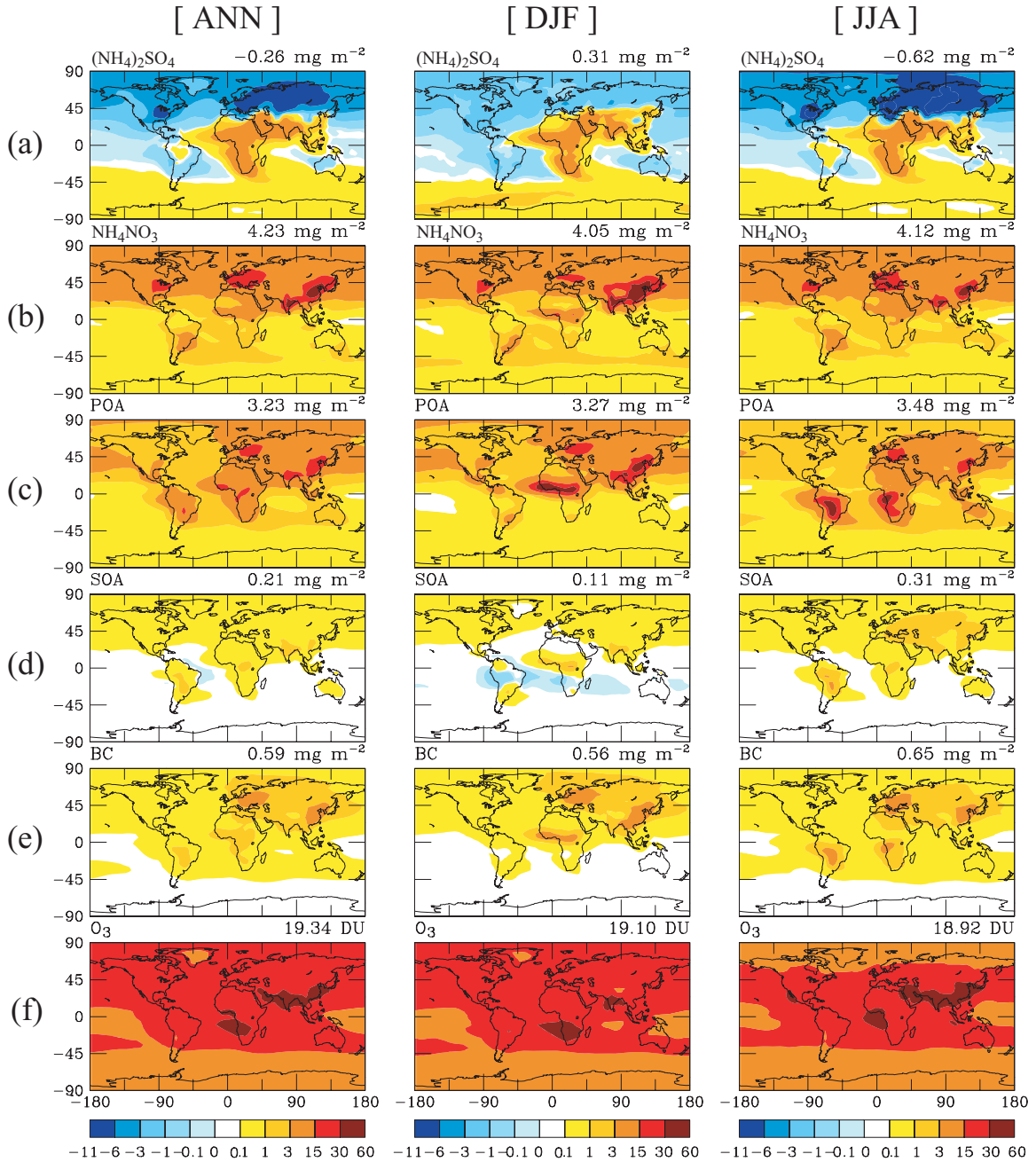


Figure 3-1. Annual and seasonal differences in column concentrations between present-day and year 2100 for anthropogenic aerosols ( $\text{mg m}^{-2}$ ) and tropospheric ozone (Dobson Units). (a) Ammonium sulfate (b) Ammonium nitrate (c) POA (d) SOA, (e) BC, and (f)  $\text{O}_3$  (ANN = annual mean, DJF = seasonal mean over December-January-February, and JJA = seasonal mean over June-July-August).

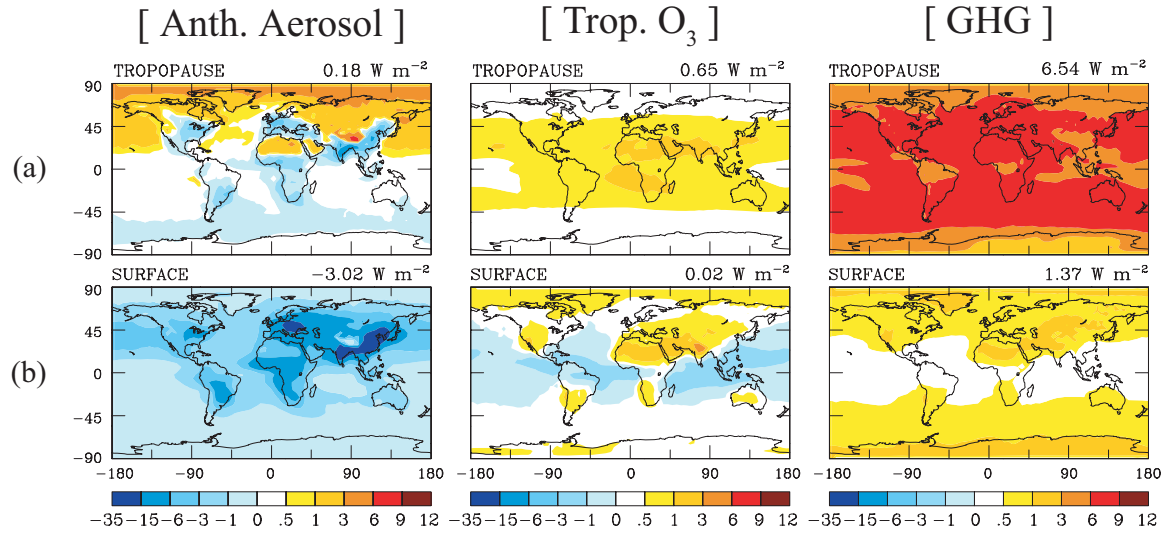


Figure 3-2. Annual mean change in instantaneous forcing ( $\text{W m}^{-2}$ ) (a) at tropopause and (b) at surface imposed by changes of anthropogenic aerosol (left column), tropospheric ozone (middle column), and greenhouse gases (right column) between present-day and year 2100.

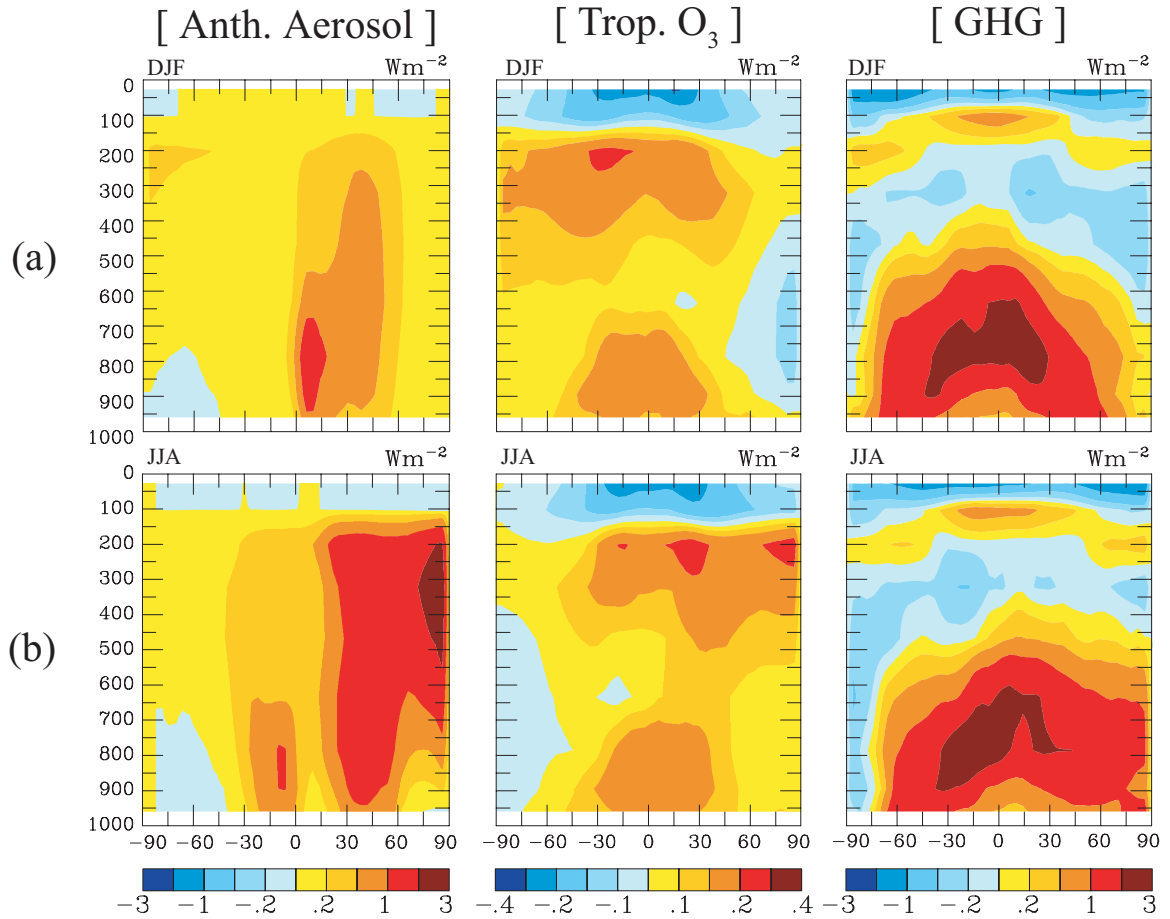


Figure 3-3. Latitude-pressure distribution of changes in atmospheric forcing ( $W m^{-2}$ ) in (a) DJF and (b) JJA imposed by changes of anthropogenic aerosol, tropospheric ozone, and GHG between present-day and year 2100.

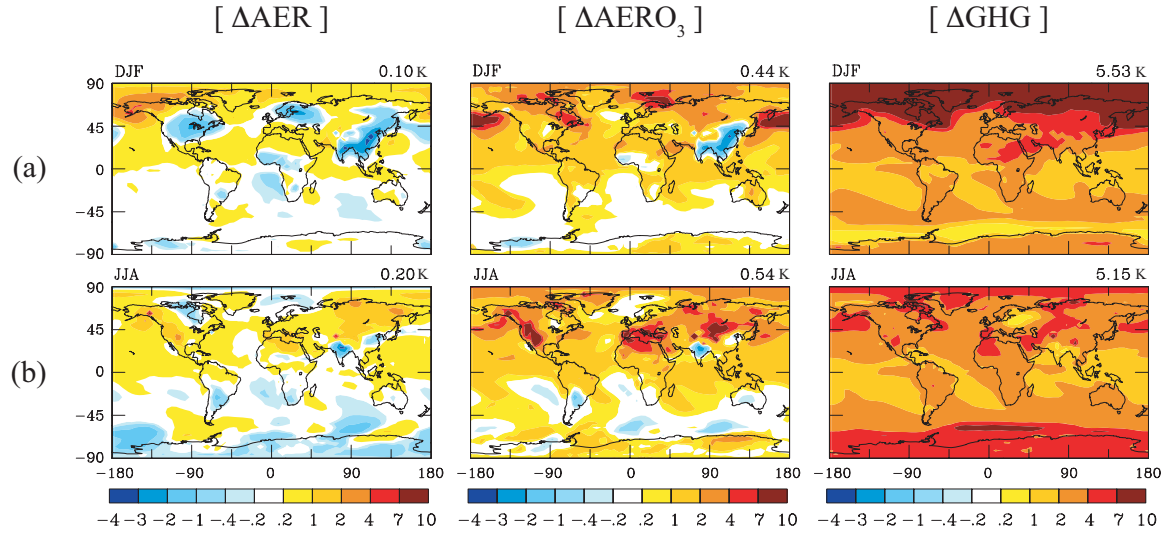


Figure 3-4. Predicted change in global surface air temperature (K) in (a) DJF and (b) JJA. Note the color scale for  $\Delta GHG$  differs from the other two.

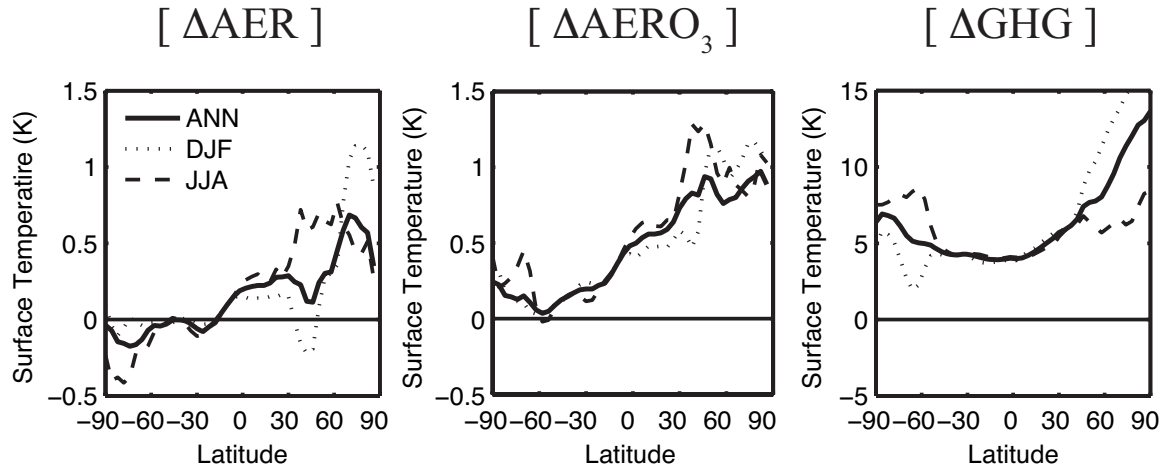


Figure 3-5. Predicted zonal mean changes in surface air temperature (K). Note the vertical scale for  $\Delta GHG$  differs from the other two.

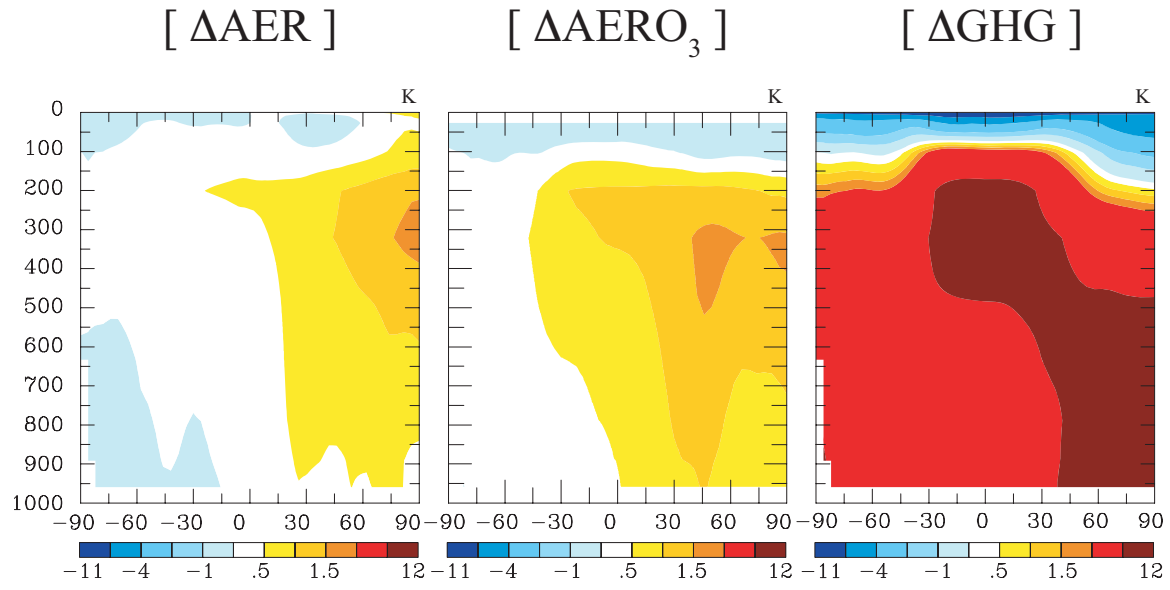


Figure 3-6. Latitude-pressure distribution of changes in annual mean temperature (K).

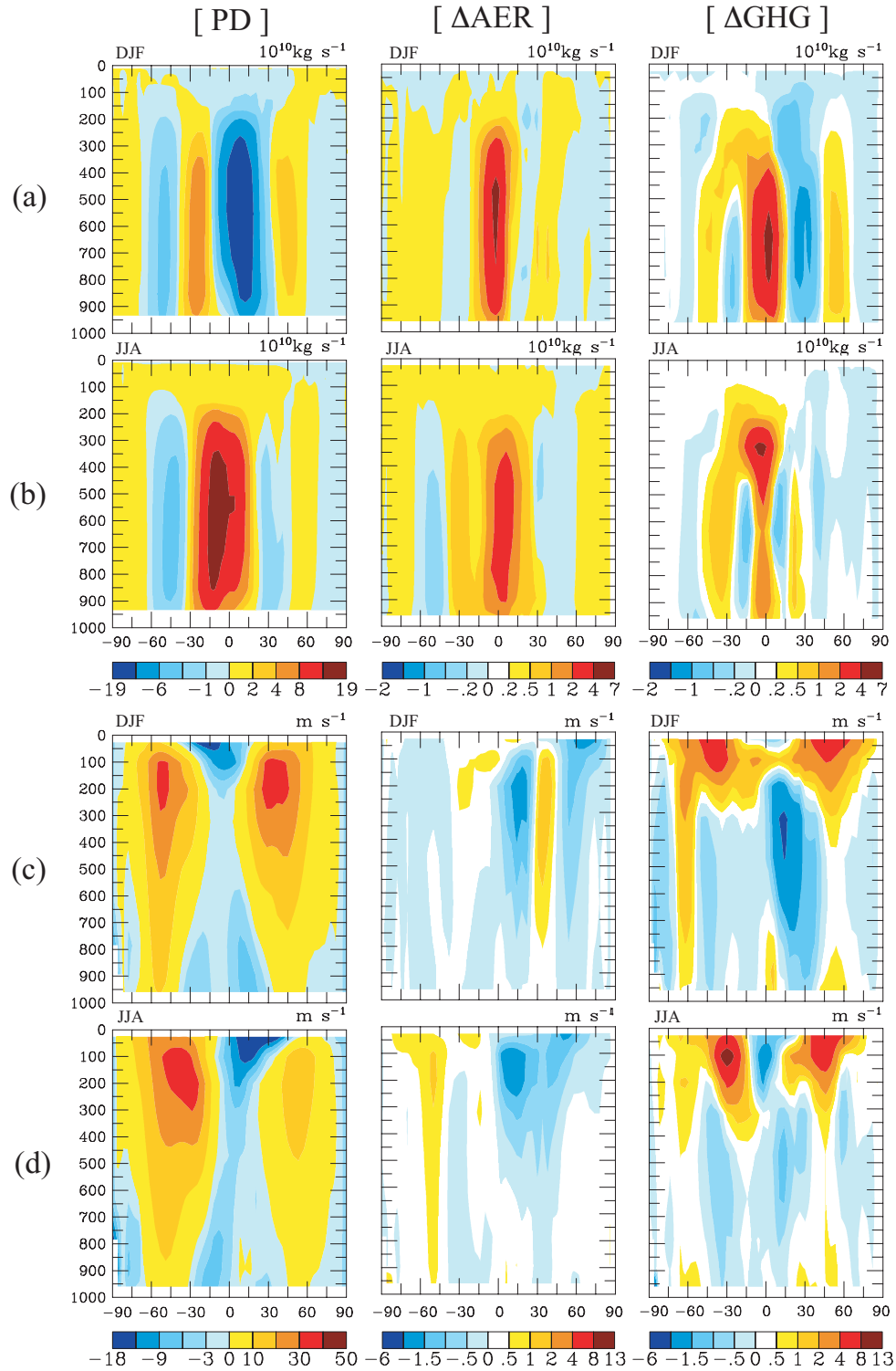


Figure 3-7. Latitude-pressure distribution of stream function ( $10^{10} \text{ kg s}^{-1}$ , positive values indicate counterclockwise flow) in (a) DJF and (b) JJA, and zonal wind ( $\text{m s}^{-1}$ , positive values indicate westerlies) in (c) DJF and (d) JJA. Left: seasonal mean in simulation PD; middle:  $\Delta\text{AER}$ ; right:  $\Delta\text{GHG}$ .

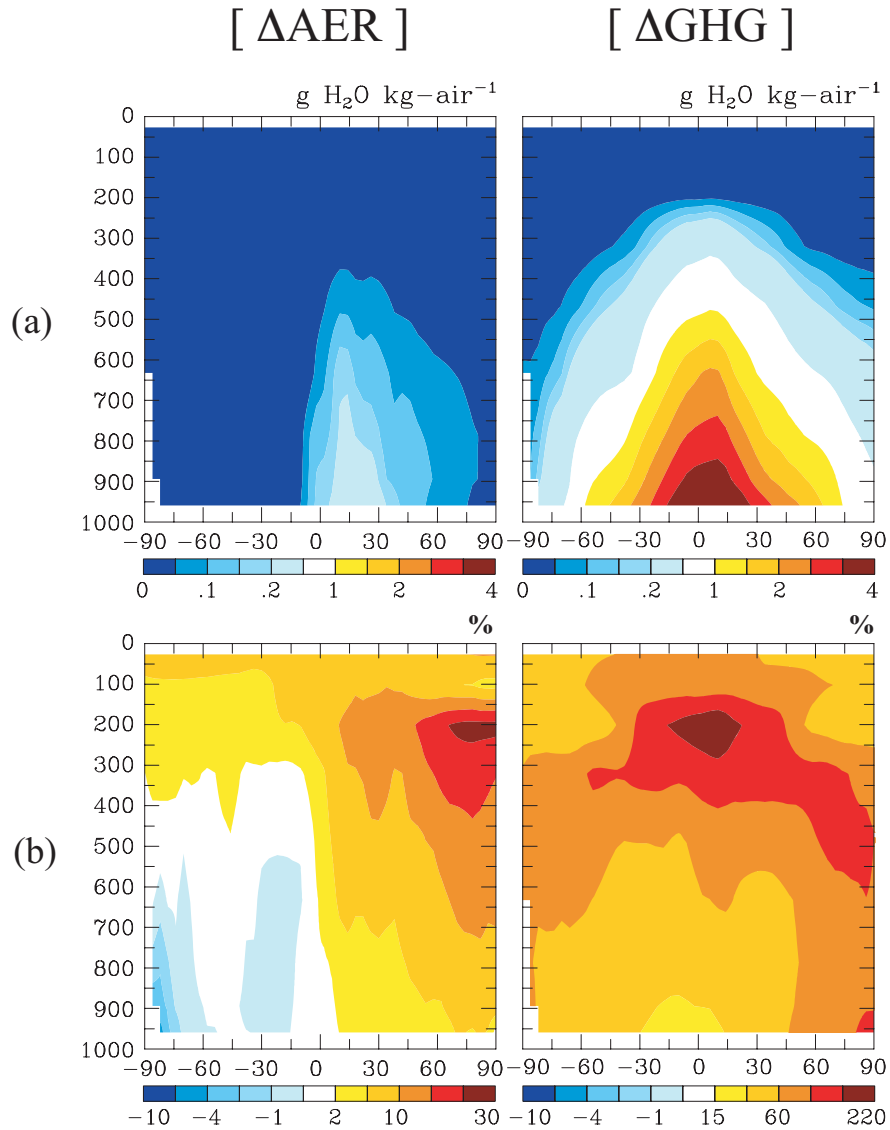


Figure 3-8. Latitude-pressure distribution of changes in annual mean specific humidity. (a) Absolute change ( $\text{g-H}_2\text{O kg-air}^{-1}$ ) and (b) relative change (%). Note the color scale in (b) differs between  $\Delta AER$  and  $\Delta GHG$ .

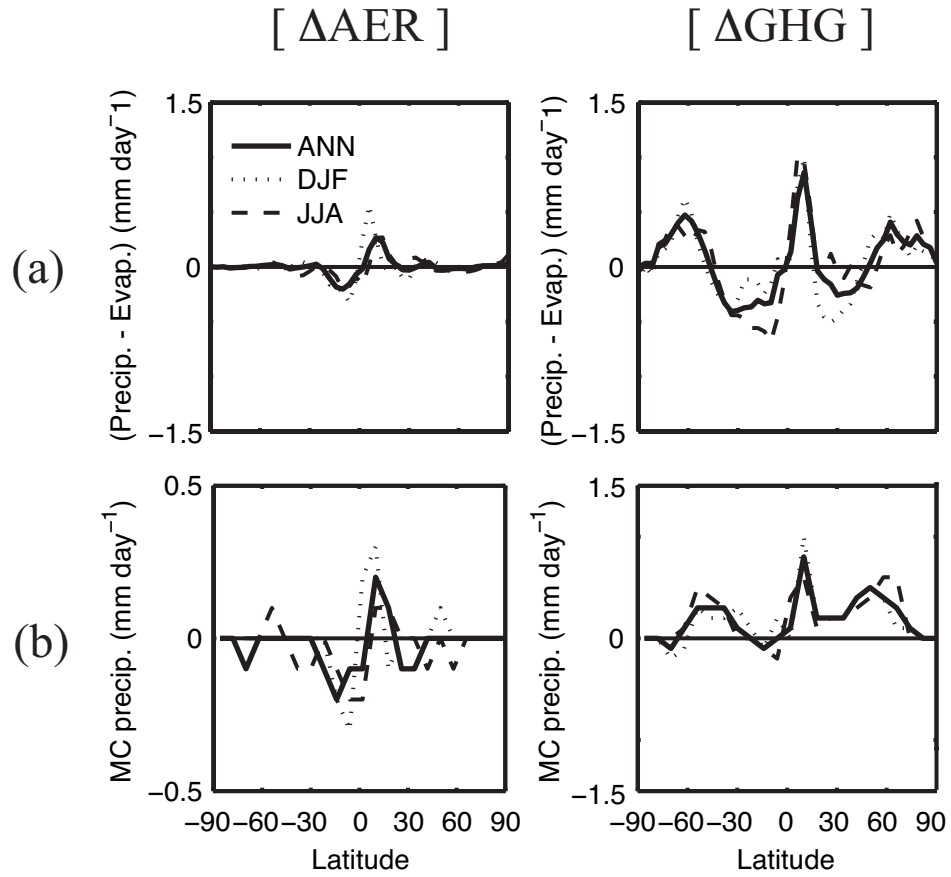


Figure 3-9. Predicted zonal mean changes in (a) excess precipitation (total precipitation minus evaporation, mm day<sup>-1</sup>) and (b) moist-convective (MC) precipitation (mm day<sup>-1</sup>). Note the vertical scales differ between  $\Delta AER$  and  $\Delta GHG$ .

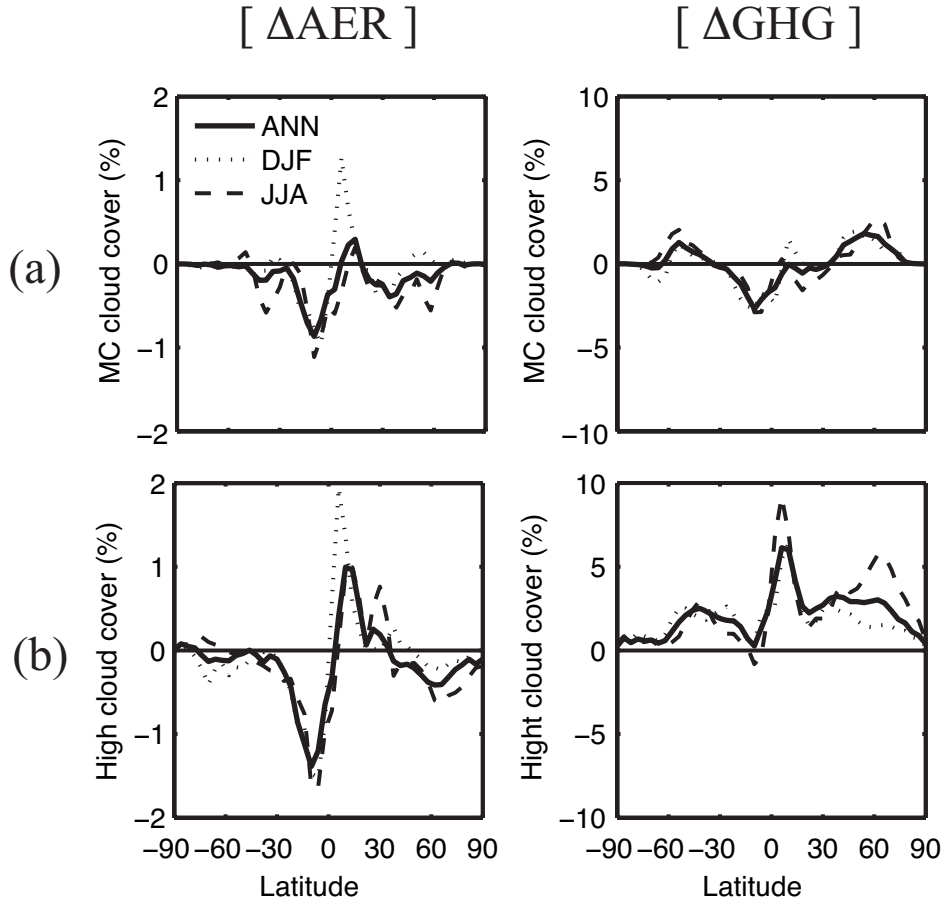


Figure 3-10. Predicted zonal mean changes in (a) moist-convective (MC) cloud cover (%), and (b) high cloud cover (%). Note the vertical scales differ between  $\Delta AER$  and  $\Delta GHG$ .

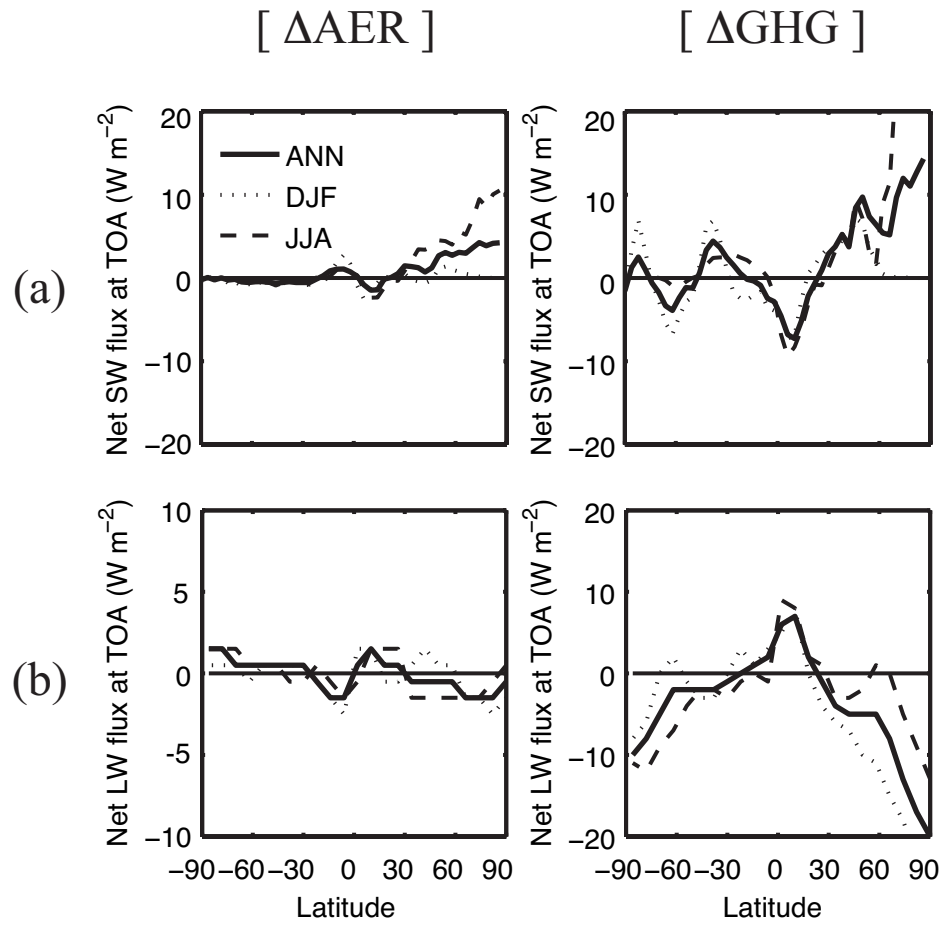


Figure 3-11. Predicted zonal mean changes in (a) net shortwave (SW) flux and (b) net longwave (LW) flux ( $\text{W m}^{-2}$ ) at TOA. Positive values correspond to downward fluxes. Note the vertical scales differ between  $\Delta\text{AER}$  and  $\Delta\text{GHG}$ .

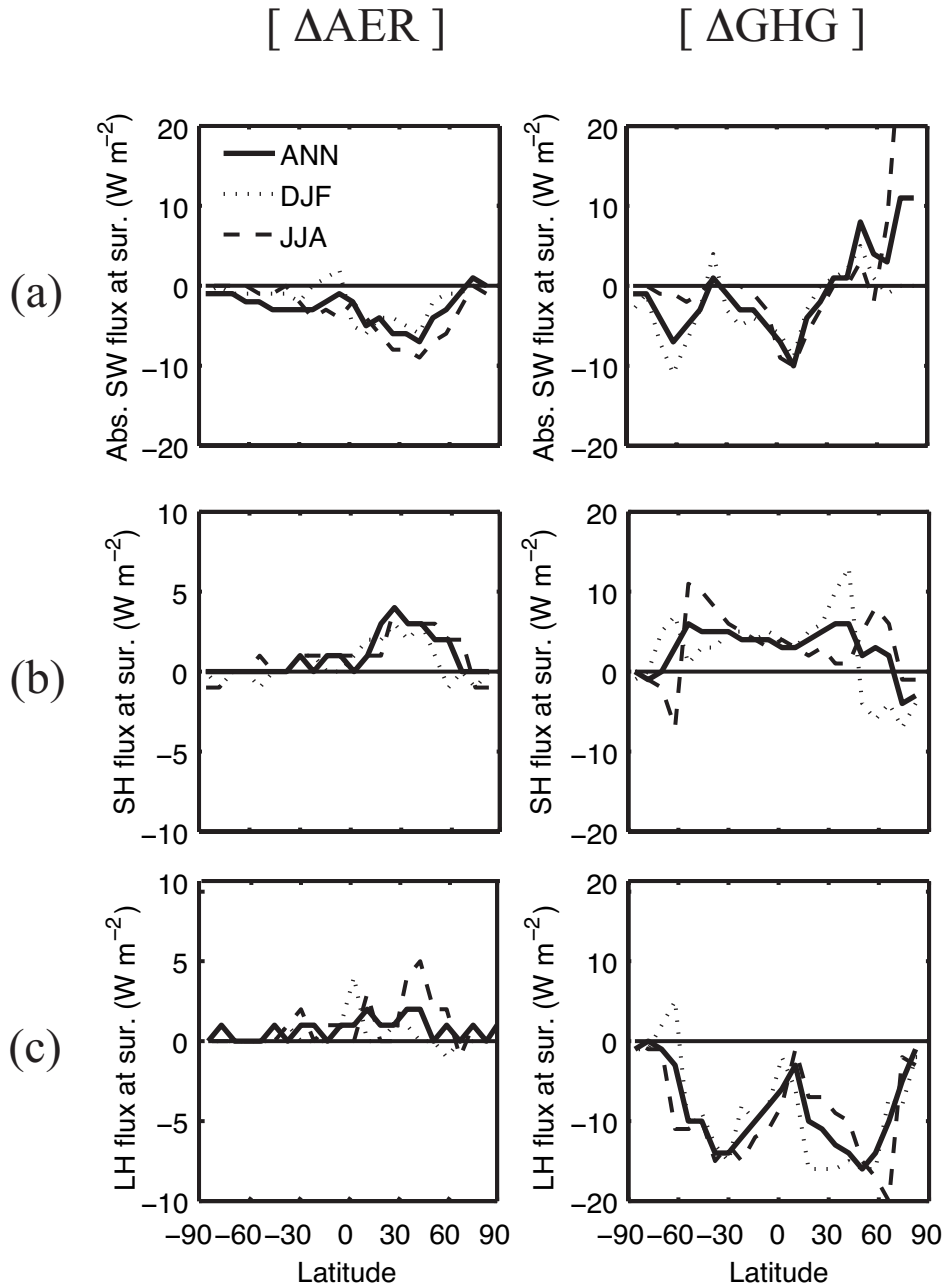


Figure 3-12. Predicted zonal mean changes in surface fluxes ( $\text{W m}^{-2}$ ) of (a) absorbed (abs.) shortwave radiation (SW, negative values indicate surface solar dimming), (b) sensible heat (SH, positive values indicate flux from atmosphere into surface), and (c) latent heat (LH, positive values indicate decreased evaporation). Note the vertical scales differ between  $\Delta$ AER and  $\Delta$ GHG.

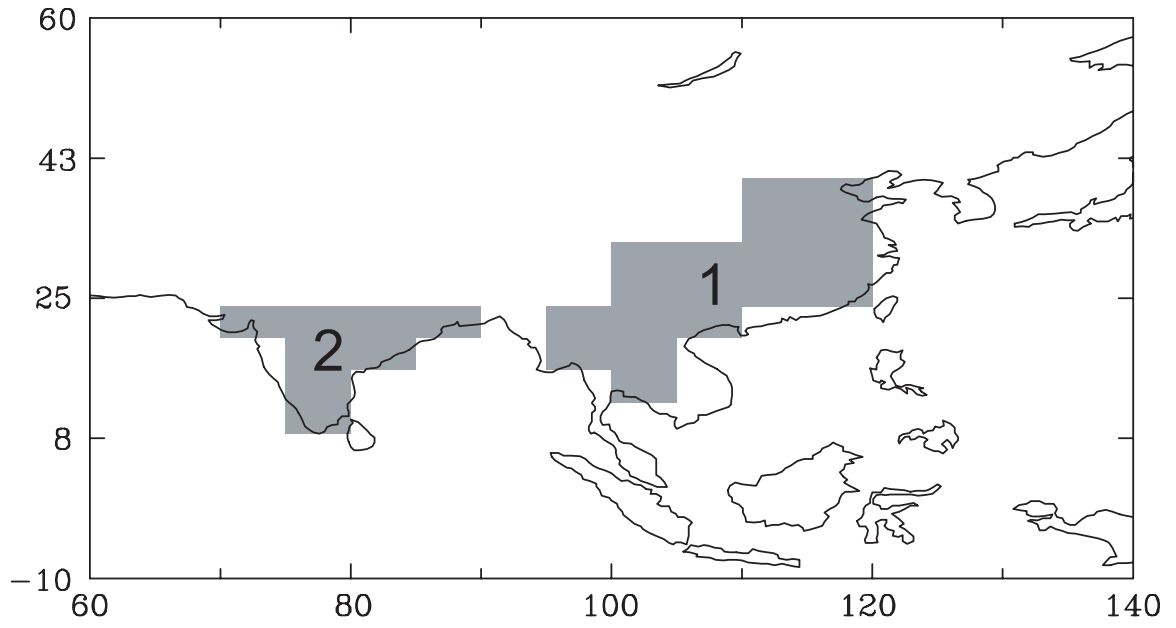


Figure 3-13. Regions (shaded) for calculating the statistics of regional climate change presented in Table 3-4. (1) East Asia. (2) South Asia.

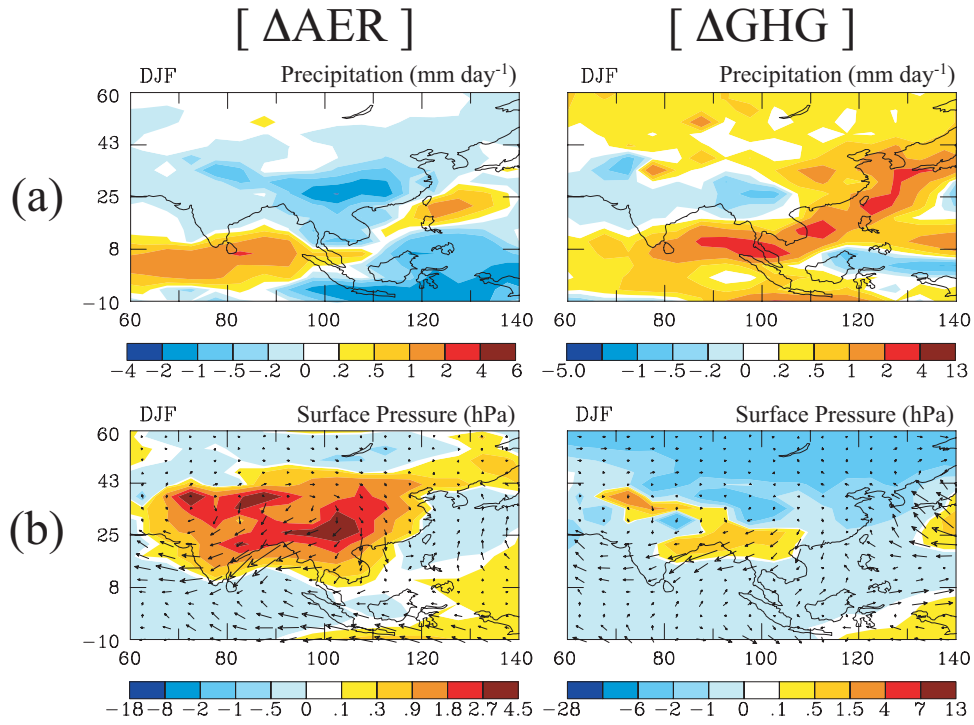


Figure 3-14. Predicted change over East and South Asia in DJF (a) in precipitation ( $\text{mm day}^{-1}$ ) and (b) in sea level pressure (color shading, hPa) and surface wind field (vector,  $\text{m s}^{-1}$ ). Note the color scale differs between  $\Delta AER$  and  $\Delta GHG$ .

# Chapter 4

---

## **Global Climate Response to Anthropogenic Aerosol Indirect Effects: Present Day and Year 2100**

Submitted for the publication in *Journal of Geophysical Research* by Wei-Ting Chen, Athanasios Nenes, Hong Liao, Peter Adams, and John Seinfeld.

## Abstract

The equilibrium response of the climate system to aerosol indirect effects (AIE) is investigated using the Goddard Institute for Space Studies (GISS) Global Climate Middle Atmosphere Model III (GISS III). A diagnostic formulation correlating cloud droplet number concentrations ( $N_c$ ) with concentrations of aerosol soluble ions is developed as a basis for the calculation. Based on offline estimates of pre-industrial (PI), present-day, and year 2100 aerosol mass concentrations from the fully coupled chemistry/aerosol/climate Unified Model, corresponding monthly averaged  $N_c$  values are derived. Explicit dependence on cloud droplet number concentrations ( $N_c$ ) is then introduced in the treatments of liquid-phase stratiform clouds in GISS III to account for both the albedo and cloud lifetime AIE. A series of 30-year equilibrium climate simulations are carried out, each with specific perturbations of  $N_c$ , the aerosol direct effect (ADE), and greenhouse gas (GHG) levels. Present-day simulated global distributions of  $N_c$ , cloud droplet size, and radiative balance are in good agreement with satellite-retrieved climatology. For perturbations of  $N_c$  alone from PI to present day, an instantaneous top-of-atmosphere (TOA) indirect forcing of  $-1.75 \text{ W m}^{-2}$  is estimated, with a global mean equilibrium surface cooling of 1.00 K, and precipitation reduction of 3.5%; substantial cooling over northern high latitudes, a southward shift of the Intertropical Convergence Zone, and a hydrological sensitivity of  $+3.46 \% \text{ K}^{-1}$  are also predicted. For estimated perturbations of  $N_c$  from present day to year 2100, an TOA indirect forcing of  $-0.81 \text{ W m}^{-2}$ , a surface cooling of 0.28 K, a decrease in precipitation of 1.0%, and a hydrological sensitivity of  $+3.71 \% \text{ K}^{-1}$  are predicted, with a statistically insignificant response in circulation. The present study, as compared to previous studies

using various versions of the GISS GCM, suggests that the climate sensitivity for AIE forcing is 50–70% of that for GHG forcing, and that the AIE can partly counteract the enhancement of the hydrological cycle owing to GHG-induced warming.

## 4.1 Introduction

Aerosols alter the energy balance of the earth-atmosphere system directly by scattering and absorbing sunlight (aerosol direct effect, ADE), and indirectly by affecting the reflectivity, lifetime, and precipitation efficiency of clouds. The so-called aerosol indirect effect (AIE), the modification of cloud optical properties (cloud albedo effect), structure, and precipitation (cloud lifetime effect) by aerosols, is judged to be the most uncertain radiative forcing in the climate system [*Intergovernmental Panel on Climate Change (IPCC)*, 2007]. General Circulation Models (GCMs) with explicit aerosol-cloud interactions are the principal tool for estimating the radiative forcing and climatic impacts of the AIE. Current GCM-based estimation of AIE radiative forcing from pre-industrial to present day for the cloud albedo effect range from  $-0.22$  to  $-1.85$   $\text{W m}^{-2}$ ; when changes in cloud lifetime and other feedbacks are included, the values vary from  $-0.29$  to  $-2.41$   $\text{W m}^{-2}$  [*IPCC*, 2007].

Climatic impacts of the present-day AIE, relative to pre-industrial conditions, have been investigated in GCM studies [*Rotstayn et al.*, 2000; *Williams et al.*, 2001; *Rotstayn and Lohmann*, 2002; *Kristjánsson et al.*, 2005]. In these studies a slab ocean with interactive sea surface temperature (SST) but fixed heat transport is coupled to the atmosphere. A similar pattern in climate responses was found in each of these studies: cooling at Northern Hemisphere high latitudes and a southward displacement of the

Intertropical Convergence Zone (ITCZ). In addition, *Kristjánsson et al.* [2005] identified a negative global cloud feedback, resulting from cloud thinning in response to the cooling in high latitudes. In studies exploring the combined impacts of present-day aerosol direct and indirect effects [*Feichter et al.*, 2004; *Kristjánsson et al.*, 2005; *Takemura et al.*, 2005], a weakening of the hydrological cycle over northern high latitudes was diagnosed; these responses are different from those to the warming induced by greenhouse gases (GHG), which, on a global scale, tends to accelerate the hydrological cycle, enhance cloud thickness, and weaken the Hadley cell [*IPCC*, 2007].

In the present work, climate responses to the AIE are studied as well, with emphasis on changes in the hydrological cycle. We address the following questions: (1) How is present-day climate affected by the anthropogenic perturbations of cloud droplet number concentration ( $N_c$ )? (2) How is future (year 2100) climate predicted to be influenced by the combined perturbations of anthropogenic GHG, aerosols, and  $N_c$ ?

Here we use equilibrium climate simulations to investigate the above questions. The simulations are performed using the Goddard Institute for Space Studies (GISS) Global Climate Middle Atmosphere Model III (referred to as GISS III hereafter) coupled to a slab ocean. The cloud scheme in the standard version of GISS III does not allow one to readily determine aerosol effects on cloud microphysics through perturbation of  $N_c$  values. Therefore modifications are made to the formulations of optical depth and autoconversion rates in liquid-phase stratiform clouds to introduce explicit dependence on offline  $N_c$  fields. In each of the simulations, specific levels of offline, monthly averaged aerosol mass concentrations and  $N_c$  values are input, and the atmospheric dynamics, hydrological cycle, and temperature are allowed to respond accordingly.

Changes in cloud optical depth, temperature, precipitation, and cloud forcing (all-sky minus clear-sky radiative fluxes) between the equilibrium climates are diagnosed.

Some comment is in order on the comparison between the changes in cloud forcing reported in this study and the “radiative forcing” of AIE reported in the literature. The values reported here, as “responses” to the perturbations in  $N_c$ , include the effects of cloud feedback. Because of the feedback mechanisms involved in the AIE, the concept of instantaneous radiative forcing (for example, as used for GHG forcing and ADE forcing) cannot be applied, especially when the cloud lifetime effect is considered. Overall AIE radiative forcing has to be determined by diagnosing the changes in cloud forcing, allowing at least the cloud water and precipitation to respond [IPCC, 2007]. Most of the previous GCM studies have used prescribed SST, in which the response of surface temperature is limited. Therefore, the values of AIE forcing reported in these studies do not include full effects of cloud-temperature feedback. In the present work, as well as in a few previous studies [Rotstayn *et al.*, 2000; Williams *et al.*, 2001; Rotstayn and Lohmann, 2002; Kristjánsson *et al.*, 2005], a coupled slab ocean is adopted to enable a full response of surface temperature, and the reported changes in cloud forcing thus include the contribution by cloud-temperature feedback.

A key ingredient in representing the AIE in GCMs is the relation of changes in aerosol amount and properties to changes in  $N_c$  and cloud droplet size distribution. In the empirical diagnostic approach,  $N_c$  is formulated as a function of aerosol mass or number concentration, based on ambient data [e.g., Boucher and Lohmann, 1995; Menon *et al.*, 2002; Dufresne *et al.*, 2005; Quaas and Boucher, 2005]. In the prognostic approach, the cloud droplet distribution is predicted based on cloud microphysics [e.g., Kristjánsson *et*

*al.*, 2005; *Takemura et al.*, 2005; *Lohmann et al.*, 2007]. While the earliest studies of the AIE employed the empirical diagnostic approach, the tendency in recent work is to adopt a prognostic microphysics approach to predict cloud droplet properties online and interactively. In the present study, we establish a new, physically based, computationally efficient formulation to relate aerosols and cloud properties diagnostically, allowing for geographical and seasonal variations of aerosol-cloud interactions.

In section 4.4.2, a description of the diagnostic aerosol-cloud formulation is provided, together with the derivations of offline aerosol mass concentrations and offline  $N_c$  values, as well as the modifications to the cloud scheme in the GISS III GCM. Experimental design of the equilibrium simulations is outlined in section 4.4.3, with the results of the simulations analyzed and discussed in sections 4.4.4 and 4.4.5.

## 4.2 Descriptions of Global Models

Three different global models were used in this study: the Unified Model developed in the National Aeronautics and Space Administration (NASA) project “Chemistry, Aerosols, and Climate: Tropospheric Unified Simulation” (termed the “CACTUS Unified Model” hereafter), the Two-Moment Aerosol Sectional microphysics model within Goddard Institute for Space Studies (GISS) GCM II’ (GISS-TOMAS hereafter), and the GISS III GCM. Table 4.1 summarizes the characteristics of each model, its usage here, and relevant references. Figure 4.1 is a flow chart of the simulations in this study, and the steps in which each model is involved. First, the CACTUS Unified Model is used, with fully coupled simulations of tropospheric chemistry, aerosol, and climate, to calculate an annual cycle of monthly averaged aerosol mass concentrations for pre-industrial (PI,

roughly corresponding to the year 1800), year 2000 (20C), and year 2100 (21C). Next, grid-by-grid correlation formulations between  $N_c$  and aerosol soluble ions are derived using GISS-TOMAS and the sectional cloud condensation nuclei (CCN) activation parameterization of *Nenes and Seinfeld* [2003] with the droplet growth kinetic modifications of *Fountoukis and Nenes* [2005] (hereafter FN). With this formulation and the aerosol mass concentrations from the CACTUS Unified Model, offline, monthly-averaged values of  $N_c$  for PI, 20C, and 21C are calculated. Finally, optical depth and autoconversion rates in the liquid-phase stratiform cloud scheme of GISS III are adjusted to include explicit dependence on  $N_c$ . A set of equilibrium climate simulations was carried out, each with specific levels of GHG, offline aerosol mass, and offline  $N_c$ . The differences between the equilibrium simulations were analyzed to identify the impacts of AIE on the hydrological cycle and future climate changes.

#### **4.2.1 CACTUS Unified Model and Offline Aerosol Mass Concentration**

The CACTUS Unified Model, based on the 4°-latitude-by-5°-longitude, 9-layer GISS GCM II', simulates the fully-coupled interactions of chemistry, aerosol, and climate [*Liao et al.*, 2003; 2004; *Liao and Seinfeld*, 2005]. The model is coupled to a Q-flux ocean, with monthly horizontal heat transport fluxes taken from *Mickley et al.* [2004]. Changes in the sea surface temperature and sea ice are determined by energy exchange with the atmosphere, ocean heat transport, and the ocean mixed layer heat capacity [*Hansen et al.*, 1984; *Russell et al.*, 1984]. The model includes detailed tropospheric O<sub>3</sub>-NO<sub>x</sub>-hydrocarbon chemistry, as well as heterogeneous processes, such as hydrolysis of N<sub>2</sub>O<sub>5</sub> and irreversible absorption of NO<sub>3</sub>, NO<sub>2</sub>, and HO<sub>2</sub> on wetted particle surfaces. Aerosol species predicted in the model include sulfate, nitrate, ammonium, black carbon

(BC), primary (POA) and secondary organic aerosol (SOA), sea salt, and mineral dust. The CACTUS Unified Model has been used in a number of climate studies to identify the influence of climate change on the predictions of tropospheric chemistry and aerosol [Liao *et al.*, 2006], the climatic impact of ADE [Chen *et al.*, 2007], and the differences between fully-coupled and offline chemistry-aerosol-climate simulations [Liao *et al.*, 2008].

In the version of the CACTUS Unified Model used here, the formation of SOA from monoterpenes is based on experimentally determined yield parameters [Griffin *et al.*, 1999a; Griffin *et al.*, 1999b; Chung and Seinfeld, 2002], assuming equilibrium partitioning; SOA formation from isoprene is not included in the current version of the model, which will be updated in future work. The aerosol semi-direct effect on clouds (i.e., through changes in the atmospheric temperature structure caused by aerosol absorption), in-cloud chemistry, and wet removal of aerosols are accounted for. The model does not include the climatic impact of AIE on the prediction of aerosol fields; within the scope of this study, this effect should be small.

Three simulations with the CACTUS Unified Model were carried out, each using emissions of aerosols, aerosol precursors, and ozone precursors corresponding to PI, 20C, and 21C, while GHG were held at present-day levels in all the simulations. Emissions for PI conditions are based on Liao *et al.* [2006], and for 20C and 21C, the emissions are based on IPCC Special Report on Emissions Scenarios (SRES) A2 (as detailed in Liao *et al.* [2006]). All three simulations were initiated by an equilibrium climate corresponding to 20C GHG and integrated for six years. Since the levels of GHG are fixed throughout the simulations, the differences between the derived PI, 20C and 21C aerosol

concentrations result entirely from emission changes. Results from the last five years in each simulation are averaged to obtain a grid-by-grid, annual cycle of monthly-averaged aerosol mass concentrations. These aerosol concentrations are used to obtain corresponding offline  $N_c$  values (section 4.2.2). Globally, sea salt is an important CCN [Pierce and Adams, 2006], and therefore is required to accurately predict  $N_c$ . Since the uncertainties related to sea salt concentrations may be significant for PI and 21C [Liao and Seinfeld, 2005], for the calculations of  $N_c$ , we use sea salt distributions derived for 20C to represent those for PI and 21C. Aerosol mass concentrations predicted are also to be used in the equilibrium climate simulations to account for the ADE forcing (section 4.2.3.3). Since the primary focus of this study is on anthropogenic aerosols, sea salt is not included in the ADE calculation in the equilibrium climate simulation.

Table 4.2 lists the predicted global annual burdens of major aerosol species, ammonium sulfate, ammonium nitrate, POA, SOA, and BC aerosols, derived for PI, 20C, and 21C. Each of the above species shows significant increase from PI to 20C. From 20C to 21C, sulfates are predicted to decrease owing to reductions in projected  $\text{SO}_2$  emissions; nitrate levels are predicted to increase more than fourfold, while POA and BC are predicted to double. Figure 4.2 shows the global annual mean column burdens of anthropogenic aerosol for PI, 20C, and 21C. Increases in peak concentrations are predicted over heavily industrialized and populated areas of South and East Asia, Europe, and the eastern United States. Outflows from the major biomass burning regions in South America and western Africa are also prominent. Predicted global column burdens of sea salt for 20C are shown in Figure 4.3. With a predicted global burden of 4.96 Tg, sea salt

concentrations are highest over the southern ocean, and lowest over the continents and western Tropical Pacific.

## **4.2.2 GISS-TOMAS Model, FN Activation Parameterization, and Derivation of Aerosol- $N_c$ Relationships**

GISS-TOMAS and the FN activation parameterization are used to provide the diagnostic relationship between aerosol levels and  $N_c$ . The size-resolved TOMAS microphysics module simulates aerosol number concentration, size distribution, composition, and CCN online within the GISS GCM II'; detailed descriptions are provided in *Adams and Seinfeld* [2002] for sulfate simulations and *Pierce and Adams* [2006] for the implementation of sea salt aerosol. In brief, the module tracks both aerosol number and mass in each size bin in the aerosol distribution. A sectional approach is applied to define the boundaries of 30 size bins (spanning approximately dry diameters of 0.01 to 10  $\mu\text{m}$ ), in terms of dry aerosol mass. Microphysical processes include coagulation, condensation/evaporation, nucleation, and in-cloud sulfur oxidation. Sulfate is assumed to exist as ammonium bisulfate, and to be internally mixed with sea salt. The FN activation parameterization is then applied online to compute nucleation scavenging of aerosol and  $N_c$  from the aerosol simulation. FN is a comprehensive and efficient formulation, which has been evaluated extensively with numerical simulations [*Fountoukis and Nenes*, 2005], as well as in situ measurements [*Meskhidze et al.*, 2005; *Fountoukis et al.*, 2007]. FN is based on the framework of an ascending adiabatic cloud parcel;  $N_c$  is determined by the maximum supersaturation,  $s_{max}$ , which is controlled by the water vapor balance and is obtained by classifying the droplets by proximity to their

critical diameter (“population splitting”). In this study, a single cloud-base updraft velocity of  $0.6 \text{ m s}^{-1}$  over land and  $0.3 \text{ m s}^{-1}$  over ocean is prescribed, based on in-situ measurements of updraft velocity in stratocumulus clouds [Fountoukis *et al.*, 2007]. Although a simple approach, using a single updraft velocity gives optimal closure between observations and theory for cloud droplet calculations in cumulus and stratocumulus clouds, provided that it expresses the average vertical velocity distribution in the boundary layer [e.g., Meskhidze *et al.*, 2005; Peng *et al.*, 2005; Fountoukis *et al.*, 2007]. For grid cells which contain both ocean and land, a weighted average of droplet number is computed based on the fractional coverage of each. The effective water vapor uptake coefficient (which affects the water vapor mass transfer coefficient during droplet formation) is set to 0.06, following the suggestions of Fountoukis *et al.* [2007]. The model was integrated for 2 years with present-day emissions of sulfur and sea salt; monthly, grid-by-grid CCN spectra are then derived from the simulations of the second year.

Based on the monthly averaged CCN spectra obtained from the GISS-TOMAS simulations, an aerosol- $N_c$  relationship is derived for each grid cell and month as follows: the aerosol concentration is varied between 0.05 and 5 times the average concentration, and the corresponding  $N_c$  is computed by application of FN (using the same updraft velocity and water vapor uptake coefficient as in the online simulation). The relationship then between aerosol amount (expressed in terms of molar concentration of total soluble ions from sulfate and sea salt,  $m_i$ , in mole  $\text{m}^{-3}$  air) and  $N_c$  ( $\text{m}^{-3}$ ) is correlated in the format proposed by Boucher and Lohmann [1995],

$$\log N_c = A + B \log m_i. \quad (4-1)$$

The coefficients  $A$  and  $B$  are computed for each grid cell in each month by least-mean squares optimization. Thereby, geographic and seasonal variations of aerosol-cloud interactions are represented by the values of the two coefficients. The diagnostic formulation developed here is particularly useful for GCM studies because: (1) It is based on aerosol soluble ions rather than mass or composition of certain aerosol species, and therefore can be applied broadly to global models; and (2) It contains key microphysical characteristics, yet is computationally efficient as compared with more detailed cloud microphysical modules.

To obtain the offline, monthly averaged  $N_c$  values for an equilibrium climate simulation, the 9-layer aerosol mass concentrations derived as described above were converted to soluble ion concentrations, by assuming that sulfate, ammonium, nitrate, and sea salt aerosols are fully soluble, POA and SOA is 80% soluble, BC is insoluble, and that each of the soluble species forms an ideal solution. A molar mass of  $0.2 \text{ kg mole}^{-1}$  and a van't Hoff factor of 1.0 are assumed for soluble organic aerosols. The  $m_i-N_c$  formulations with the derived monthly coefficients at each grid cell were applied to calculate  $N_c$  for PI, 20C, and 21C conditions. A lower limit of  $20 \text{ cm}^{-3}$  is prescribed for  $N_c$  to ensure that sufficient droplets exist in pristine marine environments [Sotiropoulou *et al.*, 2008]. The monthly  $N_c$  values were then interpolated from a vertical resolution of 9 layers into 23 layers, according to the  $\sigma$  levels of the GISS-II' and GISS III GCMs, ensuring conservation of total  $N_c$  in the entire column.

Figure 4.4a shows the annual mean differences in derived  $N_c$  at the lowest model level (972 hPa) between PI and 20C. The areas predicted to exhibit a significant  $N_c$  increase from PI to 20C are closely related to areas of enhanced anthropogenic aerosol

concentrations (Figure 4.2). For changes between 20C and 21C (Figure 4.4b), large increases in near surface  $N_c$  are predicted over China, Europe, eastern United States, South America, and southern Africa, whereas over northern high latitudes,  $N_c$  is estimated to decrease owing to the reduction of sulfate aerosols.

### **4.2.3 GISS III GCM and the Modification of Stratiform Cloud Scheme**

Detailed descriptions and evaluation of the GISS III GCM are provided in *Rind et al.* [2007]. In addition to the increase in vertical resolution from 9  $\sigma$  layers in GISS GCM II' (between surface and 10 hPa) to 23  $\sigma$  layers (between surface and 0.002 hPa), major modifications in GISS III include more sophisticated treatments in downdraft entrainment and the detrainment of cumulus condensate into an anvil similar to stratiform cloud, the addition of compensatory subsidence in moisture advection, new formulations of boundary layer temperature, moisture and scalar fluxes, and turbulent kinetic energy, as well as more correlated k intervals in the radiative scheme.

The stratiform cloud scheme in GISS III is based mainly on *Del Genio et al.* [1996]. The fractional stratiform cloudiness is determined by the difference between the relative humidity (RH) averaged over a grid cell and the RH in the cloud-free part of the cell. Processes controlling the liquid water budget include advection, condensation and evaporation of condensate and precipitation, autoconversion, cloud-top entrainment, accretion of cloud water by precipitation, and the Bergeron–Findeisen process for glaciation of supercooled water. In order to simulate AIE-related response in cloud optical properties, precipitation, and radiation, the formulations of cloud optical depth and autoconversion rate in the stratiform cloud scheme were revised, as described below.

#### 4.2.3.1 Droplet Effective Radius and Cloud Optical Depth

The stratiform cloud scheme diagnoses the cloud radiative properties based on the cloud optical depth  $\tau$  and the effective droplet radius  $r_e$ , which is related to the volume-weighted mean droplet radius  $r_v$  by

$$r_e = \kappa^{-\frac{1}{3}} r_v. \quad (4-2)$$

A single value of 0.48 is chosen for the constant  $\kappa$  [Menon *et al.*, 2002; Rind *et al.*, 2007], which corresponds to an effective variance of 0.2. The cloud optical depth  $\tau$  is then determined by,

$$\tau = \frac{3\mu P \Delta\Phi \kappa^{\frac{1}{3}}}{2\rho_w r_v \rho_{air} g}, \quad (4-3)$$

where  $\mu$  is the in-cloud liquid water content ( $\text{kg m}^{-3}$ ),  $P$  is pressure ( $\text{N m}^{-2}$ ),  $\Delta\Phi$  is the thickness of the  $\sigma$  layer,  $\rho_w$  is the density of liquid water ( $\text{kg m}^{-3}$ ),  $\rho_{air}$  is air density ( $\text{kg m}^{-3}$ ), and  $g$  is gravitational acceleration ( $\text{m s}^{-2}$ ). To account for cloud morphology in all three dimensions, the optical depth is scaled with the fractional cloudiness ( $b$ ) by  $\tau' = \tau b^{1/3}$  [Del Genio *et al.*, 1996] and then introduced into the radiative transfer calculation in the standard algorithm in GISS III [Del Genio *et al.*, 1996],  $r_v$  is determined by an empirical scaling based on the value of  $\mu$ , which implicitly assumes a constant value of  $N_c = 60 \text{ cm}^{-3}$  over ocean and  $N_c = 170 \text{ cm}^{-3}$  over land. To include the cloud albedo effect in stratiform clouds, the following equation is applied,

$$r_v = \left[ \frac{3\mu}{4\pi N_c \rho_w} \right]^{\frac{1}{3}}, \quad (4-4)$$

so that  $r_v$  is determined by  $\mu$  and the offline  $N_c$  ( $\text{m}^{-3}$ ) values imported to each grid cell on a monthly basis. Therefore,  $r_e$  and  $\tau$  are controlled by the spatial and seasonal variations of  $N_c$ , which are driven by the changes in aerosol mass and aerosol-cloud interactions. Note that equations (4-2) and (4-4) are also applied to compute the radius in droplet evaporation. Additional modifications to the scheme of *Del Genio et al.* [1996] include a change in the value of  $\kappa$  (0.67 over land, and 0.80 over ocean [*Martin et al.*, 1994]) to reflect the broader distributions of terrestrial clouds (with respect to oceanic) and constraints on the minimum and maximum values of  $r_e$  (2 and 20  $\mu\text{m}$ , respectively). The above modifications are applied to pure liquid stratiform clouds only (temperature  $> 4^\circ\text{C}$  over ocean, and  $> -10^\circ\text{C}$  over land); ice stratiform clouds (temperature  $< -40^\circ\text{C}$ ), mixed-phase stratiform clouds, as well as convective clouds, follow the scheme of *Del Genio et al.* [1996].

#### 4.2.3.2 Autoconversion Rate

The basic autoconversion formulation in GISS is related to that in *Sundqvist et al.* [1989],

$$\left. \frac{dq_l}{dt} \right|_{aut} = C_0 q_l \left[ 1 - \exp\left(-\frac{\mu}{\mu_{crit}}\right)^4 \right], \quad (4-5)$$

where  $q_l$  is the cloud liquid water mixing ratio,  $C_0$  is the limiting autoconversion rate ( $\text{s}^{-1}$ ), and  $\mu_{crit}$  is the critical cloud water content for the onset of rapid conversion. To explicitly relate  $q_l$  to  $N_c$ , this parameterization is replaced with that developed by *Khairoutdinov and Kogan* [2000] (KK hereafter), and modified to account for the fractional cloudiness in each GCM grid cell,

$$\left. \frac{dq_l}{dt} \right|_{aut} = -1350\gamma b \left( \frac{q_l}{b} \right)^{2.47} N_c^{-1.79}. \quad (4-6)$$

The tuning parameter  $\gamma$  is used to ensure that the same radiative balance is maintained before and after the replacement of the autoconversion parameterization [Hoose *et al.*, 2008]. A constraint of in-cloud liquid water content  $< 3 \text{ g m}^{-3}$  is also applied. In the typical ranges of liquid water and  $N_c$ , autoconversion rates calculated by the KK scheme can be 20 to 1000 times smaller than those by the Sundquist scheme [Penner *et al.*, 2006; Hsieh *et al.*, 2008]. When implementing the KK scheme in GISS III, proper adjustment to the autoconversion rates is needed to avoid the unintentional increase in liquid water path (LWP) and the subsequent “drift” toward a cooler climate. The value of  $\gamma$  is determined by minimizing the imbalance of top-of-atmosphere (TOA) radiation, similar to the approach in Hoose *et al.* [2008]. Starting from a present-day equilibrium predicted by the original GISS III (the first simulation in section 4.3), the modified GCM is integrated for one year, with a specific value of  $\gamma$ . The annual mean TOA net radiation is diagnosed. By testing various values between 10 and 100,  $\gamma = 40$  was found to produce the smallest net TOA radiation ( $< 0.4 \text{ W m}^{-2}$ ), and is thus used for all AIE equilibrium climate simulations.

#### 4.2.3.3 Aerosol Direct Effect

The calculation of the anthropogenic aerosol direct effect follows the work of Chen *et al.* [2007]. The monthly-averaged aerosol mass concentrations derived by the CACTUS Unified Model (section 4.2.1) are interpolated into 23 layers accordingly. Internal mixing of ammonium sulfate, ammonium nitrate, BC, POA, SOA and aerosol associated water is

assumed. The density of the internally mixed aerosol is computed as the mass-averaged density of water and all dry aerosols. Refractive indices are derived based on a volume-weighted mixing rule. The refractive index of dry nitrate is assumed the same as that of dry sulfate [Toon *et al.*, 1976], while the refractive indices for organic carbon and BC and water are from *d'Almeida et al.* [1991]. Mie theory is applied to determine extinction efficiency, single-scattering albedo, and asymmetry parameter, which are then supplied to the radiation scheme of the GCM to calculate the aerosol optical depth and the radiation fluxes. The internal mixing assumption yields a relatively high absorption efficiency per unit mass of BC.

### 4.3 Equilibrium Climate Simulations with GISS III GCM

The experimental setups of the equilibrium climate simulations with GISS III are summarized in Table 4.3. The nomenclature of the simulations is as follows:

(i) Upper-case letters denote the forcing mechanisms imposed on each simulation, with *G* for Greenhouse gas forcing, *D* for aerosol Direct effect, and *I* for aerosol Indirect effect; and

(ii) Subscripts denote the levels of the forcing agents, with *PI* for pre-industrial level, *20C* for year 2000 level, and *21C* for year 2100 level.

GHG forcing is imposed by fixing the concentrations of CO<sub>2</sub>, CH<sub>4</sub>, N<sub>2</sub>O, CFC-11, and CFC-12 at specific levels; the values, based on IPCC SRES A2, are listed in the footnotes in Table 4.3. ADE forcing is imposed by the using the offline, monthly-averaged aerosol mass concentrations from the fully-coupled CACTUS Unified Model

(sections 4.2.1 and 4.2.3.3). AIE forcing is imposed by using the offline, monthly-averaged  $N_c$  fields derived from the diagnostic formulation and aerosol soluble ion concentrations (section 4.2.2) to perturb cloud optical depth, liquid water (autoconversion), and cloud forcing. The 12-month, annual cycle of both aerosol mass and  $N_c$  is repeated throughout the entire integration. The GCM is coupled with a Q-flux ocean, and the full response of the surface temperature and hydrological cycle is obtained.

The first two simulations, carried out to obtain a starting climate for the four key simulations, were integrated for 100 years using the original version of GISS III, without droplet-dependent cloud optical depth and autoconversion:

$GD_{20C}$  — present-day equilibrium climate accounting for GHG and anthropogenic aerosol direct effect at present-day levels;

$GD_{21C}$  — year 2100 equilibrium climate accounting for GHG and anthropogenic aerosol direct effect at year 2100 levels.

The final-year climate from each of these 100-year simulations is used as the starting point for the following four 30-year equilibrium climate runs, containing the droplet-dependent processes:

$GD_{20C}I_{20C}$  — present-day equilibrium climate accounting for GHG and anthropogenic aerosol direct and indirect effects at present day levels (offline  $N_c$  values corresponding to present-day aerosol levels);

$GD_{20C}I_{PI}$  — equilibrium climate accounting for GHG and anthropogenic aerosol direct effect at present day levels and aerosol indirect effects at pre-industrial levels (offline  $N_c$  values corresponding to pre-industrial aerosol levels);

$GD_{20C}I_{21C}$  — equilibrium climate accounting for GHG and anthropogenic aerosol direct effect at present day levels, and aerosol indirect effects at year 2100 levels (offline  $N_c$  values corresponding to year 2100 aerosol levels);

$GD_{21C}I_{21C}$  — year 2100 equilibrium climate accounting for GHG, and anthropogenic aerosol direct and indirect effects at year 2100 levels (offline  $N_c$  values corresponding to year 2100 aerosol levels).

Statistics over the last 20 years of each of the above equilibrium climates are determined. Differences between the simulations are analyzed as follows:

$GD_{20C}$  vs.  $GD_{20C}I_{20C}$  — the effect of incorporating explicit droplet-dependent autoconversion and optical depth and offline  $N_c$  values on present-day equilibrium climate (section 4.4.1);

$GD_{20C}I_{20C}$  vs.  $GD_{20C}I_{PI}$  — differences in equilibrium climate and perturbation in cloud forcing owing only to changes in  $N_c$  between pre-industrial and present day (section 4.4.2);

$GD_{20C}I_{21C}$  vs.  $GD_{20C}I_{20C}$  — differences in equilibrium climate and perturbation in cloud forcing owing only to changes in  $N_c$  between present day and year 2100 (section 4.4.3), and

$GD_{21C}I_{21C}$  vs.  $GD_{20C}I_{20C}$  — differences in equilibrium climate between present day and year 2100 accounting for changes in GHG and anthropogenic aerosol direct and indirect effects (section 4.5).

When differentiating each pair of the simulations, the two-sample “usual” t-test was applied to calculate the 95% confidence intervals [Zwiers and von Storch, 1995; Chen *et al.*, 2007] (see footnote in Table 4.6). The results reported in sections 4.4 and 4.5 are statistically significant, unless otherwise explicitly noted.

To make a relevant comparison with estimated AIE radiative forcing values reported in the literature, separate 5-year forcing calculations with prescribed SST (climatology of year 1946 to 1955) and parallel radiation and stratiform cloud schemes in GISS III were also carried out, and the instantaneous forcing in each simulation relative to present day is reported in Table 4.3.

The AIE forcing in this work, as determined by the instantaneous change in TOA net cloud forcing, is  $-1.75 \text{ W m}^{-2}$  as a result of perturbation of  $N_c$  from pre-industrial to present day, a value that lies within the range in the literature ( $-0.29$  to  $-2.41 \text{ W m}^{-2}$ ). For perturbation of  $N_c$  from present day to year 2100, the predicted AIE forcing at TOA is  $-0.81 \text{ W m}^{-2}$ . Note that the estimated forcing between present day to year 2100 is ~46% of the forcing between pre-industrial to present day, although the predicted increase in aerosol mass column (Table 4.2) is of comparable magnitude in each period ( $+4.39 \text{ mg m}^{-2}$  between PI and 20C,  $+4.13 \text{ mg m}^{-2}$  between 20C and 21C). The explanation is as follows. The value of  $N_c$  is correlated with aerosol soluble mass by the power law in Equation (4-1). Since the coefficient  $B$  in Equation (4-1) is mostly between 0.5 and 1.0,

the increase in predicted  $N_c$  is therefore less dramatic than the increase in aerosol column mass. As seen in Figures 4.4a and 4.4b, the predicted increase in annual mean near-surface  $N_c$  value is  $101.8 \text{ cm}^{-3}$  from PI to 20C, but only  $58.8 \text{ cm}^{-2}$  from 20C to 21C. In addition, the radiative forcing associated with the indirect effect also depends on the spatial distribution of cloud fraction, as well as the sensitivity of cloud forcing to the perturbation of  $N_c$  values. As seen in the global maps of predicted AIE radiative forcing at TOA in Figures 4.4c and 4.4d, the pattern of AIE forcing is not directly related to the pattern of  $N_c$  perturbations, but having a more complicated spatial distribution related to cloud forcing.

The radiative forcings at the tropopause estimated to result from GHG and ADE between present and year 2100 in the simulations are  $+6.47 \text{ W m}^{-2}$  and  $+0.12 \text{ W m}^{-2}$ , respectively (Table 4.3), as determined by the instantaneous change in net radiative fluxes at the tropopause (without adjustment in stratospheric temperature); these values are close to those reported in *Chen et al.* [2007] ( $+6.58 \text{ W m}^{-2}$  for GHG and  $+0.18 \text{ W m}^{-2}$  for ADE), which were derived using the 9-layer GISS GCM II' with identical offline aerosol fields and similar GHG levels to the present work.

## 4.4 Responses of the Equilibrium Climate to Perturbations of

$N_c$

### 4.4.1 Predicted Present-Day Equilibrium Climate

Comparing simulations  $GD_{20C}$  vs.  $GD_{20C}I_{20C}$ , it is found that (Table 4.4) replacement of the autoconversion scheme results in a smaller ( $-8.3\%$ ) global annual mean LWP,

which leads to a higher ( $+1.02 \text{ W m}^{-2}$ ) surface shortwave (SW) flux, whereas the differences in predicted global annual mean surface temperature, cloud cover, and precipitation are essentially negligible. The smaller present-day LWP predicted by the modified GISS III model can be explained as follows. The offline, present-day  $N_c$  values imposed on the modified model are on average larger than the constant values of  $N_c$  implicitly assumed in the standard model in the calculation of cloud optical depth (section 4.2.3.1). This change alone causes the predicted stratiform clouds to be more reflective in the modified model. Since the new autoconversion scheme (section 4.2.3.2) was tuned to match the overall TOA radiation balance of the standard model, the tuning eventually results in a lower LWP to compensate for the previous effect.

Table 4.5 and Figure 4.5 compare several key cloud properties between the predicted present-day equilibrium climate with AIE-related processes,  $GD_{20C}I_{20C}$ , and satellite-retrieved climatology. The remote sensing instruments, observational periods, and related references are given in the table footnotes. Note that exact agreement is not expected because of different time periods as well as the fact that the simulation is an equilibrium climate corresponding to present-day forcing, whereas the data reflect the actual transient climate. Thus, the general latitudinal distributions of the variables are of most interest. The predicted zonal distributions of annual mean column-integrated  $N_c$  and cloud-top  $r_e$  for warm clouds are shown in Figures 4.5a and 4.5b, respectively, with the retrievals in *Han et al.* [1998] and *Han et al.* [1994] based on data of International Satellite Cloud Climatology Project (ISCCP). To ensure proper comparison with the satellite data, the predicted values are taken only from cloudy regions with cloud-top temperature higher than 273 K. Over the Southern Hemisphere (SH) and the Tropics, the predicted values

agree well with the retrievals, while in heavily polluted areas in mid- and high latitudes over the Northern Hemisphere (NH), the model predicts higher  $N_c$  values and smaller droplet sizes. The predicted zonal annual mean total cloud fraction is compared with the ISCCP D2 climatology [Rossow and Schiffer, 1999] in Figure 4.5c. The predicted total cloud fraction distribution generally agrees with the satellite data, with an underestimation of around 10% (absolute value) over midlatitudes and an overestimation of 10–30% in the polar regions. Figure 4.5d shows the zonal mean shortwave and longwave TOA cloud forcing (CF). While the predicted longwave cloud forcing matches well the observations of the Earth Radiation Budget Experiment (ERBE) [Kiehl and Trenberth, 1997], the model-derived shortwave cloud forcing exhibits a negative bias over the Tropics, and a positive bias in mid- to high latitudes in both hemispheres.

Table 4.5 lists the corresponding global mean values reported in several modeling studies focusing on AIE. Predictions of  $N_c$ ,  $r_e$ , and cloud forcing in simulation  $GD_{20c}I_{20c}$  generally fall within the range of previous studies. Although LWP is overestimated in the present work when compared to both observation and previous predictions, one should note the uncertainties involved in the retrieval of this variable, the difference in cloud schemes and aerosol treatments used in various global models, and the fact that the present-day equilibrium climate is about 0.6 K warmer than the actual climate [IPCC, 2007].

## 4.4.2 Effects of Change of $N_c$ from Pre-Industrial to Present Day on Equilibrium Climate

In this section, the equilibrium climate response to the AIE perturbation from pre-industrial to present day is analyzed, by comparing simulations  $GD_{20C}I_{20C}$  and  $GD_{20C}I_{PI}$ . In both simulations, the GHG and ADE forcing are fixed at the present-day level, while offline  $N_c$  fields for pre-industrial and present-day conditions are imposed respectively in each simulation. The changes in key climate variables ( $GD_{20C}I_{20C} - GD_{20C}I_{PI}$ ) are summarized in Figures 4.6 and 4.7 and the first column in Tables 4.6 and 4.7.

The maximum increase of  $N_c$  in liquid stratiform clouds (+100 to +400  $\text{cm}^{-3}$ ) is predicted to occur over  $30^\circ$ – $60^\circ\text{N}$ , from the surface to 700 hPa, as shown in the latitude-pressure profile in Figure 4.6a. The latitudinal distribution of changes in  $N_c$  at 850 hPa in Figure 4.7a reveals that the estimated increase in  $N_c$  is more pronounced in June-July-August (JJA, dotted line), and located at higher latitudes, than the increase in December-January-February (DJF, gray solid line). Over the region of maximal  $N_c$  increase, autoconversion rates are predicted to decrease, which leads to increased total (liquid plus ice) cloud water mixing ratio (+1 to +3 ppm) in the low and mid-troposphere in NH, as shown in Figure 4.6b. For the change in droplet size, the effect of larger  $N_c$  dominates that of increased cloud water, as the predicted  $r_e$  in warm stratiform cloud decreases by more than 1  $\mu\text{m}$  (Figure 4.6c). The estimated change in cloud cover is small (< 2% of absolute amount in all latitudes) for both stratiform and convective clouds, and therefore is not shown.

As a result of increased cloud optical depths associated with smaller droplet size and higher cloud water in warm stratiform clouds, negative changes in TOA SW CF of  $-2$  to  $-5 \text{ W m}^{-2}$  are predicted over  $30^{\circ}$ – $60^{\circ}$ N (Figure 4.7b). The change in cloud properties results in a predicted global cooling at the surface of  $-1.00 \text{ K}$ , leading to a climate sensitivity of  $+0.55 \text{ K m}^2 \text{ W}^{-1}$ . Figures 4.6d and 4.6e show that the predicted cooling leads to a decrease in atmospheric water vapor by reducing surface evaporation. The maximum cooling near the tropical tropopause is a result of vertical temperature convective adjustment toward the moist adiabatic lapse rate; the pattern is similar to the simulated global warming owing to increased GHG [Manabe and Wetherald, 1975], but with an opposite sign. As displayed in Figures 4.6g and 4.7c, the surface temperature is reduced more significantly in NH and over land ( $-1.3 \text{ K}$ ), with a prominent cooling over the northern middle to high latitudes. Over  $30^{\circ}$ – $60^{\circ}$ N, the surface cooling is predicted to be more substantial in JJA; this is also the season of maximum  $N_c$  increase and TOA SW CF decrease, indicating that the cooling is a direct response to perturbation of  $N_c$ . North of  $60^{\circ}$ N, however, the most significant cooling is estimated to occur in DJF, when the change in  $N_c$  and TOA SW CF is relatively small. This pattern of predicted temperature response is similar to those found in previous studies investigating present-day AIE impacts [Rotstayn *et al.*, 2000; Williams *et al.*, 2001; Rotstayn and Lohmann, 2002; Kristjánsson *et al.*, 2005].

The amplification and the difference in the seasons of peak forcing and surface temperature in the northern high latitudes are likely related to ice-albedo feedback as well as feedback mechanisms involving sea ice, ocean-atmosphere heat exchange, and atmospheric dynamics, as analyzed in Williams *et al.*, [2001] and Kristjánsson *et al.*

[2005]. The reduction in solar insolation in JJA results in less summer and autumn melting of sea ice, and the heat flux from ocean to atmosphere therefore decreases. The resulting surface cooling then leads to an increase in surface pressure and the development of an anticyclone flow in autumn, which impedes the warm advection from cyclone activities and causes a strong cooling in winter. A significant increase in sea level pressure of 2 to 3 hPa in autumn and winter, as well as a southward shift in the Pacific storm track, is also predicted in this study (not shown), consistent with the findings in the previous studies cited above. Note that the previous studies have predicted a more prominent polar amplification, which is likely associated with the difference in sea ice models, and the fact that aerosol concentrations were predicted interactively in those studies. However, considering the uncertainties in predicted sea ice and insufficient knowledge of the radiative impact of polar stratiform clouds, the actual mechanism of polar response to AIE requires more detailed studies.

A clear response in global circulation to the large inter-hemispheric difference in surface cooling is predicted, as revealed by the changes in zonal mean mass stream function in Figure 4.6f. The more substantial cooling in the NH induces an anomalous clockwise flow over the Tropics between 20°S and 20°N, and a southward displacement of the ITCZ is therefore predicted, which manifests itself by the change of distribution of precipitation in Figures 4.6h and 4.6d. Note that the response of the global circulation also feeds back to the predicted cloud forcing and cloud water. The shift of the ITCZ contributes to the reduction in TOA SW CF (Figure 4.7b, around  $-3 \text{ W m}^{-2}$ ) and the increased tropospheric cloud water mixing ratio (Figure 4.6b, +0.1 to +3 ppm) between 900–400 hPa over 0°–30°S, associated with stronger convection in this region. Around

400 hPa over the Tropics, the cloud droplet size is predicted to increase (Figure 4.6c, 0.2–1.5  $\mu\text{m}$ ), owing to the slightly higher cloud water in stratiform clouds (not shown) and the relatively small change in  $N_c$  estimated here. Note that pure liquid stratiform clouds do not frequently occur at this altitude over the Tropics, and therefore the impact of increasing droplet size should be small.

Globally, annual mean precipitation is predicted to decrease by 0.10  $\text{mm day}^{-1}$  (3.46%), especially in NH ( $-0.19 \text{ mm day}^{-1}$ ). The predicted decrease in precipitation from stratiform clouds is only 0.02  $\text{mm day}^{-1}$ , and the precipitation reduction is mostly a result of weakened convection, owing to the surface cooling. The weaker convection also leads to decreased cloud water in mid-troposphere over high latitudes and mid- to high troposphere over the Tropics (Figure 4.6b). The overall effects of all the feedbacks lead to an increase in global mean LWP in stratiform cloud ( $+0.70 \text{ g m}^{-2}$ ) but a slight decrease in total LWP ( $-0.64 \text{ g m}^{-2}$ ). The global mean change in TOA net CF is  $-1.42 \text{ W m}^{-2}$ . The time evolution of the differences in cloud forcing (not shown) between simulations shows that the SW component gradually becomes less negative and the LW component becomes less positive. Because cloud forcing is negative in SW and positive in LW, this evolution points to a slight cloud thinning during the course of the integration. The fact that the predicted change in CF at equilibrium is about 81% of the imposed instantaneous TOA forcing (Table 4.3) indicates a negative cloud feedback. Both the cloud thinning and the negative cloud feedback are similar to the reported finding in *Kristjánsson et al.* [2005].

In general, a slower hydrological cycle is predicted in response to the perturbation of  $N_c$  from pre-industrial to present day. The hydrological sensitivity, defined as the percentage change in global total precipitation normalized by global surface temperature

change, is  $3.46 \% \text{ K}^{-1}$  (Table 4.7), similar to the value reported in *Feichter et al.* [2004] for AIE ( $3.9 \% \text{ K}^{-1}$ ). Note that the value of hydrological sensitivity is usually distinct for a specific type of forcing. For example, *Feichter et al.* [2004] calculated a hydrological sensitivity of  $1.5 \% \text{ K}^{-1}$  from equilibrium response to GHG forcing alone, and the hydrological sensitivity from the multi-model ensemble average reported in *IPCC* [2007], as a transient response to GHG and all other forcings with the A2 scenario, is  $1.45 \% \text{ K}^{-1}$  for year 2080 to 2099.

#### **4.4.3 Perturbations of $N_c$ from Present Day to Year 2100 to Equilibrium Climate**

The equilibrium climate response to the AIE perturbation from present day to year 2100 is diagnosed here, by comparing simulations  $GD_{20C}I_{21C}$  and  $GD_{20C}I_{20C}$ . Present-day GHG and ADE forcings are used in both simulations, while the imposed  $N_c$  values in each simulation are for present-day and year 2100, respectively. The results ( $GD_{20C}I_{21C} - GD_{20C}I_{20C}$ ) are presented in Figures 4.8 and 4.9 and the second column of Tables 4.6 and 4.7.

In NH, the predicted  $N_c$  increase from present day to year 2100 is smaller than that from pre-industrial to present day, and the inter-hemispheric contrast is not as great. Over NH high latitudes,  $N_c$  is predicted to slightly decrease ( $-15$  to  $-20 \text{ cm}^{-3}$ ) in JJA (Figures 4.8a and 4.9a), corresponding to the estimated reduction in sulfate aerosols in this region [*Chen et al.*, 2007]. Also, the latitude of peak increase in  $N_c$  is predicted to shift southward to  $30^\circ\text{N}$ .

The changes in  $N_c$  lead to a slight increase in total cloud water (+0.1 to +0.5 ppm) and a decrease in  $r_e$  in warm stratiform clouds ( $-0.2$  to  $-0.5 \mu\text{m}$ ) in the lower troposphere (Figures 4.8b and 4.8c). The response in cloud cover is, again, insensitive to the perturbation in  $N_c$ . The predicted global mean surface cooling is  $-0.28 \text{ K}$ , with a symmetric and flat latitudinal distribution (Figures 4.8d, 4.8g, and 4.9c), and a corresponding climate sensitivity of  $+0.33 \text{ K m}^2 \text{ W}^{-1}$ . The maximum cooling near the tropical tropopause associated with water vapor feedback is still evident.

The response in general circulation to the pattern of predicted surface cooling is mostly insignificant. A sinking motion is induced over the Tropics (Figure 4.8f), leading to a suppression in annual mean precipitation by as much as  $0.2 \text{ mm day}^{-1}$  (Figure 4.8h and 4.9d), and a small reduction of cloud water in mid- to high troposphere (Figure 4.8b). The predicted global mean precipitation reduction from present day to year 2100 is  $0.03 \text{ mm day}^{-1}$  (1.04%). The predicted global mean LWP also exhibits a decrease ( $-0.62 \text{ g m}^{-2}$ ). The modeled change in TOA net CF is  $-0.28 \text{ W m}^{-2}$ , about 35% of the imposed instantaneous forcing, while a similar but weaker negative cloud feedback is also found in the time evolution of the TOA cloud forcing during the simulation. Note that although the predicted AIE forcing here is much smaller than that from pre-industrial to present day, the calculated hydrological sensitivity is  $3.71 \% \text{ K}^{-1}$ , close to that computed in the previous section, indicating that the response of the hydrological cycle to AIE forcing in GISS III is likely characterized by a value of hydrological sensitivity larger than 3.0.

## 4.5 Predicted Equilibrium Climate Response From Present Day to Year 2100 to the Combined Effects of GHG, ADE and AIE

Simulations  $GD_{21C}I_{21C}$  and  $GD_{20C}I_{20C}$  are compared in this section. Year 2100 GHG, offline aerosol fields and  $N_c$  fields were used in  $GD_{21C}I_{21C}$ , while those for present-day condition were used in  $GD_{20C}I_{20C}$ . The differences between the equilibrium climates ( $GD_{21C}I_{21C} - GD_{20C}I_{20C}$ ), revealing the response to the combined forcing of GHG, ADE, and AIE from present day to year 2100, are outlined in Figures 4.10 and 4.11 and the third column of Tables 4.6 and 4.7.

The changes in  $N_c$  are similar to those in section 4.4.3 and hence not displayed. As expected, the general pattern of the response is largely dominated by the GHG-induced warming. The increase of equilibrium global surface temperature from present day to year 2100 is predicted to be 4.59 K, leading to a climate sensitivity of  $+0.80 \text{ K m}^2 \text{ W}^{-1}$ . The warming is prominently amplified in polar regions by snow and ice albedo feedback and near the tropical tropopause through moist adiabatic adjustment (Figures 4.10b, 4.10d, and 4.11a). Although atmospheric water vapor increases considerably owing to enhanced surface evaporation (Figure 4.10c), saturation vapor pressure is also enhanced by increased temperature, following the Clausius-Clapeyron relationship. While the global averages of total LWP and stratiform liquid water are predicted be enhanced by 19.90 and 3.41  $\text{g m}^{-2}$ , the total cloud water is predicted to decrease in low and mid-troposphere, as seen in Figure 4.10a, because of the dominant effect of increased saturation vapor pressure. On the other hand, the increase in cloud water around the

tropical tropopause and mid-troposphere in high latitudes is a result of changed atmospheric circulation. A broadening and weakening of the Hadley cell is revealed in the predicted difference in mass stream function (Figure 4.11d) and in excess precipitation (total precipitation minus evaporation, Figure 4.11b); only the ascending branches in the convection zone (at 5°N in JJA and at 5°S in DJF) near the Equator are strengthened. In addition, the increased moisture is transported by midlatitude eddies from sub-tropics to mid- and high latitudes, resulting in the increase in excess precipitation and mid-tropospheric cloud water.

It is of interest to compare this present day to year 2100 equilibrium climate response to that predicted by the standard version of GISS III (i.e.,  $[GD_{21C} - GD_{20C}]$  vs.  $[GD_{21C}I_{21C} - GD_{20C}I_{20C}]$ ). According to Table 4.8, the modified GISS III, which incorporates AIE-related stratiform clouds, predicts a slightly weaker warming (4.59 K vs. 4.88 K), less precipitation increase (0.23 mm day<sup>-1</sup> vs. 0.32 mm day<sup>-1</sup>), and smaller reduction of absolute cloud cover (-2.11% vs. -2.47%). The most pronounced difference between the predicted responses is the reversed sign in the change of stratiform cloud precipitation: -0.04 mm day<sup>-1</sup> in the modified GISS III vs. +0.04 mm day<sup>-1</sup> in the standard GISS III. Figures 4.11c and 4.12c show that the standard model predicts minimal change of stratiform precipitation over Tropics and sub-Tropics, in contrast to the predicted decrease of stratiform precipitation of 0.2 to 0.3 mm day<sup>-1</sup> in the modified model over the same regions. This reveals the impact of the AIE on suppressing stratiform precipitation, which causes a small but notable decrease in global hydrological sensitivity from 2.27 % K<sup>-1</sup> in the standard version to 1.73 % K<sup>-1</sup> in the modified version (Table 4.8). The predicted climate sensitivity (+0.80 K m<sup>2</sup> W<sup>-1</sup> vs. +0.74 K m<sup>2</sup> W<sup>-1</sup>), as well as the

predicted latitudinal distributions of temperature, precipitation, and circulation changes, are similar in both versions (Figures 4.11 and 4.12).

## **4.6 Climate Sensitivities and Hydrological Sensitivities for ADE, AIE, and GHG: Comparing the Present work with Previous Related Studies**

It is of interest to compare the climate response and sensitivity for AIE forcing from present day to year 2100 estimated in the present study with those reported in two related studies focusing on ADE and GHG forcing, as given in Table 4.9. Simulations in all of the three studies were carried out using different versions of the GISS GCM, with emissions and GHG levels based on SRES A2, and with the assumption of internal aerosol mixtures for ADE. Since the model physics, the length of integrations, and number of years for statistical analyses are different in these three studies, for climate sensitivity and the hydrological sensitivity, only qualitative comparisons are addressed below.

*Chen et al.* [2007] simulated the equilibrium climate response to ADE and GHG from present day to year 2100 with the GISS II' GCM. The length of integration was 80 years, and the results over the last 30 years were diagnosed. The present-day and year 2100 offline aerosol fields used in that study are very similar to those in the present work (before interpolation from 9 to 23 vertical layers). The predicted climate sensitivity in *Chen et al.* [2007], which is the ratio of equilibrium global surface temperature response to the imposed instantaneous forcing at tropopause, is  $0.78 \text{ K m}^2 \text{ W}^{-1}$  for ADE, and 0.81

$\text{K m}^2 \text{W}^{-1}$  for GHG. The present study derives a climate sensitivity of  $0.33 \text{ K m}^2 \text{W}^{-1}$  for AIE forcing alone from present day to year 2100. From the standard GISS III the corresponding climate sensitivity is  $0.74 \text{ K m}^2 \text{W}^{-1}$  for combined forcing of GHG and ADE forcing, while from the modified GISS III the climate sensitivity is  $0.80 \text{ K m}^2 \text{W}^{-1}$  for combined forcing of GHG, ADE, and AIE. The comparison suggests that the climate efficacy, which is the ratio of climate sensitivity over that to a doubling of  $\text{CO}_2$  [Hansen *et al.*, 2005], likely falls in the range of 0.5–0.7 for AIE forcing, while that for ADE forcing is likely close to or slightly less than unity. When the forcings of GHG, ADE, and AIE are imposed simultaneously, the climate sensitivity is largely dominated by the effects of GHG. We note that the above conclusions may be applied to only GISS GCM II' and GISS III, as the sensitivity and climate efficacy predicted by other GCMs can be significantly different.

For hydrological sensitivity, the values reported in *Chen et al.* [2007] is  $-7.34 \% \text{ K}^{-1}$  for ADE and  $+2.19 \% \text{ K}^{-1}$  for GHG. Note that the predicted hydrological sensitivity is negative for ADE. This is a result of the fact that the predicted global mean surface warming ( $+0.14 \text{ K}$ ) in response to ADE forcing is a result of regional cooling (in areas with substantial increase in scattering aerosols) offset by regional warming (due to internally-mixed absorbing aerosols over highly reflective surfaces), while the global mean precipitation, especially convective precipitation, is slightly suppressed ( $-1.03\%$ ) owing to the dominant effects of evaporation reduction and lower tropospheric stability enhancement in regions exhibiting surface cooling. *Liao et al.* [2008] performed two fully-coupled chemistry-aerosol-climate calculations, one with GHG and emissions of aerosol and precursors fixed at present-day levels and the other at year 2100 levels;

therefore, the overall climatic impacts from ADE plus GHG were simulated interactively for 35 years. The predicted equilibrium global surface temperature and precipitation responses (averages from the last 20 years) are 6.0 K and 9.0%, respectively, which lead to a hydrological sensitivity of  $1.5 \text{ \% K}^{-1}$  for the fully-coupled response to ADE and GHG changes from present day to year 2100. The present study predicts a hydrological sensitivity of  $3.71 \text{ \% K}^{-1}$  for AIE forcing alone, a value that is distinct from those for ADE and GHG. The hydrological sensitivity of  $1.73 \text{ \% K}^{-1}$  for combined forcing of GHG, ADE, and AIE in the modified GISS III is closer to that derived from the fully-coupled simulations with GHG and ADE impacts in *Liao et al.* [2008]. This suggests that both the direct and indirect aerosol effects may partly counteract the enhancement of the hydrological cycle owing to the warming of GHG [*Feichter et al.*, 2004]. Deriving the climate sensitivity and hydrological sensitivity for combined impacts of GHG, ADE, and AIE with interactive aerosols and cloud droplets is highly desirable.

## 4.7 Summary and Conclusions

To investigate the climatic impacts of aerosol indirect effects with GISS III GCM, explicit dependence on  $N_c$  has been introduced to the formulations of optical depth and autoconversion rates for liquid stratiform clouds in the GCM, to account for both cloud albedo and lifetime effects. Fully-coupled chemistry-aerosol-climate simulations with the CACTUS Unified Model have been carried out to obtain offline aerosol mass concentrations. Additionally, using simulations with the GISS-TOMAS microphysics model and the FN CCN activation parameterization, grid-by-grid correlations between aerosol soluble ion concentration and  $N_c$  have been established. The diagnostic

correlations have been applied to the aerosol mass predicted in the Unified Model to compute corresponding offline  $N_c$  fields.

Two 100-year simulations using the standard GISS III have been carried out, each with GHG and aerosol direct forcing from offline aerosol mass for present day or year 2100, to provide starting climates for the four equilibrium climate simulations using the GISS III with AIE-related implementation, each integrated for 30 years. By imposing offline monthly averaged  $N_c$  for PI, present day, and year 2100 in each simulation, the climate responses to the perturbations of  $N_c$  have been analyzed. The general patterns of the climate responses are summarized below and in Table 4.10.

The perturbation of  $N_c$  from pre-industrial to present day is predicted to cause an equilibrium global surface cooling of 0.95 K, with maximum cooling at the NH high latitudes. The polar amplification is characterized by a time shift between the seasons of maximum forcing and maximum response, which is partly a result of the feedback mechanisms involving sea ice extent, ocean-atmospheric exchange, and atmospheric dynamics. The predicted inter-hemispheric temperature gradient induces an anomalous flow between 20°S and 20°N, which displaces the ITCZ southward. The predicted change in TOA net CF is  $-1.42 \text{ W m}^{-2}$ . The equilibrium global mean precipitation reduction is  $0.10 \text{ mm day}^{-1}$ , with a corresponding hydrological sensitivity of  $3.46 \% \text{ K}^{-1}$ . The results are consistent with previous GCM studies on pre-industrial to present day AIE forcing.

The perturbation of  $N_c$  from present day to year 2100, which is weaker in magnitude and has different latitudinal distribution than that from pre-industrial to present day, results in a smaller decrease of 0.28 K in predicted global surface temperature, with small

inter-hemispheric contrast. The response in precipitation and general circulation is weak; only convection between 5°S and 5°N is predicted to be suppressed, and the location of the ITCZ does not show a significant shift. A small change in TOA net CF of  $-0.28 \text{ W m}^{-2}$  is estimated. The hydrological sensitivity for AIE forcing from present day to year 2100 has a similar value of  $3.71 \% \text{ K}^{-1}$ , indicating that the response of the hydrological cycle to AIE forcing is distinct from those to GHG and ADE forcing.

In general, the simulated equilibrium climate response to the combined forcing of GHG, ADE, and AIE from present day to year 2100, dominated by GHG warming effects, agrees with previous GCM studies, with a global temperature increase of 4.59 K, maximized warming in polar regions and the tropical tropopause, broadened Hadley cell, and enhanced precipitation in the tropical convection zone and mid to high latitudes. The inclusion of AIE-related processes in the modified version of GISS III leads to a decrease in predicted stratiform precipitation and a hydrological sensitivity of  $1.73 \% \text{ K}^{-1}$ , as compared to the increase in stratiform precipitation and the higher hydrological sensitivity of  $2.27 \% \text{ K}^{-1}$  predicted by the standard model.

Comparison with results in *Chen et al.* [2007] and *Liao et al.* [2008] suggests that the GISS II' GCM and GISS III predict a smaller climate efficacy of 0.5–0.7 for AIE forcing from present day to year 2100, and lower than that for ADE forcing. The hydrological sensitivity corresponding to AIE forcing is positive and relatively higher than that for GHG forcing, while the ADE forcing, based on *Chen et al.* [2007], is predicted to lead to a negative hydrological sensitivity. The direct and indirect effects of the aerosols may therefore partly cancel out the enhancement in the hydrological cycle owing to GHG-induced warming.

Finally, we note that offline aerosols and droplet number concentrations have been used in the present study. Although the aerosol mass was derived by the fully coupled model, in the equilibrium climate calculations, the feedbacks of temperature, precipitation, cloud, and transport on distribution of aerosol and droplet number were not accounted for. A global model with the full coupling between tropospheric chemistry, aerosols, clouds, and climate is currently under development, and will be applied in future studies.

**Acknowledgment.** This work is supported by the National Aeronautics and Space Administration (NASA) Earth Observing System Interdisciplinary Science Program (EOS-IDS) and NASA grant NNX08AL85G. Hong Liao is supported by National Natural Science Foundation of China (Grants 90711004 and 40775083) and by National Basic Research Program of China (Grant No. 2006CB403706). The authors thank Prof. Qingyuan Han for providing the retrieval data for column cloud droplet concentration and effective droplet radius.

## References

- Adams, P. J., and J. H. Seinfeld (2002), Predicting global aerosol size distributions in general circulation models, *J. Geophys. Res.*, *107*, D19, doi:10.1029/2001JD001010.
- Boucher, O., and U. Lohmann (1995), The sulfate-CCN-cloud albedo effect - A sensitivity study with 2 general circulation models, *Tellus B*, *57*, 281–300.
- Chen, W.-T., H. Liao, and J. H. Seinfeld (2007), Future climate impacts of direct radiative forcing of anthropogenic aerosols, tropospheric ozone, and long-lived greenhouse gases, *J. Geophys. Res.*, *112*, D14209, doi:10.1029/2006JD008051
- Chung, S. H., and J. H. Seinfeld (2002), Global distribution and climate forcing of carbonaceous aerosols, *J. Geophys. Res.*, *107*, D19, doi:10.1029/2002JD001397.
- d’Almeida, G. A., P. Koepke, and E. P. Shettle (1991), *Atmospheric Aerosol: Global Climatology and Radiative Characteristics*, edited, A. Deepak Pub., Hampton, Va.
- Del Genio, A. D., M.-S. Yao, W. Kovari, and K. K.-W. Lo (1996), A prognostic cloud water parameterization for global climate models, *J. Clim.*, *9*, 2, 270–304.
- Dufresne, J.-L., J. Quaas, O. Boucher, S. Denvil, and L. Fairhead (2005), Contrasts in the effects on climate of anthropogenic sulfate aerosols between the 20th and the 21st century, *Geophys. Res. Lett.*, *32*, L21703, doi:10.1029/2005GL023619.
- Feichter, J., E. Roeckner, U. Lohmann, and B. Liepert (2004), Nonlinear aspects of the climate response to greenhouse gas and aerosol forcing, *J. Clim.*, *17*, 2384–2398.
- Fountoukis, C., and A. Nenes (2005), Continued development of a cloud droplet formation parameterization for global climate models, *J. Geophys. Res.*, *110*, D11.
- Fountoukis, C., A. Nenes, N. Meskhidze, R. Bahreini, G. Buzorius, W. C. Conant, H. Jonsson, S. Murphy, A. Sorooshian, V. Varutbangkul, R. C. Flagan, and J. H. Seinfeld (2007), Aerosol - cloud drop concentration closure for clouds sampled during ICARTT, *J. Geophys. Res.*, *112*, D10S30, doi:10.1029/2006JD007272
- Greenwald, T. J., G. L. Stephens, T. H. Vonder Haar, and D. L. Jackson (1993), A physical retrieval of cloud liquid water over the global oceans using Special Sensor Microwave/Imager (SSM/I) observations, *J. Geophys. Res.*, *98*, 18471–18488.
- Griffin, R. J., D. R. Cocker, R. C. Flagan, and J. H. Seinfeld (1999a), Organic aerosol formation from the oxidation of biogenic hydrocarbons, *J. Geophys. Res.*, *104*, D3, 3555–3567.

- Griffin, R. J., D. R. Cocker, J. H. Seinfeld, and D. Dabdub (1999b), Estimate of global atmospheric organic aerosol from oxidation of biogenic hydrocarbons, *Geophys. Res. Lett.*, *26*, 17, 2721–2724.
- Han, Q., W. B. Rossow, J. Chou, and R. M. Welch (1998), Global variation of column droplet concentration in low-level clouds, *Geophys. Res. Lett.*, *25*, 1419–1422.
- Han, Q., W. B. Rossow, and A. A. Lacis (1994), Near-global survey of effective droplet radii using ISCCP data, *J. Clim.*, *7*, 465–497.
- Hansen, J., M. Sato, and R. Ruedy (1997), Radiative forcing and climate response, *J. Geophys. Res.*, *102*, D6, 6831–6864.
- Hansen, J., M. Sato, R. Ruedy, L. Nazarenko, A. Lacis, G. A. Schmidt, G. Russell, I. Aleinov, M. Bauer, S. Bauer, N. Bell, B. Cairns, V. Canuto, M. Chandler, Y. Cheng, A. Del Genio, G. Faluvegi, E. Fleming, A. Friend, T. Hall, C. Jackman, M. Kelley, N. Kiang, D. Koch, J. Lean, J. Lerner, K. Lo, S. Menon, R. Miller, P. Minnis, T. Novakov, V. Oinas, J. Perlwitz, J. Perlwitz, D. Rind, A. Romanou, D. Shindell, P. Stone, S. Sun, N. Tausnev, D. Thresher, B. Wielicki, T. Wong, M. Yao, and S. Zhang (2005), Efficacy of climate forcings, *J. Geophys. Res.*, *110*, D18104, doi:10.1029/2005JD005776.
- Hoose, C., U. Lohmann, R. Bennartz, B. Croft, and G. Lesins (2008), Global simulations of aerosol processing in clouds, *Atmos. Chem. Phys. Discuss.*, *8*, 13555–13618.
- Hsieh, W. C., H. Jonsson, G. Buzorius, R. C. Flagan, J. H. Seinfeld, and A. Nenes (2008), On the representation of droplet coalescence and autoconversion: Evaluation using ambient cloud droplet size distributions submitted.
- IPCC (2007), *Climate Change 2007: The Physical Science Basis*, edited by S. Solomon et al., Cambridge University Press, Cambridge, United Kingdom and New York, NY, USA.
- Khairoutdinov, M., and Y. Kogan (2000), A new cloud physics parameterization in a large-eddy simulation model of marine stratocumulus, *Mon. Weather. Rev.*, *128*, 1, 229–243.
- Kiehl, J. T., and K. Trenberth (1997), Earth's annual global mean energy budget, *Bull. Amer. Meteorol. Soc.*, *78*, 197–208.
- Kristjánsson, J. E., T. Iversen, A. Kirkevåg, Ø. Seland, and J. Debernard (2005), Response of the climate system to aerosol direct and indirect forcing: Role of cloud feedbacks, *J. Geophys. Res.*, *110*, D24206, doi:10.1029/2005JD006299.
- Liao, H., P. J. Adams, S. H. Chung, J. H. Seinfeld, L. J. Mickley, and D. J. Jacob (2003), Interactions between tropospheric chemistry and aerosols in a unified general circulation model, *J. Geophys. Res.*, *108*, D1, 4001, doi:10.1029/2001JD001260.

- Liao, H., W.-T. Chen, and J. H. Seinfeld (2006), Role of climate change in global predictions of future tropospheric ozone and aerosols, *J. Geophys. Res.*, *111*, D12304, doi:10.1029/2005JD006852.
- Liao, H., and J. H. Seinfeld (2005), Global impacts of gas-phase chemistry-aerosol interactions on direct radiative forcing by anthropogenic aerosols and ozone, *J. Geophys. Res.*, *110*, D18208, doi:10.1029/2005JD005907.
- Liao, H., J. H. Seinfeld, P. J. Adams, and L. J. Mickley (2004), Global radiative forcing of coupled tropospheric ozone and aerosols in a unified general circulation model, *J. Geophys. Res.*, *109*, D16207, doi:10.1029/2003JD004456.
- Liao, H., Y. Zhang, W.-T. Chen, and J. H. Seinfeld (2008), Effect of chemistry-aerosol-climate coupling on predictions of future climate and future levels of tropospheric ozone and aerosols, submitted.
- Lohmann, U., P. Stier, C. Hoose, S. Ferrachat, S. Kloster, E. Roeckner, and J. Zhang (2007), Cloud microphysics and aerosol indirect effects in the global climate model ECHAM5-HAM, *Atmos. Chem. Phys.*, *7*, 3425–3446.
- Manabe, S., and R. T. Wetherald (1975), Effects of doubling CO<sub>2</sub> concentration on climate of a general circulation model, *J. Atmos. Sci.*, *32*, 1, 3-15.
- Martin, G. M., D. W. Johnson, and A. Spice (1994), The measurement and parameterization of effective radius of droplets in warm stratocumulus clouds, *J. Atmos. Sci.*, *51*, 1823–1842.
- Menon, S., A. D. Del Genio, D. Koch, and G. Tselioudis (2002), GCM Simulations of the aerosol indirect effect: Sensitivity to cloud parameterization and aerosol burden, *J. Atmos. Sci.*, *59*, 3, 692–713.
- Meskhidze, N., A. Nenes, W. C. Conant, and J. H. Seinfeld (2005), Evaluation of a new cloud droplet activation parameterization with in situ data from CRYSTAL-FACE and CSTRIFE, *J. Geophys. Res.*, *110*, D16202, doi:10.1029/2004JD005703.
- Mickley, L. J., D. J. Jacob, B. D. Field, and D. Rind (2004), Climate response to the increase in tropospheric ozone since preindustrial times: A comparison between ozone and equivalent CO<sub>2</sub> forcings, *J. Geophys. Res.*, *109*, D5106, doi:10.1029/2003JD003653.
- Nenes, A., and J. H. Seinfeld (2003), Parameterization of cloud droplet formation in global climate models, *J. Geophys. Res.*, *108*, D14.
- O'Dell, C. W., F. Wentz, and R. Bennartz (2008), Cloud liquid water path from satellite-based passive microwave observations: A new climatology over the global oceans, *J. Clim.*, *21*, 1721–1739, doi:10.1175/2007JCLI1958.1.

- Peng, Y., U. Lohmann, and R. Leaitch (2005), Importance of vertical velocity variations in the cloud droplet nucleation process of marine stratus clouds, *J. Geophys. Res.*, *110*, D21213, doi:10.1029/2004JD004922.
- Penner, J. E., J. Quaas, T. Storelvmo, T. Takemura, O. Boucher, H. Guo, A. Kirkevåg, J. E. Kristjánsson, and Ø. Seland (2006), Model intercomparison of indirect aerosol effects, *Atmos. Chem. Phys.*, *6*, 3391–3405.
- Pierce, J. R., and P. J. Adams (2006), Global evaluation of CCN formation by direct emission of sea salt and growth of ultrafine sea salt, *J. Geophys. Res.*, *111*, D06203, doi:10.1029/2005JD006186, 2006.
- Quaas, J., and O. Boucher (2005), Constraining the first aerosol indirect radiative forcing in the LMDZ GCM using POLDER and MODIS satellite data, *Geophys. Res. Lett.*, *32*, L17814, doi:10.1029/2005GL023850.
- Rind, D., J. Lerner, J. Jonas, and C. McLinden (2007), Effects of resolution and model physics on tracer transports in the NASA Goddard Institute for Space Studies general circulation models *J. Geophys. Res.*, *112*, D09315, doi:10.1029/2006JD007476.
- Rossow, W. B., and R. A. Schiffer (1999), Advances in understanding clouds from ISCCP, *Bull. Amer. Meteorol. Soc.*, *80*, 2261–2287.
- Rotstayn, L. D., and U. Lohmann (2002), Tropical rainfall trends and the indirect aerosol effect, *J. Clim.*, *15*, 15, 2103–2116.
- Rotstayn, L. D., B. F. Ryan, and J. E. Penner (2000), Precipitation changes in a GCM resulting from the indirect effects of anthropogenic aerosols, *Geophys. Res. Lett.*, *27*, 19, 3045–3048.
- Sotiropoulou, R.-E. P., N. Meskhidze, J. Kouatchou, B. Das, L. Oreopoulos, J. M. Rodriguez, and A. Nenes (2008), Aerosol-cloud interactions in the NASA GMI: Model development and indirect forcing assessments for sulfate aerosol, submitted.
- Sundqvist, H., E. Berge, and J. E. Kristjánsson (1989), Condensation and cloud parameterization studies with a mesoscale numerical weather prediction model, *Mon. Weather. Rev.*, *117*, 1641–1657.
- Takemura, T., T. Nozawa, S. Emori, T. Y. Nakajima, and T. Nakajima (2005), Simulation of climate response to aerosol direct and indirect effects with aerosol transport-radiation model, *J. Geophys. Res.*, *110*, D02202, doi:10.1029/2004JD005029.
- Toon, O. B., J. B. Pollack, and B. N. Khare (1976), Optical-constants of several atmospheric aerosol species - ammonium-sulfate, aluminum-oxide, and sodium-chloride, *J. Geophys. Res.*, *81*, 33, 5733–5748.

Weng, F., N. C. Grody, R. Ferraro, A. Basist, and D. Forsyth (1997), Cloud liquid water climatology from the Special Sensor Microwave/Imager, *J. Clim.*, *10*, 1086–1098.

Williams, K. D., A. Jones, D. L. Roberts, C. A. Senior, and M. J. Woodage (2001), The response of the climate system to the indirect effects of anthropogenic sulfate aerosol, *Clim. Dynam.*, *17*, 11, 845–856.

Zwiers, F. W., and H. von Storch (1995), Taking serial-correlation into account in tests of the mean, *J. Clim.*, *8*, 2, 336–351.

Table 4-1. Global Models in This Study

Model	Horizontal Resolution	# of $\sigma$ Layers	Model Top (hPa)	Feature	Simulations Performed in This Study	Reference
CACTUS Unified Model	4° Lat by 5° Lon	9	10	Fully coupled chemistry-aerosol-climate simulations	Derivation of offline aerosols concentrations	[ <i>Liao et al.</i> , 2003; 2004; <i>Liao and Seinfeld</i> , 2005]
GISS-TOMAS	4° Lat by 5° Lon	9	10	Size-resolved aerosol and CCN concentrations	Calculation of CCN spectra for deriving $N_c$ -aerosol correlations	[ <i>Adams and Seinfeld</i> , 2002; <i>Pierce and Adams</i> , 2006]
GISS III	4° Lat by 5° Lon	23	0.002	Cloud scheme modified to include 1 <sup>st</sup> and 2 <sup>nd</sup> AIE	Equilibrium climate simulation	[ <i>Rind et al.</i> , 2007]

Table 4-2. Global Annual Burdens (Tg dry mass) of Aerosols Derived by the Caltech Unified Model.

	Pre-Industrial	Year 2000	Year 2100
Ammonium Sulfate	0.41	2.86	2.74
Ammonium Nitrate	0.22	0.67	2.88
POA	0.009	1.24	2.88
SOA	0.16	0.28	0.38
BC	0.001	0.23	0.53
Total	0.89	5.28	9.41

Table 4-3. Experimental Design of the Equilibrium Simulations with GISS III GCM

Simulation <sup>a</sup>	I.C.	GHG <sup>b</sup>	ADE <sup>c</sup>	AIE <sup>d</sup>	Years of Integration	Instantaneous Forcing Relative to Present Day <sup>e</sup>
<i>GD<sub>20C</sub></i>	Year 1950	20C	20C	—	100	—
<i>GD<sub>21C</sub></i>	Year 1950	21C	21C	—	100	+6.59 (GHG = +6.47, ADE = +0.12)
<i>GD<sub>20C</sub>I<sub>20C</sub></i>	<i>GD<sub>20C</sub></i>	20C	20C	20C	30	—
<i>GD<sub>20C</sub>I<sub>PI</sub></i>	<i>GD<sub>20C</sub></i>	20C	20C	PI	30	-1.81 (-1.75 at TOA)
<i>GD<sub>20C</sub>I<sub>21C</sub></i>	<i>GD<sub>20C</sub></i>	20C	20C	21C	30	-0.84 (-0.81 at TOA)
<i>GD<sub>21C</sub>I<sub>21C</sub></i>	<i>GD<sub>21C</sub></i>	21C	21C	21C	30	+5.75

<sup>a</sup> In the abbreviations, upper-case letters denote the forcings imposed in each simulations: G = greenhouse gases, D = aerosol direct effects, I = aerosol indirect effects; the subscripts denote the levels of the forcing: PI=pre-industrial, 20C = year 2000, 21C = year 2100. The first two simulations were carried out with the standard GISS III, while the last four simulations were performed with the modified GISS III.

<sup>b</sup> For 20C levels, CO<sub>2</sub> = 367 ppmv, CH<sub>4</sub> = 1668 ppbv, N<sub>2</sub>O = 315 ppbv, CFC-11 = 260 pptv, and CFC-12 = 520 pptv. For 21C levels, CO<sub>2</sub> = 856 ppmv, CH<sub>4</sub> = 3578 ppbv, N<sub>2</sub>O = 445 ppbv, CFC-11 = 44 pptv, and CFC-12 = 216 pptv.

<sup>c</sup> From offline, monthly imposed aerosols of internally mixed sulfate, nitrate, ammonium, BC, POA, SOA, and water.

<sup>d</sup> From offline, monthly imposed  $N_c$  in the calculation of optical depth and autoconversion in warm stratiform clouds.

<sup>e</sup> Instantaneous forcing are derived from separate five-year forcing calculations with prescribed SST and parallel cloud scheme and radiation scheme. For GHG and ADE, forcing is defined as change in net radiative flux, while for AIE, forcing is defined as changes in net cloud forcing (i.e., clear-sky minus all-sky fluxes). Forcing values reported for *GD<sub>21C</sub>* is relative to *GD<sub>20C</sub>*, while forcing values for *GD<sub>20C</sub>I<sub>PI</sub>*, *GD<sub>20C</sub>I<sub>21C</sub>*, and *GD<sub>21C</sub>I<sub>21C</sub>* are relative to *GD<sub>20C</sub>I<sub>20C</sub>*.

Table 4-4. Global Annual Mean Values of Key Climate Variables in the Present-Day Equilibrium Simulations With and Without Explicit Droplet-Dependence in Stratiform Clouds.

Climate Variable <sup>a</sup>	<i>GD</i> <sub>20C</sub>	<i>GD</i> <sub>20C</sub> <i>I</i> <sub>20C</sub>
$T_s$ , °C	14.58	14.65
Total Cloud, %	61.64	61.59
Strat. Cloud, %	56.96	56.94
Low Cloud, %	52.60	52.30
LWP, g m <sup>-2</sup>	118.51	108.68
Precip., mm day <sup>-1</sup>	2.89	2.89
Precip. (strat.), mm day <sup>-1</sup>	0.87	0.87
Surface SW, W m <sup>-2</sup>	160.54	161.58

<sup>a</sup>  $T_s$  = surface temperature, Strat. = stratiform, LWP = liquid water path, Precip. = precipitation, SW = shortwave flux

Table 4-5. Comparison of Global Annual Mean Cloud Properties in Present-Day Simulation  $GD_{20C}I_{20C}$  With Remote Sensing Observations and Predictions in Selected GCM Studies.

	$GD_{20C}I_{20C}$	Observation	Modeling Studies
Total Column $N_c^a$ , $10^{10} \text{ m}^{-2}$	5.69	4.4 <sup>c</sup>	2.1 to 7.6 <sup>h</sup>
$N_c$ at 850 hPa, $\text{cm}^{-3}$ ,	122.22	—	75.0 to 135.0 <sup>i</sup>
$r_e$ at Cloud Top, $\mu\text{m}$	9.58	11.4 <sup>d</sup>	6.8 to 11.3 <sup>j</sup>
LWP, $\text{g m}^{-2}$	108.68 (total)	93.3 <sup>e</sup> 48.0 to 86.0 (ocean) <sup>f</sup>	41.5 to 110.0 (total) <sup>k</sup> 57.1 to 67.9 (ocean) <sup>l</sup>
TOA SW CF <sup>b</sup> , $\text{W m}^{-2}$	124.04 (ocean)	-50.0 <sup>g</sup>	-49.9 to -61.0 <sup>m</sup>

<sup>a</sup> Accounts for cloudy periods in cloudy regions only

<sup>b</sup> CF=cloud forcing

<sup>c</sup> *Han et al.* [1998] (ISCCP, average of January, April, July, and October, 1987)

<sup>d</sup> *Han et al.* [1994] (ISCCP, average of January, April, July, and October, 1987)

<sup>e</sup> *Penner et al.* [2006] (MODIS)

<sup>f</sup> *O'Dell et al.* [2008] (SSM/I, TMI, and AMSR; ocean only, January 1988 through December 2005), *Greenwald et al.* [1993] (SSM/I; ocean only), *Weng et al.* [1997] (SSM/I; ocean only)

<sup>g</sup> *Kiehl and Trenberth* [1997] (ERBE, November 1984 through February 1990)

<sup>h</sup> *Menon et al.* [2002] (GISS-II GCM with prescribed SST) and *Hoose et al.* [2008] (ECHAM5-HAM with in-cloud aerosol processing scheme and prescribed SST)

<sup>i</sup> *Penner et al.* [2006] (CAM-Oslo, LMD-Z, and CCSR GCM with prescribed SST, in experiment 6)

<sup>j</sup> *Menon et al.* [2002], *Kristjánsson et al.* [2005] (NCAR CCM3 with slab ocean, experiment ALLTOT), and *Penner et al.* [2006]

<sup>k</sup> *Kristjánsson et al.* [2005], *Penner et al.* [2006], and *Hoose et al.* [2008]

<sup>l</sup> *Lohmann et al.* [2007] (ECHAM5-HAM with prescribed SST)

<sup>m</sup> *Penner et al.* [2006] and *Hoose et al.* [2008]

Table 4-6. Changes in Annual Mean Cloud Properties Between the Equilibrium Climates<sup>a</sup>.

		$GD_{20c}I_{20c} -$ $GD_{20c}I_{PI}$	$GD_{20c}I_{21c} -$ $GD_{20c}I_{20c}$	$GD_{21c}I_{21c} -$ $GD_{20c}I_{20c}$
$\Delta$ Column $N_c$ , $10^{10} \text{ m}^{-2}$	Global	+2.68	+1.45	+1.96
	Ocean	+0.72	+0.26	+0.47
	Land	+9.29	+5.63	+6.61
	NH	+5.02	+2.54	+3.61
	SH	+0.52	+0.50	+0.35
$\Delta r_e$ at Cloud Top, $\mu\text{m}$	Global	-0.79	-0.21	+0.20
	Ocean	-0.48	-0.13	+0.31
	Land	-1.82	-0.51	-0.09
	NH	-1.17	-0.26	-0.05
	SH	-0.44	-0.17	+0.47
$\Delta$ LWP, $\text{g m}^{-2}$	Global	-0.64	-0.62	+19.90
	Ocean	-0.03	-0.20	+21.86
	Land	-2.33	-1.70	+14.94
	NH	-2.06	-0.83	+20.42
	SH	+0.78	-0.41	+19.39
$\Delta$ LWP (strat.), $\text{g m}^{-2}$	Global	+0.70	-0.20	+3.41
	Ocean	+0.59	-0.25	+2.79
	Land	+0.96	(-0.10)	+5.20
	NH	+1.24	-0.23	+4.54
	SH	+0.13	-0.16	+2.32
$\Delta$ Strat. Cloud, % (absolute)	Global	+0.55	+0.16	-1.75
	Ocean	+0.66	+0.17	-1.95
	Land	+0.28	(+0.15)	-1.24
	NH	+0.40	(+0.11)	-1.08
	SH	+0.70	+0.21	-2.42
$\Delta$ TOA SW CF, $\text{W m}^{-2}$	Global	-1.33	-0.28	(+0.01)
	Ocean	-1.34	-0.35	+0.43
	Land	-1.30	(-0.10)	-1.05
	NH	-1.46	-0.39	(-0.18)
	SH	-1.19	(-0.17)	(+0.20)
$\Delta$ Net CF, $\text{W m}^{-2}$	Global	-1.42	-0.28	-0.48
	Ocean	-1.20	-0.22	-0.28
	Land	-1.98	-0.42	-0.98
	NH	-1.96	-0.51	-0.48
	SH	-0.88	(-0.04)	-0.47

Table 4-6. (Continued)

<sup>a</sup> Differences insignificant relative to the 95% confidence intervals are parenthesized. The usual t-test takes into account the temporal correlation in each set of sample data (i.e., the global, land, ocean, or hemispherical annual average of the climate variable of interest in the last 20 years of each simulation). The sample sizes are reduced to the equivalent sample sizes  $n_e$  and  $m_e$ . The 95% confidence interval equals to  $1.98 \times s \times (1/n_e + 1/m_e)^{0.5}$  if  $n_e + m_e \geq 30$ , where  $s$  is the pooled standard deviation; for  $n_e + m_e < 30$ , the interval is determined by a lookup table. For a more detailed explanation, please refer to *Zwiers and von Storch* [1995].

Table 4-7. Similar to Table 4.6, but for Changes in Annual Mean Temperature, Precipitation, Hydrological Sensitivity, and Surface Radiative Fluxes.

		$GD_{20cI_{20c}} - GD_{20cI_{PI}}$	$GD_{20cI_{21c}} - GD_{20cI_{20c}}$	$GD_{21cI_{21c}} - GD_{20cI_{20c}}$
$\Delta T_s$ , K	Global	-1.00	-0.28	+4.59
	Ocean	-0.86	-0.24	+4.19
	Land	-1.33	-0.38	+5.60
	NH	-1.35	-0.32	+4.77
	SH	-0.65	-0.25	+4.41
$\Delta$ Precip., mm/day	Global	-0.10	-0.03	+0.23
	Ocean	-0.06	-0.01	+0.29
	Land	-0.20	-0.09	+0.10
	NH	-0.19	-0.05	+0.22
	SH	(-0.01)	-0.02	+0.25
$\Delta$ Precip. (strat.), mm/day	Global	-0.02	-0.02	-0.04
	Ocean	-0.00	-0.01	-0.06
	Land	-0.05	-0.02	+0.02
	NH	-0.03	-0.02	-0.04
	SH	-0.01	-0.01	-0.03
$\Delta$ Surface SW, $W m^{-2}$	Global	-1.62	-0.51	-1.81
	Ocean	-1.27	-0.29	-0.82
	Land	-2.54	-1.06	-4.33
	NH	-1.96	-0.59	-4.05
	SH	-1.29	-0.42	+0.43
$\Delta$ Surface LW, $W m^{-2}$	Global	-0.91	-0.34	+6.66
	Ocean	-1.01	-0.42	+7.45
	Land	-0.64	(-0.16)	+4.65
	NH	-1.20	-0.37	+7.08
	SH	-0.62	-0.32	+6.24
Climate Sensitivity, $K m^2 W^{-1}$	Global	+0.55	+0.33	+0.80
$\Delta$ Precip./ $\Delta T_s$ , % $K^{-1}$	Global	+3.46	+3.71	+1.73

Table 4-8. Change in Global Annual Mean Values of Key Climate Variables Between the Present-day and Year 2100 Equilibrium Simulations, Predicted by the Modified and Standard Version of GISS III.

	$GD_{21C}I_{21C} - GD_{20C}I_{20C}$	$GD_{21C} - GD_{20C}$
$\Delta T_s$ , K	+4.59	+4.88
Climate Sensitivity, $K m^2 W^{-1}$	+0.80	+0.74
$\Delta$ Precip., $mm day^{-1}$	+0.23	+0.32
$\Delta$ Precip. (strat.), $mm day^{-1}$	-0.04	+0.04
$\Delta$ Precip./ $\Delta T_s$ , $\% K^{-1}$	+1.73	+2.27
$\Delta$ Total Cloud, % (absolute)	-2.09	-2.49
$\Delta$ Strat. Cloud, % (absolute)	-1.75	-2.13
$\Delta$ LWP, $g m^{-2}$	+19.90	+21.62

Table 4-9. Comparisons of Present Day to Year 2100 Forcing and Climate Response Between the Present Study and Previous Related Studies

Types of Forcing	ADE	GHG	GHG+ ADE	GHG+ ADE	AIE	GHG+ ADE+ AIE
Study	<i>Chen et al.</i> [2007]	<i>Chen et al.</i> [2007]	<i>Liao et al.</i> [2008]	The present study	The present study	The present study
GCM	GISS II'	GISS II'	CACTUS Unified Model (GISS II')	Standard GISS III	Modified GISS III	Modified GISS III
Predictions of Aerosols and/ or $N_c$ in the simulations	Offline	—	Online with fully coupled chemistry and climate	Offline	Offline	Offline
Integration (diagnostic period), years	80 (last 30)	80 (last 30)	35 (last 20)	100 (last 20)	100+30 (last 20)	100+30 (last 20)
Instantaneous Forcing at tropopause, <sup>a</sup> $W m^{-2}$	+0.18	+6.54	—	+6.59	-0.84	+5.75
Equilibrium Response of Global $T_s$ , K	+0.14	+5.31	+6.00	+4.88	-0.25	+4.61
Climate Sensitivity, <sup>b</sup> $K m^2 W^{-1}$	+0.78	+0.81	—	+0.74	+0.30	+0.80
Equilibrium Response of Global Precip., %	-1.03	+11.64	+9.00	+11.07	-1.04	+8.33
Hydrological Sensitivity, % $K^{-1}$	-7.34	+2.19	+1.5	+2.27	+4.18	+1.78

<sup>a</sup> Defined as changes in net radiative flux for ADE and GHG, and defined as change in net cloud forcing for AIE.

<sup>b</sup> Note that here the climate sensitivity was calculated based on instantaneous forcing, not the adjusted forcing, which is derived by allowing the temperature in the stratosphere to adjust. In general, the adjusted forcing for GHG is typically 10–20% lower than the instantaneous forcing, while for aerosols the two are approximately equal [*Hansen et al.*, 1997].

Table 4-10. Summary of Patterns of Equilibrium Climate Response in the Present Study

	Perturbation of $N_c$ From PI to 20C	Perturbation of $N_c$ From 20C to 21C	Perturbation of GHG, ADE and $N_c$ From 20C to 21C
Change in $N_c$	Increase globally with maxima over 30°N–60°N	Maximum of increase over 15°N–45°N; slight decrease north of 60°N in JJA	Maximum of increase over 15°N–45°N; slight decrease north of 60°N in JJA
Surface Temperature	Cooling globally, with maxima at NH high lat.	Small cooling over the Tropics and sub-Tropics	Warming globally with polar amplification
Inter-hemispheric Temperature Contrast	Significant (NH much cooler than SH)	Small (NH~SH)	Small (NH slightly warmer than SH)
Liquid Water	Slightly decreased global average; increase in low to mid-troposphere; decrease in mid- to high troposphere	Slightly decreased global average	Increased global average; increase near Tropical tropopause and mid-troposphere in high lat.; decrease in low to mid-troposphere
Hadley Circulation	Anomalous sinking at 20°N and rising at 20°S; southward shift of ITCZ	Weakened Tropical convection	Broadened Hadley Cell; strengthened ascending branches in convection zone
Precipitation	Reduced global average; enhanced around 15°S	Reduced global average; maximum decrease over the Tropics	Enhanced global average; maximum increase at Equator; decreased stratiform precipitation over 45°S–45°N

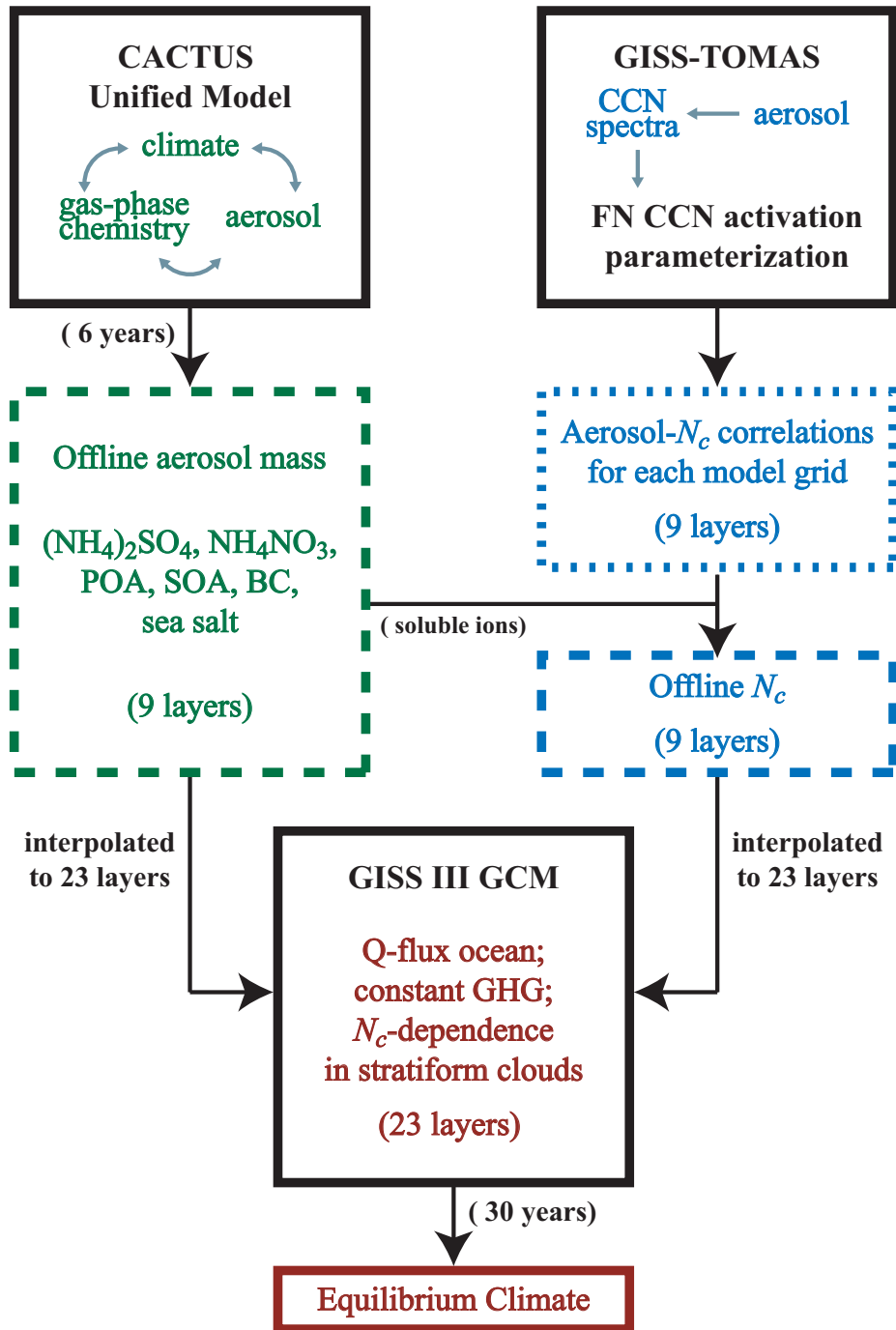


Figure 4-1. Schematic diagram for experimental design

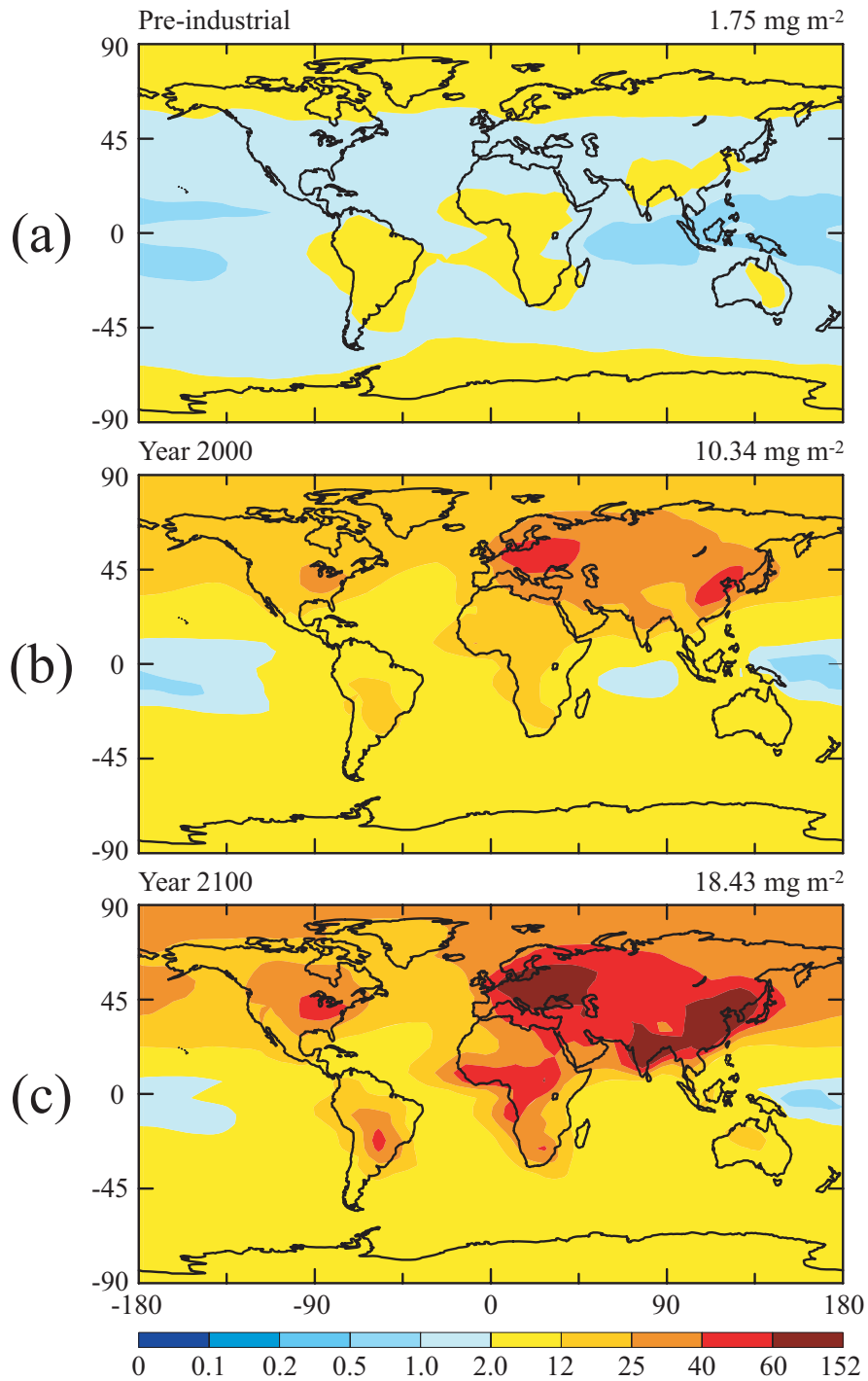


Figure 4-2. Annual mean total column burden ( $\text{mg m}^{-2}$ ) of sulfate, nitrate, ammonium, POA, SOA, and BC for (a) PI, (b) 20C, (c) 21C. Global average values are given in the upper right corner of each panel.

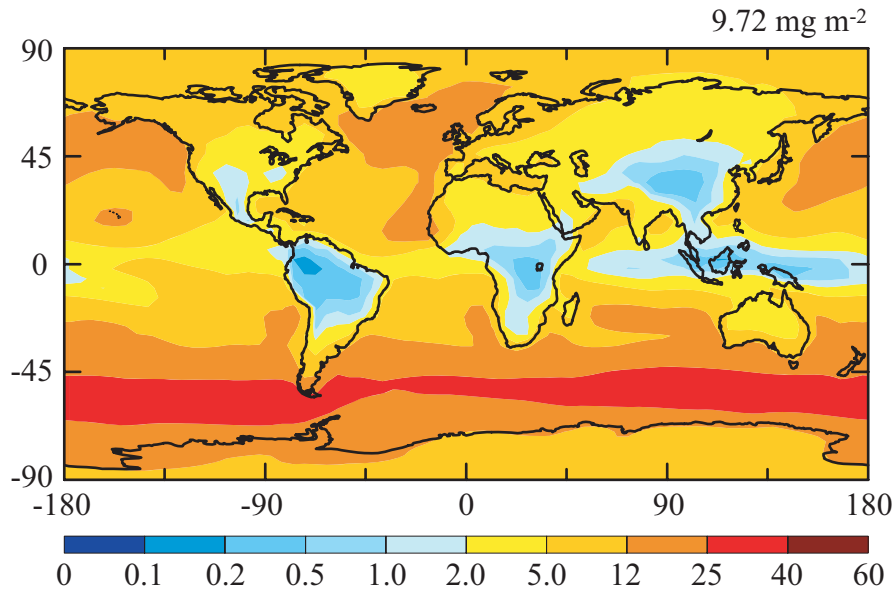


Figure 4-3. Annual mean column burden of sea salt ( $\text{mg m}^{-2}$ ) for 20C. Global average values is given in the upper right corner.

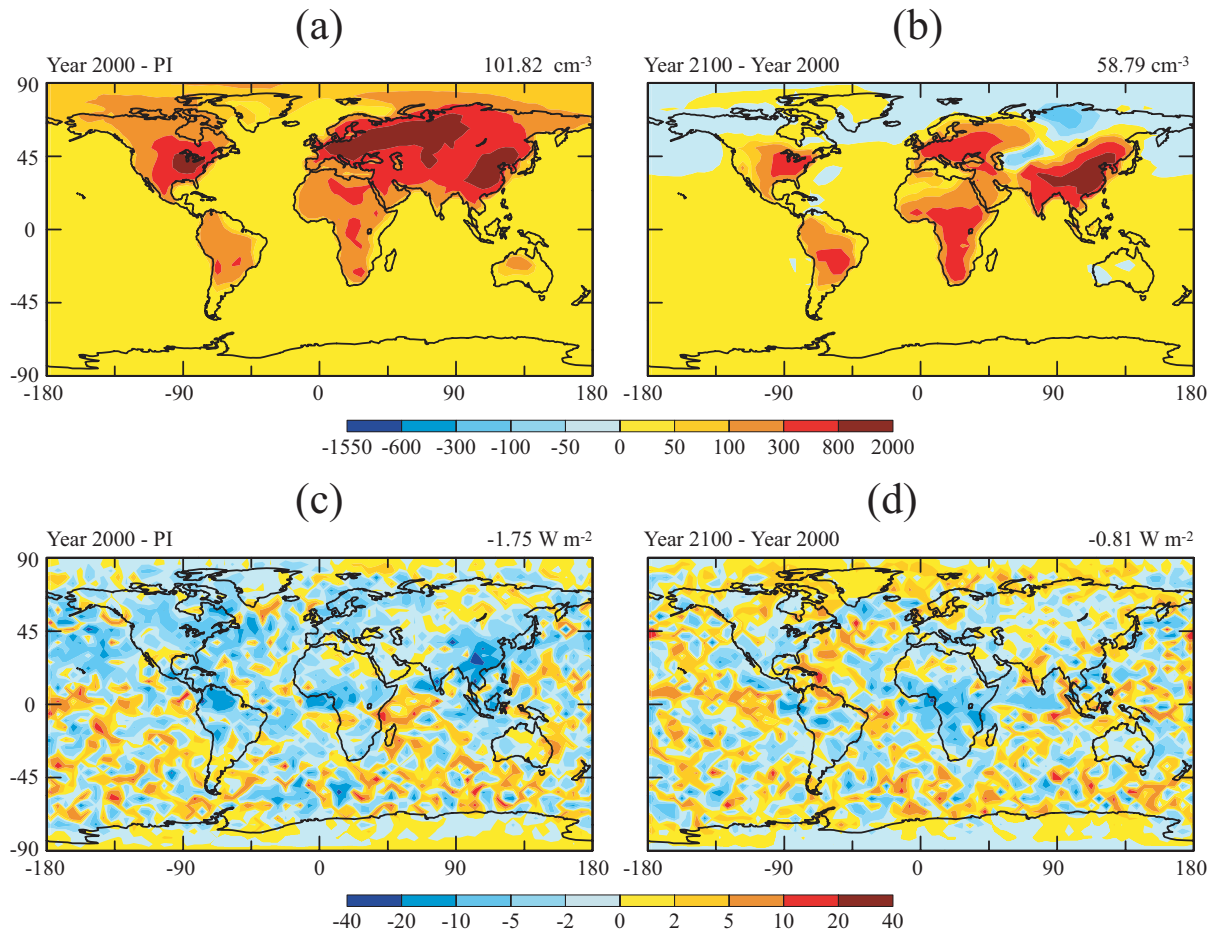


Figure 4-4. The left column shows the changes in annual mean  $N_c$  at the lowest model layer (972 hPa) (a) from PI to 20C and (b) from 20C to 21C. The right column shows the annual mean instantaneous TOA AIE forcing (i.e., changes in TOA cloud forcing) (c) from PI to 20C and (d) from 20C to 21C. Global average values are given in the upper right corner of each panel

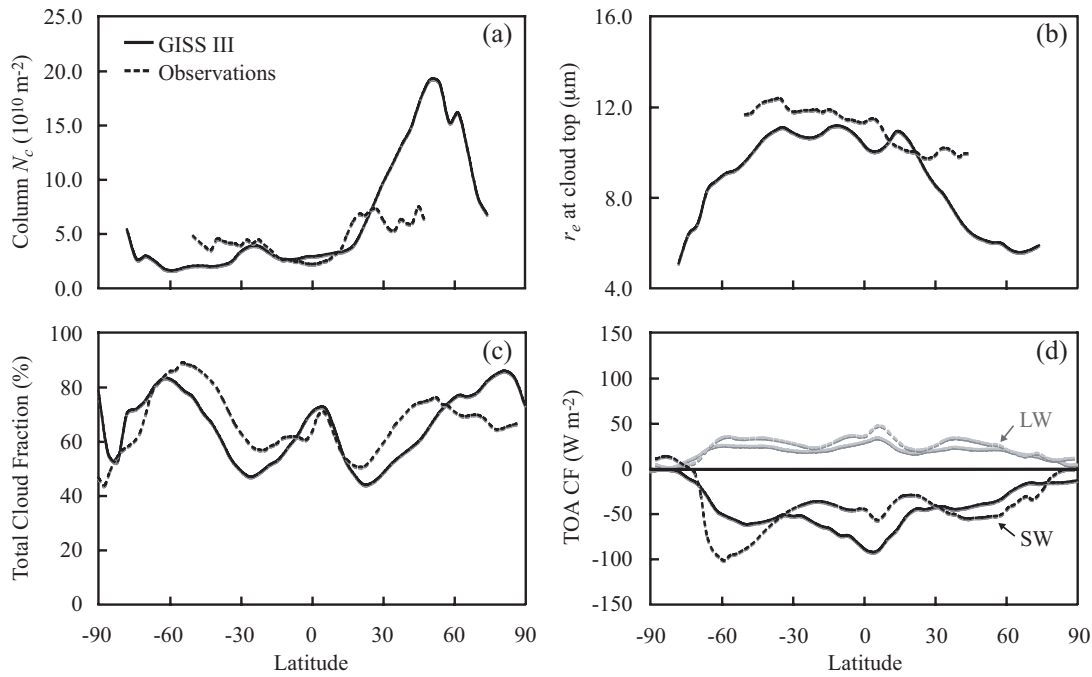


Figure 4-5. Comparisons of zonal mean cloud properties between predicted present-day equilibrium climate accounting for GHG and anthropogenic aerosol direct and indirect effects ( $DG_{20C}I_{20C}$ , solid lines) and satellite observations (dashed lines): (a) column  $N_c$ , (retrievals based on ISCCP [Han *et al.*, 1998]) (b)  $r_e$  at cloud top (retrievals based on ISCCP [Han *et al.*, 1994], for year 1987), (c) total cloud fraction (measurements from ISCCP, from July 1986 to June 2006) and (d) SW and LW cloud forcing (measurements from ERBE [Kiehl and Trenberth, 1997]; black lines for shortwave component, and gray lines for longwave component).

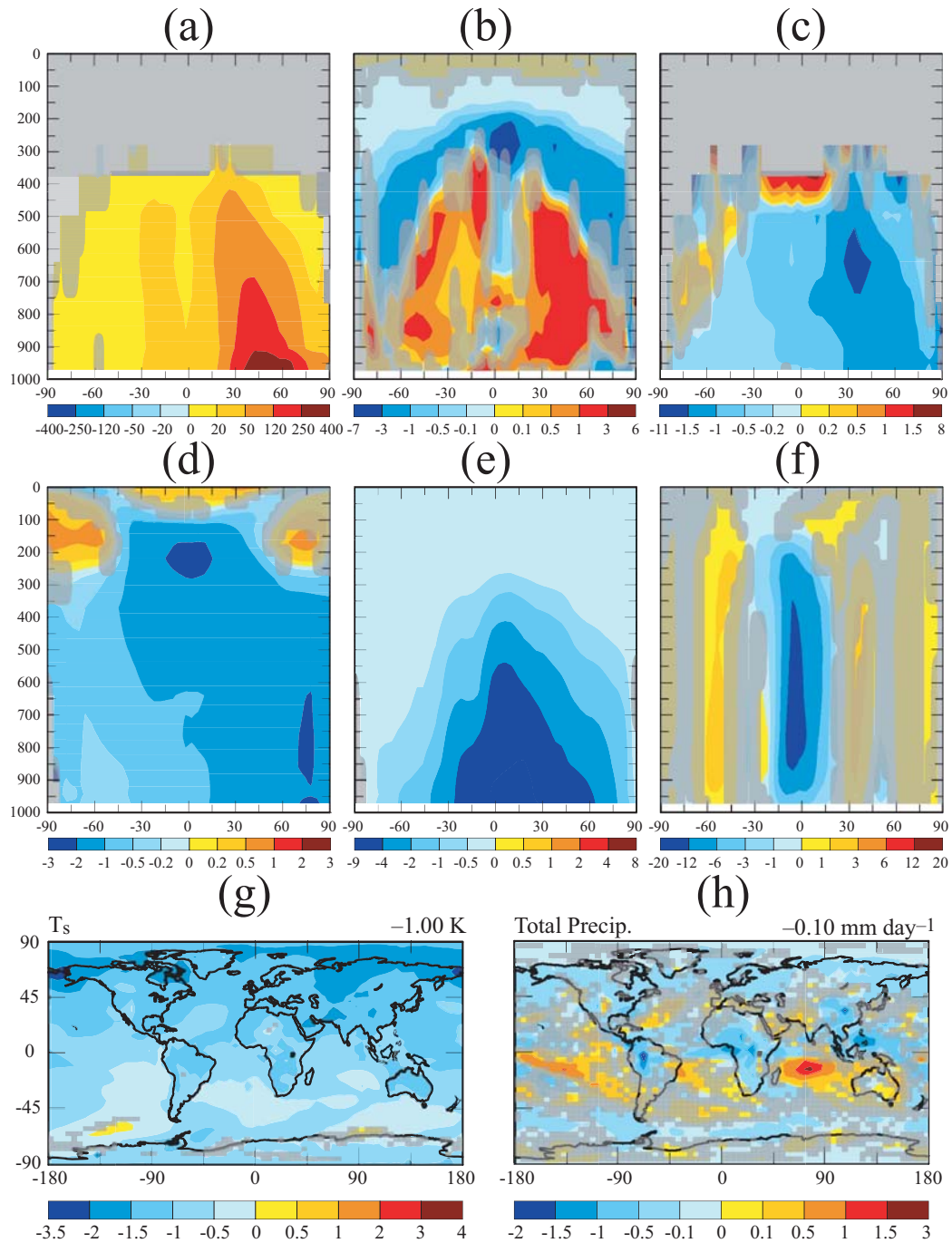


Figure 4-6. Present-day climate response to perturbation of AIE from pre-industrial to present day ( $DG_{20cI_{20c}} - DG_{20cI_{PI}}$ ): vertical zonal profiles of changes in annual mean (a)  $N_c$  in liquid stratiform clouds ( $\text{cm}^{-3}$ ), (b) total cloud water mixing ratio ( $10^{-6} \text{ kg-H}_2\text{O kg-air}^{-1}$ ), (c)  $r_e$  in liquid stratiform clouds ( $\mu\text{m}$ ) (d) temperature (K), (e) specific humidity ( $10^{-4} \text{ kg-H}_2\text{O kg-air}^{-1}$ ), and (f) mass stream function ( $10^{10} \text{ kg s}^{-1}$ , positive values indicate counterclockwise flows); annual mean changes in (g)  $T_s$  (K) and (h) Precipitation ( $\text{mm day}^{-1}$ ). Changes that insignificant relative to the 95% confidence intervals are shaded. Global average values are given in the upper right corner of (g) and (h).

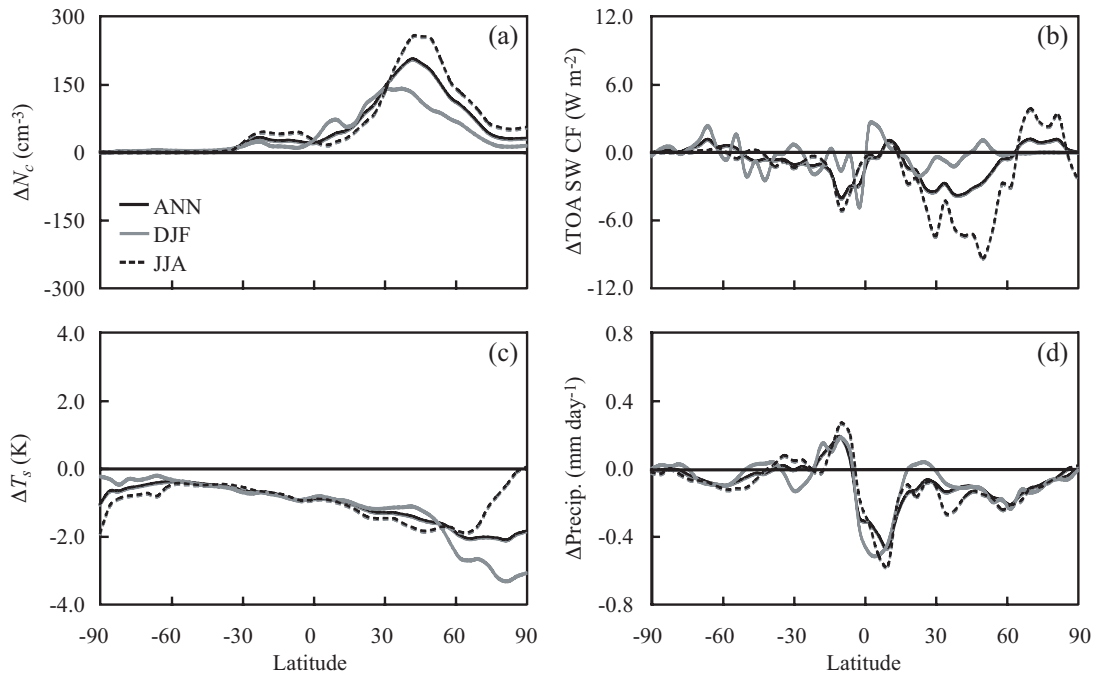


Figure 4-7. Present-day climate response to perturbation of AIE from pre-industrial to present day ( $DG_{20cI_{20c}} - DG_{20cI_{PI}}$ ): zonal mean changes in (a)  $N_c$  at 850 hPa ( $\text{cm}^{-3}$ ), (b) TOA SW CF ( $\text{W m}^{-2}$ ), (c)  $T_s$  (K), and (d) Precipitation ( $\text{mm day}^{-1}$ ) (Black solid lines for annual average, gray lines for average over DJF, and dotted lines for average over JJA).

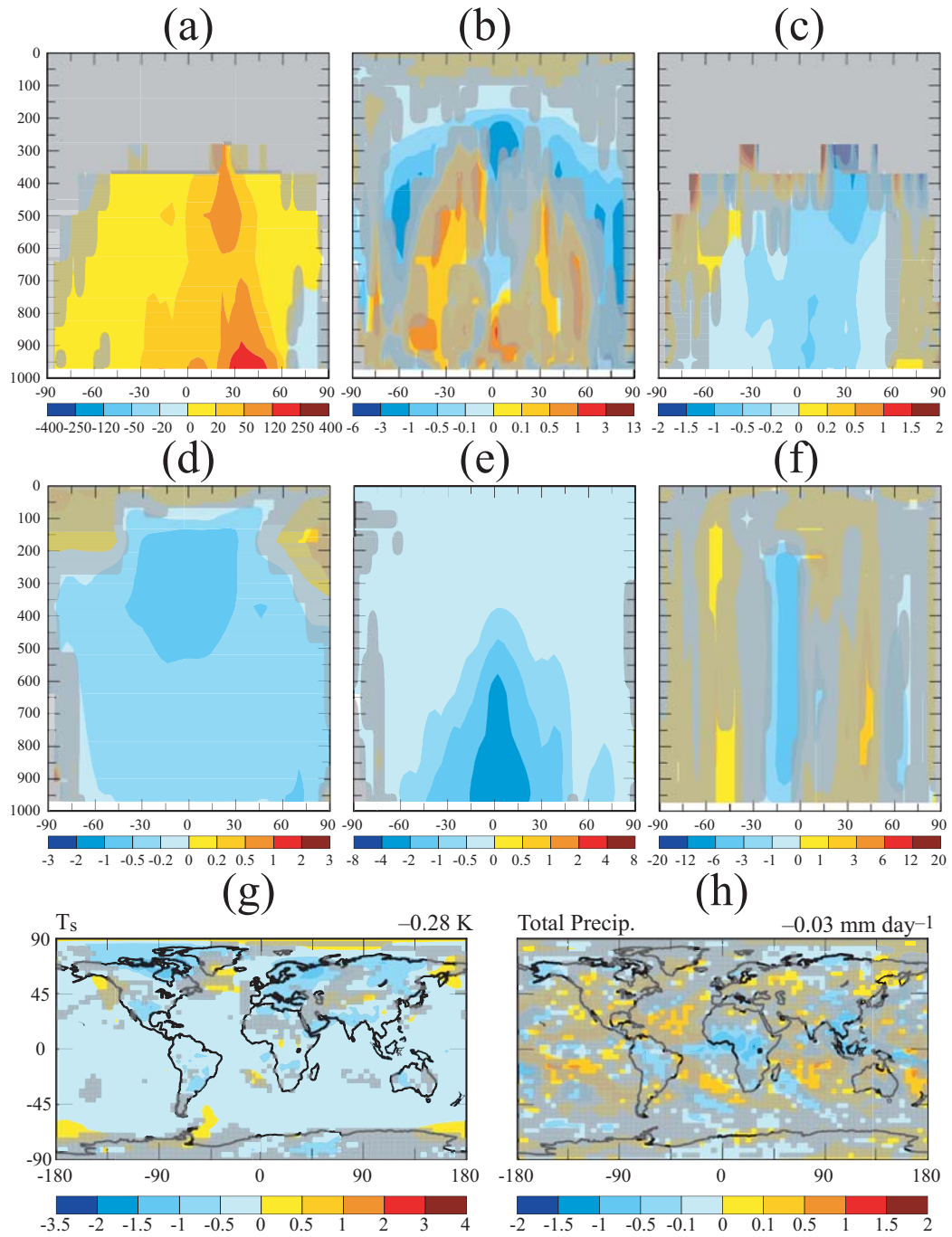


Figure 4-8. Similar to Figure 4.6 but for present-day climate response to perturbation of AIE from present day to year 2100 ( $DG_{20cI_{21c}} - DG_{20cI_{20c}}$ ).

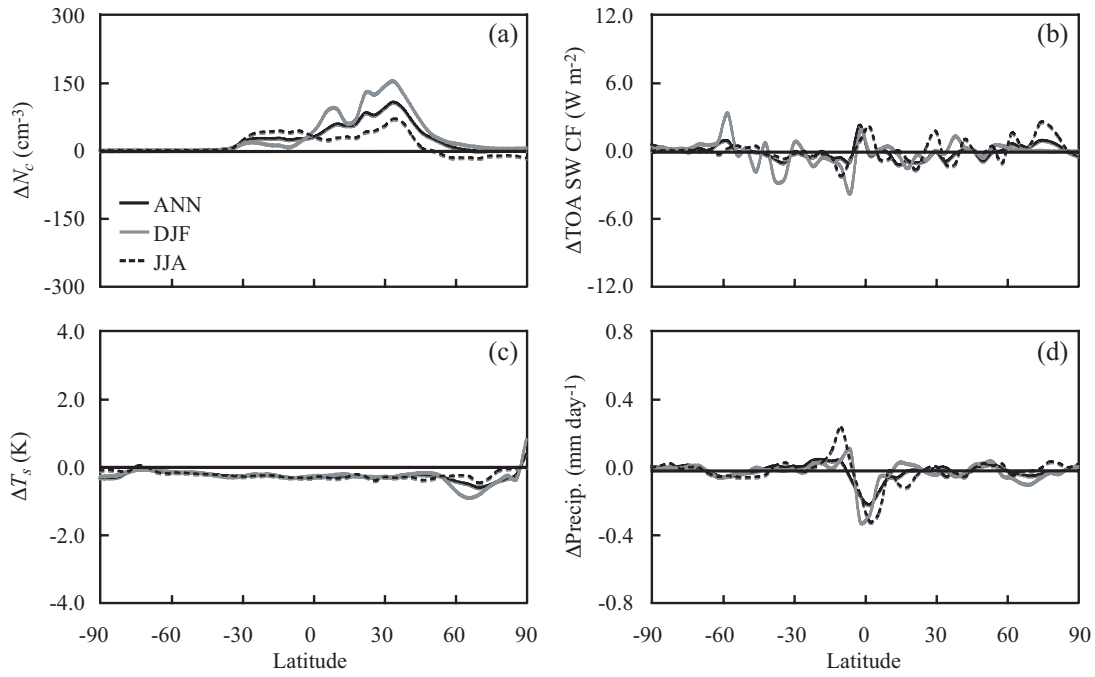


Figure 4-9. Similar to Figure 4.7 but for present-day climate response to perturbation of AIE from present day to year 2100 ( $DG_{20cI_{21c}} - DG_{20cI_{20c}}$ ). Note the vertical scales in are different.

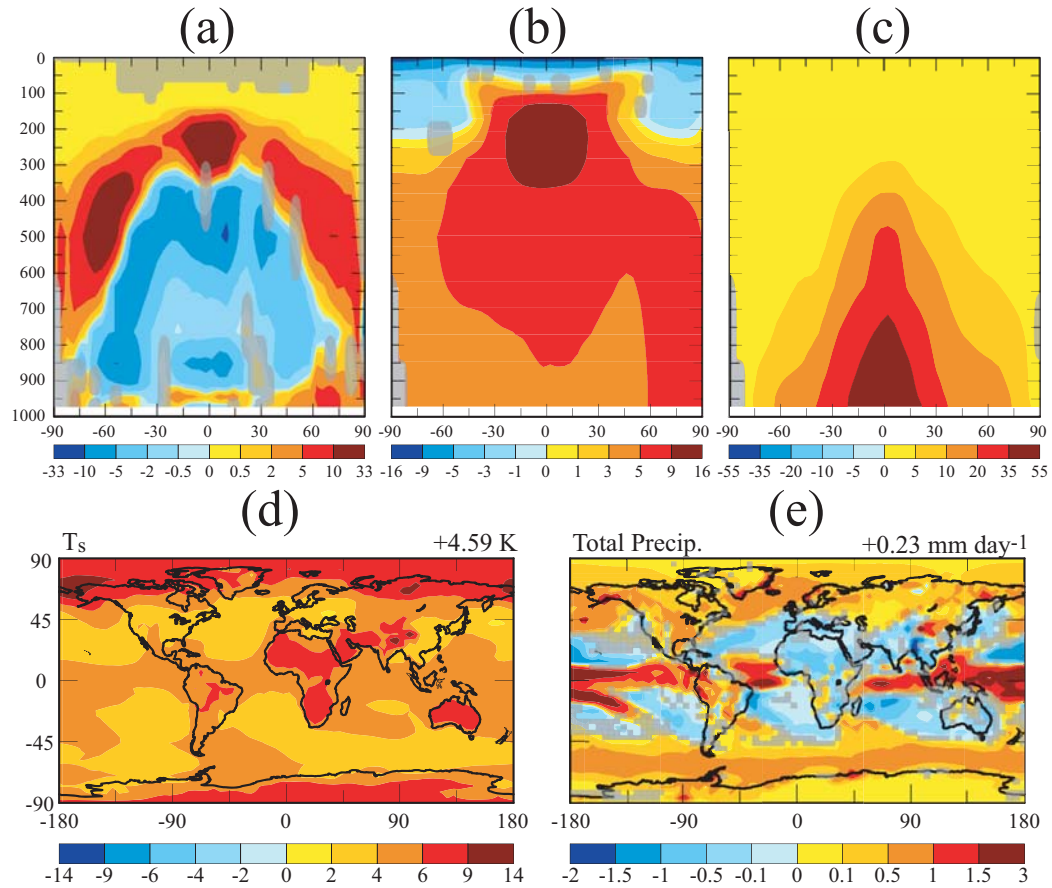


Figure 4-10. Climate responses to combined effects of GHG and anthropogenic aerosol direct and indirect effect from present day to year 2100 ( $DG_{21cI_{21c}} - DG_{20cI_{20c}}$ ): vertical zonal profiles of changes in annual mean (a) total cloud water mixing ratio ( $10^{-6}$  kg-H<sub>2</sub>O kg-air<sup>-1</sup>), (b) temperature (K), and (c) specific humidity ( $10^{-4}$  kg-H<sub>2</sub>O kg-air<sup>-1</sup>); annual mean changes in (d)  $T_s$  (K) and (e) Precipitation (mm day<sup>-1</sup>). Global average values are given in the upper right corner of (d) and (e). Note the color scales are different from previous figures.

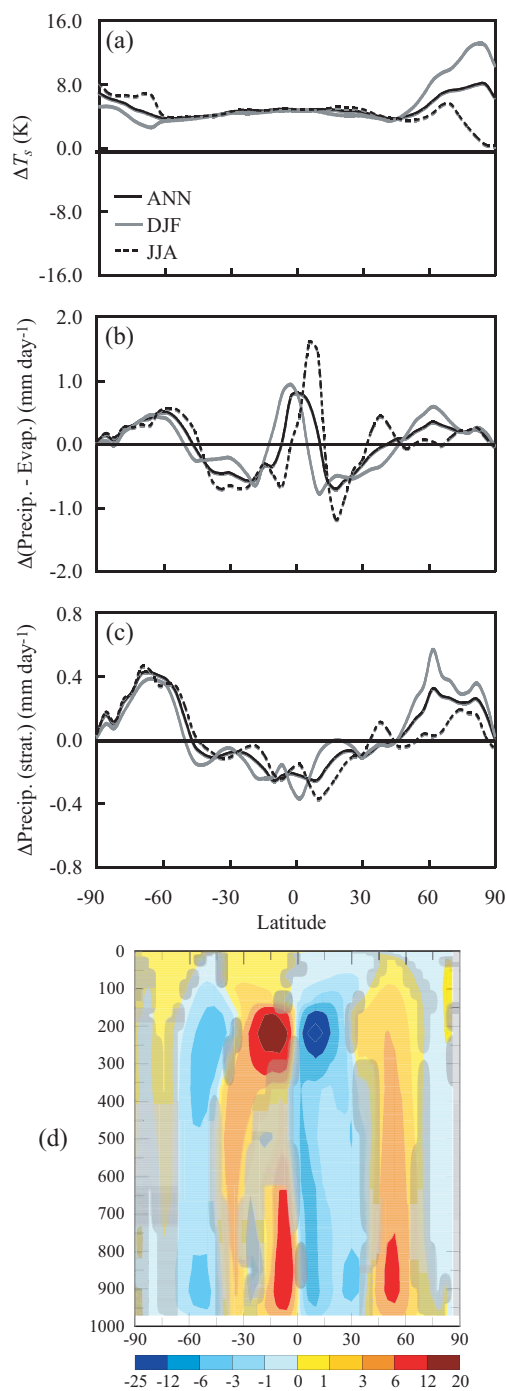


Figure 4-11. Climate responses to combined effects of GHG and anthropogenic aerosol direct and indirect effect from present day to year 2100 ( $DG_{21C}I_{21C} - DG_{20C}I_{20C}$ ): zonal mean changes in (a)  $T_s$  (K), (b) excess precipitation (total precipitation minus evaporation,  $\text{mm day}^{-1}$ ), and (c) precipitation from stratiform clouds ( $\text{mm day}^{-1}$ ), and vertical zonal profiles of changes in annual mean (d) mass stream function ( $10^{10} \text{ kg s}^{-1}$ ). (In (a)–(c), black solid lines for annual average, gray lines for average over DJF, and dotted lines for average over JJA)

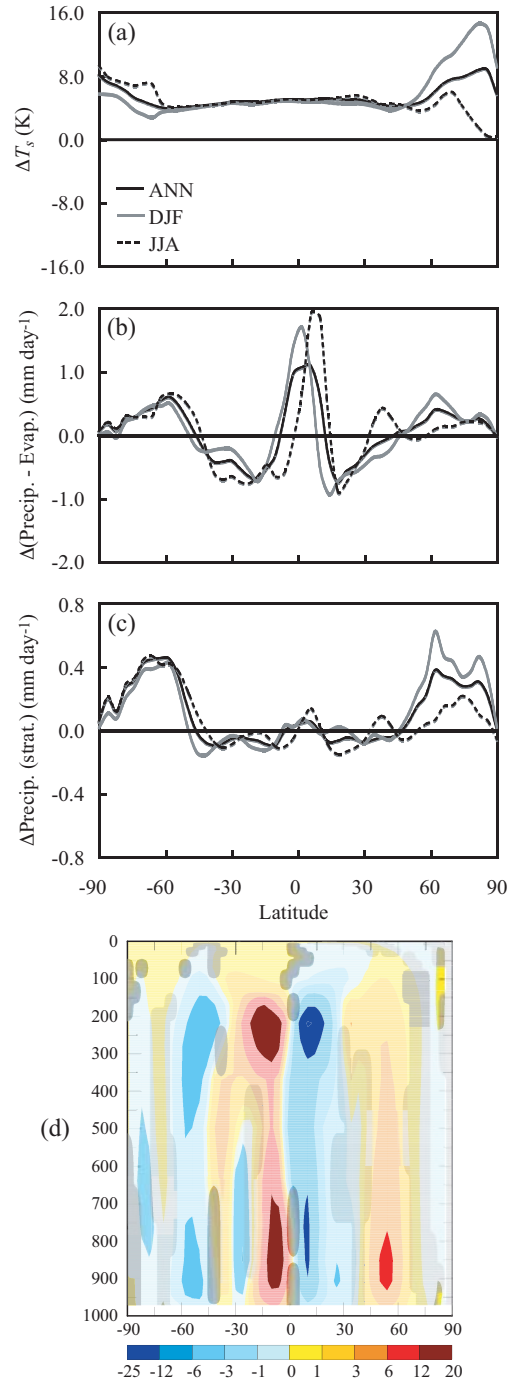


Figure 4-12. Similar to Figure 4-11, but for climate responses from present day to year 2100 predicted by the standard version of GISS III ( $DG_{21C} - DG_{20C}$ ).

**Part II. Sensitivity of Multiangle  
Imaging to the Optical and  
Microphysical Properties of  
Biomass Burning Aerosols**

## Chapter 5

---

# **Sensitivity of Multiangle Imaging to the Optical and Microphysical Properties of Biomass Burning Aerosols**

Published in *Journal of Geophysical Research* (2008) by Wei-Ting Chen, Ralph A. Kahn, David Nelson, Kevin Yau, and John H. Seinfeld, 113, D10203, doi:10.1029/2007JD009414.

Copyright © 2008 American Geophysical Union. Reprinted with permission from American Geophysical Union.

## Abstract

The treatment of biomass burning (BB) carbonaceous particles in the Multi-angle Imaging SpectroRadiometer (MISR) Standard Aerosol Retrieval Algorithm is assessed, and algorithm refinements are suggested, based on a theoretical sensitivity analysis and comparisons with near-coincident AERONET measurements at representative BB sites. Over the natural ranges of BB aerosol microphysical and optical properties observed in past field campaigns, patterns of retrieved Aerosol Optical Depth (AOD), particle size, and single scattering albedo (SSA) are evaluated. Based on the theoretical analysis, assuming total column AOD of 0.2, over a dark, uniform surface, MISR can distinguish two to three groups in each of size and SSA, except when the assumed atmospheric particles are significantly absorbing (mid-visible SSA  $\sim 0.84$ ), or of medium sizes (mean radius  $\sim 0.13 \mu\text{m}$ ); sensitivity to absorbing, medium-large size particles increases considerably when the assumed column AOD is raised to 0.5. MISR Research Aerosol Retrievals confirm the theoretical results, based on coincident AERONET inversions under BB-dominated conditions. When BB is externally mixed with dust in the atmosphere, dust optical model and surface reflection uncertainties, along with spatial variability, contribute to differences between the Research Retrievals and AERONET. These results suggest specific refinements to the MISR Standard Aerosol Algorithm complement of component particles and mixtures. They also highlight the importance for satellite aerosol retrievals of surface reflectance characterization, with accuracies that can be difficult to achieve with coupled surface-aerosol algorithms in some higher AOD situations.

## 5.1 Introduction

Satellite remote sensing provides frequent, long-term global monitoring for tropospheric aerosols. The Multiangle Imaging SpectroRadiometer (MISR) aboard the NASA Earth Observing System (EOS) Terra satellite contributes a great deal of information about aerosol characteristics through its multi-angle, multi-spectral measurements. MISR images Earth at nine view angles (nadir plus  $26.1^\circ$ ,  $45.6^\circ$ ,  $60.0^\circ$ , and  $70.5^\circ$  in the forward and aft directions along the spacecraft track) and in four spectral bands (446, 558, 672, and 867 nm). Operational since early 2000, MISR observes Earth successively along a  $\sim 360$  km wide swath and obtains global coverage once in nine days at the Equator with a spatial resolution of 275 m to 1 km. The retrieval products include land surface, cloud, and aerosol properties [*Diner et al.*, 1998].

Deriving aerosol microphysical properties is a major objective of the MISR program. The MISR Standard Aerosol Retrieval Algorithm obtains aerosol optical depth (AOD) and aerosol type at a resolution of 17.6 km, by analyzing MISR top-of-atmosphere radiances from  $16 \times 16$  pixel patches of 1.1-km resolution [*Diner et al.*, 1999]. To systematically improve the MISR Standard Retrieval Algorithm, which automatically processes all the MISR data, it is necessary to explore in greater detail the properties of individual aerosol components. A series of theoretical studies was carried out to assess the multidimensional sensitivity of the MISR aerosol retrieval algorithm prior to launch. Observed radiances over cloud-free, dark water conditions were simulated by systematically varying aerosol optical depths (AODs) and microphysical properties (generic retrievals; [*Kahn et al.*, 1997; 1998]) or by varying the proportions of multi-

component aerosol mixtures (climatological retrievals; [Kahn *et al.*, 2001]), to determine the ranges of component model properties giving acceptable matches to the measurements. The generic retrievals, in which the aerosol population is specified by monomodal, log-normal size distributions of uniform composition, demonstrated the capability to distinguish aerosols in three to five size groups, two to four compositional groups (by single scattering albedo) [Kahn *et al.*, 1998], and spherical versus nonspherical shape [Kahn *et al.*, 1997], under average viewing conditions. In addition, the climatological retrievals, in which the aerosol is assumed to be an external mixture consisting of various fractions of component particles having fixed microphysical properties, are able to identify mixtures containing typical sea salt, dust, and black carbon to within 20 percent or better of each component's AOD fraction; maritime and continental aerosol air masses can also be distinguished. Total optical depth is constrained to at least 0.05 or 20 percent, whichever is larger; however, particle microphysical property information in the MISR data decreases for AOD below about 0.15 to 0.2 [Kahn *et al.*, 2001; 2005a].

Carbonaceous particles emitted by biomass burning (BB) activities are one of the tropospheric aerosol species that pose great challenges to climate study. The Intergovernmental Panel on Climate Change (IPCC) estimated the global, annual average direct radiative forcing of BB aerosols to be  $+0.03 \pm 0.12$  W/m<sup>2</sup>, but the level of scientific understanding is considered low [Forster *et al.*, 2007], and the regional, seasonal impact can be much higher and more uncertain. BB aerosol emissions in the Northern Hemisphere are concentrated in India, Southern China, and Southeast Asia, usually peaking from March to April, in North American boreal forest from June to September,

and also in the Sahel region (West Africa) from November to March. Intense BB in the Southern Hemisphere occurs from August to October, mostly in the Amazonian forest of South America and in Tropical and Southern Africa [*Duncan et al.*, 2003], and from October to January in Australia. Large burning events also occur in boreal forest and dry grassland due to lightning, abnormal droughts, or arson, such as the Siberian forest fires in 1997, the tropical rain forest fire in Indonesia from 1997 to 1998, and the Southern California fires in October 2003 and 2007. It is estimated that about 25.0 Tg of primary organic carbon and 3.3 Tg of black carbon is released annually by BB [*Bond et al.*, 2004; *Andreae and Merlet*, 2001]. Improved knowledge of BB smoke properties, amounts, and spatial distribution globally, to which MISR observations can contribute, will enhance current understanding of the role BB particles play in climate, regional visibility, and public health.

Validation with AERONET AOD measurements shows that, over BB sites during the peak of burning season, MISR AOD (version 12) generally exhibits a low bias with large uncertainty; adding to the algorithm climatology more absorbing spherical particle components is suggested to reduce the discrepancies [*Kahn et al.*, 2005a]. However, MISR aerosol property retrievals over BB regions have never been validated with great details. Therefore, in this study we aim to suggest refinements to the BB particle models assumed in the current MISR Standard Aerosol Algorithm, by assessing the sensitivity of MISR to BB aerosol properties, through a combination of theoretical analyses and data retrieval studies.

The paper is organized as follows: the strengths and limitations of Version 17 MISR Standard Aerosol retrievals are assessed, by comparing coincident MISR and AEROSOL

RObotic NETwork (AERONET) measurements at sites in major BB regions during the year 2001 burning season. This motivates the work presented in subsequent sections. To identify BB aerosol components missing from the Standard algorithm, recently published data on BB aerosols, especially physical and optical parameters, are summarized briefly in section 5.3. Based on the summarized data, a set of 16 BB particle component models is selected to represent natural BB smoke type, and the ability of MISR to distinguish among them is explored theoretically in section 5.4. MISR Research Aerosol Retrievals are carried out in section 5.5 for representative cases chosen from section 5.2, using the BB components identified in section 5.3, and detailed surface characterization. The results and discussions are summarized in the final section.

## **5.2 Near-Coincident MISR-AERONET Measurements in Major BB Regions**

### **5.2.1 Data Selection**

To understand the performance of MISR retrievals over land for ambient BB particles, near-coincident MISR and AERONET events at eight AERONET sites located in major BB regions are analyzed (Table 5-1). MISR Standard Aerosol Retrieval products, version 17, from December 2000 through August 2001, are compared in this study with AERONET version 2, level 1.5 measurements. These data cover the entire burning season in W. Africa and part of the burning season in S. Africa and S. America, providing typical BB cases in these regions. To ensure meaningful comparisons of particle microphysical properties, only those cases with mid-visible AERONET AOD

larger than 0.15 are taken for the analysis. There are 24 qualifying, coincident cases over this period, for which the locations are listed in Table 5-1. Available AERONET direct sun AOD measurements within  $\pm 1$  hour, and single scattering albedo (SSA, the ratio of the scattering efficiency to the total extinction efficiency) and size distribution almucantar inversions within  $\pm 2$  hours of MISR overflight are averaged. Spectral AOD and SSA are interpolated linearly between the nearest AERONET channel pairs to the MISR channel effective wavelengths.

MISR Standard Aerosol Retrieval Algorithm compares the observed top-of-atmosphere (TOA) radiance for the MISR channels with a database of simulated radiances. The radiance database is developed by assuming a range of candidate aerosol mixtures and optical depths. The mixtures consist of three component particle optical models with specified component fractions, and each component has unique microphysical properties, representing some part of the range of size distributions, spectral SSA, and sphericity found in naturally occurring aerosols [Diner *et al.*, 1999]. Several  $\chi^2$  tests are used to assess the degree to which observed radiances match modeled radiances. AOD and aerosol type are retrieved based on those mixtures from the database that meet the acceptance criteria [e.g., Kahn *et al.*, 2001].

AERONET is a globally distributed remote sensing network of automated Sun-sky scanning CIMEL radiometers [Holben *et al.*, 1998], providing daily ground-based observations of spectral AOD. Because standardized instrumentation, calibration, and retrieval algorithms are used in the entire network, AERONET data are suitable for comparisons across different regions [Dubovik *et al.*, 2002]. AERONET AOD measurements and aerosol property inversions serve as useful references for MISR

retrieval validation, but we note that AERONET-retrieved particle properties come with greater uncertainties than AERONET AOD values. Uncertainty of AERONET AOD is generally within 0.01–0.02 [Holben *et al.*, 1998], whereas for BB aerosols with high AOD ( $AOD_{440} > 0.5$ ), the error of AERONET volume size distribution and SSA is estimated to be around 25% and 0.03, respectively, and the error increases significantly with lower aerosol loading, especially for SSA. The uncertainties of AERONET particle property retrievals are mainly related to the error in angular pointing and the inaccuracy in accounting for ground reflectance [Dubovik *et al.*, 2000; Sinyuk *et al.*, 2007].

## 5.2.2 Comparison of Near-coincident MISR-AERONET BB Cases

Figure 5-1a shows the AERONET mid-visible AOD (hereafter  $AOD_A$ ) and mid-visible SSA (hereafter  $SSA_A$ ) for all 24 qualifying cases. In general, when the aerosols are absorbing ( $SSA_A = 0.80$ – $0.90$ ), mid-visible AOD is smaller than 0.6, whereas in the less absorbing to weakly absorbing cases ( $SSA_A = 0.90$ – $0.99$ ), mid-visible AOD can be as low as 0.17 and as high as 1.74. Figure 5-1b shows the difference of AOD between MISR v17 and AERONET data ( $AOD_{M-A}$ ) against  $AOD_A$ . MISR v17 AOD ( $AOD_M$ ) shows small and unbiased deviation (within  $\pm 20\%$ ) with respect to AERONET when  $AOD_A$  is below 0.5. In cases with  $AOD_A > 0.5$ ,  $AOD_M$  is apparently underestimated; in some extreme cases with  $AOD_A$  around 1.5 to 1.7, the differences can be as significant as  $-0.7$  to  $-1$ . Figure 5-1c plots  $SSA_A$  versus the MISR-AERONET SSA differences ( $SSA_{M-A}$ ). The overestimation of SSA by the MISR v17 Standard Algorithm ( $SSA_M$ ) is pervasive, and increases as the atmosphere becomes more absorbing. The discrepancies increase from  $+0.05$  when  $SSA_A$  is 0.9 to as much as  $+0.15$  when  $SSA_A$  is 0.80. That is,  $SSA_M$  is pretty close to unity for all cases, whereas  $SSA_A$  varies between 0.8 and 1.0.

To explore this behavior further, we separate the cases into four distinct groups based on the patterns of differences in AOD, SSA, Ångstrom Exponent ( $\text{\AA}$ ), and SSA spectral dependence ( $\alpha_{\omega_0}$ ). The relevant quantities are plotted in Figures 5-1d–h. The wavelength dependence of SSA is defined by fitting the spectral SSA to the power law relationship,

$$\omega_0(\lambda) \propto \lambda^{-\alpha_{\omega_0}}, \quad (5-1)$$

and  $\alpha_{\omega_0}$  is calculated as the slope of the linear regression of the logarithm:

$$\ln \omega_0(\lambda_i) = a_0 - \alpha_{\omega_0} \ln \lambda_i, \quad (5-2)$$

where  $\lambda_i$ 's represent discrete channels measured by the instruments, and  $a_0$  is a constant. This is similar to the manner in which the Ångstrom Exponent represents the spectral slope of AOD. Based on field measurement data, BB particles generally exhibit positive  $\alpha_{\omega_0}$  values (i.e. decreasing SSA with increasing wavelength); this will be discussed in detail in section 5.3.

Figures 5-1e and 5-1f show that Group 1 (black diamonds) is distinguished by high Ångstrom Exponent and high SSA spectral dependence. Further, Groups 2 (red triangles), 3 (green rectangles), and 4 (yellow circles) differ in their mid-visible AOD and SSA ranges. The four case groupings, along with the regional and seasonal distribution of cases, are summarized in Table 5-2. Most cases occur during the major burning season of each region, but no significant seasonal differences can be identified with the limited data set of cloud-free coincidences available. Group 1 includes cases from South America and Southern Africa, whereas the events of the other three groups are located exclusively in W. Africa.

MISR v17 AOD number fractions of spherical particles are also examined for the four case groups, as listed in Table 5-2. Groups 1 and 2 have higher fractional contribution to AOD by spherical particles (between 0.8 to 1.0), whereas groups 3 and 4 exhibit a wide range of spherical fractions (0.2 to 0.6 for group 3; 0.5 to 1.0 for group 4). The 48-hour back trajectories at 0.5 km, 1.5 km, and 3 km altitude calculated by the NOAA HYbrid Single-Particle Lagrangian Integrated Trajectory (HYSPLIT) model [Draxler and Rolph, 2003] (not shown) suggest that the Group 1 cases have clean continental or maritime air mass origins, whereas in the other groups, 12 of the 16 W. Africa cases have air masses that passed over the Sahara before reaching the fire region. The higher MISR aerosol sphericity fraction, more absorbing SSA, larger Ångstrom Exponent, noticeably steeper and positive SSA spectral slopes, and air mass origins suggest that cases in Group 1 are likely dominated solely by BB particles, whereas cases in other groups probably contain mixtures of BB with various fractions of weakly absorbing, medium to coarse size ( $r_{pg,N}$  around 0.5 to 1  $\mu\text{m}$ ) dust particles. For each group, the unique patterns of AOD and/or SSA discrepancies, and the likely reasons for these discrepancies, are discussed subsequently.

### **Case Group 1 — BB Dominated**

For Group 1, MISR underestimates AOD by a small but systematic amount ( $AOD_{M-A} = -0.17-0$ ), and in most cases, substantially overestimates SSA ( $SSA_{M-A} = 0.05-0.14$ ), compared to AERONET (Figure 5-1d). In conditions when  $\mathring{A}_A > 1.8$ , low biases in Ångstrom Exponent occur ( $\mathring{A}_{M-A} = -0.6$  and  $+0.2$ , Figure 5-1g). SSA spectral slope is also underestimated by around 0.1 in several cases in this group (Figure 5-1h).

We expect that the underestimation of MISR v17 AOD and Ångstrom Exponent results from higher SSA and weaker SSA spectral slope retrieved by the Standard Algorithm. When the MISR retrieval algorithm overestimates SSA, the retrieved AOD tends to be lower than it would otherwise be, in order to compensate for the larger amount of scattering contributed by the particles to the observed TOA radiance [*Kahn et al., 2005a*]. The retrieved SSA spectral dependence influences not only the retrieved mid-visible SSA (and therefore the AOD), but also the spectral dependence of AOD (i.e., Ångstrom Exponent). Large, positive  $\alpha_{\omega_0}$  is typically seen in absorbing BB particles in most field measurements, as discussed later in section 5.3. In the MISR v17 Standard Aerosol Retrieval Algorithm, the spherical absorbing particle components in the assumed particle climatology do cover the observed range of mid-visible SSA from 0.80 to 0.90, however, none of these components has a sufficiently steep, positive  $\alpha_{\omega_0}$  to match those measured in the field. These factors likely explain the abovementioned discrepancies.

Note that, although the discrepancy in retrieved particle size can also produce Ångstrom Exponent biases, the number-weighted fine mode geometric mean radius in the MISR v17 retrievals (around 0.06  $\mu\text{m}$  for all cases in group 1) agrees reasonably well with the fine mode size in the corresponding AERONET inversions (0.06–0.10  $\mu\text{m}$ ), so a discrepancy in size retrieval is less likely the reason for the AOD deviation of this group.

### **Case group 2 — BB-Dust mixed, $0.6 < \text{AOD} < 0.9$**

Group 2 has moderately high  $\text{AOD}_A$  (0.5–0.9), Ångstrom Exponent between 0.2 and 0.8, absorbing  $\text{SSA}_A$  (0.82–0.92), and flat to moderately negative SSA spectral dependence ( $\alpha_{\omega_0 A} = -0.11$  to  $-0.01$ ), and likely contains mixtures of BB particles with

some dust (Figure 5-1 and Table 5-2). Similar to cases of Group 1, MISR v17 also systematically underestimates AOD ( $AOD_{M-A} = -0.3$  to  $-0.1$ ) in Group 2. MISR overestimates SSA ( $SSA_{M-A} \sim 0.1$ ), Ångstrom Exponent ( $\mathring{A}_{M-A} = -0.1$  to  $+0.9$ ), and SSA spectral slope ( $\alpha_{\omega_0, M-A} = 0.06$  to  $0.09$ ) for this group.

Dust particles generally exhibit an SSA spectral dependence (i.e.  $\alpha_{\omega_0} < 0$ ) opposite to those of BB particles. Examples of dust particle optical models assumed in MISR v17 Aerosol Retrieval Algorithm can be found in Table 5-8. Dust models SSAs increase with increasing wavelength, but are steeper at shorter wavelengths and flatter at longer wavelengths than the relationship in Equation (5-2). When the atmosphere contains both BB and dust particles, the positive and negative SSA wavelength dependences partly cancel with each other, and as a result, SSA of the entire mixture exhibits a flatter spectral slope.

However, the assumed mixture climatology in the MISR v17 Aerosol Retrieval Algorithm does not have the combinations of absorbing spherical particles with dust particles likely to be present in these cases. The Standard Retrievals pick mixtures consisting of dust plus non-absorbing spherical particles, which result in an overestimation in mid-visible SSA and SSA spectral dependence, and therefore the retrievals are biased low in AOD and high in Ångstrom Exponent.

### **Case group 3 — BB-Dust mixed, AOD < 0.6**

Group 3 has  $AOD_A < 0.6$ , Ångstrom Exponent  $< 1$ , weakly absorbing SSA ( $SSA_A = 0.93$ – $0.99$ ), flat to moderately negative SSA spectral dependences ( $\alpha_{\omega_0, A} = -0.08$  to  $-$

0.01), and higher dust fractions (fraction spherical is as low as 0.4; Table 5-2) than Group 2. Unlike the systematic AOD low bias in Group 2, differences in mid-visible AOD are constrained to within  $\pm 0.1$  with unbiased distribution. There is also a small positive bias in MISR mid-visible SSA ( $SSA_{M-A} = 0-0.05$ ), SSA spectral dependence ( $\alpha_{\omega_0, M-A} = -0.02$  to  $+0.07$ ), and Ångstrom Exponent ( $\mathring{A}_{M-A} = 0.1-0.5$ ) for Group 3. As discussed earlier, these discrepancies are likely related to the limited selections BB-dust mixtures in the climatology of MISR Standard Aerosol Retrieval Algorithm. Because of the higher fractional contribution of dust to total AOD, the biases are less significant than those seen in group 2.

#### **Case group 4 — BB-Dust mixed, AOD > 0.9**

Group 4 has significantly higher AOD ( $AOD_A = 0.9-1.7$ ), small Ångstrom Exponent ( $\mathring{A}_A = 0.2-0.4$ ), weakly absorbing SSA ( $SSA_A = 0.93-0.96$ ), and moderately negative SSA spectral dependence ( $\alpha_{\omega_0, A} \sim -0.08$ ). Overall, the mixture properties are very similar to those derived for Group 3, but with substantially higher AOD. MISR significantly underestimates the mid-visible AOD ( $AOD_{M-A} = -1.0$  to  $-0.2$ ) and slightly overestimates the SSA spectral slope ( $\alpha_{\omega_0, M-A} = 0.02-0.07$ ) despite the small difference in SSA ( $SSA_{M-A} \sim 0.05$ ). Ångstrom Exponent is also overestimated by as much as 0.5.

The underestimation in AOD for this group probably results from factors other than the SSA and SSA spectral slope options available in aerosol climatology of the MISR v17 Algorithm. A major challenge in aerosol retrieval over land is that one cannot assume a dark surface, as is often true in the red and near-infrared bands over deep water, and as we adopt in the theoretical study (section 5.4) to simulate good viewing

conditions. Aerosol properties retrieved from space can be very sensitive to surface condition. MISR provides simultaneous retrievals of atmospheric aerosols and the three-parameter, semi-empirical Rahman-Pinty-Verstraete (RPV) bidirectional reflectance distribution function (BRDF) surface model [Rahman *et al.*, 1993] at nine camera angles and four wavelengths [Martonchik *et al.*, 1998; 2002]; the first parameter characterizes the intensity of the surface reflectance, the second parameter indicates the level of symmetric surface anisotropy (the degree of “bowl” or “bell” shape), and the third represents the relative amount of forward and backward scattering from the surface. Under less hazy atmospheric conditions, the atmospheric contribution to the satellite signal is proportionately lower, and MISR surface property retrievals are expected to be more reliable.

To assess the surface contribution to the top-of-atmosphere signal, we examine MISR surface parameters retrieved at the study locations, for the same viewing geometry, on less hazy days within a few weeks before or after each MISR-AERONET coincident event, and compare them with the values retrieved for the hazy days. In three of the four cases of group 4, the MISR Standard Algorithm retrieves much higher surface reflectance under hazy conditions; the first parameter in the RPV BRDF model is up to five times higher. (The fourth case has no successful surface retrieval on the hazy day owing to cloud contamination.) Since the surface itself probably did not change this dramatically between the clear and the hazy day, we conclude that poor separation of surface and atmospheric signals by the retrieval algorithm is likely to contribute significantly to the AOD underestimation seen in these very hazy cases.

The analyses in this section, as summarized in Table 5-2, provide important suggestion for refining MISR retrievals for BB and dust-BB mixed cases. For BB-dominated cases, MISR v17 overestimates mid-visible SSA and underestimates mid-visible AOD, Ångstrom Exponent, and SSA spectral dependence. To eliminate these discrepancies, absorbing, spherical particle components with optical and microphysical properties matching BB smoke values observed in the field should be included in the retrieval algorithm particle climatology. For BB-dust mixed cases with moderate aerosol loadings, MISR v17 overestimates SSA, Ångstrom Exponent, and SSA spectral slope and underestimates AOD, suggesting that mixtures of absorbing, spherical BB particles with dust models should be added to the mixture selection in the algorithm. In addition, the algorithm's ability to separate surface from atmospheric contributions for extremely hazy conditions (mid-visible AOD > 0.8) needs to be refined.

### **5.3 BB Particle Property Characterization**

In the previous section, we referenced BB particle microphysical properties obtained from better-constrained sub-orbital observations, for use in the satellite retrieval algorithm. The purpose of this brief section is to identify likely natural ranges of BB particle size, SSA, and refractive index, from data reported in the published literature.

*Reid et al.* [2005a, b] give a comprehensive review of BB particle occurrence, properties, and evolution, and *Bond and Bergstrom* [2006] summarize the measured optical properties of light-absorbing carbon. Readers who wish to understand the current knowledge of gas-phase and particle-phase chemistry, associated particle microphysical and optical properties, and the issues related to comparing measurements among different

instruments and inversion techniques should refer to these publications. Table 5-3 lists references providing ambient BB aerosol size and optical properties. Most of the data sources are field campaigns in major biomass burning areas, obtained since the late 1980's, such as SCAR-B (Smoke, Clouds, and Radiation-Brazil) and SAFARI (Southern African Regional Science Initiative) 2000. Another important data source is the continuous ground-based observation from AERONET.

Although we seek to understand how BB physical properties vary with region, smoke age, vegetation type, and combustion phase, it is difficult to identify specific trends when comparing measurements made with different in-situ instruments and retrieval techniques. Data collected from the literature are summarized in Table 5-4, showing the averages and ranges of reported values. Based on the plume age information reported in the literature, for timescales relevant to satellite measurements, we categorize data collected from plumes less than one day old as fresh smoke, whereas plumes one to three days old as aged smoke. If the plume is older than three days, or if plume age is not reported, the data are categorized as regional haze. Therefore regional haze can cover the widest range of smoke ages, combustion efficiencies, and flame phases. Note that the averages in Table 5-4 are simply the means of all available measurements; they are not corrected for different instrument and sampling biases, and can only be considered as a general indication of the parameters in each plume category.

BB aerosol size distributions are usually expressed in terms of normalized log-normal distributions,

$$\frac{dN(r_{p,N})}{d\ln r_{p,N}} = \frac{1}{(2\pi)^{\frac{1}{2}} \ln \sigma_g} \exp\left[-\frac{(\ln r_{p,N} - \ln r_{pg,N})^2}{2 \ln^2 \sigma_g}\right], \quad (5-3)$$

where  $dN(r_{p,N})$  the particle number concentration in a  $d\ln r_{p,N}$  interval,  $r_{pg,N}$  is the geometric mean radius, and  $\sigma_g$  is the geometric standard deviation. We summarize here only measurements for spherical, fine-mode ( $r_{pg,N} < 1.0 \mu\text{m}$ ) particles, which are dominated by carbonaceous particles generated by combustion processes. Figures 5-2a and 5-2b give the values of fine mode  $r_{pg,N}$  and  $\sigma_g$ , assembled from the data sources in Table 5-3. The vertical lines display the mean values for fresh smoke, aged smoke, and regional haze (colored red, blue, and green, respectively), whereas the grey bars show the ranges of reported values. In general,  $r_{pg,N}$  is about  $0.05 \mu\text{m}$  larger and  $\sigma_g$  is  $0.05\text{--}0.1$  smaller for aged plumes than for fresh plumes, suggesting growth during aging, a fairly well-established phenomenon [e.g., Reid *et al.*, 2005a; b]. The data for regional haze, which covers smokes of various ages, generally shows an average size between those of fresh and aged plumes, and a much larger range of  $\sigma_g$ . On a regional basis,  $r_{pg,N}$  and  $\sigma_g$  for Amazon BB aerosol seem to be generally larger than those in Africa, whereas the aged plumes in North America seem to exhibit the largest particle size. Besides fine-mode particles, in the literature reporting multi-modal size measurements, small fractions of coarse-mode particles, with  $r_{pg,N}$  around  $1.0$  to  $1.5 \mu\text{m}$ , are also mentioned [e.g. Haywood *et al.*, 2003b; Kreidenweis *et al.*, 2001], mostly as soil re-suspended by pyro-cumulus thermal updrafts, ash-debris [Reid and Hobbs, 1998], and transported mineral dust. In the sensitivity study of section 5.4, we consider only the fine-mode particles. Coarse-mode particles will be considered in the Research Retrievals of section 5.5.

Figure 5-2c shows the reported ranges of published SSA at  $\lambda = 550$  nm ( $\omega_{0,550}$ ). Fresh plumes generally exhibit the smallest mid-visible SSA ( $\omega_{0,550}$  around 0.85). The increase of SSA with plume age is attributed to the growth of particles into a size range where scattering is a large proportion of total extinction [e.g., *Hobbs et al.*, 1997]. Some studies have shown that the southern African savanna smoke is the most absorbing [*Dubovik et al.*, 2002; *Eck et al.*, 2003a], presumably because biomass in the savanna ecosystem tends to be consumed by flaming combustion, which produces a higher fraction of black carbon (BC) than smoldering combustion.

In addition, the wavelength dependence of SSA can also vary significantly (not shown in Figure 5-2). The spectral slope of SSA, as defined by  $\alpha_{\omega_0}$  in Equation (5-2), is expected to be steeper (0.1–0.4) for BB particles having mid-visible SSA lower than around 0.85 [e.g., *Hobbs et al.*, 1997; *Reid and Hobbs*, 1998; *Eck et al.*, 2003b; *Haywood et al.*, 2003b], whereas  $\alpha_{\omega_0}$  is thought to be flatter (0.05–0.1) for particles having mid-visible SSA exceeding 0.85 [e.g., *Dubovik et al.*, 2002; *Eck et al.*, 2003b; *Haywood et al.*, 2003a, b]. This expectation is difficult to confirm for lack of sufficient simultaneous, multi-channel measurements.

Also, most sources do not explicitly report the ambient relative humidity during measurement, and sometimes it is not clear whether wet or dry particles were measured. In fact, changes in hygroscopicity with chemical aging, and the effects of particle hygroscopic growth on particle optical properties are the most uncertain properties for BB aerosols [*Reid et al.*, 2005b; *Petters et al.*, 2006]. As a result, it is difficult to correct the reported data for hygroscopic growth. Instead, we study a parameter space that covers

the range of sizes and SSA likely to include BB particles under most natural conditions (see section 5.4).

Refractive index ( $n_r - in_i$ ) governs particle scattering and absorption. The real ( $n_r$ ) and imaginary ( $n_i$ ) parts are both functions of wavelength. Figures 5-2d and 5-2e show published  $n_r$  and  $n_i$  values, respectively, for BB aerosols at 550 nm. Some of these values were calculated assuming: (1) a given mixing rule, such as BC core with organic carbon (OC) shell, or homogeneous mixing, (2) average mass or volume fraction of BC in the particle, and (3) aerosol density, using experimental values of refractive indices for pure substances (1.75–0.44*i* at 550 nm for BC;  $n_r = 1.52$  to 1.54 and  $n_i = 0$  to 0.0035 for OC at all wavelengths) [e.g., *Haywood et al., 2003b; Trentmann et al., 2002*]. Other data were taken from inversions of radiometric measurements [e.g., *Yamasoe et al., 1998*]. Although  $n_{r,550}$  for regional haze covers the range of 1.44 to 1.55, its value is generally smaller than that of younger aerosols. As expected from the observed increase in SSA as smoke ages, fresh smoke has a higher  $n_i$  value, especially in North America ( $n_{i,550} \sim 0.06$ ).

## 5.4 Theoretical Sensitivity Study for BB Aerosol Components

As discussed in section 5.3, the size and optical properties of BB particles can vary tremendously with ambient conditions. To understand the precision with which we can expect MISR to distinguish among BB particles of different sizes and optical properties, over the range of natural variation, we perform a theoretical sensitivity study before proposing specific updates to the representative BB particle models in the Standard Algorithm.

The theoretical study aims at answering two important questions. (1) If the atmospheric aerosol is dominated spherical particles having a given size distribution and SSA within the natural BB particle range, how precisely can the size and SSA be retrieved from TOA MISR radiances under good but not necessarily ideal conditions? (2) How does retrieval sensitivity to size and SSA vary when the atmospheric aerosol properties change? In addition to indicating which spherical components should be included in the Standard Aerosol Retrieval Algorithm to represent BB particles, the theoretical study conclusions will help in interpreting results of actual retrievals for BB cases, as we do in section 5.5.

Our approach follows *Kahn et al.* [2001]. We set up the Research Aerosol Retrieval algorithm with simulated TOA reflectances for a range of aerosol mixtures and optical depths, to serve as the “comparison space.” For each test, we select one component and AOD, as the “atmosphere.” The simulated reflectances for this component are treated as measurements in the retrieval process. The retrieved range of AODs and particle types is then compared to the “atmosphere,” to establish the sensitivity of the retrieval method. In this case, we focus the study on the two-dimensional particle property space of size and SSA for spherical particles, representing the natural range of BB components.

#### **5.4.1 BB Aerosol Components and Mixing Groups**

A set of 16 spherical aerosol components is developed for the sensitivity study radiance simulations (Table 5-5) that captures the observed range of natural BB particle properties based on Table 5-4. Each aerosol component is defined by a fixed composition and unimodal, log-normal size distribution. They span sizes from very small ( $r_{pg,N} = 0.04$

$\mu\text{m}$ ) to large ( $r_{pg,N} = 0.16 \mu\text{m}$ ) and mid-visible SSA values from very absorbing ( $\omega_{0,558} = 0.74$ ) to weakly absorbing ( $\omega_{0,558} = 0.94$ ). As discussed earlier, the wavelength dependence of SSA,  $\alpha_{\omega_0}$ , may also vary with particle type. Here we do not control for this parameter explicitly; rather, we chose  $\alpha_{\omega_0} = 0.37$  for very absorbing particles [e.g. *Hobbs et al.*, 1997; *Reid and Hobbs*, 1998], 0.15 for absorbing particles, and 0.07 for less and weakly absorbing ones.

We create a range of mixtures, to be used as the comparison space in the Research Retrieval algorithm, by defining eight “mixing groups” (Table 5-6). Each mixing group is a set of external, four-component aerosol mixtures, with the proportion of each component allowed to vary from 0 to 100 percent, following *Kahn et al.* [2001]. The components are selected from the 16 given in Table 5-5. Mixing groups 1 to 4 aim at exploring sensitivity to particle size by choosing components having similar mid-visible SSA values but different radii (Table 5-6). Mixing groups 5 to 8, containing components having similar radii but different SSAs, are intended to test MISR’s sensitivity to SSA.

#### **5.4.2 Radiative Transfer Simulations, and the $\chi^2$ Test Variables for Evaluating Agreement Between Simulated Reflectances in the Sensitivity Test**

Sensitivity calculations were carried out for sixteen atmospheres, each assumed to contain 100 percent of one of eight component particles selected to span the size-SSA space (as listed in footnote (a) in Table 5-6), and with total column AOD of 0.2 or 0.5. The TOA equivalent reflectances are simulated by the radiative transfer (RT) code

developed by the MISR team [Martonchik *et al.*, 1998] based on the matrix operator method [Grant and Hunt, 1968]. Following the assumptions adopted in previous theoretical calculations [e.g., Kahn *et al.*, 1997; 2001; Kalashnikova and Kahn, 2006], a cloud-free, Rayleigh scattering atmosphere over a Fresnel-reflecting dark water surface, with 1 atm surface pressure,  $2.5 \text{ m s}^{-1}$  wind speed, and a standard mid-latitude lapse rate profile is assumed. The aerosols are assumed to be concentrated in a single near-surface layer, and the influence of their vertical distribution is neglected for these tests. These assumptions are designed to simulate good but not ideal viewing conditions, with the understanding that as actual conditions degrade, so will the sensitivity of the MISR retrievals. The TOA radiance for all MISR view angles and wavelengths is derived. The ratio of the radiances multiplied by  $\pi$  to the exo-atmospheric solar irradiance then gives the equivalent reflectances.

The same radiative transfer code and assumptions about surface and atmospheric condition are also applied to calculate the equivalent reflectances of the entire comparison space of eight mixing groups listed in Table 5-6. Mixtures comprised of all possible combinations of the four components in a mixing group are considered, with the AOD fraction of each component allowed to vary from 0 to 100 percent in 5 percent increments. Comparison space reflectances are calculated also as a function of total column AOD from 0 to 1, in intervals of 0.05.

Theoretical retrievals are then performed for the 16 atmospheres. The algorithm assesses how closely the reflectances produced for all the mixtures and AODs in the comparison space match those of the atmosphere, based on the  $\chi^2$  statistical formalism described in detail in Kahn *et al.* [1997, 1998, 2001]. Briefly,  $\chi^2_{abs}$ ,  $\chi^2_{geom}$ , and  $\chi^2_{spec}$

compares absolute reflectances, reflectance ratios normalized to one view angle, and reflectance ratios normalized to one wavelength, respectively, between the atmosphere and the comparison space. Each test variable is normalized by the number of channels used. The reflectances of a four-component mixture are considered indistinguishable from those of the atmosphere if the maximum of the three  $\chi^2$  test variables,

$$\chi^2_{max} = \text{Max} \{ \chi^2_{abs}, \chi^2_{geom}, \chi^2_{spec} \} \quad (5-4)$$

is less than a chosen constraint.  $\chi^2_{max} < 1$  means the average difference between the atmosphere and a comparison model is less than the associated measurement error. In this study the criterion for a comparison model to be considered a match is  $\chi^2_{max} < 1.5$ . This choice aims at realistically characterizing MISR sensitivity to aerosol properties under natural, good, but not ideal observing conditions [Kahn *et al.*, 2001]. The smaller the range of comparison models, in particle size, SSA, and AOD, that produce acceptable matches to the atmosphere, the greater the measurement sensitivity.

### 5.4.3 Results of MISR Theoretical Sensitivity to BB Components

Figures 5-3 and 5-4 display the sensitivity results for the eight atmosphere AOD = 0.2 and the eight atmosphere AOD = 0.5 cases, respectively. Each sub-panel of these figures is a plot, with particle size increasing along the horizontal axis and SSA decreasing up the vertical axis, presenting the range of comparison models that produce acceptable matches to a specific atmosphere component. The number designation of the atmosphere component for each panel is given in the upper-left corner. For reference, the panel in the lower left of each figure shows the locations of all 16 components used for the entire sensitivity study (Table 5-5) in this same size-SSA space.

Green dots in each sub-panel locate the component particles tested against the corresponding atmosphere, and the circled areas around them are proportional to the retrieved AOD fractional contribution for the components. Larger circles indicate that a larger fraction of that component provided an acceptable match to the atmosphere in the retrieval results. (The gray circle in the lower left reference panel is a scale for the size of the 100 percent circle.) In each sub-panel, the circle of *minimum* retrieved fraction for the atmosphere component itself (the “correct” answer) is shaded red and that of the *maximum* fraction is blue. For components in the retrieval comparison space having different size and/or SSA, the circles are black if the maximum retrieved fraction is higher than about 20 percent; otherwise the circles are shaded gray. (The 20% value is selected for illustration, because component retrievals are apparently significant if they comprise more than about 20% of the total column AOD, based on previous sensitivity analysis [*Kahn et al.*, 2001].)

So, for example, in the top middle panel of Figure 5-3, for which the atmosphere is assumed to contain 100% of Particle #3, 80–100% of the total column AOD was assigned to Particle 3 by the retrieval algorithm from all mixtures and AODs tested; no mixtures containing more than 20% of any other component produced an acceptable match to the simulated TOA reflectances except a slightly larger particle having the same SSA (Particle #4). In contrast, for the middle sub-panel of this figure, showing the retrieval results when the atmosphere contains Particle #7, the solution space includes AOD fractions of this particle ranging from less than 0.2 up to 1.0, and mixtures containing significant fractions of particles having the same size but SSA ranging from 0.75 to 0.95 also provide acceptable matches to the simulated TOA reflectances. So in this case, there

is poor sensitivity to SSA, but still relatively good sensitivity to particle size. Also note that the sub-panels are organized in the overall figure so that atmospheres containing more absorbing particles are at the top and those containing larger particles are to the right. This is indicated with labels at the bottom and the left sides of the figure, making it easy to identify the variations in size and SSA sensitivity by comparing adjacent sub-plots.

For the parameter space of Figures 5-3 and 5-4, the sub-panels at the corners generally show the highest sensitivity, indicated by the very large red circles and fewer (or no) small black circles. So MISR can accurately retrieve particles at the extremes of SSA (either very absorbing or weakly absorbing) and size (either small or large). Sub-panels in the top row of Figure 5-3 demonstrate that SSA can be accurately retrieved when the atmosphere contains very absorbing particles ( $\omega_{0,558} \sim 0.74$ ) for any size category, even for total column AOD of 0.2. However, sub-panels in the second row show that MISR has poor sensitivity to SSA when the atmospheric components are absorbing ( $\omega_{0,558} \sim 0.84$ ); the retrieved SSA spans very absorbing to weakly absorbing for particles of all sizes (black circles in the vertical direction), and the sensitivity does not improve when the atmospheric AOD is raised to 0.5 (Figure 5-4).

For size discrimination, sub-panels in the left columns of Figures 5-3 and 5-4 show that the sizes of very small to small size ( $r_{pg,N} = 0.04\text{--}0.07 \mu\text{m}$ ) can be successfully retrieved in all SSA categories in both the AOD = 0.2 and 0.5 cases. Sub-panels in the right columns show that the size of large particles ( $r_{pg,N} \sim 0.16 \mu\text{m}$ ) can be accurately retrieved only when AOD = 0.5. On the other hand, sub-panels in the middle column show that atmospheric components of medium size ( $r_{pg,N} \sim 0.13 \mu\text{m}$ ) can be separated

from components of small size but not from those of large size, especially for absorbing to weakly absorbing particles; size sensitivity to medium-large particle improves somewhat when AOD is increased to 0.5.

In the theoretical calculations, retrieved total column AOD is constrained to at least  $\pm 0.05$  in all cases. The overall sensitivity results are summarized in Table 5-7, which captures components contributing 20 percent or more to the total mid-visible AOD. Generally, in the parameter space covered by representative BB aerosol types, it is possible for MISR to identify two to three size categories. Two to three SSA categories can be identified when the atmospheric particles are very absorbing, or are less to weakly absorbing, but sensitivity to SSA is poor for absorbing particles ( $\omega_{0,558} \sim 0.84$ ). *Kahn et al.* [2001] showed that, under good viewing conditions, MISR can distinguish three to five size bins with an uncertainty of about 20 percent in particle component mid-visible AOD; also among spherical components, MISR can distinguish two to four groups in SSA. The results in this study are consistent with, and add considerable detail to the conclusions in *Kahn et al.* [2001].

We also performed a similar sensitivity analysis for non-absorbing particles ( $\omega_0 = 1.0$  for all wavelength) in the above four size categories, though they are not shown in Figures 5-3 and 5-4 to reduce clutter. The results indicate that MISR can successfully separate non-absorbing particles (e.g., sulfates) from BB components of similar sizes, even for a total column AOD of 0.2. In addition, the theoretical sensitivity of MISR to particle sphericity was investigated by *Kahn et al.* [1997] and *Kalashnikova and Kahn* [2006], so it is not repeated here. These studies conclude that over calm ocean surface, MISR can distinguish non-spherical, absorbing particles (e.g., mineral dust) from

spherical, absorbing particles over the natural range of particle sizes and  $\text{AOD} > 0.05$ , and the optical depth itself is retrieved to the accuracy of at least 0.05 or 10%.

## **5.5 MISR Research Retrieval Study of Field Cases with Proposed BB Components and Detailed Surface Characterization**

In this section we perform detailed Research Retrieval analysis on four near-coincident MISR-AERONET cases from section 5.2, one from each case group. The objective is to assess the impact of adding BB component models and possibly improving surface characterization on MISR Standard aerosol retrieval results, by comparing the Research with the MISR v17 Standard Retrievals. We also examine the uncertainties introduced by spatial variability, by analyzing multiple patches in the vicinity of the AERONET surface station for each case. The MISR Research Aerosol Retrieval Algorithm is similar to the Standard Algorithm, which uses observed MISR TOA radiances but surface properties obtained under clean air conditions (section 5.1.1). The major differences between the Research and the Standard algorithms of relevance here are (1) the Research algorithm allows four components in the mixture climatology, whereas the Standard Retrievals allows three, (2) the surface properties in the Research Retrievals can be prescribed, whereas the Standard Retrievals automatically use the RPV bidirectional surface model retrieved simultaneously by MISR, and (3) pixel patches of arbitrary size and location can be analyzed with the Research algorithm, whereas the Standard algorithm operates automatically on a fixed grid of 16 by 16 pixel patches.

In addition to the 16 BB component models (Table 5-5), two representative dust particle models [*Kalashnikova et al., 2005*], one accumulation mode sulfate model, and two coarse mode sea salt models were included in the particle climatology of the Research Retrieval Algorithm for this study; their properties are given in Table 5-8. Along with the 8 mixing groups in Table 5-6, 37 additional mixing groups (not shown) of BB components with dust, sulfate, and sea salt were added to the comparison space, to account for realistic field conditions.

### **5.5.1 Patches and Surface Characterization for Selected Field Cases**

Cuiaba-Miranda on Aug. 31, 2001 (Cuiaba-Miranda\_20010831), Ilorin on Feb. 24, 2001 (Ilorin\_20010224), Ouagadougou on Dec. 18, 2000 (Ouagadougou\_20001218), and Ilorin on Feb. 17, 2001 (Ilorin\_20010217) were chosen to represent the four groups discussed in section 5.2. For each case, MISR Research Retrievals were performed on four to seven 3 by 3 pixel patches. One patch was chosen at the exact location of the AERONET site (patch P0). The other patches were chosen at locations close to the AERONET sites where dark and homogenous surface is present in the MISR image (The homogeneity criterion used requires the variance of the band-corrected equivalent reflectance for the clean-day orbit to be < 10% of the mean.) Table 5-9 lists the MISR overpass orbits and patch locations for the four selected cases. Multiple patches are chosen for each case because the surface conditions around the AERONET site may be variable. Comparisons among various darkest patches reveal the impact of scene spatial variability.

As mentioned in section 5.2, successful aerosol retrievals depend heavily on having accurate surface characterization. Surface properties are especially difficult to retrieve under thick aerosol layers in hazy conditions. However, when the atmosphere is relatively clear, the TOA radiance comes primarily from the surface, especially at near-nadir view angles, yielding more accurate surface retrievals. For the Research Retrieval studies, to maximize surface characterization quality, we retrieve the surface RPV parameters for the targets of interest on the clearest, cloudless days having the same viewing geometry (i.e., the same Terra orbital “path”), and occurring as soon as possible before or after the hazy day orbit. (We call these "clean day orbits" hereafter.) With the assumption that the surface properties stay relatively constant over the period between the hazy and clean day orbits, the clean day RPV retrievals should provide more reliable surface characterization, especially for cases having hazy day AOD near or larger than unity.

For the clean day surface retrievals, we constrain the atmospheric aerosols with coincident AERONET data (Table 5-8). The clean day surface RPV for each patch is retrieved as follows: first, the aerosol contributions to the TOA radiance is simulated by a forward RT model [e.g., *Kahn et al.*, 2005b], assuming AOD, size distribution, and SSA for all patches in the region equal the coincident AERONET inversions on that day; taking into account the aerosol contribution, we iterate the model over surface RPV parameter ranges, initialized by the RPV values retrieved by the MISR v17 Standard Retrievals, until the modeled equivalent reflectances fit the observed MISR equivalent reflectance well for each patch. The MISR orbits and the AERONET AOD on the clean days are also listed in Table 5-9.

It should be noted that high optical depth conditions usually prevail for one to three months during the burning seasons, and are often followed immediately by cloudy and rainy seasons. This limits the availability of good clean days, so we had to balance temporal proximity to the hazy day against the desired low AOD conditions when selecting clean days. As a result, the clean day orbit 2001/03/12, chosen for Ilorin\_20010224, and 2001/01/19, for Ouagadougou\_20001218, have mid-visible AODs of 0.6 and 0.34, respectively. These AODs are only somewhat lower than the corresponding hazy days (0.884 and 0.530); yet these are the cleanest days available within a reasonable time range. In addition, surface RPV values for Ilorin on 2001/02/01 (which is the clean day for Ilorin\_20010217) at patch P0 were not retrieved by the MISR Standard Algorithm; therefore RPV parameters retrieved on 2000/11/13 at P0 were used instead as the initial guess to start the iteration. This should not produce any significant difference in the derived clean day RPV, considering that the surface RPV values retrieved for nearby patches between 2001/02/01 and 2000/11/13 differed only by about 10%, and that the surface contribution dominates the TOA radiance under clear conditions.

### **5.5.2 MISR Research Retrievals of Selected Field Cases**

The results of Research Retrievals for the four chosen cases are present below. For each case, the patch having the lowest  $\chi^2$  values in the Research Retrieval is designated the “best patch”, whereas the patches having  $\chi^2$  lower than 1.5 are denoted “accepted patches.” Tables 5-10, 5-11, and 5-12 summarize the Research Retrieval results for AOD, size distribution, and SSA, respectively. In these tables, the Research Retrieval results for

the best-fit mixture of patch P0 (the exact of location of AERONET site) and of the best patch are shown, along with the range spanned by best-fit mixtures of all accepted patches, the coincident AERONET measurements and the best-fit MISR\_v17 Standard Retrieval results for patch P0. Note that the P0 patch, though co-located with AERONET, may fail to meet the scene uniformity conditions required to achieve a good satellite aerosol retrieval result. Other, nearby patches can usually be found having much better surface characteristics for retrievals, and given differences in MISR and AERONET spatial-temporal sampling, are as likely to contain comparable aerosol properties.

#### **Cuiaba-Miranda\_20010831 (Case Group 1 — BB Dominated)**

For this biomass-dominated case, AERONET derives  $AOD_A$  of 0.34 and a high  $\mathring{A}_A$  of 1.82. The MISR v17 retrieval slightly underestimates mid-visible AOD by 0.04 (around 12%) and Ångstrom Exponent by 0.24, compared to AERONET. Of the Research Algorithm results, the lowest  $\chi^2$  (0.39) occurs for patch P2; the retrieved AOD is 0.35, the same as the MISR v17 retrieval, and AOD retrieved at the four accepted patches ranges between 0.30 to 0.35, covering the values in both AERONET and MISR v17 (Table 5-10). (Note that the Research Retrieval was run with an AOD resolution of 0.05, so these results represent agreement.) The Research Retrieval Ångstrom Exponents range from 1.74 to 2.03 for the patches, higher than the MISR v17 results and bracketing the AERONET measurements. The comparisons of wavelength-dependent AOD retrievals are illustrated in Figure 5-5a. The black solid line is the spectral AOD from AERONET, the black dashed line is the MISR v17 result, and the gray solid line and the gray dotted line are the Research Retrievals at the best patch and P0, respectively. There is close agreement among all the results for this case

AERONET inversions derive a dominant AOD fraction (93%) of fine mode particles with  $r_{pg,N}$  around  $0.10 \mu\text{m}$ , and 7% of coarse mode, around  $0.62 \mu\text{m}$  in size (Table 5-11). Figure 5-6a compares the number size distribution of AERONET (green line), MISR v17 (blue line), and the Research Retrievals (red line for the best patch, yellow line for patch P0, and gray lines for the other accepted patches). The MISR v17 Algorithm retrieves a fine mode and coarse mode size of  $0.06$  and  $1.0 \mu\text{m}$ , respectively, which is a reasonable match considering the sensitivity of the MISR size retrievals, and the limited number of particles the Standard Algorithm can consider in practice. In the Research Retrievals, the dominant fine mode size is  $0.07 \mu\text{m}$  (15–80%) and  $0.13 \mu\text{m}$  (0–60%), whereas the coarse mode size is  $0.5 \mu\text{m}$ . The major difference in size retrievals between MISR v17 and the Research Retrievals is the fractionation of fine mode versus coarse mode; the fine mode fraction increases from 80% in MISR v17 to 95–100% in the Research Retrievals. This difference is within the 20% particle type retrieval uncertainty we found in the theoretical sensitivity study of section 5.4, and it partially explains the higher Ångstrom Exponents in the Research Retrieval results.

For SSA measurements, AERONET shows an absorbing  $SSS_A$  of 0.80, and a steep, positive  $\alpha_{\omega_0 A}$  of 0.16) (Table 5-12). Compared to AERONET, the MISR v17 Algorithm overestimates total mid-visible SSA by 0.12, and derives a flatter SSA spectral dependence ( $\alpha_{\omega_0 M-A} = -0.13$ ). These differences are in part a result of the limited selection of particles in the Standard Retrieval. The SSA obtained by the Research Retrievals is between 0.90 and 0.84, closer to AERONET than MISR v17. Recall that in the theoretical sensitivity study, MISR has low sensitivity to SSA for absorbing ( $\omega_{0,558} \sim 0.84$ ) particles in small to medium ( $0.07$ – $0.13 \mu\text{m}$ ) sizes. The steepest slope, which is

very close to that seen in AERONET, is retrieved at the best patch, where the lowest SSA of 0.84 is also retrieved. The retrieved SSA spectral slope ranges between 0.07 and 0.15 in the Research Retrievals, suggesting that scene variability, combined with sampling differences, may make a significant contribution to the MISR-AERONET differences in this case.

Note that a high  $\chi^2$  value is derived at P0 by the Research Algorithm. TOA reflectances computed by the Research Algorithm from the given clean day surface and possible BB-dominated mixing groups all show too weak backward scattering and too strong forward scattering in all wavelengths, compared to the observations, which are responsible for the high  $\chi^2$  value. However, retrievals of particle size and SSA at P0 are still within the theoretical sensitivity range of those at the low- $\chi^2$  patches, and therefore the high forward scattering in the computed TOA reflectances is more likely from the surface. Note that the spectral RPV parameters for P0 obtained for the clean day and hazy day orbits do not differ significantly. The P0 site was selected based on the AERONET location, not on meeting the surface uniformity criteria applied for the other retrieval patches, so the P0 surface properties may not be well characterized by the three-parameter RPV model. The uncertainty in aerosol retrievals due to surface characterization error can be identified and resolved by carrying out aerosol retrievals at a selection of nearby patches having similar surface properties, as done in this study. This should be consideration when designing future Standard Retrieval algorithms.

**Ilorin\_20010224 (Case Group 2 — BB-Dust mixed,  $0.5 < \text{AOD} < 0.9$ )**

The second case has moderately high AOD with a BB-dust mixture, for which the  $AOD_A$  is 0.88 and  $\mathring{A}_A$  is 0.52. The MISR v17 retrieval underestimates mid-visible AOD by 28%, and overestimates the Ångstrom Exponent by 0.27, compared to AERONET (Table 5-10). The best patch (P1), as determined by the Research Algorithm Retrieval  $\chi^2$  residuals, has  $AOD = 1.0$ , 14% higher than AERONET, and  $\mathring{A} = 0.72$ , well within the sensitivity range of the AERONET value, based on the sensitivity study in section 5.4. Figure 5-5b shows that the Research Retrieval at the best patch has similar AOD spectral shape as MISR v17 but is closer in magnitude to AERONET; however, the spectral slope is somewhat steeper than AERONET. Results at P0 and P1 bracket the range of AOD and Ångstrom Exponent spanned by all three accepted patches, and suggest high spatial variability in the scene for this case.

Although the MISR v17 Standard Algorithm retrieves similar fine mode size (0.06  $\mu\text{m}$ ), coarse mode size (0.5  $\mu\text{m}$  dust), and fine mode fraction (54%) as that of AERONET (Figure 5-6b), retrieved mid-visible SSA in MISR v17 is much higher ( $SSA_M = 1.00$ , compared to  $SSA_A = 0.92$ ), which at least partly explains the low bias in  $AOD_M$ . For an aerosol retrieval algorithm based on scattered light (e.g., MISR, MODIS), smaller AOD would be inferred to match the observed brightness if an overestimated SSA is adopted [Kahn *et al.*, 2005b]. The Research Retrieval, however, derives fine mode particle of larger size (0.13 to 0.16  $\mu\text{m}$ ) and 20–40% smaller fraction of 0.5  $\mu\text{m}$  dust, compared to AERONET and MISR v17, but the mid-visible SSA (0.90 to 0.93) is closer to AERONET than MISR v17. In short, MISR v17 is close to AERONET in fine and coarse mode sizes and fraction, but is biased low in AOD and biased high in SSA; the Research Retrieval is close to AERONET in AOD, coarse mode size and SSA, but has larger fine

mode size and smaller dust fraction. It should also be noted that the expected accuracy of the AERONET size distribution is 15–25% for radii over 0.5  $\mu\text{m}$ . Both MISR and AERONET size distribution retrievals under dusty condition are yet to be validated with independent field data [Kalashnikova and Kahn, 2006].

Note that the components and mixtures retrieved by the MISR v17 Algorithm are all included in the comparison space of the Research Retrieval algorithm. In the Research Retrievals for all patches, the best-fit mixtures have much better  $\chi^2$  values than that for the MISR v17 solution ( $\chi^2 > 6$ ). This is caused mainly by surface characterization differences, i.e., surface properties derived from hazy versus clean day data. In our three BB-dust mixed cases, the third RPV parameter (designated “b”) derived from the clean day data generally exhibits a steeper spectral dependence and/or a more negative value, as shown in Figure 5-7. This indicates that a stronger backward scattering from the surface, especially in the shorter wavelengths, is retrieved on cleaner days. On hazy days having moderate to high AOD, however, some forward scattering from the aerosols may be inaccurately attributed to the surface. Therefore, when the clean day surface is used, to match the observed hazy day TOA reflectances, stronger forward scattering in shorter wavelengths from the atmosphere is required. This explains the lower dust fraction derived in the Research Retrieval, since the spectral asymmetry factors (positive, i.e., forward scattering) for the BB spherical models are higher in short wavelengths, whereas the opposite is true for the dust models. The retrieval matches the observed brightness by combining higher total scattering from more fine mode particles with a larger fine mode particle size.

Also note that, based on the theoretical sensitivity results, MISR has only moderate sensitivity to the fine mode components selected by the Research Retrieval; the range of fine mode size (0.13 to 0.16  $\mu\text{m}$ ) and mid-visible SSA (0.90 to 0.93) retrieved by the Research Algorithm are consistent with the 20% sensitivity range in the theoretical sensitivity for an atmosphere consisting of a medium, less absorbing component (i.e. Particle #11 in Table 5-5:  $r_{pg,N} = 0.13 \mu\text{m}$  and  $\omega_{0,558} = 0.90$ ) with AOD = 0.5. On the other hand, for column AOD > 0.5, MISR is expected to have high sensitivity (especially in size) to the fine mode particle retrieved by AERONET ( $r_{pg,N} \sim 0.06 \mu\text{m}$ ,  $SSA_A \sim 0.92$ ), and even though similar components (e.g., Particles #10 and #14) are included in the comparison space, only < 15% fractional AOD is retrieved by the Research Algorithm (except at P0). With the agreement in AOD and SSA between AERONET and the Research Retrievals, the difference in fine mode size and dust fraction is well within observational uncertainty, considering the differences in AERONET and MISR Research Retrieval Algorithm representative dust models, the sampling difference between the instruments, and the spatial variability in this case.

### **Ouagadougou\_20001218 (Case Group 3 — BB-Dust mixed, AOD < 0.5)**

For this low AOD, BB-dust mixture case, there is a slight AOD underestimation by MISR v17 ( $AOD_M = 0.43$ ) relative to AERONET ( $AOD_A = 0.53$ ), and a slight overestimation of Ångström Exponent ( $\text{Å}_M = 0.50$ ,  $\text{Å}_A = 0.41$ ). In the Research Retrievals, moderate spatial variability is observed for this case.  $\tau_{558}$  at the best patch (P3) is 0.5, in better agreement with AERONET than MISR v17, whereas the range spanned by all accepted patches is from 0.4 to 0.5. Ångström Exponent at all four accepted patches in

the Research Retrieval is higher than AERONET and MISR v17 (from 0.79 to 1.49). The AOD spectrum in Figure 5-5c shows that, although AODs from the Research Retrieval at the best patch are closer to AERONET measurements in the blue and green channels, underestimation occurs at longer wavelengths, but the results are overall within the range of expected sensitivity.

Size and SSA retrievals are similar to those seen in the second case. The MISR v17 Algorithm obtains good agreement in size distribution and fine mode fraction (Table 5-11 and Figure 5-6c), but retrieves a nearly non-absorbing mid-visible SSA (0.99, Table 5-12) owing to the lack of absorbing fine mode components in the solution space. The Research Retrievals derive larger fine mode particles ( $r_{pg,N} = 0.13\text{--}0.16\ \mu\text{m}$ ) and higher fine mode fraction (95–100%) for all accepted patches because the clean day surface was used (Figure 5-7b). There is improved agreement in mid-visible SSA (0.899–0.935) to AERONET ( $SSA_A = 0.94$ ), although the SSA spectral slope in the Research Retrievals (+0.05 to +0.07) does not agree with AERONET (−0.07) as well as MISR v17 (−0.05) does. Again, considering the complexity of aerosol retrieval over land, the size and SSA retrieved by MISR and AERONET can exhibit similar levels of uncertainty.

#### **Ilorin\_20010217 (Case Group 4 — BB-Dust mixed, AOD > 0.9)**

For this extremely high AOD case ( $AOD_A = 1.74$ ) containing BB-dust mixtures, the most significant discrepancy in the MISR v17 retrievals is the underestimation of AOD by 0.96 (55%), which we expect is associated with difficulties in separating surface and atmospheric contributions to the satellite signals. The first surface RPV parameters (not shown) for clean day orbit, which roughly characterize brightness, are 55–70% less in all

eight patches than those retrieved by the Standard Algorithm on the hazy day. The third RPV parameters (Figure 5-7c) are also more negative for the clean day orbit, indicating more forward scattering should be attributed to the atmosphere. The use of clean day surface RPV in the Research Retrieval effectively eliminates the large low bias in  $AOD_M$ . The mid-visible AOD retrieved by the Research Algorithm is much closer to the AERONET value for all patches: 2.0 at patch P0 with a very high  $\chi^2$  of 6.83, and 1.55 at the best patch (P1). The range spanned by all the accepted patches is between 1.2 to 1.55. Figure 5-5d shows that the Research Algorithm obtains better agreement in the AOD magnitude, but steeper spectral slopes (higher Ångström Exponent), whereas the MISR v17 retrievals derive much lower AOD in all wavelengths, but Ångström Exponents closer to the AERONET measurements.

Table 5-11 and Figure 5-6d show that MISR v17 matches the AERONET size distribution well, capturing the two modes of 0.06 and 0.68  $\mu\text{m}$  with a fine mode fraction of around 35%. The accepted patches in the Research Retrievals (pink line and gray lines in Figure 5-6d) also show reasonable agreements with AERONET, having a larger fine mode size (0.07–0.13  $\mu\text{m}$ ), a coarse mode size of 0.5  $\mu\text{m}$ , and slightly higher fine mode fraction (50–60%). The MISR v17 retrievals derive a nearly non-absorbing mid-visible SSA (0.99, Table 5-12), whereas the Research Retrievals agree closely with AERONET ( $SSA_A = 0.93$ ), having a range between 0.90 and 0.92. SSA spectral slopes retrieved by the MISR v17 Standard Algorithm (–0.05) and by the Research Algorithm (–0.08 to –0.11) both match the value measured by AERONET (–0.08) fairly well. The results of lower dust fraction, larger fine mode, and better SSA agreement to AERONET are

similar to the results in the previous two cases, and may represent similar uncertainty for size and SSA retrievals in an atmosphere containing mixtures of BB and dust particles.

## 5.6 Summary and Conclusions

Biomass burning aerosols, because they are optically absorbing and highly variable spatially and temporally, are among the most uncertain climate forcing agents. The global multiangle, multi-spectral measurements made by the MISR instrument provide valuable information that can help improve our understanding of this important tropospheric constituent. To obtain as much information from the algorithm, and to ensure correct interpretation of the results, we systematically explored instrument sensitivity to particle properties, and assessed the performance of those component properties assumed in the instrument's Standard Algorithm.

Classifying coincident MISR and AERONET cases at major BB sites revealed distinct patterns of AOD and SSA discrepancies. Analyses of cases in each of four classes led to suggestions for specific refinements of the current MISR Standard Aerosol Retrieval Algorithm: the need to add to the algorithm particle climatology (1) absorbing particles having steeper SSA spectral dependence and (2) mixtures of dust and absorbing spherical particles. The comparison also shows the importance of refining the Standard algorithm surface representation for aerosol retrievals in some situations, when the mid-visible AOD exceeds about 0.5.

As reviewed in section 5.3, measurements from past BB field campaigns have established relationships between BB aerosol microscopical and optical properties, as

well as vegetation type, plume age, and fire phase. Based on our theoretical sensitivity study covering the observed range of BB particle size and mid-visible SSA, with about 20 percent uncertainty in fractional, mid-visible column AOD, MISR is able to differentiate particles in two to three categories each of size (very small to small, medium, large) and SSA (very absorbing, absorbing, weakly to less absorbing) over dark surfaces. The detailed result depends on the actual size distribution and SSA of the atmospheric component. For a total column AOD of 0.2 or less, MISR has poor sensitivity to size and SSA when the assumed atmospheric particles are absorbing or of medium sizes, but increases considerably when the column AOD is raised to 0.5. The retrieved total column AOD is constrained to at least  $\pm 0.05$  for these situations.

Research Retrievals were carried out for representative cases, with the proposed BB components and mixtures and importantly, with prescribed surface properties derived on days having relatively low aerosol loading. AOD from the MISR Research Retrieval for the patches having the best-fitting results were consistently in better agreement with AERONET than the MISR v17 Standard Retrievals. For cases with AOD < 1.0, retrieved AODs were within 14%, whereas for the extreme case with AOD  $\sim 1.7$ , the Research Algorithm constrained the AOD to within 0.19 (11%), even when the MISR and AERONET particle properties did not agree well.

For the BB-dominated example, in addition to the improved AOD results, size, SSA, and  $\alpha_{\omega_0}$  retrievals were in agreement with AERONET, and the size and SSA retrieval sensitivity was similar to that in the theoretical study. In the three mixed BB-dust cases, the atmosphere consisted of a bi-modal distribution containing an absorbing, spherical

fine mode component and a comparable amount of a coarse mode component. Also, high spatial variability of aerosol amount and properties was evident from Research Retrieval results over multiple, closely spaced patches. The Research Retrievals derived a larger fine mode size and lower coarse mode fraction than AERONET, but showed closer agreement in SSA. The difference in fine mode size and fraction can be attributed to the combination of uncertainties in surface characterization, representative non-spherical particle modeling for both MISR and AERONET, sampling differences, and spatial variability.

The MISR results can be compared with the validation studies performed for Moderate Resolution Imaging Spectroradiometer (MODIS) BB aerosol retrievals over land. MODIS AOD retrieval results are sensitive to the prescribed particle SSA, which, unlike MISR, is not constrained by observations in the retrieval process, but is assigned *a priori* to each geographic region as a function of season [Remer *et al.*, 2005; Levy *et al.*, 2007b]. Ichoku *et al.* [2003] found that lowering the mid-visible SSA from 0.90 to 0.86 essentially eliminates the prevailing low bias of MODIS AOD (compared to AERONET) during SAFARI 2000. Our case study showed that the spectral dependence of SSA is also an important parameter for retrieving BB particles. When particle models with steeper SSA spectral slopes, as observed under ambient conditions, are included in the Research Retrieval Algorithm particle climatology, the high bias in retrieved SSA and low bias in AOD in the MISR Standard Retrievals were simultaneously eliminated for the BB-dominated cases.

Mi *et al.* [2007] evaluated the MODIS AOD retrievals over land at two AERONET sites in China. They found that the recently released Collection 5 MODIS aerosol land

algorithm (C005), which uses a more sophisticated assumption for surface reflectance (as a function of vegetation type and scattering angle) and spheroidal models for representative dust particles [Levy *et al.*, 2007a], retrieves AODs in better agreement to AERONET than the previous C004 algorithm, which uses a fixed surface reflectance ratio and spherical coarse models. The results in *Mi et al.* [2007] cannot be compared directly to this study, because of the large differences between the MODIS and MISR instruments and retrieval algorithms. However, our results for the mixed BB-dust case with extremely high AOD, and the comparisons among patches with different surface conditions for each case, also demonstrate the importance of detailed and accurate surface characterization for successfully retrieving aerosol amount and properties over land. New strategies for constraining surface properties should be considered when aerosol retrieval algorithms are developed for the future.

**Acknowledgment.** We thank the AERONET network site managers for granting the use of AERONET data, and Alexander Smirnov for many helpful suggestions on AERONET data quality. The authors gratefully acknowledge the NOAA Air Resources Laboratory (ARL) for providing the HYSPLIT transport and dispersion model used in this publication. The authors also thank Barbara Gaitley at the Jet Propulsion Laboratory (JPL), California Institute of Technology (Caltech), for the help in processing the MISR-AERONET coincident data, and y and Michael Bull at JPL, Caltech for advice regarding the MISR standard aerosol retrieval algorithm implementation. The work of R. Kahn, K. Yau, and D. Nelson is supported in part by NASA's Climate and Radiation Research and Analysis Program, under H. Maring, NASA's Atmospheric Composition Program under

P. DeCola, and the EOS-MISR instrument project; it is performed at the JPL, Caltech, under contract with NASA, and at the NASA Goddard Space Flight Center.

## References

- Abel, S., J. M. Haywood, E. J. Highwood, J. Li, and P. R. Buseck (2003), Evolution of biomass burning aerosol properties from an agricultural fire in south Africa, *Geophys. Res. Lett.*, *30*, 15, 1783, doi:10.1029/2003GL017342.
- Ackerman, T. P., A. J. Braverman, D. J. Diner, T. L. Anderson, R. A. Kahn, J. V. Martonchik, J. E. Penner, P. J. Rasch, B. A. Wielicki, and B. Yu (2004), Integrating and interpreting aerosol observations and models within the PARAGON framework, *Bull. Am. Met. Soc.*, *85*, 1523–1533.
- Anderson, B. E., W. B. Grant, G. L. Gregory, E. V. Browell, J. E. Collins Jr., G. W. Sachse, D. R. Bagwell, C. H. Hudgins, D. R. Blake, and N. J. Blake (1996), Aerosols from biomass burning over the tropical South Atlantic region: Distributions and impacts, *J. Geophys. Res.*, *101*(D19), 24,117–24,137.
- Andreae, M. O., and P. Merlet (2001), Emission of trace gases and aerosols from biomass burning, *Global Biogeochem. Cycles*, *15*(4), 955–966.
- Bergstrom, R. W., P. Pilewskie, B. Schmid, and P. B. Russell (2003), Estimates of the spectral aerosol single scattering albedo and aerosol radiative effects during SAFARI 2000, *J. Geophys. Res.*, *108*(D13), 8474, doi:10.1029/2002JD002435.
- Bond, T. C., and R. W. Bergstrom (2006), Light absorption by carbonaceous particles: An investigative review, *Aerosol Sci. and Tech.*, *40*, 27–67.
- Bond, T. C., D. G. Streets, K. F. Yarber, S. M. Nelson, J.-H. Woo, and Z. Klimont (2004) A technology-based global inventory of black and organic carbon emissions from combustion, *J. Geophys. Res.*, *109*(D14), D14203, doi:10.1029/2003JD003697.
- Collins, W. D., P. J. Rasch, B. E. Eaton, B. V. Khattatov, J.-F. Lamarque, and C. S. Zender (2001), Simulating aerosols using a chemical transport model with assimilation of satellite aerosol retrievals: Methodology for INDOEX, *J. Geophys. Res.*, *106*(D7), 7313–7336.
- Diner, D. J., J. C. Beckert, T. H. Reilly, C. J. Bruegge, J. E. Conel, R. A. Kahn, J. V. Martonchik, T. P. Ackerman, R. Davies, S. A. W. Gerstl, H. R. Gordon, J.-P. Muller, R. B. Myneni, P. J. Sellers, B. Pinty, and M. M. Verstraete (1998), Multi-angle imaging spectroradiometer (MISR) instrument description and experiment overview, *IEEE Trans. Geosci. Remote Sens.*, *36*, 1072–1087.
- Diner, D. J., W. A. Abdou, T. P. Ackerman, K. Crean, H. R. Gordon, R. A. Kahn, J. V. Martonchik, S. McMuldroy, S. R. Paradise, B. Pinty, M. M. Verstraete, M. Wang, and R. A. West (2001), MISR level 2 aerosol retrieval algorithm theoretical basis, *Rep. JPL D-11400, Rev. E*, Jet Propul. Lab., Pasadena, Calif.

- Draxler, R. R., and G. D. Rolph, (2003), HYSPLIT (HYbrid Single-Particle Lagrangian Integrated Trajectory) Model access via NOAA ARL READY Website (<http://www.arl.noaa.gov/ready/hysplit4.html>). NOAA Air Resources Laboratory, Silver Spring, MD.
- Dubovik, O., B. N. Holben, Y. J. Kaufman, M. Yamasoe, A. Smirnov, D. Tanré, and I. Slutsker (1998), Single-scattering albedo of smoke retrieved from the sky radiance and solar transmittance measured from ground, *J. Geophys. Res.*, *103*(D24), 31,903–31,923.
- Dubovik, O., A. Smirnov, B. N. Holben, M. D. King, Y. J. Kaufman, T. F. Eck, and I. Slutsker (2000), Accuracy assessments of aerosol optical properties retrieved from Aerosol Robotic Network (AERONET) sun and sky radiance measurements, *J. Geophys. Res.*, *105*, 9791–9806.
- Dubovik, O., B. N. Holben, T. F. Eck, A. Smirnov, Y. J. Kaufman, M. D. King, D. Tanré, and I. Slutsker (2002), Variability of absorption and optical properties of key aerosol types observed in worldwide locations, *J. Atmos. Sci.*, *59*, 590–608.
- Duncan, B. N., R. V. Martin, A. C. Staudt, R. Yevich, and J. A. Logan (2003), Interannual and seasonal variability of biomass burning emissions constrained by satellite observations, *J. Geophys. Res.*, *108*(D2), 4100, doi:10.1029/2002JD002378.
- Eck, T. F., B. N. Holben, I. Slutsker, and A. Setzer (1998), Measurements of irradiance attenuation and estimation of aerosol single scattering albedo for biomass burning aerosols in Amazonia, *J. Geophys. Res.*, *103*(D24), 31,865–31,878.
- Eck, T. F., B. N. Holben, J. S. Reid, N. T. O'Neill, J. S. Schafer, O. Dubovik, A. Smirnov, M. A. Yamasoe, and P. Artaxo (2003a), High aerosol optical depth biomass burning events: a comparison of optical properties for different source regions, *Geophys. Res. Lett.*, *30*, 2035, doi:10.1029/2003GL017861.
- Eck, T. F., B. N. Holben, D. E. Ward, M. M. Mukelabai, O. Dubovik, A. Smirnov, J. S. Schafer, N. C. Hsu, S. J. Piketh, A. Queface, J. L. Roux, R. J. Swap, and I. Slutsker (2003b), Variability of biomass burning aerosol optical characteristics in southern Africa during the SAFARI 2000 dry season campaign and a comparison of single scattering albedo estimates from radiometric measurements, *J. Geophys. Res.*, *108*(D13), 8477, doi:10.1029/2002JD002321.
- Einfeld, W., D. E. Ward, and C. C. Hardy (1991), Effects of fire behavior on prescribed fire smoke characteristics: A case study in *Global Biomass Burning: Atmospheric, Climatic, and Biospheric Implications*, edited by J. S. Levine, pp. 412–419, MIT Press, Cambridge, Mass.
- Formenti, P., W. Elbert, W. Maenhaut, J. Haywood, S. Osborne, and M. O. Andreae (2003), Inorganic carbonaceous aerosols during the Southern African Regional Science Initiative (SAFARI 2000) experiment: Chemical characteristics, physical

properties, and emission data for smoke from African biomass burning, *J. Geophys. Res.*, 108(D13), 8488, doi:10.1029/2002JD002408.

- Forster, P., V. Ramaswamy, P. Artaxo, T. Berntsen, R. Betts, D. W. Fahey, J. Haywood, J. Lean, D. C. Lowe, G. Myhre, J. Nganga, R. Prinn, G. Raga, M. Schulz, and R. Van Dorland (2007) Changes in Atmospheric Constituents and in Radiative Forcing in *Climate Change 2007: The Physical Science Basis. Contribution of Working Group I to the Fourth Assessment Report of the Intergovernmental Panel on Climate Change*, edited by S. Solomon, D. Qin, M. Manning, Z. Chen, M. Marquis, K. B. Averyt, M. Tignor, and H. L. Miller, pp. 129–234, Cambridge University Press, Cambridge, UK and New York, NY, USA.
- Guyon, P., B. Graham, J. Beck, O. Boucher, E. Gerasopoulos, O. L. Mayol-Bracero, G. C. Roberts, P. Artaxo, and M. O. Andreae (2003), Physical properties and concentration of aerosol particles over the Amazon tropical forest during background and biomass burning conditions, *Atmos. Chem. Phys.*, 3, 951–967.
- Grant, I. P., and G. E. Hunt (1968), Solution of radiative transfer problems using invariant  $S_n$  method, *Mon. Not. R. Astron. Soc.*, 141, 1–27.
- Haywood, J. M., P. N. Francis, O. Dubovik, M. Glew, and B. N. Holben (2003a), Comparison of aerosol size distributions, radiative properties, and optical depths determined by aircraft observations and Sun photometers during SAFARI 2000, *J. Geophys. Res.*, 108(D13), 8471, doi:10.1029/2002JD002250.
- Haywood, J. M., S. R. Osborne, P. N. Francis, A. Keil, P. Formenti, M. O. Andreae, and P. H. Kaye (2003b), The mean physical and optical properties of regional haze dominated by biomass burning aerosol measured from the C-130 aircraft during SAFARI 2000, *J. Geophys. Res.*, 108(D13), 8473, doi:10.1029/2002JD002226.
- Hobbs, P. V., J. S. Reid, J. A. Herring, J. D. Nance, R. E. Weiss, J. L. Ross, D. A. Hegg, R. D. Ottmar, and C. Lioussé (1996), Particle and trace-gas measurements in the smoke from prescribed burns of forest products in the Pacific Northwest, in *Biomass Burning and Global Change*, edited by J. S. Levine, pp. 697–715, MIT Press, Cambridge, Mass.
- Hobbs, P. V., J. S. Reid, R. A. Kotchenruther, R. J. Ferek, and R. Weiss (1997), Direct radiative forcing by smoke from biomass burning, *Science*, 275, 1776–1778.
- Holben, B. N., Y. J. Kaufman, A. W. Setzer, D. D. Tanré, and D. E. Ward (1991), Optical properties of aerosol emissions from biomass burning in the Tropics, BASE-A, in *Global Biomass Burning: Atmospheric, Climatic and Biospheric Implications*, edited by J. S. Levine, pp. 403–411, MIT Press, Cambridge, Mass.
- Holben, B. N., T. F. Eck, I. Slutsker, D. Tanré, J. P. Buis, A. Setzer, E. Vermote, J. A. Reagan, Y. J. Kaufman, T. Nakajima, F. Lavenu, I. Jankowiak, and A. Smirnov (1998), AERONET: A federated instrument network and data archive for aerosol characterization, *Remote Sens. Environ.*, 66, 1–16.

- Ichoku, C., L. A. Remer, Y. J. Kaufman, R. Levy, D. A. Chu, D. Tanré, and B. N. Holben (2003), MODIS observation of aerosols and estimation of aerosol radiative forcing over southern Africa during SAFARI 2000, *J. Geophys. Res.*, *108*(D13), 8499, doi:10.1029/2002JD002366.
- Iziomon, M. G. and U. Lohman (2003), Optical and meteorological properties of smoke-dominated haze at the ARM Southern Great Plains Central Facility, *Geophys. Res. Lett.*, *30*, 3, 1123, doi:10.1029/2002GL016606.
- Kahn, R. A., R. West, D. McDonald, B. Rheingans, and M. I. Mishchenko (1997), Sensitivity of multiangle remote sensing observations to aerosol sphericity, *J. Geophys. Res.*, *102*(D14), 16,861–16,870.
- Kahn, R. A., P. Banerjee, and D. McDonald (2001), Sensitivity of multiangle imaging to natural mixtures of aerosols over ocean, *J. Geophys. Res.*, *106*(D16), 18,219–18,238.
- Kahn, R. A., P. Banerjee, D. McDonald, and D. J. Diner (1998), Sensitivity of multiangle imaging to aerosol optical depth and to pure-particle size distribution and composition over ocean, *103*(D24), 32,195–32,213.
- Kahn, R. A., B. Gaitley, J. V. Martonchik, D. J. Diner, K. A. Crean, and B. N. Holben (2005a), Multiangle imaging spectroradiometer (MISR) global aerosol optical depth validation based on 2 years of coincident aerosol robotic network (AERONET) observations, *J. Geophys. Res.*, *110*(D10), doi:10:1029/2004JD004706.
- Kahn, R. A., W.-H. Li, J. V. Martonchik, C. Bruegge, D. J. Diner, B. Gaitley, W. Abdou, O. Dubovik, B. N. Holben, S. Smirnov, Z. Jin, and D. Clark, (2005b), MISR low-light-level calibration, and implications for aerosol retrieval over dark water, *J. Atmosph. Sci.*, *62*, 1032–1062.
- Kalashnikova, O., R. A. Kahn, I. N. Sokolik, and W.-H. Li (2005), Ability of multiangle remote sensing observations to identify and distinguish mineral dust types: Optical models and retrievals of optically thick plumes, *J. Geophys. Res.*, *110*(D18), D18S14, doi:10.1029/2004JD004550.
- Kalashnikova, O., and R. A. Kahn (2006), Ability of multiangle remote sensing observations to identify and distinguish mineral dust types: 2. Sensitivity over dark water, *J. Geophys. Res.*, *111*, D11207, doi:10.1029/2005JD006756.
- Kreidenweis, S. M., L. A. Remer, R. Brientjes, and O. Dubovik (2001), Smoke aerosol from biomass burning in Mexico: Hygroscopic smoke optical model, *J. Geophys. Res.*, *106*(D5), 4831–4844.
- Le Canut, P., M. O. Andreae, G. W. Harris, F. G. Wienhold, and T. Zenker (1996a), Aerosol optical properties over southern Africa during SAFARI-92, in *Biomass Burning and Global change*, edited by J. S. Levine, pp. 441–459, MIT Press, Cambridge, Mass.

- Le Canut, P., M. O. Andreae, G. W. Harris, F. G. Wienhold, and T. Zenker (1996b), Airborne studies of emissions from savanna fires in southern Africa 1. Aerosol emission measured with a laser optical particle counter, *J. Geophys. Res.*, *101*(D19), 23,615–23,630.
- Levy, R. C., L. A. Remer, S. Mattoo, E. Vermote, and Y. J. Kaufman (2007a), Second-generation operational algorithm: Retrieval of aerosol properties over land from inversion of Moderate Resolution Imaging Spectroradiometer spectral reflectance, *J. Geophys. Res.*, *112*, D13211, doi:10.1029/2006JD007811.
- Levy, R. C., L. A. Remer, and O. Dubovik (2007b), Global aerosol optical models and application to MODIS aerosol retrieval over land, *J. Geophys. Res.*, *112*, D13210, doi:10.1029/2006JD007815.
- Magi, B. I., P. V. Hobbs, B. Schmid, and J. Redemann (2003), Vertical profile of light scattering, light absorption, and single-scattering albedo during the dry, biomass burning season in southern Africa and comparisons of in situ and remote sensing measurements of aerosol optical depth, *J. Geophys. Res.*, *108*(D13), 8504, doi:10.1029/2002JD002361.
- Martins, J. V., P. Artaxo, P. V. Hobbs, C. Liou, H. Cashier, Y. J. Kaufman, and A. Plana-Fattori (1996), Particle size distributions, elemental compositions, carbon measurements, and optical properties of smoke from biomass burning in the Pacific Northwest of the United States, in *Biomass Burning and Global Change*, edited by J. S. Levine, pp. 716–732, MIT Press, Cambridge, Mass.
- Martins, J. V., P. Artaxo, C. Liou, J. S. Reid, P. V. Hobbs, and Y. J. Kaufman (1998), Effects of black carbon content, particle size, and mixing on light absorption by aerosols from biomass burning in Brazil, *J. Geophys. Res.*, *103*(D24), 32,041–32,050.
- Martonchik, J. V., D. J. Diner, K. A. Crean, and M. A. Bull (2002), Regional aerosol retrieval results from MISR, *IEEE Trans, Geosci. Remote Sens.*, *40*, 1520–1531.
- Martonchik, J. V., D. J. Diner, R. A. Kahn, T. P. Ackerman, M. M. Verstraete, B. Pinty, and H. R. Gordon (1998), Techniques for the retrieval of aerosol properties over land and ocean using multiangle imaging, *IEEE Trans, Geosci. Remote Sens.*, *36*, 1212–1227.
- Mi, W., Z. Li, X. Xia, B. N. Holben, R. C. Levy, F. Zhao, H. Chen, and M. Cribb (2007), Evaluation of the Moderate Resolution Imaging Spectroradiometer aerosol products at two Aerosol Robotic Network stations in China, *J. Geophys. Res.*, *112*, D22S08, doi:10.1029/2007JD008474.
- Miller, J. R., and N. T. O'Neill (1997), Multi-altitude airborne observations of isolation effects of forest fire smoke aerosols at BOREAS: Estimates of aerosol optical parameters, *J. Geophys. Res.*, *102*(D24), 29,729–29,736.

- Petters, M. D., A. J. Prenni, S. M. Kreidenweis, P. J. DeMott, A. Matsunaga, Y. B. Lim, and P. J. Ziemann (2006), Chemical aging and the hydrophobic-to-hydrophilic conversion of carbonaceous aerosol, *Geophys. Res. Lett.*, *33*, 24, L24806, doi:10.1029/2006GL027249.
- Pilewskie, P., J. Pommier, R. W. Bergstrom, W. Gore, S. Howard, M. Rabbette, B. Schmid, P. V. Hobbs, and S. C. Tsay (2003), Solar spectral radiative forcing during the Southern African regional science Initiative, *J. Geophys. Res.*, *108*(D13), 8486, doi:10.1029/2002JD002411.
- Pósfai, M., R. Simonics, J. Li, P. V. Hobbs, and P. R. Buseck (2003), Individual aerosol particles from biomass burning in southern Africa: 1. Compositions and size distributions of carbonaceous particles, *J. Geophys. Res.*, *108*(D13), 8483, doi:10.1029/2002JD002291.
- Radke, L. F., D. A. Hegg, P. V. Hobbs, J. D. Nance, J. H. Lyons, K. K. Laursen, R. E. Weiss, P. J. Riggan, and D. E. Ward (1991), Particulate and trace gas emissions from large biomass fires in North America, in *Global Biomass Burning: Atmospheric, Climatic and Biospheric Implications*, edited by J. S. Levine, pp. 209–224, MIT Press, Cambridge, Mass.
- Radke, L. F., D. A. Hegg, J. H. Lyons, C. A. Brock, P. V. Hobbs, R. Weiss, and R. Rasmussen (1988), Airborne measurements on smokes from biomass burning, in *Aerosols and Climate*, edited by P. V. Hobbs and M. P. McCormick, pp. 411–422, Deepak Publishing, Hampton, VA.
- Rahman, H., B. Pinty, and M. Verstraete (1993), Coupled surface atmosphere reflectance (CSAR) model, 2, Semiempirical surface model usable with NOAA advanced very high resolution radiometer data, *J. Geophys. Res.*, *98*(D11), 20,791–20,801.
- Reid, J. S., and P. V. Hobbs (1998), Physical and optical properties of young smoke from individual biomass fires in Brazil, *J. Geophys. Res.*, *103*(D24), 32,013–32,030.
- Reid, J. S., P. V. Hobbs, C. Lioussé, J. V. Martins, R. E. Weiss, and T. F. Eck (1998a), Comparisons of techniques for measuring shortwave absorption and black carbon content of aerosols from biomass burning in Brazil, *J. Geophys. Res.*, *103*(D24), 32,031–32,040.
- Reid, J. S., P. V. Hobbs, R. J. Ferek, D. K. Blake, J. V. Martins, M. R. Dunlap, and C. Lioussé (1998b), Physical, chemical, and optical properties of regional hazes dominated by smoke in Brazil, *J. Geophys. Res.*, *103*(D24), 32,059–32,080.
- Reid, J. S., T. F. Eck, S. A. Christopher, P. V. Hobbs, and B. N. Holben (1999), Use of the Ångström exponent to estimate the variability of optical and physical properties of aging smoke particles in Brazil, *J. Geophys. Res.*, *104*(D22), 27,473–27,489.

- Reid, J. S., R. Koppmann, T. F. Eck, and D. P. Eleuterio (2005a), A review of biomass burning emissions, part II: Intensive physical properties of biomass burning particles, *Atmos. Chem. Phys.*, *5*, 799–825.
- Reid, J. S., T. F. Eck, S. A. Christopher, R. Koppmann, O. Dubovik, D. P. Eleuterio, B. N. Holben, E. A. Reid, and J. Zhang (2005b), A review of biomass burning emissions, part III: Intensive optical properties of biomass burning particles, *Atmos. Chem. Phys.*, *4*, 827–849.
- Remer, L. A., Y. J. Kaufman, B. N. Holben, A. M. Thompson, and D. McNamara (1998), Biomass burning aerosol size distribution and modeled optical properties, *J. Geophys. Res.*, *103*(D24), 31,879–31,891.
- Remer, L. A., Y. J. Kaufman, D. Tanré, S. Mattoo, D. A. Chu, J. V. Martins, R. R. Li, C. Ichoku, R. C. Levy, R. G. Kleidman, T. F. Eck, E. Vermote, and B. N. Holben (2005), The MODIS aerosol algorithm, products, and validation, *J. Atmos. Sci.*, *62*(4), 947–973.
- Sinyuk, A., O. Dubovik, B. Holben, T. F. Eck, F.-M. Breon, J. Martonchik, R. Kahn, D. Diner, E. F. Vermote, Y. J. Kaufman, J. C. Roger, T. Lapyonok, and I. Slutsker (2007), Simultaneous retrieval of aerosol and surface properties from a combination of AERONET and satellite data, *Remote Sensing Environ.*, *107*, 90–108, doi:10.1016/j.rse.2006.07.022.
- Trentmann, J., M. O. Andreae, H.-F. Graf, P. V. Hobbs, R. D. Ottmar, and T. Trautmann (2002), Simulation of a biomass-burning plume: Comparison of model results with observations, *J. Geophys. Res.*, *107*(D2), 4013, doi:10.1029/2001JD000410.
- Yamasoe, M. A., Y. J. Kaufman, O. Dubovik, L. A. Remer, B. N. Holben, and P. Artaxo (1998), Retrieval of the real part of the refractive index of smoke particles from Sun/sky measurements during SCAR-B, *J. Geophys. Res.*, *103*(D24), 31,893–31,902.
- Zhang, J., S. A. Christopher, and B. N. Holben (2001), Intercomparison of smoke aerosol optical thickness derived from GOES 8 imager and ground-based Sun photometers, *J. Geophys. Res.*, *106*(D7), 7387–7397.

Table 5-1. AERONET Sites in Major BB Regions Selected for Coincident MISR-AERONET Measurement Comparisons

Site	Lat.	Lon.	Alt., m	# of all cases	# of $\tau_{558} > 0.15$ cases
W. Africa					
Banizoumbou	13.53	2.67	250	7	5
Ilorin	8.32	4.33	350	5	5
Ouagadougou	12.18	-1.38	290	7	7
S. Africa					
Mongu	-15.25	23.15	1107	3	1
Skukuza	-24.98	31.58	150	8	3
S. America					
Alta Floresta	-9.92	-56.02	175	0	0
Belterra	-2.65	-54.95	70	1	1
Cuiaba-Miranda	-15.72	-56.02	210	2	2
				(total = 33)	(total = 24)

Table 5-2. Characteristics of Four Groups of BB Cases, Based on Comparisons of AOD and SSA for Coincident MISR-AERONET Measurements

Group	Location–Season (# of Cases)	MISR-AERONET Comparison	Ambient Aerosol	Possible Reason for MISR Discrepancies
1	S. America–Aug (3) S. Africa–Mar, Jun, Aug (4)  (total = 7 cases)	$AOD_A = 0.2$ to $0.5$ $AOD_{M-A} = -0.17$ to $0$ $\dot{A}_A = 1.4$ to $1.9$ $\dot{A}_{M-A} = -0.6$ to $+0.2$ $SSA_A = 0.80$ to $0.91$ $SSA_{M-A} = 0.05$ to $0.14$ $\alpha_{\omega_0 A} = 0.08$ to $0.17$ $\alpha_{\omega_0 M-A} = -0.16$ to $-0.10$ MISR AOD spherical fraction = $0.8$ to $1.0$	BB- dominated	SSA spectral dependence in MISR component particle models is not sufficiently steep
2	W. Africa–Jan, Feb, Mar (4)  (total = 4 cases)	$AOD_A = 0.5$ to $0.9$ $AOD_{M-A} = -0.3$ to $-0.1$ $\dot{A}_A = 0.2$ to $0.8$ $\dot{A}_{M-A} = -0.1$ to $+0.9$ $SSA_A = 0.82$ to $0.92$ $SSA_{M-A} = 0.08$ to $0.13$ $\alpha_{\omega_0 A} = -0.11$ to $-0.01$ $\alpha_{\omega_0 M-A} = 0.06$ to $0.09$ MISR AOD spherical fraction = $0.8$ to $1.0$	BB-dust mixed	No BB-dust mixtures in MISR mixture climatology
3	W. Africa–Dec, Jan, Mar, Jun (9)  (total = 9 cases)	$AOD_A = 0.2$ to $0.6$ $AOD_{M-A} = -0.1$ to $+0.1$ $\dot{A}_A = 0.1$ to $0.8$ $\dot{A}_{M-A} = 0.1$ to $0.5$ $SSA_A = 0.93$ to $0.99$ $SSA_{M-A} = 0.01$ to $0.05$ $\alpha_{\omega_0 A} = -0.08$ to $-0.01$ $\alpha_{\omega_0 M-A} = -0.02$ to $+0.07$ MISR AOD spherical fraction = $0.4$ to $1.0$	BB-dust mixed	No BB-dust mixtures in MISR mixture climatology

(Continued)

Group	Location–Season ( # of Cases)	MISR-AERONET Comparison	Ambient Aerosol	Possible Reason for MISR Discrepancies
4	W. Africa–Dec, Feb (4)  (total = 4 cases)	$AOD_A = 0.9$ to $1.7$ $AOD_{M-A} = -1.0$ to $-0.2$ $\dot{A}_A = 0.2$ to $0.4$ $\dot{A}_{M-A} = 0$ to $+0.5$ $SSA_A = 0.93$ to $0.96$ $SSA_{M-A} = 0.04$ to $0.06$ $\alpha_{\omega_0 A} = -0.08$ to $-0.07$ $\alpha_{\omega_0 M-A} = 0.02$ to $0.07$ MISR AOD spherical fraction = $0.5$ to $1.0$	BB-dust mixed	Poor separation of surface and aerosol properties in the MISR retrieval

Table 5-3. BB Aerosol Physical and Optical Property References Covered in This Review of the Field Experiment Literature

Region	Field Experiment	Experimental Period	Vegetation	Reference for Parameter <sup>d</sup>		
				Size <sup>a</sup>	SSA <sup>b</sup>	$n_r$ - $in_i$ <sup>c</sup>
S. Africa	SAFARI-92	Aug–Oct 1992	savanna	1	---	---
	SAFARI 2000	Aug–Sep 2000	savanna	2	3	4
	SAFARI 2001	Aug–Sep 2001	savanna	---	5	---
	AERONET	1995–2000	savanna	6	6	6
Amazon Basin	BASE-A	Sep 1989	cerrado	7	---	---
	LBA- EUSTACH	1999	forest	8	8	8
	TRACE A	Sep–Ocy 1992	forest	9	9	---
	SCAR-B	Aug–Sep 1995	forest/ cerrado	10	11	12
	AERONET	1993–1994; 1998– 1999; 2002	forest	6	6	6
	AERONET	1993–1995	cerrado	13	13	13
N. America	Indept. Study	Sep 1986–Sep 1989	boreal forest	14	15	---
	ARM SGP	1997–2001	N/A	---	16	---
	AERONET	1994–1998; 2002	boreal forest	6	6	6
(California)	Indept. Study	Dec 1986; Jun 1987	chaparral	---	15	---
(Pacific NW)	SCAR-C	Sep 1994	boreal forest	17	17	18
(Canada)	BOREAS	Jul–Aug 1994	boreal forest	---	19	---
Central America	Indept. Study	Maay 1998	N/A	20	21	20

<sup>a</sup>Size distribution parameters.

<sup>b</sup>Single scattering albedo.

<sup>c</sup>Refractive index.

<sup>d</sup>Reference:

1. *Le Canut et al.* [1996a, b].

2. *Eck et al.* [2003b]; *Haywood et al.* [2003b]; *Pósfai et al.* [2003].

3. *Abel et al.* [2003]; *Bergstrom et al.* [2003]; *Eck et al.* [2003b]; *Formenti et al.* [2003]; *Haywood et al.* [2003a, b]; *Pilewskie et al.* [2003].

4. *Haywood et al.* [2003a, b].

5. *Magi et al.* [2003].

Table 5-3. (Continued)

<sup>d</sup>Reference (continued):

6. *Dubovik et al.* [2002]; *Eck et al.* [2003a].
7. *Holben, et al.* [1991].
8. *Guyon et al.* [2003].
9. *Anderson et al.* [1996].
10. *Reid and Hobbs* [1998]; *Reid et al.* [1998b]; *Reid, et al.* [1999]; *Remer et al.* [1998].
11. *Dubovik et al.* [1998]; *Eck et al.* [1998]; *Hobbs et al.* [1997]; *Martins et al.* [1998]; *Reid and Hobbs* [1998]; *Reid et al.* [1998a, b]; *Reid et al.* [1999]; *Remer et al.* [1998].
12. *Eck et al.* [1998]; *Yamasoe et al.* [1998].
13. *Dubovik et al.* [2002].
14. *Einfeld et al.* [1991]; *Radke et al.* [1991].
15. *Radke et al.* [1988]; *Radke et al.* [1991].
16. *Iziomon and Lohman* [2003].
17. *Hobbs et al.* [1996]; *Martins et al.* [1996]; *Trentmann et al.* [2002].
18. *Trentmann et al.* [2002].
19. *Miller and O'Neill* [1997].
20. *Kreidenweis et al.* [2001].
21. *Kreidenweis et al.* [2001]; *Zhang et al.* [2001].

Table 5-4. Profiles of Fresh Plumes, Aged Plumes, and Haze Based on the Literature<sup>a</sup>

Parameter	Fresh Plume (< One Day Old)	Aged Plume (1 to 3 Days Old)	Regional Haze (> 3 Days Old or Mixed Age)
$r_{pg,N_s}$ $\mu\text{m}$	0.03–0.17 (0.074) n = 13	0.08–0.20 (0.12) n = 10	0.03–0.14 (0.07) n = 24
$\sigma_g$	1.30–1.91 (1.68) n = 13	1.25–1.65 (0.49) n = 10	1.30–2.01 (1.67) n = 24
$\omega_{0,450}$	0.77–0.86 (0.83) n = 6	0.87–0.94 (0.91) n = 17	0.84–0.87 (0.86) n = 3
$\omega_{0,550}$	0.70–0.94 (0.84) n = 32	0.78–0.94 (0.88) n = 33	0.79–0.94 (0.85) n = 38
$\omega_{0,670}$	0.60 (0.60) n = 1	0.86–0.88 (0.87) n = 6	0.84–0.98 (0.92) n = 9
$\omega_{0,700}$	0.67–0.80 (0.74) n = 6	0.83–0.91 (0.87) n = 17	0.69–0.75 (0.72) n = 3
$\omega_{0,870}$	N/A (N/A) n = 0	0.83–0.92 (0.85) n = 8	0.80–0.96 (0.86) n = 12
$n_{r,550}$	1.50–1.54 (1.53) n = 4	1.50–1.54 (1.52) n = 5	1.43–1.55 (1.50) n = 6

<sup>a</sup>The first row for each parameter shows the range, second row, the average in parentheses, and third row, the number of reported values.

Table 5-5. BB Aerosol Component Models

#	Component Model	$r_{pg,N}$ $\mu\text{m}$	$\sigma_g$	$\omega_{0,446}$	$\omega_{0,558}$	$\omega_{0,672}$	$\omega_{0,867}$	$n_r$ (all $\lambda$ 's)	Description
1	VS_VA	0.04	1.6	0.782	0.737	0.691	0.613	1.50	very small, very absorbing
2	S_VA	0.07	1.6	0.782	0.737	0.691	0.613	1.50	small, very absorbing
3	M_VA	0.13	1.6	0.782	0.737	0.691	0.613	1.50	medium, very absorbing
4	L_VA	0.16	1.6	0.782	0.737	0.691	0.613	1.50	large, very absorbing
5	VS_A	0.04	1.6	0.861	0.838	0.816	0.777	1.50	very small, absorbing
6	S_A	0.07	1.6	0.861	0.838	0.816	0.777	1.50	small, absorbing
7	M_A	0.13	1.6	0.861	0.838	0.816	0.777	1.50	medium, absorbing
8	L_A	0.16	1.6	0.861	0.838	0.816	0.777	1.50	large, absorbing
9	VS_LA	0.04	1.6	0.910	0.899	0.888	0.868	1.50	very small, less absorbing
10	S_LA	0.07	1.6	0.910	0.899	0.888	0.868	1.50	small, less absorbing
11	M_LA	0.13	1.6	0.910	0.899	0.888	0.868	1.50	medium, less absorbing
12	L_LA	0.16	1.6	0.910	0.899	0.888	0.868	1.50	large, less absorbing
13	VS_WA	0.04	1.6	0.950	0.939	0.928	0.908	1.50	very small, weakly absorbing
14	S_WA	0.07	1.6	0.950	0.939	0.928	0.908	1.50	small, weakly absorbing
15	M_WA	0.13	1.6	0.950	0.939	0.928	0.908	1.50	medium, weakly absorbing
16	L_WA	0.16	1.6	0.950	0.939	0.928	0.908	1.50	large, weakly absorbing

Table 5-6. BB Aerosol Mixing Groups<sup>a,b</sup>

Mixing Group (Description)	Component 1	Component 2	Component 3	Component 4
M1 (SSA=VA; size=VS)	1_VS_VA	2_S_VA	3_M_VA	4_L_VA
M2 (SSA=A; size=VS)	5_VS_A	6_S_A	7_M_A	8_L_A
M3 (SSA=LA; size=VS)	9_VS_LA	10_S_LA	11_M_LA	12_L_LA
M4 (SSA=WA; size=VS)	13_VS_WA	14_S_WA	15_M_WA	16_L_WA
M5 (SSA=VA)	1_VS_VA	5_VS_A	9_VS_LA	13_VS_W
M6 (SSA=VA)	2_S_VA	6_S_A	10_S_LA	14_S_WA
M7 (SSA=VA)	3_M_VA	7_M_A	11_M_LA	15_M_WA
M8 (SSA=VA)	4_L_VA	8_L_A	12_L_LA	16_L_WA

<sup>a</sup>Target atmospheric components chosen to model BB particles in the theoretical sensitivity study, of which the AOD is set to 0.2 or 0.5, are 1\_VS\_VA, 3\_M\_VA, 4\_L\_VA, 6\_S\_A, 7\_M\_A, 8\_L\_A, 11\_M\_LA, and 16\_L\_WA.

<sup>b</sup>VS = very small, S = small, M = medium, and L = large; VA = very absorbing, A = absorbing, LA = less absorbing, and WA = weakly absorbing.

Table 5-7. Summary of Sensitivity Results for Unimodal BB Particle Cases<sup>a</sup>

<b>Size Discrimination</b>				
Atmospheric Component	Retrieved AOD and Particle Size (Assumed AOD = 0.2)		Retrieved AOD and Particle Size (Assumed AOD = 0.5)	
	AOD	Size	AOD	Size
<u>SSA = very absorbing</u>				
Very small (1_VS_VA)	0.20	very small	0.50	very small
Medium (3_M_VA)	0.20	medium to large	0.50	medium
Large (4_L_VA)	0.20	medium to large	0.45– 0.50	large
<u>SSA = absorbing</u>				
Small (6_S_A)	0.20	small	0.50	small
Medium (7_M_A)	0.20	medium to large	0.50	medium to large
Large (8_L_A)	0.20	medium to large	0.50	large
<u>SSA = weakly–less absorbing</u>				
Medium (11_M_LA)	0.20	medium to large	0.50	medium to large
Large (16_L_WA)	0.20	medium to large	0.50	large
<b>SSA Discrimination</b>				
Atmospheric Component	Retrieved AOD and Particle SSA <sup>a</sup> (Assumed AOD = 0.2)		Retrieved AOD and Particles SSA <sup>a</sup> (Assumed AOD = 0.5)	
	AOD	SSA	AOD	SSA
<u>Size = very small–small</u>				
Very absorbing (1_VS_VA)	0.20	very absorbing	0.50	very absorbing
Absorbing (6_S_A)	0.20	very to weakly absorbing	0.50	very to weakly absorbing.
<u>Size = medium</u>				
Very absorbing (3_M_VA)	0.20	very absorbing	0.50	very absorbing
Absorbing (7_M_A)	0.20	very to weakly absorbing	0.50	very to weakly absorbing
Less absorbing (11_M_LA)	0.20	absorbing to weakly absorbing	0.50	absorbing to weakly absorbing

Table 5-7. (Continued)

<b>SSA Discrimination</b>				
Atmospheric Component	Retrieved AOD and Particle SSA <sup>a</sup> (Assumed AOD = 0.2)		Retrieved AOD and Particles SSA <sup>a</sup> (Assumed AOD = 0.5)	
	AOD	SSA	AOD	SSA
<u>Size = large</u>				
Very absorbing (4_L_VA)	0.20	very absorbing	0.45– 0.50	very absorbing
Absorbing (8_L_A)	0.20	very to weakly absorbing	0.50	very to weakly absorbing
Weakly absorbing (16_L_WA)	0.20	less to weakly absorbing	0.50	weakly absorbing

<sup>a</sup>Retrieved Particles refer to the components that contribute over 20% to the total aerosol optical depth, for retrieval results obtained with  $\chi^2_{max} < 1.5$ .

Table 5-8. Additional Components Used in the MISR Research Aerosol Retrieval Algorithm for the Four Representative Coincident BB Cases

Component Model	$r_{pg,N}$ , $\mu\text{m}^a$	$\sigma_g$	$\omega_{0,446}$	$\omega_{0,558}$	$\omega_{0,672}$	$\omega_{0,867}$	$n_r$ (all $\lambda$ 's)	Description
Medium dust	0.50	1.5	0.919	0.977	0.994	0.997	1.51	weakly absorbing grains <sup>b</sup>
Coarse dust	1.00	2.0	0.810	0.902	0.971	0.983	1.51	weakly absorbing spheroids <sup>b</sup>
Sulfate	0.06	1.7	1.000	1.000	1.000	1.000	1.45	small, non-absorbing sphere <sup>c</sup>
Medium sea salt	0.50	1.8 5	1.000	1.000	1.000	1.000	1.45	medium, non-absorbing sphere <sup>c</sup>
Coarse sea salt	1.00	1.9	1.000	1.000	1.000	1.000	1.45	large, non-absorbing sphere <sup>c</sup>

<sup>a</sup>Size distribution lower and upper cut -offs are 0.1 and 1.0  $\mu\text{m}$  for medium dust, 0.1 and 6.0  $\mu\text{m}$  for coarse dust, 0.00274 and 0.747  $\mu\text{m}$  for sulfate, 0.0132 and 8.88  $\mu\text{m}$  for medium sea salt, 0.0221 and 19.8  $\mu\text{m}$  for coarse sea salt.

<sup>b</sup>Dust models from *Kalashnikova et al.*, [2005].

<sup>c</sup>Models from the MISR v17 Standard Algorithm.

Table 5-9. Additional Components Used in the MISR Research Aerosol Retrieval Algorithm for the Four Representative Coincident BB Cases

Case Group	1 (BB-Dominated)	2 (BB-Dust Mixed)	3 (BB-Dust Mixed)	4 (BB-Dust Mixed)
Site	Cuiaba-Miranda	Ilorin	Ouagadougou	Ilorin
MISR Path	227	191	195	190
Block	103	84	81	84
Hazy Day Date	2001/08/31	2001/02/24	2000/12/18	2001/02/17
Overpass (UTC)	14:16:13	10:31:41	10:56:28	10:25:44
Orbit	9061	6321	5331	6219
Clean Day Date	2001/07/30	2001/03/12	2001/01/19	2001/02/01 (2000/11/13) <sup>b</sup>
Overpass (UTC)	14:17:10	10:30:52	10:55:39	10:25:57 (10:27:17)
Orbit	8595	6554	5797	5986 (4821)
$AOD_A^a$	$0.12 \pm 0.00$	$0.61 \pm 0.00$	$0.35 \pm 0.01$	$0.41 \pm 0.02$ (0.22) <sup>c</sup>
P0	-15.72°N, -56.02°E	8.31°N, 4.33°E	12.18°N, -1.39°E	8.31°N, 4.33°E
P1	-15.59°N, -55.84°E	8.57°N, 4.67°E	12.36°N, -1.08°E	8.25°N, 4.60°E
P2	-15.56°N, -56.03°E	8.58°N, 4.35°E	12.37°N, -1.17°E	8.27°N, 4.75°E
P3	-15.40°N, -56.09°E	8.61°N, 4.06°E	12.11°N, -1.77°E	8.39°N, 4.71°E
P4	-15.60°N, -56.09°E	8.53°N, 4.01°E	11.99°N, -1.36°E	8.55°N, 4.30°E
P5	-15.85°N, -56.17°E	—	12.05°N, -1.38°E	8.58°N, 4.00°E
P6	-16.03°N, -56.01°E	—	12.14°N, -1.39°E	8.40°N, 3.67°E
P7	—	—	—	8.29°N, 4.10°E

<sup>a</sup>Coincident AERONET Version 2, level 1.5 AOD measurements. Reported values are the mean of all available measurements interpolated linearly between the nearest AERONET channel pairs, usually 440 or 500 nm and 675 nm; within  $\pm 1$  hour of the MISR overflight.

<sup>b</sup>Surface RPV values for P0 in this case were not retrieved by the Standard Algorithm on 2001/02/01, so those retrieved on 2000/11/13, of which the orbital information is parenthesized, are used for P0 instead.

<sup>c</sup>No AERONET AOD measurement available. Reported value is MISR\_v17 AOD.

Table 5-10. AOD at 558 nm and Angstrom Exponent from AERONET Measurements, MISR v17 Standard Retrieval and Research Retrieval Results, for the Four Coincident BB Cases<sup>a</sup>

Site	Cuiaba-Miranda	Ilorin	Ouagadougou	Ilorin
Hazy Day Date	2001/08/31	2001/02/24	2000/12/18	2001/02/17
# of Patches Having $\chi^2 < 1.5$	5	3	3	5
Best $\chi^2$ in Research Retrieval (patch #)	0.39 (P2)	0.88 (P1)	0.35 (P3)	0.54 (P1)
$\chi^2$ in Research Retrieval at P0	6.56	1.24	1.38	6.83
Mid-visible AOD				
AERONET ( $AOD_A$ )	$0.34 \pm 0.01$	$0.88 \pm 0.00$	$0.53 \pm 0.01$	$1.74 \pm 0.03$
MISR_v17_3x3 ( $AOD_M$ )	0.30	0.63	0.43	0.78
Research-Best	0.35	1.00	0.50	1.55
Research-P0	0.45	0.75	0.40	2.00
(Research-Range)	(0.30–0.35)	(0.75–1.00)	(0.40–0.50)	(1.20–1.55)
Ångstrom Exponent				
AERONET ( $\text{Å}_A$ )	1.82	0.52	0.41	0.41
MISR_v17_3x3 ( $\text{Å}_M$ )	1.58	0.79	0.50	0.54
Research-best	1.86	0.72	0.79	0.78
Research-P0	1.69	1.47	1.33	0.71
(Research-Range)	(1.74–2.03)	(0.72–1.47)	(0.79–1.40)	(0.44–0.78)

<sup>a</sup>AERONET = coincident AERONET Version 2, level 1.5 measurements. Reported values are the mean of all available measurements interpolated linearly between the nearest AERONET channel pairs, usually 440 or 500 nm and 675 nm; within  $\pm 1$  hour of the MISR overflight for AOD, and  $\pm 2$  hours for SSA and size distribution. MISR\_v17 = best-fit mixture in the MISR v17 Standard Retrieval results for the 17.6 km region containing the AERONET site. Research = best-fit mixture from the Research Retrieval, using surface RPV derived for the corresponding clean day; results at the patch having the lowest  $\chi^2$  (-Best), at patch P0, and the range spanned by best-mixtures in all patches having  $\chi^2 < 1.5$  (-Range, parenthesized) are reported.

Table 5-11. Aerosol Fine Mode Fraction, Fine Mode Size, and Coarse Mode Size From AERONET Measurements, MISR v17 Standard Retrievals, and Research Retrieval Results, for the Four Coincident BB Cases

Site	Cuiaba-Miranda	Ilorin	Ouagadougou	Ilorin
Hazy Day Date	2001/08/31	2001/02/24	2000/12/18	2001/02/17
Spherical AOD Fraction at 558 nm				
AERONET	93%	44%	33%	35%
MISR_v17	100%	60%	40%	40%
Research-Best	100%	80%	95%	60%
Research-P0	95%	95%	100%	85%
(Research-Range)	(95-100%)	(80-100%)	(95-100%)	(50-60%)
Spherical Particle Size ( $\mu\text{m}$ ) and Fraction				
AERONET	0.10 $\pm$ 0.00 (93%)	0.06 $\pm$ 0.00 (44%)	0.06 $\pm$ 0.00 (33%)	0.06 $\pm$ 0.00 (35%)
MISR_v17	0.06, 80% 1.00, 20%	0.06, 54% 1.00, 6%	0.06, 36% 1.00, 4%	0.06, 36% 1.00, 4%
Research-Best	0.04, 40% 0.07, 15% 0.13, 15% 0.16, 30%	0.07, 5% 0.13, 10% 0.16, 65%	0.16, 95%	0.07, 30% 0.13, 25% 0.16, 5%
Research-P0	0.07, 60% 0.16, 35%	0.07, 40% 0.13, 45% 0.16, 10%	0.04, 5% 0.13, 80% 0.16, 15%	0.16, 85%
(Research-Range)	(0.04, 15–40%) (0.07, 15–80%) (0.13, 0–60%) (0.16, 0–30%)	(0.07, 5–40%) (0.13, 10–45%) (0.16, 10–75%)	(0.04, 0–25%) (0.07, 0–10%) (0.13, 0–80%) (0.16, 15–95%)	(0.04, 0–10%) (0.07, 0–30%) (0.13, 25–50%) (0.16, 0–40%)

Table 5-11. (Continued)

Site	Cuiaba-Miranda	Ilorin	Ouagadougou	Ilorin
Hazy Day Date	2001/08/31	2001/02/24	2000/12/18	2001/02/17
Nonspherical Particle Size ( $\mu\text{m}$ ) and Fraction				
AERONET	$0.62 \pm 0.02$ (7%)	$0.66 \pm 0.04$ (56%)	$0.80 \pm 0.01$ (67%)	$0.68 \pm 0.05$ (65%)
MISR_v17	—, 0%	0.50, 40%	0.50, 60%	0.50, 60%
Research-Best	—, 0%	0.50, 20%	0.50, 5%	0.50, 40%
Research-P0	0.50, 5%	0.50, 5%	—, 0%	1.00, 15%
(Research-Range)	(0.50, 0–5%)	(0.50, 0–20%)	(0.50, 0–5%)	(0.50, 0–55%)

Table 5-12. Total and Fine Mode SSA and SSA Spectral Dependence From AERONET Measurements, MISR v17 Standard Retrieval, and Research Retrieval Results, for the Four Coincident BB Cases

Site	Cuiaba-Miranda	Ilorin	Ouagadougou	Ilorin
Hazy Day Date	2001/08/31	2001/02/24	2000/12/18	2001/02/17
Total Mid-visible SSA				
AERONET ( $SSA_A$ )	$0.80 \pm 0.01$	$0.92 \pm 0.01$	$0.94 \pm 0.00$	$0.93 \pm 0.01$
MISR_v17 ( $SSA_M$ )	0.92	1.00	0.99	0.99
Research-Best	0.838	0.939	0.935	0.900
Research-P0	0.903	0.903	0.939	0.931
(Research-Range)	(0.838–0.899)	(0.899–0.935)	(0.899–0.939)	(0.900–0.931)
SSA spectral dependence				
AERONET ( $\alpha_{\omega_0 A}$ )	+0.16	-0.07	-0.07	-0.08
MISR_v17 ( $\alpha_{\omega_0 M}$ )	+0.03	-0.01	-0.05	-0.05
Research-Best	+0.07	0.00	+0.05	-0.08
Research-P0	+0.15	+0.06	+0.07	+0.02
(Research-Range)	(+0.07 to +0.15)	(0.00 to +0.06)	(0.00 to +0.07)	(-0.11 to +0.02)

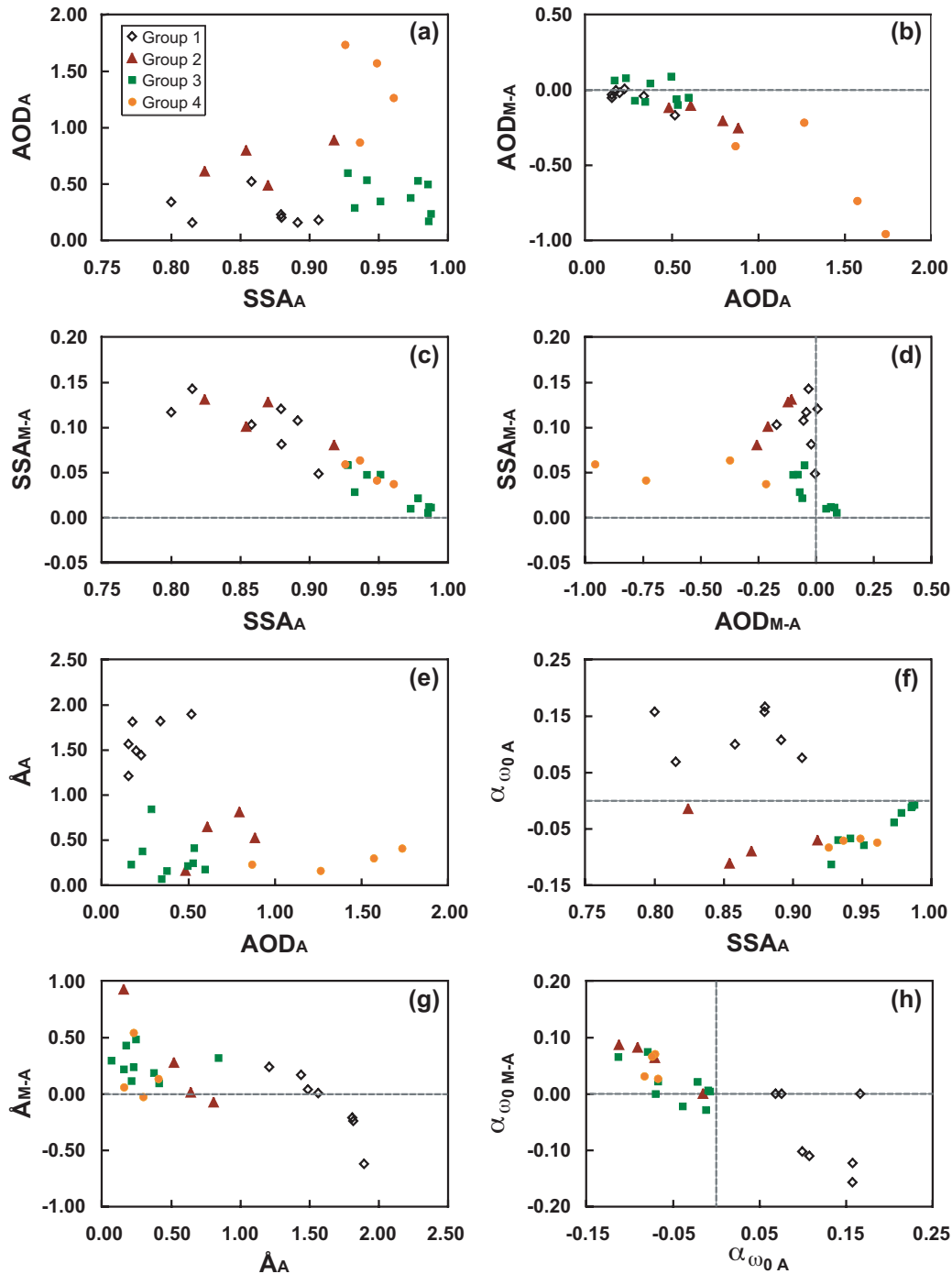


Figure 5-1. Comparisons among coincident MISR-AERONET BB cases with mid-visible AOD > 0.15: (a) AERONET mid-visible AOD ( $AOD_A$ ) vs. SSA ( $SSA_A$ ), (b)  $AOD_A$  vs. difference in AOD ( $AOD_{M-A}$ ), (c)  $SSA_A$  vs. difference in SSA ( $SSA_{M-A}$ ), (d)  $AOD_{M-A}$  vs.  $SSA_{M-A}$ , (e) AERONET Ångstrom Exponent ( $\hat{A}_A$ ) vs.  $AOD_{M-A}$ , (f) AERONET SSA spectral dependence ( $\alpha_{\omega_0 A}$ ) vs.  $SSA_A$ , (g)  $\hat{A}_A$  vs. difference in Ångstrom Exponent ( $\hat{A}_{M-A}$ ), (h)  $\alpha_{\omega_0 A}$  vs. difference in SSA spectral dependence ( $\alpha_{\omega_0 M-A}$ ). In each panel, cases are categorized into four groups (see text for details): black diamonds for group 1, red triangles for group 2, green squares for group 3, and yellow circles for group 4.

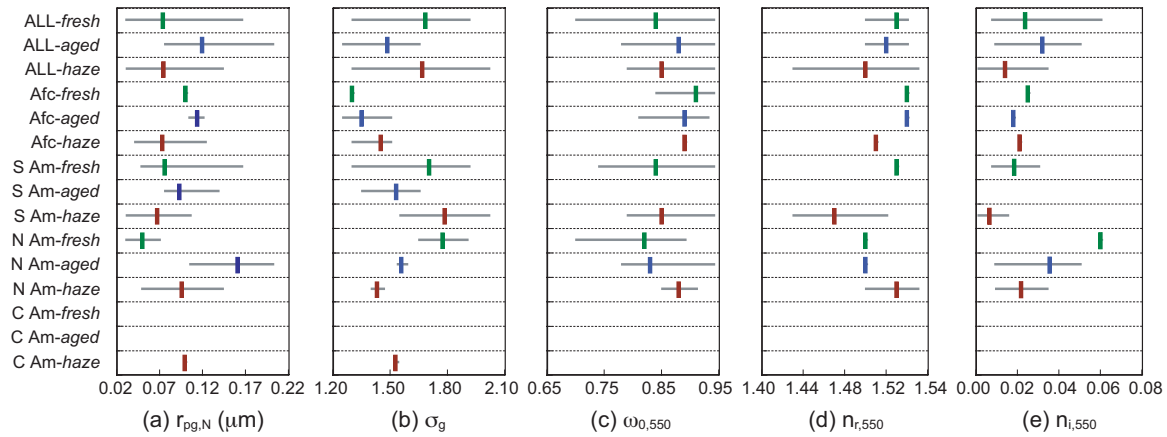


Figure 5-2. The means (vertical lines) and ranges (grey bars) of reported physical and optical parameter values for haze, aged, and fresh plumes in different regions: (a) number-weighted geometric mean radius ( $r_{pg,N}$ ), (b) geometric standard deviation ( $\sigma_g$ ), (c) single scattering albedo at 550 nm ( $\omega_{0,550}$ ), (d) real part of refractive index ( $n_r$ ) at 550 nm, and (e) imaginary part of refractive index ( $n_i$ ) at 550 nm. The vertical lines are red for fresh plumes (< 1 day old), blue for aged plumes (1–3 days old), and green for regional haze (> 3 days old or mixed). (Abbreviations: Afc = Africa, S Am = South America, N Am = North America, C Am = Central America)

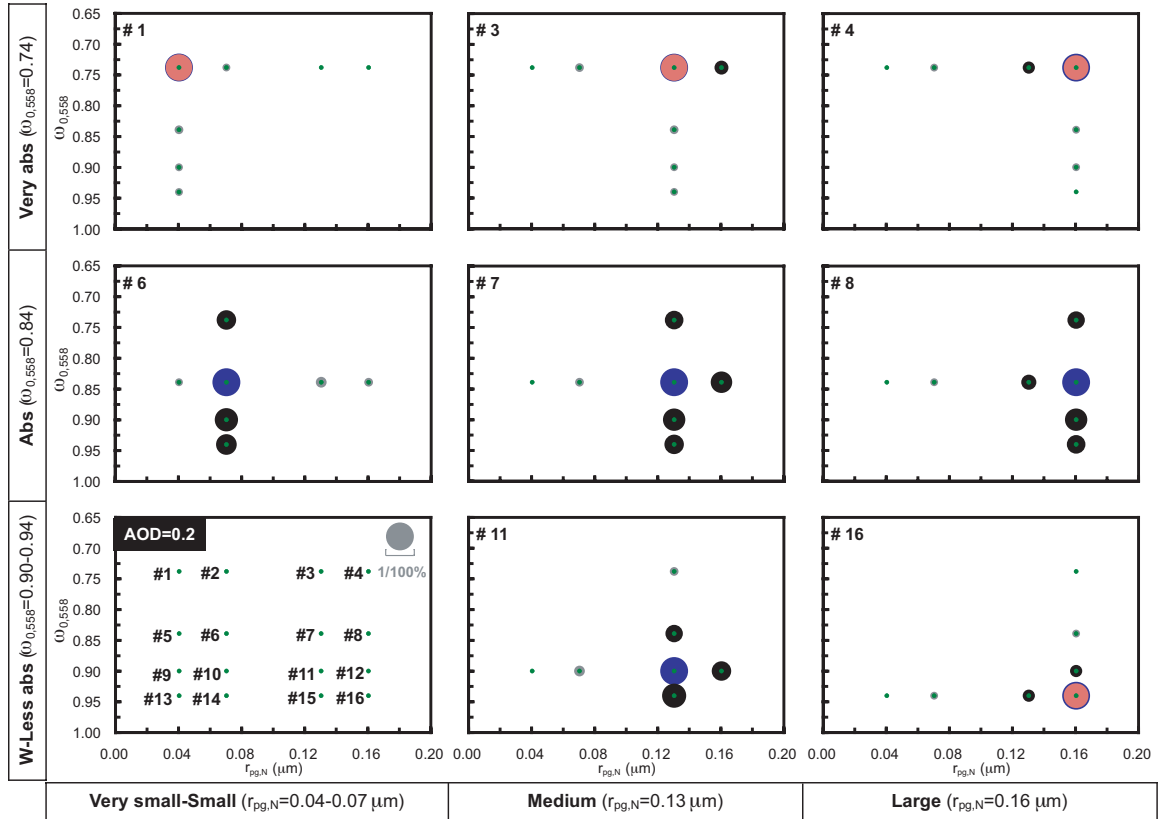


Figure 5-3. Sensitivity results of eight target atmospheric BB components assuming AOD = 0.2. Each individual sub-plot shows the results for comparisons against one target atmospheric component (marked at the upper-left corner of each sub-plot), with the comparison space  $r_{pg,N}$  and  $\omega_{0,558}$  values organized along the x and y axes, respectively. Overall, the plot array is arranged by the  $r_{pg,N}$  and  $\omega_{0,558}$  of the target atmospheric components (marked at the bottom and the left of the plate). The lower-left sub-plot shows positions of all components on the  $r_{pg,N}$ - $\omega_{0,558}$  plane (green spots). Retrieved component fractions are proportional to the area of colored circles; the gray circle in the lower-left plot is the scale of 100% fraction. For the target atmospheric component in each panel, the red circle shows the minimum retrieved fraction, and the blue shows the maximum fraction. For the other components, the circle shows only the maximum fraction, and is shaded black if more than 20%, otherwise, gray. Conditions of 1 atm surface pressure and  $2.5 \text{ ms}^{-1}$  wind speed, for mid-latitude geometry, over a dark water surface, are assumed in these radiative transfer calculations.

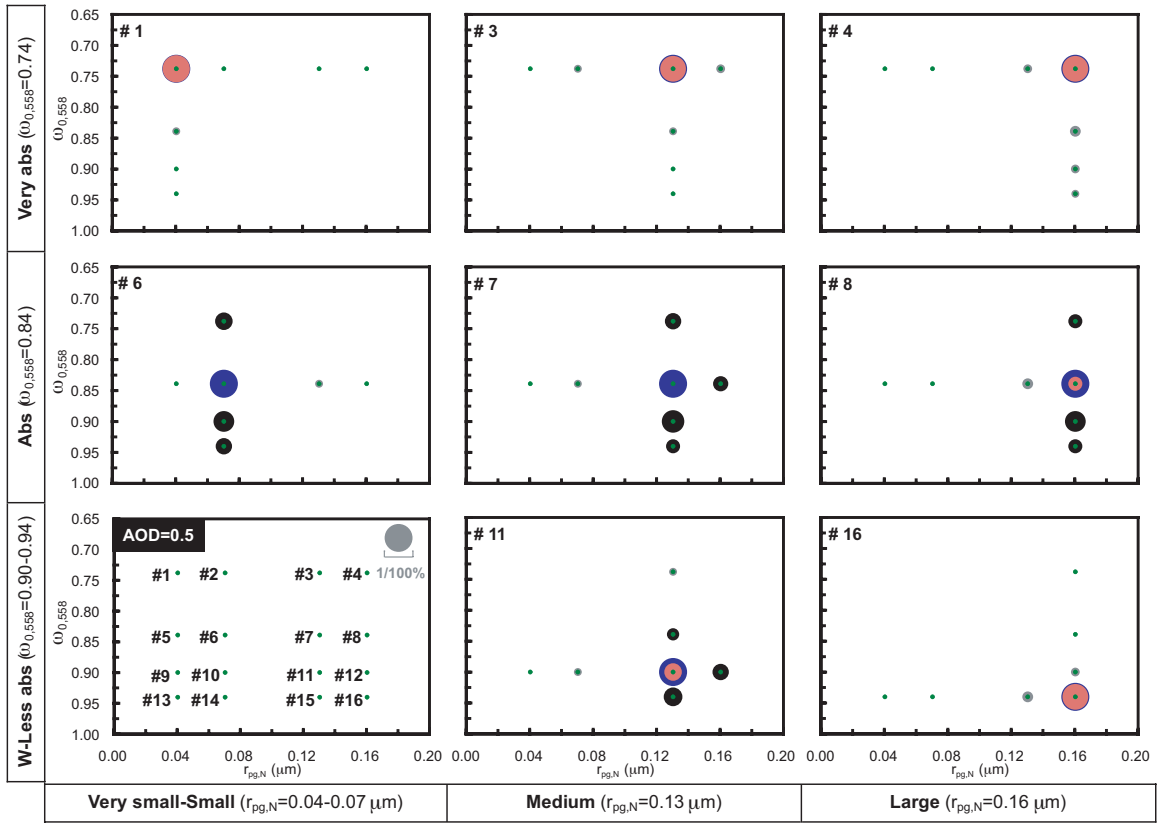


Figure 5-4. Same as Figure 5-3, but for atmospheric BB components with having AOD = 0.5.

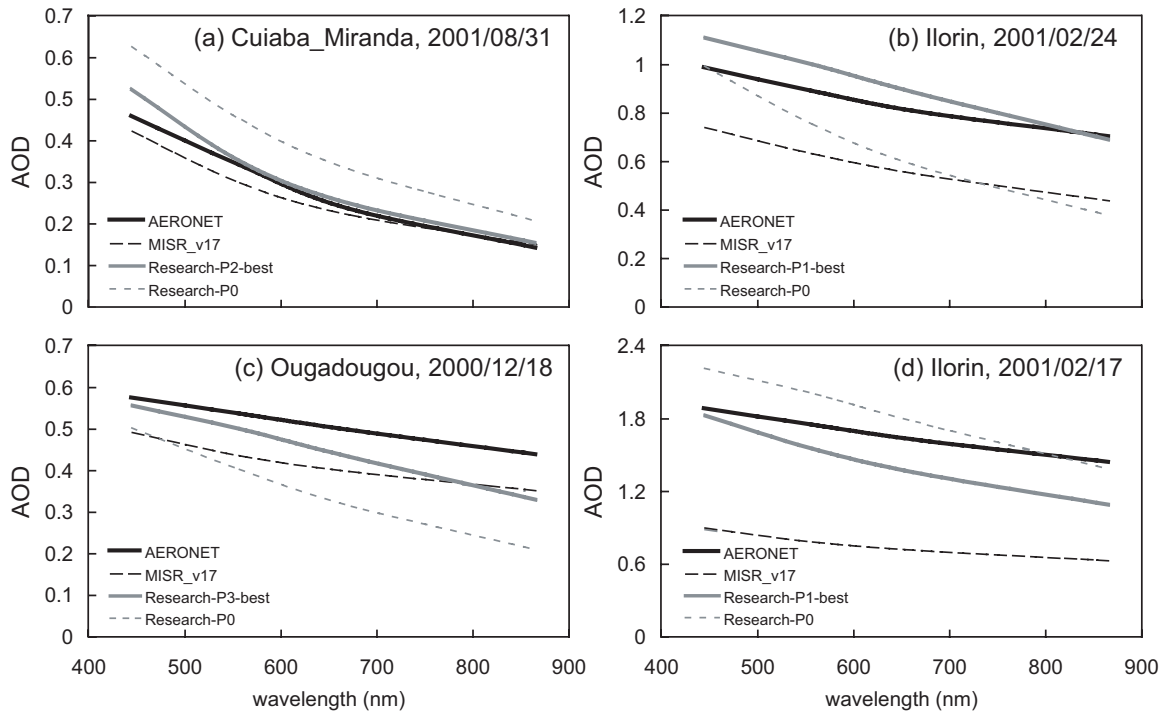


Figure 5-5. Spectral AOD for coincident AERONET measurements (black solid lines), best-fit MISR v17 Standard Retrievals (black dashed lines), and best-fit Research Retrievals for all patches (gray solid lines for patch with lowest  $\chi^2$ , gray dotted lines for patch P0) for the four coincident BB cases.

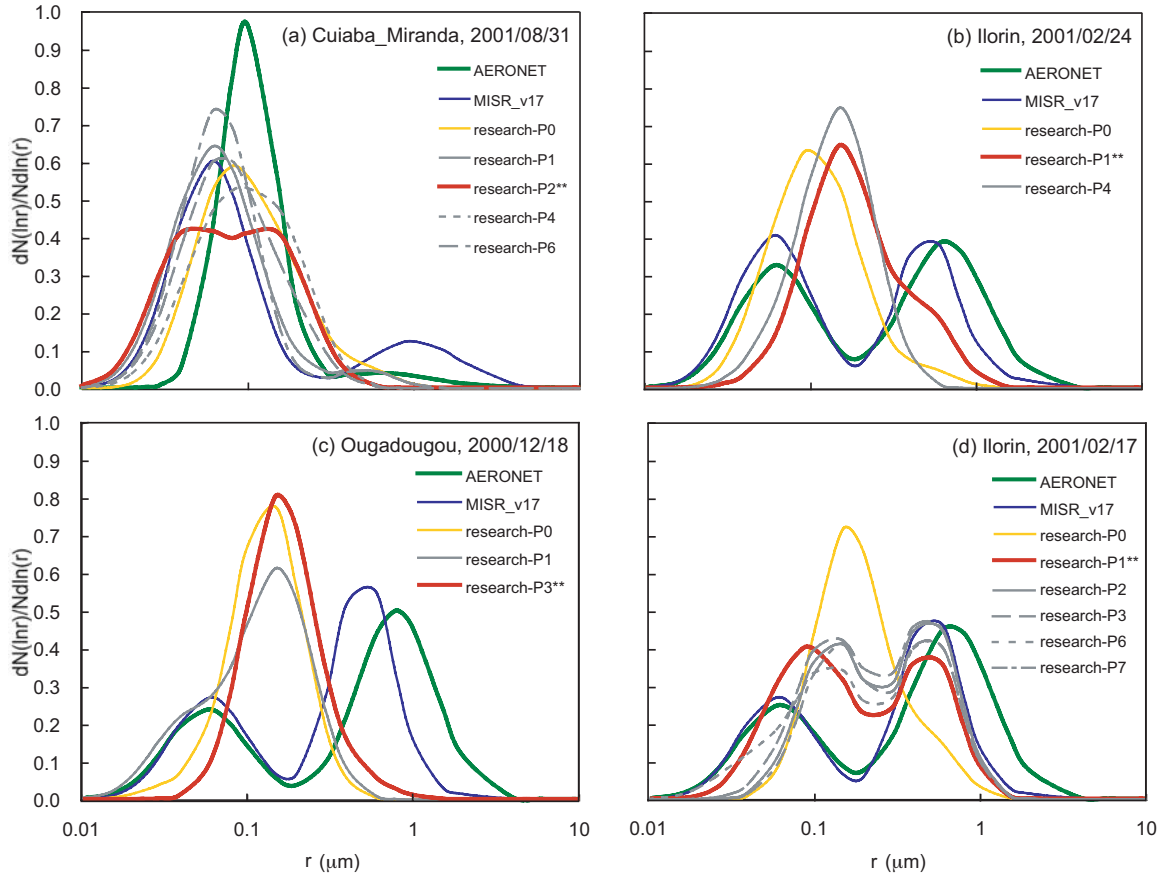


Figure 5-6. Normalized number size distributions for coincident AERONET measurements (green lines), best-fit MISR v17 Standard Retrievals (blue lines), and best-fit Research Retrievals (red lines for the best patch, yellow lines for P0, and gray lines for patches with  $\chi^2 < 1.5$ ) for the four coincident BB cases. The best patch is also denoted by \*\* in the legend.

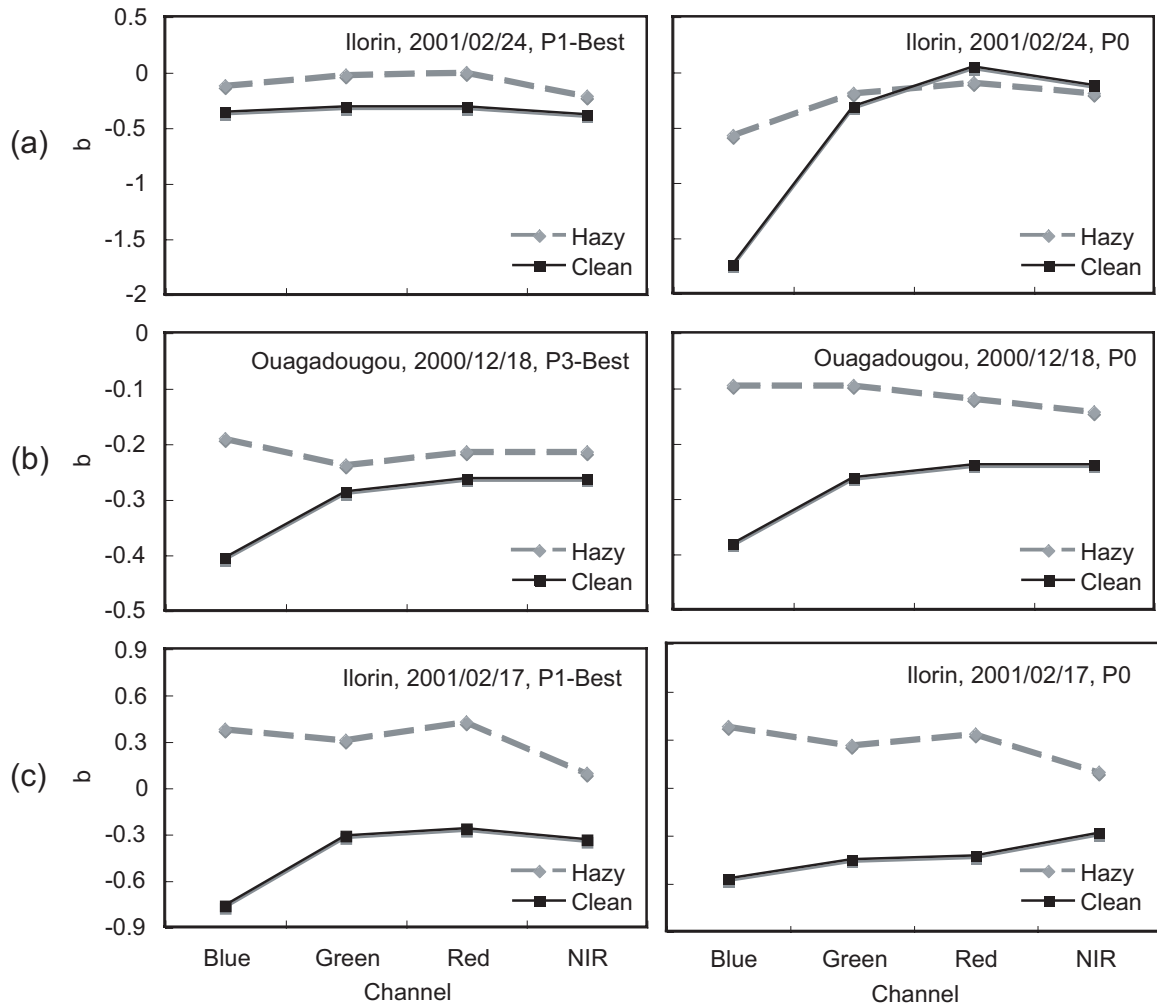


Figure 5-7. The third surface RPV parameter retrieved by the MISR v17 Standard Algorithm at all four MISR channels for hazy day (gray dashed lines) and the clean day orbit (black solid lines) for (a) Ilorin\_2001/02/24, (b) Ouagadougou\_2000/12/18, and (c) Ilorin\_2001/02/17. For each case, plots are shown for the best patch (left) and for P0 (right).